UNIVERSIDADE DE LISBOA
INSTITUTO SUPERIOR TÉCNICO

Channel Modelling for Polarised Off-Body Communications with Dynamic Users

Kenan Turbić

Supervisor: Doctor Luís Manuel de Jesus Sousa Correia
Co-Supervisor: Doctor Marko Beko

Thesis approved in public session to obtain the PhD Degree in
Electrical and Computer Engineering

Jury final classification: *Pass with Distinction and Honour*

2019

UNIVERSIDADE DE LISBOA
INSTITUTO SUPERIOR TÉCNICO

Channel Modelling for Polarised Off-Body Communications with Dynamic Users

Kenan Turbić

Supervisor: Doctor Luís Manuel de Jesus Sousa Correia
Co-Supervisor: Doctor Marko Beko

Thesis approved in public session to obtain the PhD Degree in
Electrical and Computer Engineering

Jury final classification: *Pass with Distinction and Honour*

Jury

Chairperson: Doctor Mário Alexandre Teles de Figueiredo,
Instituto Superior Técnico, Universidade de Lisboa

Members of the Committee:

Doctor Filipe Duarte dos Santos Cardoso,
Escola Superior de Tecnologia de Setúbal, Instituto Politécnico de Setúbal;

Doctor Luís Manuel de Jesus Sousa Correia,
Instituto Superior Técnico, Universidade de Lisboa;

Doctor Katsuyuki Haneda,
School of Electrical Engineering, Aalto University, Finlândia;

Doctor Custódio José de Oliveira Peixeiro,
Instituto Superior Técnico, Universidade de Lisboa;

Doctor António José Castelo Branco Rodrigues,
Instituto Superior Técnico, Universidade de Lisboa.

2019

To my parents,
Jadranka and Zahid Turbić

Acknowledgments

First of all, I would like to express my gratitude to my supervisor, Prof. Luis M. Correia, for his guidance and support during the development of this thesis. His broad professional experience, valuable organisational skills and constructive criticism helped to keep this work on track. I am particularly grateful for the unique opportunities that allowed to meet and collaborate with researchers from all around Europe, which not only helped to improve this thesis, but also allowed me to meet people I consider life-long friends. I would also like to thank my co-supervisor, Prof. Marko Beko, whose comments played a valuable role in improving this dissertation.

My gratitude also goes to Dr. Slawomir J. Ambroziak from the Technical University of Gdansk, Poland, with whom I was intensively collaborating during the PhD. His contributions to our joint work are well appreciated, but I am also very grateful to him and his family for a warm hospitality during my visit to Gdansk, to perform measurements.

I would also like to acknowledge the COST Action CA15104, IRACON. Participation in these meetings and discussions with other researchers had a valuable impact on this thesis, but also sparked ideas for future work. Some of the work presented in this thesis was also financially supported by IRACON, namely the wideband off-body channel measurement campaign in Gdansk.

I am tankful to my fellow colleagues and friends, Behnam Rouzbehani and Mojgan Barahman, with whom I was sharing the ups and downs during our PhD fellowships. I will always remember our discussions and jokes that helped us to bare through the chaotic moments. My gratitude also goes to the rest of the GROW team, Vera Almeida and Ema Caterre, whose help made work easier during this period.

I am very thankful for all the great people I have met during my PhD fellowship. My life in Lisbon certainly would not be as pleasant without Jelena and Aleksandar Ilić, whose friendship I highly appreciate. A special thanks goes to Diego Felix de Souza and Wilmer Da Silva Marcial, for all the fun times we had together in Lisbon.

I have to express my deep gratitude to Prof. Kenan Suruliz from University of Sarajevo, my first academic mentor, whom I highly admire both as a professional and an individual. His enthusiasm and diverse scientific knowledge greatly affected my curiosity as a student, having a major effect on my further development and academic choices.

I would like to thank my dear Gizem, for her support and encouragement when it was needed the most. Her unique spirit and enthusiasm was cheering me up, even when she was going through her own PhD struggles.

Finally, my deepest gratitude goes to my parents, Jadranka and Zahid Turbić, for their unconditional love, support and encouragement throughout my life and the years of the PhD. Without them, I would never have gotten to this point and this thesis would never have been written.

Abstract

This thesis presents a channel model for off-body communication with dynamic users, which considers the depolarisation effect and takes the important influence of user mobility into account. A geometry-based propagation channel model was developed, where the depolarisation effects due to propagation path geometry, scattering mechanisms, antennas' polarisation characteristics and their orientations are considered. An analytical mobility model for wearable antennas was also developed to account for the effects of user's motion, with parameters calculated from high-resolution Motion Capture data; the position and antenna orientation errors in between the two are below 3.2 cm and 9°, respectively. The channel model is used to simulate scenarios with the user at a fixed distance from the off-body antenna, walking or running in place, considering free space propagation and scattering on a cylinder centred around the user. Simulation results show that significant polarisation mismatch losses occur due to wearable antenna rotations, resulting in the received power variation up to 37.5 dB for the Line-of-Sight component and 41.4 dB for the scattered one, in the considered scenarios. User's motion and wearable antenna placement have an important impact on channel characteristics. That is, antenna placements on the arms and legs yield larger and faster signal variations compared to those on less dynamic body parts as the torso and head, hence presenting themselves as less favourable from the system performance perspective. The importance of modelling the polarisation aspect of the channel is demonstrated by comparing simulation results between polarised and non-polarised channel models in a free space propagation scenario, where the difference in between the two is observed to be up to 53 dB.

Keywords: Wireless Communications, Body Area Networks, Signal Depolarisation, Dynamic Users, Radio Channel Modelling.

Sažetak

Ova doktorska disertacija predstavlja razvoj modela komunikacijskog kanala između fiksne antene i uređaja na tijelu korisnika u pokretu, a koji uzima u ozir depolarizaciju signala te uticaj korisnikovog kretanja. U prvom koraku je razvijen propagacijski model koji obuhvata depolarizacijske efekte vezane za geometriju putanja signala između antena, propagacijske mehanizme, polarizacijske karakteristike antena, te njihovu orijentaciju. Potom je razvijen analitički model kretanja antena nošenih na tijelu, da bi se uzeli u obzir efekti pokreta korisnika. Parameteri ovog modela su određeni na osnovu Motion Capture podataka visoke rezolucije, sa maksimalnom dobijenom greškom u poziciji i orijentaciji antene od 3.2 cm, odnosno 9°. Model kanala je korišten za simulaciju scenarija u kojima korisnik hoda ili trči u mjestu, na konstantnoj udaljenosti od fiksne antene, razmatrajući propagaciju u slobodnom prostoru i refleksije na cilintričnoj površi sa korisnikom u centru. Rezultati simulacije pokazuju da rotacija antene tokom kretanja korisnika uzrokuje značajne gubitke uslijed polarizacijskog nesklada između antene i dolazećeg radio talasa, što u razmatranim scenarijima dalje rezultira varijacijom prijemne snage do 37.5 dB u slobodnom prostoru, te 41.4 dB u slučaju višeputanjske propagacije. Kretanje korisnika i položaj antene na tijelu imaju značajan uticaj na karakteristike kanala. Varijacije prijemnog signala dobijenog sa antena postavljenih na rukama i nogama su veće i brže nego kada su antene postavljene na manje dinamičnim dijelovima tijela, npr. torzo i glava, bivajući tako manje pogodnim sa aspekta performansi sistema. Na primjeru scenarija sa propagacijom u slobodnom prostoru, važnost modeliranja depolarizacije signala u komunikacijskom kanalu je demonstrirana poređenjem rezultata simulacije dobijenih korištanjem modela kanala koji uzima i onog koji ne uzima u obzir polarizaciju, gdje je uočena razlika i do 53 dB.

Ključne riječi: Bežične komunikacije, Komunikacijske mreže na tijelu, Depolarizacija signala, Dinamični korisnici, Modeliranje radio kanala.

Resumo

Esta tese apresenta um modelo de canal para comunicações extra-corpo com utilizadores dinâmicos, que considera o efeito de despolarização e contabiliza a importante influência da mobilidade do utilizador. Foi desenvolvido um modelo de canal de propagação baseado em geometria, onde se considera o efeito de despolarização devido à geometria do percurso de propagação, aos mecanismos de rerradiação, e às características de polarização e orientação das antenas. Desenvolveu-se também um modelo analítico para antenas usáveis no corpo que contabiliza os efeitos da mobilidade do utilizador, com parâmetros calculados a partir de dados de alta-resolução de Motion Capture; os erros na posição e orientação da antena entre as duas abordagens é inferior a 3.2 cm e 9°, respetivamente. O modelo de canal é usado para simular cenários com o utilizador a uma distância fixa da antena externa, andando ou correndo no lugar, considerando propagação em espaço livre, e rerradiação num cilindro centrado no utilizador. Os resultados de simulação mostram que ocorrem perdas significativas por desadaptação de polarização devido à rotação das antenas usáveis, resultando em variações na potência de receção até 37.5 dB para a componente de linha de vista e 41.4 dB para a de rerradiação, nos cenários analisados. A mobilidade dos utilizadores e a localização das antenas usáveis têm uma grande influência nas características do canal: antenas nos braços e nas pernas levam a variações do sinal grandes e rápidas, comparadas com as que ocorrem em partes menos dinâmicas do corpo, como a cabeça e o tronco, apresentando-se como localizações menos favoráveis do ponto de vista de desempenho do sistema. A importância de modelar a polarização do canal é demonstrada pela comparação de resultados de simulação, entre os casos de modelos contabilizando ou não a polarização num ambiente de espaço livre, com a diferença atingindo 53. dB.

Palavras-chave: Comunicações sem-fios, Redes Corporais, Despolarização do sinal, Utilizadores Dinâmicos, Modelação de canais rádio.

Table of Contents

List of Figures

List of Tables

List of Acronyms

3D	Three-dimensional
AAoA	Azimuth Angle of Arrival
AAoD	Azimuth Angle of Departure
AIC	Akaike Information Criterion
AoA	Angle of Arrival
AoD	Angle of Departure
AP	Access Point
BAN	Body Area Network
BCC	Body Coupled Communication
CIR	Channel Impulse Response
CP	Co-Polarisation
CPR	Co-Polarisation Ratio
CSMA-CA	Carrier Sense Multiple Access with Collision Avoidance
DoA	Direction of Arrival
DoD	Direction of Departure
DS-SS	Direct Sequence Spread Spectrum
EAoA	Elevation Angle of Arrival
EAoD	Elevation Angle of Departure
EIRP	Equivalent Isotropically Radiated Power
EM	Electromagnetic
FEC	Forward Error Correction
GBSC	Geometry-Based Stochastic Channel
GO	Geometrical Optics
GoF	Goodness of Fit
GTDe	Geometrical Theory of Depolarisation
H	Horizontal (polarisation)
HCI	Human-Computer Interface
ICC	Inductive Coupled Communication
IF	Intermediate Frequency
IR-UWB	Impulse Radio UWB

ISM	Industrial, Scientific and Medical
LAN	Local Area Network
LoS	Line-of-Sight
MAC	Medium Access Control
MIMO	Multiple-Input Multiple-Output
mmWave	Millimetre Wave
MoCap	Motion Capture
MPC	Multipath Component
MPL	Mean Path Loss
NLoS	Non-LoS
PAN	Personal Area Network
PDF	Probability Density Function
PHY	Physical layer
PLF	Polarisation Loss Factor
QLoS	Quasi-LoS
RMSE	Root Mean Square Error
RPGM	Reference Point Group Mobility
Rx	Receiver
SAR	Specific Absorption Rate
Sc	Scatterer
Tx	Transmitter
UTD	Uniform Theory of Diffraction
UWB	Ultra-wideband
V	Vertical (polarisation)
VNA	Vector Network Analyser
VR	Virtual Reality
WAN	Wide Area Network
WSN	Wireless Sensor Network
XP	Cross-Polarisation
XPD	Cross-Polarisation Discrimination
XPI	Cross-Polarisation Isolation
XPR	Cross-Polarisation Ratio

List of Symbols

α_w	Wedge inner angle
β_r	Regularising term weight for CIR path estimation
χ^2	χ^2 test statistic
χ^2_{crit}	χ^2 test statistic critical value
$\Delta h_{t/s}$	Tx/Sc height relative to Rx
ΔL_{ls}	Large-scale fading
$\Delta\mathbf{r}$	Wearable antenna periodic displacement
$\Delta\tau$	Delay resolution in CIR
ΔL_{ss}	Small-scale fading
ϵ_r	Relative dielectric constant
γ_i	Euler rotation angles for antenna orientation
$\mathbf{\Gamma}_{r/d}$	Reflection/diffraction matrix
λ	Wavelength
μ	Mean value
μ_L	Log mean parameter of Lognormal distribution
Ω_{Nak}	Scale parameter of Nakagami-m distribution
$\phi_i^{t/d}$	Incidence/diffraction angle with respect to the 0-face of the wedge
ϕ_{max}	Maximum antenna gain direction azimuth
φ_n	Phase of *n*-th multipath component
ϕ_s	Sc position azimuth in the scatterning cylinder
$\hat{\phi}_{t/r}$	AAoD/AAoA in the global coordinate system
$\phi_{t/r}$	AAoD/AAoA in the Tx/Rx antenna's local coordinate system
ϕ_u	User orientation angle
ψ_i	Diffraction incidence angle with respect to the edge
$\hat{\psi}_{t/r}$	EAoD/EAoA in the global coordinate system
$\psi_{t/r}$	EAoD/EAoA in the Tx/Rx antenna's local coordinate system
σ	Standard deviation
σ_L	Log standard deviation parameter of Lognormal distribution
σ_{Ray}	Scale parameter of Rayleigh distribution
σ_{Rice}	Scale parameter of Rice distribution

σ_τ	Delay spread
τ	Propagation delay
$\overline{\tau}$	Mean excess delay
ϑ_e	Angle between the conventional and edge-fixed planes of incidence
ϑ_i	Incidence/reflection angle
$\vartheta_i^{0/n}$	Incidence/reflection angle at the $0/n$-face of the wedge
ϑ_{LoS}	Angle between Tx and Rx θ-polarisations in LoS direction
$\vartheta_{pol}^{i/r}$	Incident/reflected signal polarisation angle, relative to incidence plane normal
$\vartheta_{pol}^{ta/ra}$	Tx/Rx antenna polarisation angle, relative to θ-polarisation
$\vartheta_{t/r}$	Angle between Tx/Rx antenna's θ-polarisation in DoD/DoA, and incidance plane normal
$\vartheta_{ta/ra}$	Angle between Tx/Rx antenna θ-polarisation and V-polarised reference in DoD/DoA
$\vartheta_{ts/rs}$	Angle between Tx/Rx antenna θ-polarisation and V-polarised reference in DoD/DoA

$\mathbf{a}_0$	Average antenna displacement vector (Fourier series representation)
A_n	Amplitude of n-th multipath component
$\mathbf{a}_n^{c/s}$	Amplitude of n-th harmonic's cosine/sine component for antenna displacement (Fourier series representation)
A_{sf}^n	Wavefront spreading factor of n-th multipath component
$b_{0,i}$	Average value of i-th Euler angle in Fourier series representation
$b_{n,i}^{c/s}$	Amplitude of n-th harmonic's cosine/sine component for i-th Euler angle in Fourier series representation
c	Speed of light
d	Horizontal distance between the Tx and Rx antennas
$D_{i/r}^{0/n}$	Diffraction coefficient for incidence/reflection associated with $0/n$-face of the wedge
$r_{ts/rs}$	Horizontal distance between the Tx/Rx and Sc
f	Frequency
f_c	Carrier frequency
f_D	Doppler shift frequency
$g_{t/r}^{\theta/\phi}$	Complex Tx/Rx antenna gain in θ/ϕ-polarisation
$G_{t/r}$	Total Tx/Rx antenna gain
$\mathbf{g}_{t/r}$	Field pattern with components in θ and ϕ directions of the Tx/Rx antenna
h_{ap}	AP height
h_{ch}	Complex baseband channel transmission coefficient
$\mathbf{H}_p$	Path polarisation matrix
$\hat{\mathbf{H}}_p$	Path polarisation matrix for vertical Tx and Rx antennas
$h_{t/r/s}$	Tx/Rx/Sc height

k	Propagation constant
$\mathbf{k}$	LoS component DoD/DoA unit vector
$\mathbf{k}_{t/r}$	MPC DoD/DoA unit vector
L_{pl}	Instantaneous path loss
$\overline{L_{pl}}$	Mean path loss
L_{PLF}	Polarisation loss factor
L_{sh}	Body-shadowing loss
L_{sh}^{max}	Maximum body-shadowing loss
m_{Nak}	Shape parameter of Nakagami-m distribution
n_{α}	Wedge inner angle parameter
N_h	Number of harmonics in Fourier series
N_p	Number of propagation paths
n_{pl}	Path loss exponent
N_{τ}	Number of considered delays for CIR deconvolution procedure
$\hat{N}_{\tau}$	Number of significant paths estimated in CIR
$P_{t/r}$	Tx/Rx signal power
$\mathbf{Q}$	Rotation matrix
r	Slant distance between the Tx and Rx
R^2	Coefficient of determination
$\mathbf{r}_{0/d}$	User's motion start/destination position
$\mathbf{r}_{ap}$	AP position vector
R_{loss}	Reflection loss
$R_{\perp/\parallel}$	Reflection coefficient for polarisation perpendicular/parallel to the incidence plane
R_s	Scattering cylinder radius
$\mathbf{r}_{t/r/s}$	Tx/Rx/Sc position vector
$r_{ts/rs}$	Slant distance between the Tx/Rx antenna and Sc
s_{21}	Transmission coefficient between Tx and Rx antennas ports (S-parameter)
s_{Rice}	Non-centrality parameter of Rice distribution
T	User's motion cycle period
t	Time
T_w	Pulse width
$\mathbf{u}_{\perp/\parallel}^{t/r}$	Incidence plane perpendicular/parallel polarisation unit vector
$\hat{\mathbf{u}}_{\perp/\parallel}^{t/r}$	Edge-fixed Incidence/diffraction plane perpendicular/parallel polarisation unit vector
$\mathbf{u}_{\theta/\phi}^{t/r}$	θ/ϕ-polarisaiton unit vector
$\mathbf{u}_v$	User's motion direction unit vector

$\mathbf{u}_{V/H}^{t/r}$	V/H -polarisation unit vector
$\mathbf{u}_{x/y/z}$	$x/y/z$ -axis unit vectors of global coordinate system
$\mathbf{u}_{x/y/z}^{a}$	$x/y/z$ -axis unit vectors of wearable antenna's local coordinate system
$\mathbf{u}_{x/y/z}^{t/r/s}$	$x/y/z$ -axis unit vectors of Tx/Rx/Sc local coordinate system
$\mathbf{v}_{t/r}$	Tx/Rx antenna velocity vector
v_u	User's motion velocity
w	Pulse waveform
X_{pd}	Cross-polarisation discrimination
$X_{pi}^{t/r}$	Antenna cross-polarisation isolation
$X_{pr}^{t/r}$	Cross-polarisation ratio

List of Software

Calc2latex	Macro for exporting tables from Libreoffice Calc to LaTex (Shohei Abe)
CVX	MATLAB Software for Disciplined Convex Programming (GNU GPLv3)
Inkscape	Vector graphics editor (GNU GPL v2.0)
JabRef	Reference management system (GNU GPL v2.0)
LaTeX	Document preparation and text processing language
MATLAB	Multi-paradigm numerical computing environment (MathWorks)
MoCap	MATLAB toolbox for work with MoCap data (N. D. Lawrence)
TexStudio	LaTeX Editor (GNU GPL v2.0)
Ubuntu	Linux Operating System (Canonical Ltd.)
WriteTex	LaTex editor extension for Inkscape (Wang Long Qi)

Chapter 1

Introduction

This chapter provides an overview of the work developed within the thesis, presents the motivation for the performed research, its main objectives and challenges, points out the main achievements and outlines the novelty. The publications that have disseminated some parts of this work are listed. A detailed structure of the thesis is presented at the end of the chapter.

1.1 Motivation and the main goals

Wireless communications are constantly evolving, where everyone has witnessed the fast transformation of mobile communication systems over the last decades. With their pursue of connectivity anywhere and at any given time, there are only a handful places one can find themselves nowadays without coverage. With networks, the services evolved as well; once voice-call only, one is now able to stream music from an apparently unlimited online database or watch a high-quality video while commuting to work in public transport. This interconnected evolution in systems and services was supported by the transformation of personal communication devices, to the point that nowadays one calls ”phone” to a device that performs a multitude of different tasks, a phone call being just one of them.

To satisfy the increasing capacity demand imposed by these new services, and tailor the network to its specific spatial distribution, the service area has been fragmented into finer units over which fewer users are served with better quality. This trend of shrinking the focus areas emerged from a number of reasons, where the efficient use resources, coexistence, security and system control issues are among the most important ones. One had a transformation from large networks covering wide areas, to Local Area Networks (LANs) that handle communications for a single institution, all the way to Personal Area Networks (PANs) for the exchange of information among personal devices, typically within a room.

The latter emerged as technology advancements allowed for wired communications to be replaced by radio in many applications, the wireless mouse and keyboard being popular examples. This transformation went so far that today one uses wireless devices for all sorts applications, including contact-less payment, car-keys, computer unlocking dongles, and recently even wireless headphones. The evolution is so fast that well-known electronics manufacturers are already omitting the ”old-fashioned” headphone jacks from their smartphones and tablets.

With personal devices carried in clothes or worn by the user, communication is closely confined to the user’s body and its immediate vicinity, and the concept of Body Area Networks (BANs) naturally emerges. Nowadays, one has smart watches, glasses or even jewellery exchanging data with a smartphone in carried in a pocket, while a more peculiar example of body-centric communication involves devices implanted inside the human body. There are many existing systems that fall under the hat of BANs, especially less widely know ones, beyond the popular consumer electronics.

Consisting of multiple wearable devices equipped with sensors, actuators and communication modules, BANs capable of operating autonomously and continuously for long periods of time are ought to be exploited in a vast range of applications, from life-saving to leisure [1]. BANs have drawn the attention of the research community and their potential was recognised in various domains, healthcare, military and sports industry being the main drivers of technology development. Although wearable networking is a somewhat newer concept, it is based on technology that has been available for decades now [2]. Some of the most representative historical examples are shown in Fig. 1.1.

The sports industry seems to be the hottest market for BAN technologies, where the available devices range from the fitness monitoring devices for recreational athletes to professional systems, rapidly adopted by sports teams in the everlasting search for the ways to prevent the injuries and improve the

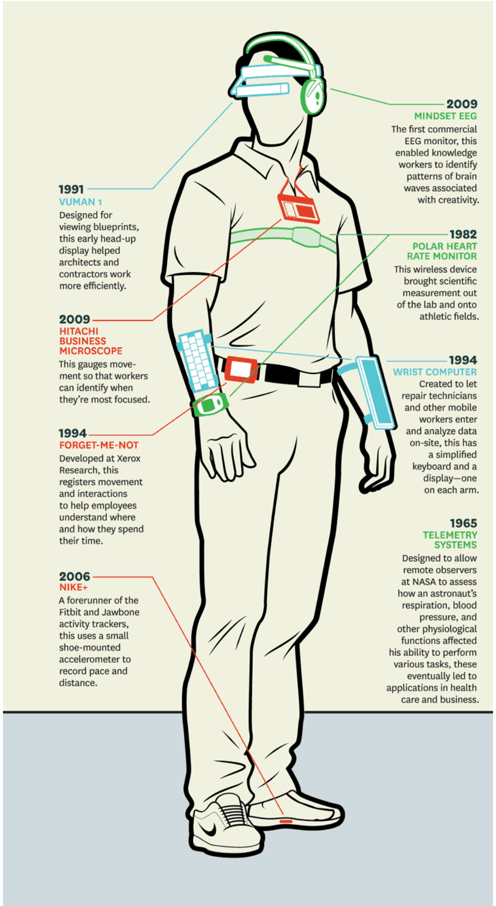

Figure 1.1: History of wearable devices (adopted from [2]).

performance of their athletes. The latter lead Major League Baseball, in the United States, to approve two wearable biometric devices for use during the 2016 season [3].

While the available systems already demonstrate the potential of BANs, their implications are even greater and the full potential is yet to be reached. As an example, in a concept similar to the camera drone Lilly which records video while tracking a user equipped with a wireless device [4], BANs can allow advanced and intuitive control of robots and machines with simple gestures, but also ensure the robot-human awareness and safe interaction in the environments of next-generation factories. Furthermore, BAN systems monitoring user's health and environment can warn the user of dangerous situations, thus playing a role of an artificial "spider-sense", i.e. a real-life equivalent to that from the "The Amazing Spider-Man" comic-book. In a somewhat more distant future, together with the advances in virtual and augmented reality technologies, BANs can make science-fiction concepts, like the "holodeck" from Star Trek series, a reality.

The performance of BANs highly relies on the ability to exchange information among body-worn devices, a wearable device and the nearby infrastructure, or between BANs. The latter two communication scenarios are particularly important, as they allow for a BAN to interact with its surroundings and achieve its full potential. With seamless mobility being paramount, radio is a likely choice for facilitating the information exchange in BANs, and almost an exclusive one for off-body communications. While providing all the convenience of being wireless, the radio channel is characterised by very challenging conditions. In order to overcome these and ensure communications' quality, such as required by delicate BAN applications in emergency healthcare, for example, the underlying propagation phenomena have to be well-understood and modelled.

While a considerable progress has been made in BAN channel modelling, with contributions from a large number of authors worldwide, there are several open issues and effects yet to be properly understood. As a matter of fact, the channel modelling approach should be generally changed to better match the peculiar characteristics of BAN communications. The models available in literature typically adopt statistical approaches initially developed for mobile communications channels, while their suitability for BAN channels is questionable. More precisely, these models assume that the channel is non-stationary over fairly large local areas, an assumption that typically does not hold in the latter due to effects associated with user's motion.

One can easily expect that the wearable antenna rotation on a dynamic user yields gain variations and polarisation mismatch losses. With signal propagation over the Line-of-Sight (LoS) path being particularly affected, channel characteristics can vary considerably over short distances traversed by the user. Moreover, the imposed signal variations are often periodic, due to cyclic nature of walking and running motions. The body-shadowing effects are an additional source of deviation from the typical assumptions, where a wearable antenna can move from being visible to the off-body Access Point (AP) to being shadowed by the user, as a matter of rotation.

While statistical path loss models capture the global channel characteristics on average, they fail to properly separate different sources of received signal variation, as necessary for appropriate representation of their dynamics. Therefore, multipath propagation effects have to be separated from those associated with wearable antenna dynamics, in order to properly take the influence of user's motion into account. A lack of off-body channel models that consider these important effect is the main motivation for the work presented in the thesis.

The main goal was to develop a simple geometry-based channel model for off-body communications, which considers signal depolarisation and user's motion, while being simple to use. It should facilitate different wearable antenna placements and typical user motions, i.e. walking and running. In order to achieve this goal, the following objectives were set:

1. to develop a theoretical geometry-based off-body channel model that takes the polarisation aspect into account, and considers antennas' radiation characteristics;
2. to develop a mobility model for wearable antennas on dynamic users and expand the channel model to take the effects of users' motion into account;
3. to develop a Geometry-Based Stochastic Channel (GBSC) model based on a simplified geometry of the propagation environment, i.e. a scattering cylinder,
4. to implement the model in a simulator and investigate off-body channel characteristics, with the focus on the depolarisation mechanisms and on the effects of user's dynamics.

The developed model should allow for dynamic off-body channel simulation, for performance analysis of different system designs and evaluation of signal processing algorithms designed to improve system performance. In summary, the main goal of the thesis was to develop a realistic yet simple BAN channel model for polarised off-body communications with dynamic users, facilitating different wearable antenna placements and user activities.

1.2 Novelty

Although the off-body BAN communications channel has received quite some attention in recent years, many open issues remain regarding the understanding and modelling of specific phenomena within. There is a general lack of channel models, where the existing ones typically adopt traditional modelling approaches that fail to capture the peculiar aspects of BAN channels, the depolarisation effect and the influence of dynamic users' motion being of main concern. While providing valuable modelling guidelines, the polarised channel models developed for other radio systems, such as mobile communication networks, are inadequate for BANs, as the latter are characterised by lower transmitter (Tx) powers, low antenna heights and significant influence of user dynamics.

The novelty of this work is two-fold. First, an analytical mobility model for wearables in BANs with dynamic users was developed, considering different on-body antenna placements and user's motions. The model is simple yet realistic, as its parameters were calculated from high-resolution motion data obtained for a real person. It is suitable for use with a variety of propagation channel models and can allow for analytical inference in simplified scenarios. Second, the antenna mobility model was employed with a geometry-based off-body propagation channel model, which takes signal depolarisation due scattering into account. Combining the two is the main novelty of this work, as joint modelling of the depolarisation effect and the influence of user dynamics was not previously reported in literature, to the best of the author's knowledge. The developed model allows for realistic simulation of off-body communications scenarios with dynamic users, facilitating performance evaluation and system design optimisation.

1.3 Research strategy and impact

The three main research questions posed in this thesis were:

1. *What are the main depolarisation mechanisms in off-body communications with dynamic users?*
2. *How does user's motion affect channel's characteristics?*
3. *How can one appropriately model and simulate a dynamic polarised off-body channel with the least computational effort?*

In order to answer these questions, a channel model for polarised off-body communications with dynamic users was developed over several phases. A geometry-based channel model with a static user was developed first, with the polarisation aspect being considered. In order to expand the channel model to take the influence of user's motion into account, an analytical mobility model for wearable antennas in BANs with users walking or running was derived, with Motion Capture data used to calculate its parameters. The obtained dynamic model was then implemented in a simulator, and used to investigate the depolarisation mechanisms in the off-body channel with a dynamic user. Channel characteristics were also analysed, based on data from narrow- and wideband channel measurements, allowing for a comparison with the observations made from simulation results.

This work was developed within the framework of the COST Action CA15104, Inclusive Radio Communication Networks for 5G and Beylond (RACON) [5]. The participation in this project and regular attendance to its meetings allowed for interaction with researchers working on similar topics in Europe and worldwide, with whom the work was discussed and from whom valuable criticism was received. Most importantly, the experience obtained in these interactions inspired parts of this thesis and many ideas for future work.

Parts of the work presented in this thesis were already disseminated in several papers, published or submitted for publishing in international journals and conferences, as well as in internal reports prepared and presented within IRACON:

[Book chapters]

- K. Turbic, K. Cwalina and L. M. Correia, "BAN Channel Measurements and Modelling," in *Inclusive Radio Communication Networks for 5G and Beyond*, C. Oestges, Ed. Cambridge, MA, USA: Academic Press, 2020. In preparation.

[Journals]

- K. Turbic, L. M. Correia, and M. Beko, "A Channel Model for Polarised Off-Body Communications with Dynamic Users," *IEEE Transactions on Antennas and Propagation*, 2018, Revised, under review.
- ——, "A Mobility Model for Wearable Antennas on Dynamic Users," *IEEE Access*, vol. 6, no. 1, pp. 63 635–63 648, Dec. 2018. [Online]. Available: `https://doi.org/10.1109/ACCESS.2018.2877500`
- K. Turbic, S. J. Ambroziak, and L. M. Correia, "Characteristics of the Polarised Off-Body Channel in Indoor Environments," *EURASIP Journal on Wireless Communications and Networking*, vol. 2017, no. 1, p. 174, Oct. 2017. [Online]. Available: `https://doi.org/10.1186/s13638-017-0956-6`
- S. J. Ambroziak, L. M. Correia, R. J. Katulski, M. Mackowiak, C. Oliveira, J. Sadowski, and K. Turbic, "An Off-Body Channel Model for Body Area Networks in Indoor Environments," *IEEE Transactions on Antennas and Propagation*, vol. 64, no. 9, pp. 4022–4035, Sep. 2016. [Online]. Available: `http://dx.doi.org/10.1109/TAP.2016.2586510`

[Conferences]

- K. Turbic, S. J. Ambroziak, L. M. Correia, and M. Beko, "Wideband Off-Body Channel Characteristics With Dynamic User," in *Proc. of EuCAP'19 - 13th European Conference on Antennas and Propagation*, Krakow, Poland, Mar. 2019.
- K. Turbic, S. J. Ambroziak, and L. M. Correia, "A Body-Shadowing Model for Off-Body and Body-to-Body Communications," in *Proc. of URSI'18 - Baltic URSI Symposium*, Poznan, Poland, May 2018. [Online]. Available: `https://doi.org/10.23919/URSI.2018.8406703`

- ——, “Fading Characteristics for Dynamic Body-to-Body Channels in Indoor and Outdoor Environments,” in *Proc. of EuCAP’18 - 12th European Conference on Antennas and Propagation*, London, UK, Apr. 2018. [Online]. Available: `https://doi.org/10.1049/cp.2018.0987`

- ——, “An Empirical Model for the Polarisation Characteristics of Indoor Off-Body Channels,” in *Proc. of EuCAP’17 - 11th European Conference on Antennas and Propagation*, Paris, France, Mar. 2017. [Online]. Available: `https://doi.org/10.23919/EuCAP.2017.7928136`

- S. J. Ambroziak, K. Turbic, and L. M. Correia, “An Approach to Mean Path Loss Model Estimation for Off-Body Channels,” in *Proc. of ISMICT’17 - 11th International Symposium on Medical Information and Communication Technology*, Lisbon, Portugal, Feb. 2017. [Online]. Available: `https://doi.org/10.1109/ISMICT.2017.7891762`

- S. J. Ambroziak, L. M. Correia, and K. Turbic, “Radio Channel Measurements in Body-to-Body Communications in Different Scenarios,” in *Proc. of URSI AP-RASC 2016 - URSI Asia-Pacific Radio Science Conference*, Seoul, Korea, Aug. 2016. [Online]. Available: `https://doi.org/10.1109/URSIAP-RASC.2016.7601348`

- S. J. Ambroziak, K. Turbic, C. Oliveira, L. M. Correia, and R. J. Katulski, “Fading modelling in dynamic off-body channels,” in *Proc. of EuCAP’16 - 10th European Conference on Antennas and Propagation*, Davos, Switzerland, Apr. 2016. [Online]. Available: `http://dx.doi.org/10.1109/EuCAP.2016.7481768`

[Internal reports]

- K. Turbic, S. J. Ambroziak, L. M. Correia, and M. Beko, “Wideband Off-Body Channel Characteristics With Dynamic User,” TD(19)09013. Dublin, Ireland: COST Action CA15104 (IRACON) meeting, Jan. 2019.

- K. Turbic, L. M. Correia, and M. Beko, “A Channel Model for Polarised Off-Body Communications with Dynamic Users,” TD(18)08011. Podgorica, Montenegro: COST Action CA15104 (IRACON) meeting, Oct. 2018.

- K. Turbic, S. J. Ambroziak, L. M. Correia, and M. Beko, “Wideband Channel Measurements for Polarised Indoor Off-Body Communications,” TD(18)07063. Cartagena, Spain: COST Action CA15104 (IRACON) meeting, May 2018.

- K. Turbic, S. J. Ambroziak, and L. M. Correia, “A Body-Shadowing Model for Off-Body and Body-to-Body Communications,” TD(18)06031. Nicosia, Cyprus: COST Action CA15104 (IRACON) meeting, Jan. 2018.

- K. Turbic, L. M. Correia, and M. Beko, “A Channel Model for Off-Body Communications with Dynamic Users,” TD(17)05054. Graz, Austria: COST Action CA15104 (IRACON) meeting, Sep. 2017.

- ——, “A Motion Model for Wearable Antennas in BANs,” TD(17)04043. Lund, Sweden: COST Action CA15104 (IRACON) meeting, May 2017.

- K. Turbic, L. M. Correia, and S. J. Ambroziak, “An Approach to Mean Path Loss Model Estimation for Off-Body Channels,” TD(17)03006. Lisbon, Portugal: COST Action CA15104 (IRACON) meeting, Feb. 2017.

- K. Turbic, L. M. Correia, and M. Beko, “Influence of User’s Motion on Signal Depolarisation in Off-Body Channel,” TD(17)03044. Lisbon, Portugal: COST Action CA15104 (IRACON) meeting, Feb. 2017.

- ——, “Geometry-Based Polarised Static Off-Body Channel Model,” TD(16)02010. Durham, UK: COST Action CA15104 (IRACON) meeting, Oct. 2016.

Par of the work presented in this thesis was developed in collaboration with colleagues from Gdansk University of Technology (GUT), primarily Dr. Slawomir J. Ambroziak. His main contribution includes preparation of measurement equipment and software, used for narrow- and wideband off-body channel measurements performed as a part of this work (Chapter 5). This collaboration also resulted in several joint conference and journal publications, as indicated above.

1.4 Structure of the Dissertation

This thesis is structured in eight chapters, the rest of the document being organised as follows.

Chapter 2 gives an overview of BANs, discussing potential applications and imposed requirements, available communication technologies, general architecture and finally focusing on the wireless communication channel and propagation phenomena within. The final section presents an overview of the state of the art in off-body BAN channel modelling, with the focus on the depolarisation effect and on the influence of user dynamics.

Chapter 3 presents a geometry-based polarised off-body channel model, which takes free-space propagation, reflections and diffractions into account, while allowing for arbitrary antenna orientations, polarisations and radiation characteristics to be specified. The depolarisation effect in the channel is modelled by polarisation matrices associated with each propagation path, being derived from the scenario geometry. A general model formulation is provided first, followed by a derivation of the polarisation matrices for free-space propagation, reflection and diffraction, considering an arbitrary environment geometry. A mobility model for wearable antennas with dynamic is presented, facilitating 14 different on-body antenna placements and user walking and running motions. With the employment of the mobility model, the final channel model for off-body communication with dynamic users is obtained. Finally, a simplified scattering environment with scatterers distributed on a cylinder centred around the user is presented, allowing for further simplification of the model discussed at the end of the chapter.

Chapter 4 describes the model implementation and development of an off-body channel simulator. The structure of the simulator is outlined and its components described in detail, indicating the underlying mathematical models within each one. Its parameters are listed and their specification described, as well as the considered output metrics. Finally, the performance of the simulator is assessed in the final section; the model was used to recreate several scenarios from literature, specifically chosen to assess different aspects of the simulator.

Chapter 5 describes two indoor off-body channel measurement campaigns, which provided data for the analysis in this thesis. These campaigns were carried out in collaboration with colleagues at Gdansk University of Technology (Gdansk, Poland), who provided the facilities and prepared the measurement equipment. They involved narrow- and wideband channel measurements in an indoor office environment, considering scenarios with different wearable antenna placements and both user activities. General information about the measurements is provided first, followed by a detailed description of the environment, scenarios, methodology and equipment.

Chapter 6 presents the analysis of the obtained measurement data, the off-body channel polarisation characteristics, the influence of user's motion being the focus. Data processing procedures are outlined first, providing the expressions used to calculate the considered metrics. This is followed by the channel characterisation analysis, with the modelling aspects and implications on the system design being discussed. Finally, the available measurements data are used to validate the developed channel model, were a comparison is performed for a selected set of measurement scenarios recreated in the simulator.

Chapter 7 presents the simulation-based analysis of the off-body channel characteristics using the developed simulator. The considered scenarios are chosen to investigate the signal depolarisation effects as well as the impact of user's motion on the channel. These involve user walking and running motions, with different wearable antenna placements chosen for their specific motion dynamics, but also being representative of popular BAN applications The depolarisation mechanisms in the channel are discussed and analysed in detail, both effects associated with scattering mechanisms and the influence of the user dynamics being considered.

Finally, Chapter 8 concludes the thesis by summarising the presented work, recalling the main goals, shortly describing the undertaken steps and discussing the met objectives. The main results of the thesis are summarised and the potential improvements of the developed simulator are discussed. Some of the remaining open issues are outlined, pointing out directions for future work.

Chapter 2

An overview of Body Area Networks

This chapter gives an overview of BANs, discussing potential applications and imposed requirements, available communication technologies and general architecture, and finally focusing on the wireless communications channel, as the main topic of interest for the work developed within this thesis. The mechanisms governing channel characteristics are considered, with a focus on specific aspects of body-centric propagation. An overview of the state of the art in off-body BAN channel modelling is also presented, with a particular attention given to the depolarisation effect and influence of user dynamics. Open issues and existing gaps in the available literature are identified at the end of the chapter.

2.1 Applications

Consisting of multiple wearable devices equipped with sensors, actuators and communication modules, BANs operating autonomously and continuously for long periods of time are ought to be exploited in various applications, ranging from life-saving to leisure, always with a general purpose to improve the quality of human life. With the ability to continuously monitor the body/environment parameters and provide a remote access to the collected data in real-time, BANs not only promise to revolutionise healthcare and increase patient handling efficiency, but also provide means to prevent accidents and improve safety of emergency rescue missions, military teams on the ground, astronauts in space exploration missions, professional drivers, etc. Furthermore, the access to the user's biometric characteristics makes BANs suitable for advanced multi-level authentication in facilities requiring high-level security. Similarly, BANs can allow easy and fast exchange of information between people passing by each other or while shaking hands [6].

BAN applications in healthcare are numerous, including health monitoring for different purposes, e.g. detecting critical patients and prioritising treatment in emergency rooms, and monitoring elderly people's health without requiring a visit to the hospital. These applications help to improve the efficiency of delivering the medical service and reduce the load of healthcare centres, faced with an increasing rate of elderly patients [7]. Moreover, the extensive databases of medical data collected by BANs can be subjected to data mining algorithms, in order to extract disease-specific patterns and improve the early stage diagnosis [8]. BANs can be also used for wireless endoscopy, where ingestible capsules with built-in cameras [9] will not only allow for the examination of previously unreachable areas, but also provide a less uncomfortable experience for patients.

The employment of BANs for close-loop control will show their true power, where autonomously operating devices can significantly improve the life quality of diabetes patients or people with disabilities. For the former, a BAN could act as an artificial pancreas, by continuously monitoring blood sugar levels and injecting insulin accordingly, whereas in the latter case it can provide smart prosthetics for amputee patients, a speech synthesiser for mute, pacemaker adjustments for heart disease patients, etc.

BANs can be also employed for accident prevention, where their monitoring capabilities can be exploited to detect health incidences or sleepy drivers, nauseous construction workers, high environmental risks, etc. In collaboration with the surrounding environment, a BAN can trigger safety mechanisms to avoid lethal accidents, potentially playing an important role in reducing the number of casualties in road accidents, currently being among the top 10 causes of death in the world [10].

Owing to their capability to monitor user's health, environment and equipment conditions in real-time, BANs are attractive for many applications in which users are exposed to harsh environments. Such are public safety and rescue services, which can benefit from BANs employed for providing the logistics support in terms of positioning, coordination and safety warnings for ground team members when the high risk situations are encountered, e.g. a fireman entering the room with high CO_2 levels, whilst the oxygen level in the carried tank is low. Similar benefits are available for military ground units, where collaborating BANs of an infantry team can detect the direction of the incoming enemy fire and allow the team to quickly organise and respond to a threat. Additionally, BANs can improve the efficiency of medical support teams by providing the position of a wounded soldier and information about the injury in real time. An illustration of a military application is shown in Fig. 2.1; BANs are employed on each soldier to facilitate exchange of data in between on-body sensors, while BANs communicate with each other and with an external AP, which exploits satellite communication for data delivery to remote headquarters.

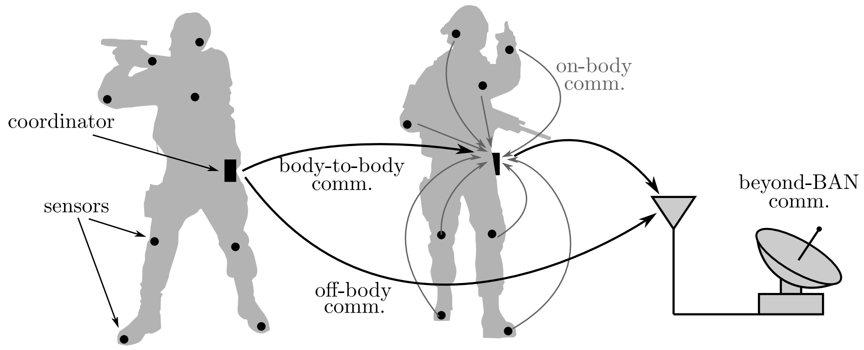

Figure 2.1: Illustration of a military BAN application (adapted from art obtained at [11]).

Alongside coordination in between humans, BANs can allow intuitive and straightforward interface for different pieces of equipment. As an example, a drone can collaborate with BANs worn by ground team members and track their position, monitor the surrounding area and give a warning if any danger is detected. With simple hand gestures, a soldier can also navigate the drone to inspect a suspicious area without risking the lives of human team members.

The entertainment industry can benefit from BANs in various ways, where these systems are foreseen to revolutionise Human-Computer Interface (HCI). As wireless motion tracking technologies are already commercially available, it is a matter of time when more complex BAN-based controllers will appear and allow for realistic video game controls or navigation through Virtual Reality (VR).

In sports industry, BANs can be used to comprehensively monitor performance of athletes and improve training efficiency in the everlasting pursue to push limits. Similarly, by monitoring the recovery process and adjusting therapy, BANs can shorten the time after injury before the athlete returns to full training intensity. Moreover, the collective performance information obtained for individual athletes can be used to adapt the team's tactics to the current condition of its members. Considering the budgets of world class sports teams and the benefits BANs can deliver, the sports industry is anticipated to be the main technology driver in the future.

2.2 Ongoing research and existing projects

As the interest for BANs grew over the past years, a number of related projects were developed, ranging from small prototypes and smart-phone applications to full-scale systems that involve on-body data collection, off-body communications and remote access [12, 13]. The considered applications include large-scale healthcare and rescue support systems, personal wearable health monitoring, military and space exploration support, motion tracking, and personal data exchange.

Among the most notable projects involving full-scale system development are CodeBlue [14], AID-N (Advanced Health and Disaster Aid Network) [15], and SMART (Scalable Medical Alert and Response Technology) [16]. These systems are primarily designed to improve patient handling efficiency by providing a communication infrastructure for patient monitoring in large healthcare centres and emergency rooms, or on-site during the post-disaster rescue support.

Serving as a proof of concept, the majority of BAN projects developed personal monitoring systems for various applications. While a common set of sensors is used in most of these systems, the differences are in the number of acquired signals, data processing methods and the employed communication technology. Several notable projects in this domain are listed in what follows. LiveNet [17] and WHMS (Wearable Health Monitoring System) [8] are representative examples of systems capable of providing a real-time feedback to the user, remote access to medical personnel, and long-term monitoring for personalised health profile development. MagIC (Maglietta Interattiva Computerizzata) [18], WEALTHY [19] and Smart Vest [20] aim at the individuals affected by cardiovascular diseases. These systems are using washable conductive yarns integrated in clothes for on-body communication, and the radio for off-body transmission. Some of the projects consider specific diseases, in a search for previously unavailable means of treatment and diagnosis, e.g. HealthGear [21] and AUBADE [22]; the former aims to improve sleep apnea diagnosis, whereas the latter is an emotion monitoring system for users operating under extreme stress conditions or patients suffering from psychological disorders.

Projects like Mercury [23] and WiMoCA (The Wireless Sensor Node for a Motion Capture System with Accelerometers) [24] employ multiple distributed on-body devices equipped with tri-axial accelerometers and gyroscopes for motion tracking. While the former is primarily designed for treatment of patients with neuromotor disorders, the latter also considers HCI application.

As the possibilities of BANs attract great attention from the military, projects as LifeGuard [25], GTWM (Georgia Tech Wearable Motherboard) [26], and WPSM (Warfighter Physiological Status Monitoring) system [27] consider BAN-based uniforms for next-generation soldiers. These systems are intended to continuously monitor user's health, motion and surrounding environment, and provide feedback to the user and/or a remote logistics support centre. The LifeGuard project initially considered BANs employed on astronauts during space exploration missions, but expanded its scope to military applications due to similar system requirements.

The employment of BANs for personal data exchange was demonstrated by Zimmerman [28]. The developed system also introduced the concept of Body Coupled Communication (BCC) (Section 2.4). It was designed for information exchange among wearable devices, for instance, while two users handshake.

2.3 Requirements

BAN applications often impose conflicting requirements [29], which compel system designers to find a compromise for each application, since they cannot satisfy all requirements in general. The main requirements include comfort, safety, security, energy efficiency, reliability, low latency, ease of use, and scalability.

The requirement for comfort implies that the devices should be small, compact and made of materials appropriate for use inside the body or in contact with the skin [7]. Unfortunately, such materials typically have undesirable electrical characteristics, thus yielding higher losses and increased power consumption.

The safety requirement primarily imposes restrictions on the amount of Electromagnetic (EM) radiation to which the body can be exposed. The established exposure limits are derived by considering risks following from increased tissue temperature due to EM energy absorption. The extreme body proximity grants this requirement a considerably higher priority in BANs than in other wireless systems. The limits are most commonly specified by Specific Absorption Rate (SAR) values, representing a measure of the rate at which the energy is absorbed per mass of tissue. For the frequencies beyond a few GHz the exposure limits are given in terms of incident power density, as most of the energy is absorbed near the body surface in this case. Table 2.1 provides a summary of worldwide adopted exposure limits for general public in the frequency range most common for BANs, as extracted from ICNIRP Guidelines 1998 [30] and IEEE/ANSI C95.1-2005 [31]. Though reducing the Tx power in order to meet exposure limits also works in favour of data confidentiality, BAN coexistence and energy efficiency, it also affects the communications range.

Table 2.1: Exposure limits for general public, as given in [30, pp. 509], [31, pp. 20,25].

Guidelines	ICNIRP 1998	IEEE/ANSI C95.1-2005		
Frequencies [Hz]	100 k - 10 G	100 k - 3 G	3 G - 5 G	5 G - 10 G
Whole body average SAR [W/kg]	0.08	0.08	-	-
Peak local SAR, head/trunk [W/kg]*	2	2	-	-
Peak local SAR, extremities [W/kg]*	4	4	-	-
RMS power density [W/m^2]†	-	-	10	10
Averaging time [min]	6	6	30	$150/f_{[\mathrm{GHz}]}$

*spatially averaged over any 10 g of contiguous tissue with nearly homogeneous electrical properties

†spatially averaged over any contiguous area corresponding to $100\lambda^2_{[\mathrm{cm}]}$

The security requirement is paramount for large number of BAN applications, primarily in healthcare and military, where a security breach has devastating and potentially lethal consequences. Therefore, reliable security mechanisms are required to ensure data confidentiality, integrity and authenticity. The redundancy introduced by these mechanisms results in increased power consumption and longer processing delays. However, it is important to acknowledge the security issue as the key factor to limit the widespread employment of BANs in critical applications [32].

In addition to high security levels, critical medical and military applications also require high reliability, fault tolerance and robustness to interference. This means that BANs have to provide a robust communications channel whenever data transmission is needed, and allow fast recovery after outages. Nevertheless, this is a very challenging task to achieve while ensuring seamless coexistence with other devices operating in populated frequency bands, such as Industrial, Scientific and Medical (ISM). Reliability is typically improved by either providing multiple communication paths among nodes or employing

Forward Error Correction (FEC) codes, both solutions conflicting with the requirements for comfort and energy efficiency.

The limited energy available to battery-powered devices requires them to operate efficiently and consume least energy possible. While implants are a peculiar example where autonomous operation is required for years, the requirement to recharge batteries of multiple body-worn devices daily will certainly affect users' enthusiasm. Therefore, BANs should be able to operate continuously over long periods of time, i.e. from several days to months. One way of achieving these goals is by resorting to classic energy saving mechanisms, such as reduced duty cycle communication, which negatively reflects on system delay, being critical in some medical applications. Alternative options include the use of wireless energy transmission mechanisms for effortless battery recharge [33], or employment of harvesting techniques to scavenge energy by exploiting thermoelectric and piezoelectric effects [34, 35].

In applications where a quick reaction is of importance, e.g. interactive control, BANs must ensure low latency and fast connection establishment. Other applications demand high data rates to support transmission of high quality music and video content in real-time. These two requirements are clearly in contradiction with the security and reliability ones.

Finally, one should consider that BANs will be mostly handled by non-technicians, e.g. patients, caregivers and athletes. Therefore, they should be simple to employ, scalable, and capable of self-configuring. In general, BANs should be able to cope with dynamic changes in network topology, allow for effortless upgrade, enhancement and introduction of new nodes, thereby, complying with the plug-and-play concept.

2.4 Communication systems

Several different communication technologies have been used in BANs, including wired communications, Inductive Coupled Communications (ICCs), BCCs and radio. Some of these systems are more suited for certain BAN applications than the others.

Wired communications assume that the nodes are physically connected by wires or conducting garments. While these systems have a certain advantage regarding security and reliability issues, they involve uncomfortable wiring. Apart from being excluded as an option for communication with implants and off-body devices, wires can limit user's movement and are prone to wear out due to constant twisting when the user is dynamic. Classical wired communications are suitable for use only if users are wearing special suits and are not involved in very dynamic activities, such as in the case of military pilots, Formula 1 drivers or astronauts [25]. Smart textiles overcome the common drawbacks associated with wires by allowing integration of power distribution, communication and sensing circuitry of a BAN within washable clothes [36]. In addition to comfort, their ability to conform with different shapes has the additional advantage of providing a firm and stable contact between sensors and the body.

With ICC [37], the transmission channel is established between two magnetic-coupled coils at the Tx and receiver (Rx) sides, with the transmission mechanism being described by Faraday's law of induction. Since the voltage induced in the Rx coil is inversely proportional to the cube of distance, the coupling exists only for very short Tx-Rx separations. The channel quality highly depends on the coils' alignment, while being independent of the surrounding tissue. Since the inductive coupling also facilitates power transfer, the same coils can provide both the communication link and the power supply for the coupled pair. Since the two impose conflicting requirements on the coil design [38], the system designer has either to optimise the trade-off in a single-coil design or use two separately optimised coils. ICC is suitable for information exchange between external devices and passive near-surface implants, animal identification being the most widespread application.

In BCC, the Tx and Rx couple with the user's body and use it as a transmission medium [39, 40]. Based on the coupling principle, one can distinguish between capacitive and galvanic BCCs, while both result in guided wave propagation at higher frequencies, at which the body acts as a wave-guide. These two types of BCCs are illustrated in Fig. 2.2.

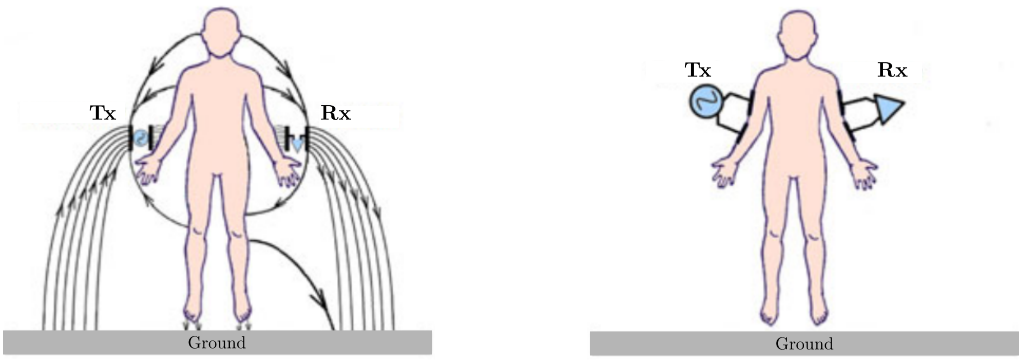

a) Capacitive BCC.

b) Galvanic BCC.

Figure 2.2: Two types of BCC (adapted from [39]).

Capacitive BCC requires one of the Tx/Rx electrodes to be in contact with the body and the other to float in the environment, e.g. touching the ground, assuming the two are electrically isolated [6]. The Tx and Rx couple to the body through capacitive links created by the electrodes in contact with the skin, thus establishing a direct communication path. Similarly, the floating electrodes capacitively couple to the environment, thus providing a return path and closing the communication circuit. Transmission is achieved as the Tx disturbs the potential of the environment and the Rx detects them by sensing variations in the electric field in between its electrodes. At frequencies below 10 MHz, the field is quasi-static and the communication system can be modelled as an electric circuit in which the body is represented by a simple RC network or a perfect conductor [41].

Galvanic BCC exploits ionic properties of body fluids for signal transmission, with both Tx/Rx electrodes being in contact with the body. By applying a variable voltage between its electrodes, the Tx induces currents into the body and the Rx senses potentials developed on the skin surface [42]. As in the capacitive BCC, the induced fields at low frequencies are quasi-static and the communication system can be modelled as an electric circuit, while the body cannot be modelled as a perfect conductor in this case. At frequencies below 10 kHz, it is represented by a mash of complex impedances corresponding to different layers of body tissues, whereas a much simpler circuit can be used in the range between 10 kHz and 10 MHz [43].

At frequencies above 50 MHz, the field induced by either capacitive or galvanic body coupled Tx is not quasi-static and the guided wave propagation occurs, with the creeping (surface) waves presenting themselves as the dominant mechanism [44]. For better performance, Tx and Rx are typically modified to exploit benefits of both coupling methods [45]. While the signal is still confined to the body in this case, at frequencies above 300 MHz the human body becomes comparable to the wavelength and radiates power into the environment, in which case the security and energy efficiency advantages of BCC are lost.

Although the aforementioned communication systems are associated with certain advantages, radio is by far the most considered option for BAN communications, due to the convenience of cordless transmission and a number of existing mature technologies. Considering their design goals, the most relevant ones are Bluetooth, Bluetooth Low Energy (Bluetooth LE), ZigBee and Ultra-wideband (UWB). The main characteristics of these communication systems are summarised in Table 2.2.

Table 2.2: Radio technologies employed in BANs (adapted from [12, 13]).

Technology	Frequency band [MHz]	Channel bandwidth [MHz]	Number of channels	Data rate [b/s]	Typical range [m]	Availability
Bluetooth	2 400 - 2 483.5	1	79	3 M	10 - 100	Worldwide
Bluetooth LE	2 400 - 2 483.5	2	40	1 M	10	Worldwide
Zigbee	779 - 787	2	4	250 k	10 - 75	China
	868 - 870		1	20 k		EU, Japan
	902 - 928		10	40 k		US, Canada
	2 360 - 2 400		15	250 k		US
	2 400 - 2 483.5		16	250 k		Worldwide
UWB	3 244.8 - 4 742.4	499.2	3	480 M	$<$10	US, Europe
	6 240 - 10 233.6		8			

Bluetooth (IEEE 802.15.1) [46, 47] was initially created by Ericsson for connecting personal devices in order to exchange audio and data in the 2.4 GHz ISM band. The operating devices are organised in small star topology networks (piconets) with a single master node coordinating up to 7 others (slaves). By allowing slave nodes to join multiple piconets, larger networks (scatternets) can be established. While the range and available data rates make Bluetooth suitable for off-body transmission of aggregated BAN data, the high duty cycle and consequent energy inefficiency are its unfavourable characteristics.

Bluetooth LE [48] was proposed by Nokia as an energy efficient and low cost alternative to Bluetooth, primarily intended for communication in between sensors and a mobile phone. At the expense of reduced range and data rate (Table 2.2), the new Physical layer (PHY) design introduced for peripheral devices (stand-alone) aims to allow a year long operation on a button cell battery, but also to reduce synchronisation time to milliseconds, compared with seconds in Bluetooth. The latter makes Bluetooth LE convenient for delay-critical BAN applications. In order to allow for the existing communication infrastructure to be used, Bluetooth LE also supports devices (dual-mode) capable of communicating with both single-mode and Bluetooth devices.

ZigBee (IEEE 802.15.4) [49, 50] was initially designed for the Wireless Sensor Networks (WSNs), where energy efficiency, low cost and scalability are the main design goals, data rate being less important. It uses Direct Sequence Spread Spectrum (DS-SS) to combat interference from coexisting devices. Carrier Sense Multiple Access with Collision Avoidance (CSMA-CA) is used for medium sharing in both synchronous (beacon enabled) and asynchronous (non-beacon enabled) modes of operation, where the former allows devices to ”sleep” during the inactivity periods for improved energy efficiency. By allowing for multi-hop transmission, ZigBee can extend nodes’ coverage and also circumvent the direct propagation path obstructions, thus improving the communication reliability.

UWB (IEEE 802.15.4a) [51] is a common reference for radio communication system with operating bandwidth exceeding 500 MHz or 20% of the arithmetic centre frequency. The most popular of such systems is the Impulse Radio UWB (IR-UWB), which feeds the series of narrow pulses directly to the Tx antenna, while time hopping is exploited for medium sharing. The wide bandwidth yields high capacity, but also imposes challenges when trying to ensure a flat transfer function. This is proven to be a difficult task with such bandwidths, where even antennas act as pulse shaping filters. Moreover, the corresponding fine resolution in time allows for RAKE receivers to be employed for fading mitigation and use of UWB for precise positioning in indoor environments, but also requires strict synchronisation. With its Tx power density required to satisfy the -41.3 dBm/MHz regulation limit, UWB signals are of the same order as noise and spurious emissions. This makes it convenient for operation around the equipment sensitive to EM radiation, e.g. in hospitals, but also suitable for on-body communication due to low corresponding exposure levels.

Finally, one should note that the mentioned radio systems were adopted as an IEEE 802.15.6 standard for BANs [52], with two PHY specifications, summarised in Table 2.3, with the frequency range, number of allocated channels and Tx constraints being indicated.

Table 2.3: Frequency bands used for BANs, according to [52].

Frequencies [MHz]	Channel bandwidth [Hz]	Number of channels	Transmit constraint	Communication
402 – 405	300 k	10	-40, -16 dBm EiRP	Narrowband
420 – 450	320 k	12	–10 dBm EiRP	
863 – 870	400 k	14		
902 – 928		60		
950 – 958		16		
2 360 – 2 400	1 M	39		
2 400 – 2 483.5		79		
3 244.8 – 4 742.4	499.2 M	3	-41.3 dBm/MHz	UWB
6 240 – 10 233.6		8		

2.5 Architecture

The architecture of a BAN-based network depends on the application, ranging from a simple on-body network to a full-scale one which interconnects with a Wide Area Network (WAN) to facilitate communication with remote locations. An example in healthcare is shown in Fig. 2.3, consisting of the intra-, inter- and beyond-BAN segments [13].

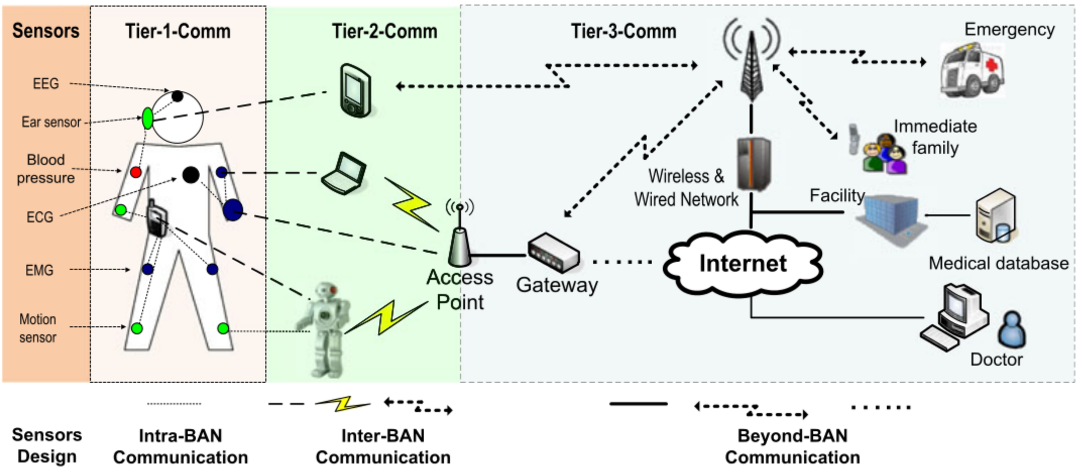

Figure 2.3: A general architecture of a BAN-based health monitoring system (extracted from [13]).

The intra-BAN segment enables in- and on-body communications, and is responsible for data exchange in between body-worn and/or implanted sensors and actuators. Its nodes are commonly arranged in a single- or two-hops star topology, with a central coordinator device in charge for synchronisation, data aggregation and off-body transmission. This part of the network has to ensure that the application-specific requirements are fulfilled, while dealing with constrained power supply. Therefore, the employed Medium Access Control (MAC) layer and routing protocols are required not only to achieve maximum throughput with minimum delay, but also to maximise battery lifetime while preserving data authenticity, integrity and confidentiality.

The inter-BAN component is responsible for off-body communications with the nearby infrastructure, thus facilitating data transmission in between the on-body nodes and external APs, or other BANs. As it is crucial to ensure user mobility, radio communications is the standard choice herein. Alternatively, BCCs can be used in applications where establishing a physical contact with the environment is part of the user's activity. The communication protocols employed in this segment must ensure quick and effortless connection, allowing for the information exchange to finish within short periods of time that the user spends in the service area of an AP. While the energy-efficiency issue is not as critical as in the inter-BAN segment, the security and QoS mechanisms have to be employed.

The beyond-BAN segment includes the backbone infrastructure for communications of a large number of devices. Upon being delivered from a BAN to the AP, data is carried through the core network and delivered to the final destination, e.g. a medical centre. In order to handle the aggregated load from different users, this segment has to provide enough throughput. Since it is most likely to rely on networks shared with other systems, with an uncontrolled access by many entities, security mechanisms have to be implemented. Due to accessibility and global availability, internet LAN or the core network of a mobile system are typically exploited for beyond-BAN communications.

2.6 Radio propagation in BANs

The ability of radio communications to provide seamless mobility makes these systems an obvious choice for BANs. On the other hand, the radio channel is characterised by severe Rx signal degradations, where ensuring the required communication quality may be a difficult task. Besides the additive noise, the Rx signal is subjected to random variations as the Tx and/or Rx move in space. The total path loss in the channel can be factorised into three main components, i.e. propagation loss, large- and small-scales fading.

The propagation loss represents the average signal attenuation due to energy diffusion and absorption in the propagation medium. It is a deterministic quantity, which determines the average signal attenuation for a given Tx-Rx distance, being typically represented by the standard log-distance model [53].

The large-scale fading represents the variation of the local average Rx power as the user moves over the environment. It is primarily associated with obstructions of the direct propagation path, i.e. shadowing, but it is also associated with the general changes in the local propagation environment. Two types of shadowing are distinguished in off-body channels: body-shadowing from the user, and shadowing from the objects or other people in the surrounding environment. The former is due to partial or full obstructions of propagation paths by the user's body, and the latter is caused by barriers, cars and pedestrians around the user. Due to the random nature of human motion, the described obstructions of the propagation path occur in a random manner, where the resulting Rx power variations are typically described by the Lognormal distribution [54].

The small-scale fading represents random signal variations due to multipath propagation effects, where multiple replicas of the Tx signal arrive at the Rx antenna after reflecting, diffracting or scattering from objects in the environment [53]. These Multipath Components (MPCs) arrive with different delays, phases and amplitudes, due to differences in path lengths and attenuation exhibited in their paths. The signal at the output of Rx antenna is a phasor sum of MPCs, which interfere in a constructive or a destructive manners, depending on their relative phases. Since the path length difference of $\lambda/2$ yields a relative phase of 180°, the Rx signal can change drastically as the Tx or Rx move by a fraction of a wavelength. Therefore, even at low user velocities associated with BANs scenarios, the Rx signal can exhibit a fairly fast variation with the user moving or changing posture. Although less severe, small-scale fading also occurs due to the movement of objects with which the propagating waves interact, cars in the street and people in the user's surroundings being the most notable examples.

The distribution of scatterers in indoor and outdoor environments yield different multipath configurations. The enclosed indoor space is characterised with dense arrival of strong MPCs from all directions, while the open outdoor space yields somewhat sparser arrivals, fewer directions and weaker MPCs. The latter is attributed to the low Tx power in BANs, and greater distances in between the user and scatterers in outdoor environments. While signal variation due to multipath fading is deterministic in theory, the complexity of real environments makes the tracing of all contributing MPCs impossible, thus, small-scale fading is typically modelled as a stochastic process.

Signal depolarisation is an important effect in the channel, which results in losses due to mismatched polarisation of the Rx antenna and the arriving MPCs. It arises due to physical misalignment of the Tx and Rx antennas, but also due to polarisation dependent scattering effects. The former directly affects the LoS component, thus having a strong influence on channel conditions, where antenna rotation can result in a low Rx power even with the clear LoS path. The latter is due to unequal treatment of differently polarised waves interacting with objects depending on their EM properties, thus the polarisation characteristics of the channel being dependent on the particular environment in which the communication takes place.

Finally, one should note that the wearable antennas' radiation patterns are commonly considered as inseparable parts of the BAN channel, due to random gain variations experienced when the user is in motion. On the one hand, these variations can be attributed to variable antenna efficiency [55] and distortion of the radiation pattern due to twisting/stretching and varying distance from the body. On the other hand, the dominant MPCs' directions of departure/arrival (DoDs/DoAs) vary randomly due to wearable antenna rotation associated with user's motion, where the magnitudes of these variations depend on their on-body placement and user's activity [56]. One should note that with the antennas being considered as an integral part of the channel, gain variations are mostly embedded within the large-scale fading component, when the typical path loss component extraction procedure is applied.

2.7 State of the art

With the growing interest in BANs, channel modelling for these systems has become an active research area. As it is of main interest for the work presented in this thesis, the most notable off-body channel modelling studies are reviewed in this section, where a special attention is given to the depolarisation effect and the influence of user dynamics.

2.7.1 General overview

A number of off-body channel studies are available in literature, most of which are based on narrowband measurements and the proposed models are empirical [57]. The authors typically adopt the standard three-component statistical path loss model [58, 59]. While a deterministic log-distance model is used for the Mean Path Loss (MPL), statistical models are used for large- and small-scales fading. The Log-normal distribution is commonly adopted for large-scale fading, while the Rice and Nakagami-m ones are typical choices for the small-scale fading.

A slightly different approach is taken by some authors [60, 61, 62], where fading components are considered jointly. In this case, Rx signal variations are represented as a composite fading, with its distribution being derived from a product of two random variables representing each of the fading components. In [60], the authors consider κ-μ and Log-normal distributions for small- and large-scales signal variations, respectively, the obtained composite fading distribution fitting measurements very well. However, the Probability Density Function (PDF) cannot be obtained in a closed analytical form and relies on numerical integration, hence, being somewhat impractical for use. A similar approach is found in

[61], where the Gamma distribution is considered for large-scale fading instead. In [63], the authors consider η - μ distribution for small-scale variations and additionally assume that the mean power is subject to large-scale variation with the Inverse Gamma distribution.

Similar modelling approaches are adopted for the body-to-body channel, where the most notable work on its statistical description is performed by Cotton et al. [60, 64, 65, 66, 67, 68, 69]. Therein, the authors adopt the log-distance model for MPL and advocate the κ-μ distribution as a statistical model for composite fading. Based on a comparison against measurements available for indoor [64, 65] and outdoor [67, 68, 69] environments, the proposed statistical model is reported to outperform other common fading distributions, most notably the Nakagami-m one. The standard path loss model is also adopted in [70, 71], where the Log-normal and Rice distributions are used for large- and small-scales fading, respectively. In order to model the body shadowing losses, the authors propose a modification of the log-distance MPL model, specifying its parameters depending on users' mutual orientation. Thereby, the full-body blockage loss is represented by the orientation-dependent intercept term, whose values are tabulated in [70], while a piece-wise linear model is proposed in [71].

One should note that the large-scale variations in these models are typically attributed to body shadowing, even when LoS is unobstructed. While partial path obstructions certainly contribute to these variations, it seems that the contribution of shadowing effects is a minor one in the latter case, to the best of the author's judgement. The most dominant contributors are likely to be the wearable antenna gain variation, periodic polarisation mismatch losses due to antenna rotation on a dynamic user, and the local average Rx power variation with changing scattering conditions across the environment.

With the rising popularity of Millimetre Wave (mmWave) communications for the next-generation mobile networks, BANs operating at these frequencies have received attention as well. A few reported studies consider the off-body channel, almost exclusively based on narrowband measurements in the licence-free band at 60 GHz. The standard three-component path loss modelling approach is adopted for mmWave off-body channels as well, with MPL represented by a log-distance model [72], and a statistical approach taken for large- and small-scales fading [73, 62]. The model parameters are typically reported for LoS and Non-LoS (NLoS) propagation conditions, according to body shadowing from the user. In [73], the authors report the Gamma distribution as an appropriate model for large-scale fading, and Rice and Nakagami-m distributions for small-scale one in the LoS and NLoS cases, respectively. Based on the same measurement set, the authors revisit the NLoS channel in [73], and propose the η-μ/Inverse Gamma distribution for the composite fading, as previously applied at 5.8 GHz [63].

In addition to these dedicated BAN studies, all of which consider the antenna placement on the chest, a few mmWave mobile off-body channel studies with a dynamic pedestrian user are also relevant for BAN communications [74, 75]. Some of the scenarios considered therein, i.e. with the mobile terminal placed in a pocket or held against the head, can be considered as BAN ones. Both of these studies are based on narrowband measurements at 60 GHz, and adopt the same statistical model as in [73]; the difference being in the considered location of the AP. While the off-body antenna is on a stand in [74], a ceiling-mounted one is considered in [75].

Only a few other mobile off-body channel studies actually consider user effects. In [76], the authors use ray-tracing to investigate the user's influence of body shadowing on the channel, where blockage effects are represented as a part of the mobile terminal's radiation pattern. Although a scenario with the user walking is investigated, only the linear forward motion is considered. In [77], the authors show that even the small changes in the antenna height can yield a significant Rx signal variation in the LoS case at mmWave frequencies [77], due to the interference between LoS and ground-reflected components [78, 79]. While this study demonstrates the importance of taking antenna mobility into account, the statistical model assumed by the authors does not reflect the realistic characteristics of human motion.

2.7.2 Depolarisation effect

The interest in better describing the depolarisation effect arose, as it was noticed that polarisation can be exploited as an additional degree of freedom in the channel, in order to improve communication quality by means of polarisation diversity [80], or increase the available data rates by means of polarisation multiplexing [81]. Recently, the employment of dual-polarised antennas is considered for preserving high data rates in Multiple-Input Multiple-Output (MIMO) systems when the channel matrix is rank-deficient due to a strong LoS component, i.e. the keyhole effect. Moreover, the importance of the depolarisation effect is even greater if mmWave communications are employed; the higher propagation losses and fewer significant signal components in the channel, compared to frequencies below 6 GHz [82], result in a strong impact of depolarisation on mmWaves [83]. The impact is even more significant if beamforming is employed [84], as the channel then effectively relies on a single component, i.e. LoS or a specular reflection.

The existing models for depolarisation effect in mobile channels are typically statistical and based on measurements, while only few studies provide physical models explaining the actual source of depolarisation. In [85], the authors consider the depolarisation effect due to antenna mismatch, where polarisation rotation angle for the LoS component is derived based on geometry, for arbitrary antennas' orientations. The depolarisation of MPCs is typically modelled by introducing factors dependent on the Co-Polarisation Ratio (CPR) and Cross-Polarisation Ratio (XPR). A step towards better modelling of the depolarisation effect in NLoS conditions is made by Geometrical Theory of Depolarisation (GTDe), proposed in [86], where the orthogonal polarisation components of an MPC reflected from a scatterer on the cylinder centred around the mobile antenna is derived from the scenario geometry, taking the relative positions of the Tx, Rx and scatterer (Sc) into account. However, this model only considers reflections from perfectly conducting surfaces, whereas the depolarisation due to realistic scattering is considered in [87, 88].

Only a few authors have considered signal depolarisation in the off-body BAN channel. The analysis of the antenna polarisation mismatch based on a simple simulation scenario is presented in [89]. The possibility to exploit polarisation diversity for off-body communications is considered in several measurement-based studies. In [90], the authors consider a joint polarisation and spatial diversity achieved with dual-polarised wearable antennas, observing a great potential for system performance improvement; moreover, the authors report that the wearable antenna's polarisation changes from linear (in free space) to elliptical, when placed on the body. This work is further expanded in [91], where the polarisation and spatial diversity are considered at the off-body side as well. A similar study is presented in [92], where diversity gains achieved using linearly and circularly polarised antennas are compared.

A unique modelling treatment of the depolarisation effect in BAN channels is given in [93, 94], where an on-body channel model is developed based on the GTDe [86]. The coupling coefficients in between the vertical (V) and horizontal (H) polarisations at the Tx and Rx are derived from geometry, for scatterers distributed on a cylinder centred around the on-body Rx antenna. While initially considering reflections from perfectly conducting surfaces [93], the model was expanded to account for realistic scattering [94]. One should note that the proposed model is applicable for the off-body channel, as the scattering in the environment is fairly similar. It is important to note that this model considers only a static user and fixed antennas' orientations.

The influence of body dynamics on depolarisation in the on-body channel is considered in [95], where the authors use animation software to extract motion patterns in order to apply them to the body phantom in EM simulation software. As simulations were performed for free space, this paper considers only depolarisation due to interaction with the body and Tx-Rx antenna polarisation mismatch due to antenna rotation during motion.

2.7.3 Influence of user dynamics

The influence of user's motion on BAN channels is an important one. While changing antenna position yields signal variations associated with multipath fading and body shadowing [96], its rotation imposes variations in the gain and polarisation mismatch associated with MPCs arriving at the Rx. For the LoS component, the latter is primarily due to physical misalignment between the antennas on the two communication ends [85, 97].

Most of the studies related to dynamic BAN channels are based on measurements [65, 98], where the proposed empirical models consider the influence of motion only through parameters of the statistical distributions for path loss. In a more theoretical approach [99, 100], the authors use an autoregressive model to represent the temporal and cross-correlation properties of on-body channels for a dynamic user. While in this case the Rx signal characteristics for the dynamic user are represented directly within a statistical channel model, a more detailed mobility model is required for use with ray-tracing or GBSC models [101]. Several proposals, discussed in what follows, have been presented by researchers.

Adopting the existing approach used for mobile communications networks [102], the mobility models proposed in [103] and [104] are based on a general Reference Point Group Mobility (RPGM) framework. The motion of an antenna is modelled as a composition of the motion of a reference point associated with a group of antennas within the same BAN, and the individual motion of the antenna relative to this reference. In both proposed models, the former is represented by a set of straight path segments with randomly chosen direction and velocities, and the latter by a random displacement vector. While [103] assumes horizontal motion, the model in [104] is three-dimensional (3D) and additionally considers different user activities. However, it should be pointed out that these models only consider the antennas' positions, and generally fail to capture the true characteristics of human motion.

Following the initial proposal in [105, 106], some authors have used animation software to obtain realistic human body motion for on-body channel simulations [95, 107, 108, 109]; this software is used to generate a sequence of postures for virtual body phantom models in numerical EM simulators. In [110] and [111], the authors use animation software to obtain wearable antenna positions for the body-to-body channel and inter-BAN interference simulations based on ray-tracing. A similar approach is used in [56] to extract on-body antenna motion, in order to analyse its influence on the radiation pattern during movement. The authors further use this approach for body-to-body channel simulations based on a GBSC model in [112].

In order to eliminate the need for animation software, the authors in [113] used a skeleton-based motion model with Motion Capture (MoCap) data to obtain postures of a simplified cylinder-based body phantom for EM simulations. A similar approach is used to obtain the time-varying distances between wearable antennas in [114, 115], in order to improve the on-body channel simulations based on statistical models [116]. Together with a cylinder-based body model, the motion model is further exploited to account for body shadowing losses by performing a simple LoS obstruction test. A similar skeleton-based model is used to obtain the antennas' positions and orientations for their individual mobility within the RPGM model adopted in [117]. With the user's forward motion (i.e. reference point) generated by an agent-based simulation, the mobility model is used as an input to a ray-tracer for dynamic on-, off- and body-to-body channels simulation.

2.7.4 Open issues

From the presented overview of the previous work available in the literature on off-body channel models, several open issues can be identified, mainly related to the modelling of the depolarisation effect and the influence of user dynamics. While some progress is made towards understanding signal depolarisation from mostly measurement-based off-body channel characterisation studies, very few modelling efforts were made to the date [93, 94]. It is important to note here that the depolarisation effect has received considerably more attention in the mobile channel studies [118], but although the reported findings provide a valuable insight into the depolarisation mechanisms, applicability of the available models is limited. Even though the similarities between the mobile and off-body channels are obvious, the main differences follow from the latter being associated with shorter distances and low-elevated antennas. These characteristics in turn make a significant difference in the channel depolarisation characteristics, according to GTDe [86]. Moreover, with the antennas worn on clothes, one anticipates far greater influence of user dynamics in the off-body channel than in the mobile one.

In a similar way, the applicability of the findings considering the depolarisation effect in the on-body channel is also limited, as different propagation mechanisms dominate the channel. More precisely, the polarisation relative to the body surface is important in the on-body channel, where the one perpendicular to the body yields better channel conditions than the tangential one, due to the strong excited creeping (surface) wave propagating around the body when the Tx and Rx are placed on opposite sides of the body [95, 119]. On the other hand, the creeping wave propagation is far less significant in the off-body channel, which is dominated by the scattering mechanisms in the surrounding environment. Therefore, the polarisation with respect to the objects in the environment is more important in this case, as the reflection, diffraction and scattering characteristics are dependent on it [120]. Moreover, with the different relative motion in between the Tx and Rx antennas in these channels, the influence of user dynamics is different as well. Therefore, dedicated studies are required to address the peculiarities of the off-body channel.

The influence of user's motion on BAN channels has been addressed by several researchers, where the use of realistic MoCap data allowed for a notable progress in the investigation of these effects. However, mobility models based on MoCap data are limited by their resolution and size, whereas the required data storage and involved calculations considerably add to the complexity of a simulator [113, 117]. While being acceptable when the skeleton-based model is also used to modify the posture of the body phantom in full-wave on-body channel simulations [107, 95], this complexity is beyond the required one if only position and orientation of the antenna are needed, e.g. in GBSC channel models [121, 122].

Most of the available studies consider only the antenna's position, whereas its orientation is considered only by a few authors [56, 113, 117]. Moreover, the models for wearable antenna rotations in [56] and [117] are not complete. Since the authors considered only the normal vector to the patch antenna plane for its orientation in [56], the rotation about this axis is neglected. Similarly, due to limitations of the used MoCap data and the method used to obtain the orientation vectors, the rotation about the vertical axis of the antenna is neglected in [117]. However, these two rotations can have an important impact on the channel, where the former can yield significant depolarisation losses and the latter variations in the antenna gain and Cross-Polarisation Isolation (XPI), in directions of the arriving MPCs.

Finally, one should note that there is a general lack of off-body channel models that consider its polarisation aspect. Most importantly, none of the available models provide a joint treatment of the depolarisation effect and the influence of user's motion, to the best of the author's knowledge. Therefore, there is a clear need for deriving such a model. In addition to the depolarisation effect due to scattering in the environment, this model should specifically address the impact of wearable antenna rotation during motion. The outlined open issues are addressed in this thesis, which is devoted to the development of a novel channel model for polarised off-body communication with dynamic users. Such a channel model is not only paramount for optimised system design in terms of energy efficiency, but also allows for the performance evaluation of multi-polarised antenna systems [118], i.e. employed to mitigate fading [80], increase capacity [81], or to facilitate medium sharing among users [123].

Chapter 3

Channel model development

This chapter presents the development of a geometry-based polarised channel model for off-body communication with dynamic users. A general formulation of the propagation model is presented first, assuming static antennas with arbitrary orientations. Polarisation matrices, modelling the depolarisation effect for different propagation mechanisms, are derived for the LoS, reflected and diffracted signal components, considering an arbitrary geometry of the propagation environment. An analytical mobility model for wearable antennas on dynamic users is then developed in order to take the influence of user's motion into account. Finally, a simplified scattering environment geometry is considered and a simple GBSC model formulation with fewer modelling parameters is derived at the end of the chapter.

3.1 Channel impulse response

In radio communications, the signal emitted by the Tx antenna propagates towards the Rx over multiple paths, both directly over the LoS path and after interacting with objects in the propagation environment, through mechanisms of reflection, diffraction and scattering. This is illustrated in Fig. 3.1, for an off-body communications scenario in an indoor environment, where the propagation phenomena associated with the depicted MPCs is indicated.

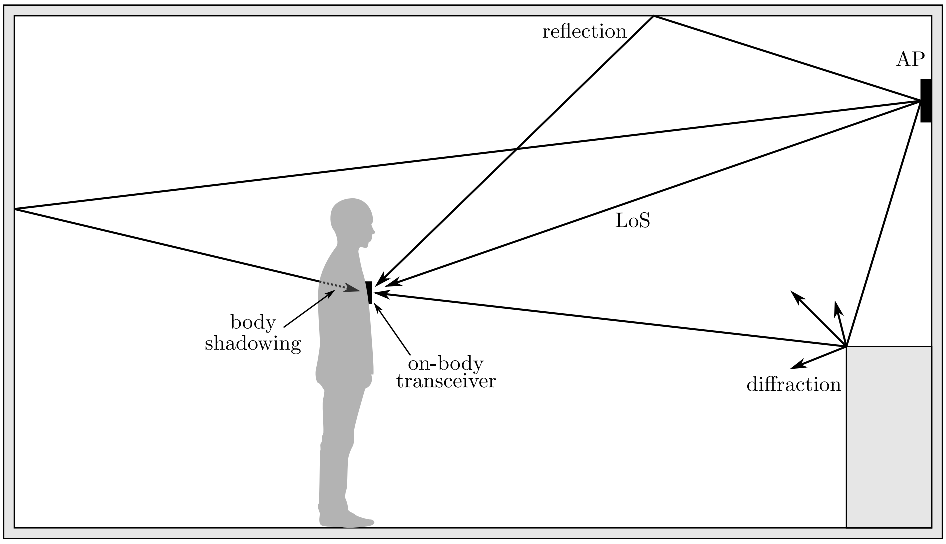

Figure 3.1: Considered propagation problem.

With multipath propagation taking place in the environment, the channel can be described by the complex baseband Channel Impulse Response (CIR) given by [124]:

$$h_{ch}(t,\tau) = \sum_{n=1}^{N_p(t)} A_n(t) e^{-j2\pi f_c \tau_n(t)} e^{-j2\pi f_D^n(t)\, t}\, \delta(\tau - \tau_n(t)) \tag{3.1}$$

where:

- t : observation time;
- τ : delay relative to the observation time;
- N_p : number of propagation paths;
- A_n : n-th component's complex amplitude;
- τ_n : n-th component's path delay;
- f_D^n : n-th component's Doppler shift frequency;
- f_c : carrier frequency;
- δ : Dirac delta function.

For narrowband communications, where the inverse of the signal bandwidth is much smaller than the maximum path delay, the channel can be represented by the complex baseband transmission coefficient:

$$h_{ch}(t) = \sum_{n=1}^{N_p(t)} A_n(t) e^{-j2\pi f_c \tau_n(t)} e^{-j2\pi f_D^n(t)\, t} \tag{3.2}$$

As indicated in (3.1) and (3.2), due to the movement of the antennas and scatterers[1], the number of MPCs arriving at the Rx antenna, their delays, amplitudes and Doppler shifts are time-variant in general. However, in most scenarios these changes are slow and negligible over local areas, hence, the time-dependence is typically neglected and constant values are assumed.

The complex amplitudes of the individual MPCs in (3.1) and (3.2) depend on the involved propagation mechanisms, with the general expression being:

$$A_n = \frac{\lambda}{4\pi} A_{sf}^n \, \mathbf{g}_r^H(\phi_r^n, \psi_r^n)_{[1\times2]} \, \mathbf{H}_{p\,[2\times2]}^n \, \mathbf{g}_t(\phi_t^n, \psi_t^n)_{[2\times1]} \tag{3.3}$$

where:

- λ : wavelength;
- A_{sf}^n : wavefront spreading factor;
- $\phi_{t/r}^n$: azimuth angle of departure/arrival (AAoD/AAoA);
- $\psi_{t/r}^n$: elevation angle of departure/arrival (EAoD/EAoA);
- $\mathbf{g}_{t/r}$: polarimetric gain vector of the Tx/Rx antenna;
- $\mathbf{H}_p^n$: path polarisation matrix;
- $(\,.\,)^H$: conjugate transpose (Hermitian).

The spreading factor models the dependence of the wavefront power density on distance, being determined by the wavefront geometry. For the LoS component and MPCs reflected from flat surfaces, the wavefront is spherical and the spreading factor is obtained as the inverse of the path length, while the geometry of the diffracted MPCs' wavefront yields a different form, as given in [125, 126].

The components of the gain vectors in (3.3) are the antenna field gains in θ- and ϕ-polarisations, assumed complex to facilitate arbitrary polarisations. These gains are specified in the antennas' local coordinate systems, i.e. associated with the angles of departure/arrival (AoD/AoA), i.e. $\phi_{t/r}^n$ and $\psi_{t/r}^n$, being defined accordingly (the upper/lower sign corresponds to index t/r):

$$\phi_{t/r}^n = \arctan\left(\frac{\pm\mathbf{k}_{t/r}^n \cdot \mathbf{u}_y^{t/r}}{\pm\mathbf{k}_{t/r}^n \cdot \mathbf{u}_x^{t/r}}\right) \tag{3.4}$$

$$\psi_{t/r}^n = \arcsin\left(\pm\mathbf{k}_{t/r}^n \cdot \mathbf{u}_z^{t/r}\right) \tag{3.5}$$

where:

- $\mathbf{k}_{t/r}^n$: DoD/DoA unit vector of the n-th MPC;
- $\mathbf{u}_{x/y/z}^{t/r}$: unit vector(s) along the $x/y/z$ axis of the Tx/Rx antenna coordinate system.

Fig. 3.2 illustrates these angles for a Tx antenna, taken as a patch represented by a dark grey rectangle, whose plane lies within the Y-Z plane of the associated local coordinate system, defined by vectors $\mathbf{u}_y^t$ and $\mathbf{u}_z^t$.

One should note that the depolarisation effect is jointly modelled by the gain vectors and the polarisation matrix in (3.3). While the former account for the imperfect antenna XPI, the latter models depolarisation due to interaction in between the MPC and objects on its path. The polarisation matrix

[1] The term "scatterer" is used in a loose sense, i.e. as a common reference for any object the MPCs interact with.

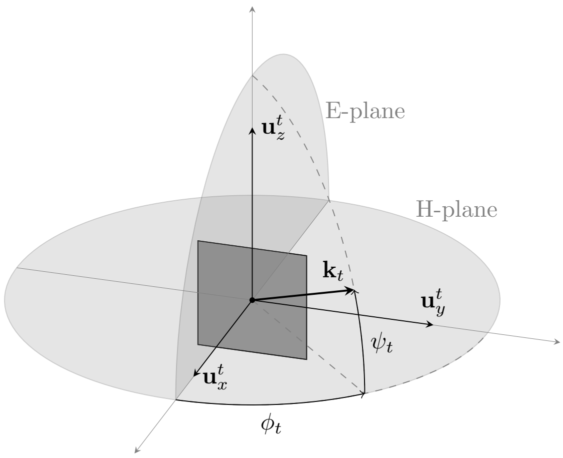

Figure 3.2: AAoD and EAoD in the Tx antenna's local coordinate system.

has different forms, depending on the involved propagation mechanism, being determined by the path geometry and the antennas' orientations.

The time-variant MPCs' phases due to the Doppler shift, as the result of relative motion in between the antennas and/or scatterers, are the principal cause of small-scale fading variations in the radio channel. The Doppler shift frequencies in (3.1) and (3.2) are obtained according to the following expressions for the LoS component and MPCs, respectively[2]:

$$f_D^{LoS} = -\frac{f_c}{c}\left(\mathbf{v}_r - \mathbf{v}_t\right)\cdot\mathbf{k} \tag{3.6}$$

$$f_D^{n} = -\frac{f_c}{c}\left(\mathbf{v}_r\cdot\mathbf{k}_r^n - \mathbf{v}_t\cdot\mathbf{k}_t^n\right) \tag{3.7}$$

where:

- $\mathbf{v}_{t/r}$: velocity vector of the Tx/Rx antenna;
- $\mathbf{k}$: common LoS DoD/DoA unit vector;
- c : speed of light.

One should note that (3.7) assumes fixed static scatterers, where the considered Doppler shift is due to the relative motion in between the antennas and their closest scatterers with which the MPC interacts on its path. In general, one has to take the relative motion in between the successive scatterers into account as well. Nevertheless, these effects are beyond the scope of this thesis and static scattering points are assumed.

3.2 Polarisation matrix

The polarisation matrix in (3.3) is the modelling term that takes signal depolarisation into account, and it is the central term in the polarised channel model developed in this thesis. It can be derived from geometry, by following the principles of Geometrical Optics (GO) and Uniform Theory of Diffraction (UTD). This section first presents a general model for the polarisation matrix, considering LoS propagation, reflection and diffraction, followed by its derivation for an arbitrary propagation environment geometry.

[2]The vectors herein are defined in physical 3D space, and the multiplication operation denotes their dot-product.

3.2.1 General model

Depolarisation of the LoS component is primarily caused by physical misalignment of the Tx and Rx antennas. Following a similar approach to the one in [85], the polarisation matrix for this component is represented as:

$$\mathbf{H}^{LoS}_{p\,[2\times2]} = \mathbf{Q}(\vartheta_{LoS})_{[2\times2]} \tag{3.8}$$

where:

- $\mathbf{Q}$: rotation matrix, i.e.

$$\mathbf{Q}_{[2\times2]}(\vartheta) = \begin{bmatrix} \cos(\vartheta) & \sin(\vartheta) \\ -\sin(\vartheta) & \cos(\vartheta) \end{bmatrix} \tag{3.9}$$

- ϑ_{LoS} : LoS mismatch angle.

The LoS mismatch angle is the one in between vectors associated with the θ-polarisations of the Tx and Rx antennas, i.e. $\mathbf{u}^t_\theta$ and $\mathbf{u}^r_\theta$. It can be derived from geometry, given the orientations of the antennas, as demonstrated in [127] for a dipole and in [85] for an arbitrary antenna. One should note that the LoS mismatch angle and the polarimetric gain vectors jointly determine the total polarisation mismatch angle, which directly translates to Polarisation Loss Factor (PLF) [55].

Following an approach similar to the one adopted in [83, 128], the channel polarisation matrix of an MPC can be represented as a sequence of linear transformations along its path. For the first-order MPCs, i.e. reflected or diffracted, the polarisation matrix has the form:

$$\mathbf{H}_{p\,[2\times2]} = \mathbf{Q}(\vartheta_r)_{[2\times2]}\,\mathbf{\Gamma}_{r/d\,[2\times2]}\,\mathbf{Q}(\vartheta_t)_{[2\times2]} \tag{3.10}$$

where:

- $\mathbf{\Gamma}_{r/d}$: scattering (reflection/diffraction) matrix.
- $\vartheta_{t/r}$: Tx/Rx mismatch angle.

The mismatch angles correspond to those in between the antennas' orthogonal polarisation components, i.e. $\mathbf{u}^{t/r}_\theta$ and $\mathbf{u}^{t/r}_\phi$, and directions perpendicular and parallel to the incidence plane, i.e. $\mathbf{u}_\perp$ and $\mathbf{u}^{t/r}_\parallel$, as illustrated in Fig. 3.3. These angles jointly model the depolarisation due to inclination of the incidence plane [86, 93], and the physical orientation of the antennas [85]. The polarisation matrix of the higher-order MPCs is obtained by applying the same principle along the paths.

The scattering matrix models the depolarisation and attenuation of an MPC interacting with an object in the environment, and its form depends on the particular propagation mechanism. For reflected MPCs, this matrix is diagonal [124], i.e.

$$\mathbf{\Gamma}_{r\,[2\times2]} = \begin{bmatrix} R_\perp(\vartheta_i) & 0 \\ 0 & R_\parallel(\vartheta_i) \end{bmatrix} \tag{3.11}$$

where:

- ϑ_i : incidence angle;

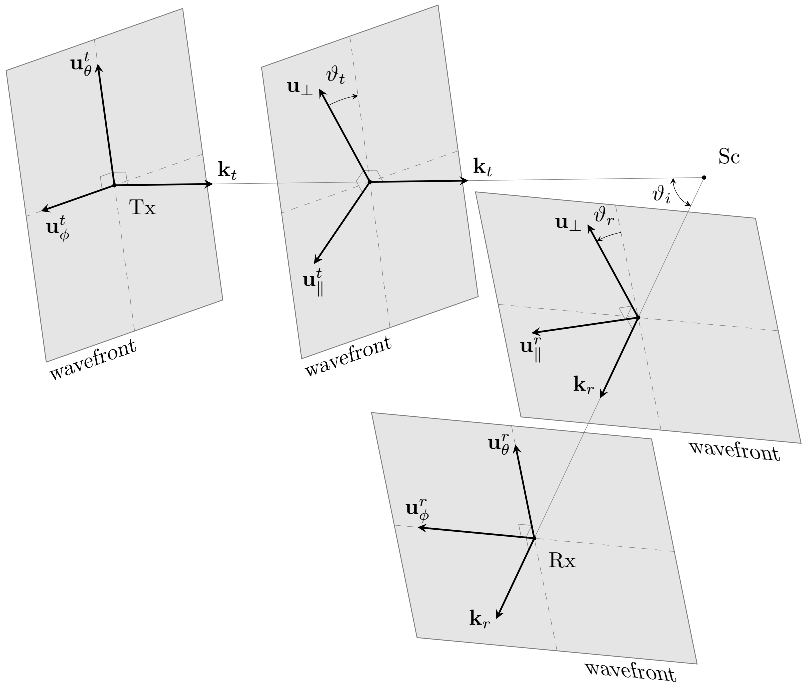

Figure 3.3: Polarisation directions and mismatch angles in space, for the first-order MPCs.

- $R_{\perp/\parallel}$: reflection coefficient for polarisation perpendicular/parallel to the incidence plane.

Considering the typical (non-magnetic) dielectric materials, the reflection coefficients are given by [124]:

$$R_\perp = \frac{\cos(\vartheta_i) - \sqrt{\epsilon_r - \sin^2(\vartheta_i)}}{\cos(\vartheta_i) + \sqrt{\epsilon_r - \sin^2(\vartheta_i)}} \tag{3.12}$$

$$R_\parallel = \frac{\epsilon_r \cos(\vartheta_i) - \sqrt{\epsilon_r - \sin^2(\vartheta_i)}}{\epsilon_r \cos(\vartheta_i) + \sqrt{\epsilon_r - \sin^2(\vartheta_i)}} \tag{3.13}$$

where:

- ϵ_r : relative dielectric constant of the surface material.

The exhibited reflection loss and the reflected field's polarisation angle can be determined from the reflection coefficients, according to:

$$R_{loss} = \sqrt{R_\perp^2 \cos\vartheta_{pol}^i + R_\parallel^2 \sin\vartheta_{pol}^i} \tag{3.14}$$

$$\vartheta_{pol}^r = \arctan\left(\frac{R_\parallel \sin\vartheta_{pol}^i}{R_\perp \cos\vartheta_{pol}^i}\right) \tag{3.15}$$

where:

- θ_{pol}^i : incident polarisation angle, with respect to the incidence plane normal vector.

For diffracted MPCs, according to [125, 129], with a simple rearrangement, the diffraction matrix $\mathbf{\Gamma}_d$ is given as:

$$\mathbf{\Gamma}_{d\,[2\times2]} = -(D_i^0 + D_i^n)\mathbf{Q}(2\vartheta_e)_{[2\times2]} + D_r^0\,\mathbf{\Gamma}_r(\vartheta_i^0)_{[2\times2]} + D_r^n\,\mathbf{\Gamma}_r(\vartheta_i^n)_{[2\times2]} \tag{3.16}$$

where:

- ϑ_e : angle between the conventional and edge-fixed planes of incidence;
- $\vartheta_i^{0/n}$: angle of incidence at the $0/n$-face of the wedge;
- $D_{i/r}^{0/n}$: diffraction coefficient for incidence/reflection associated with the $0/n$-face of the wedge.

According to UTD, the diffraction coefficients are given as (the upper/lower sign corresponding to superscript $0/n$) [126, Ch. 6]:

$$D_i^{0/n} = \frac{-\,e^{-j\frac{\pi}{4}}}{2n_\alpha\sqrt{2\pi k}\,\sin(\psi_i)}\,\cot\left[\frac{\pi \mp (\phi_i^d - \phi_i^t)}{2n_\alpha}\right] F[kL_d a_d^{\mp}(\phi_i^d - \phi_i^t)] \tag{3.17}$$

$$D_r^{0/n} = \frac{-\,e^{-j\frac{\pi}{4}}}{2n_\alpha\sqrt{2\pi k}\,\sin(\psi_i)}\,\cot\left[\frac{\pi \mp (\phi_i^d + \phi_i^t)}{2n_\alpha}\right] F[kL_d a_d^{\mp}(\phi_i^d + \phi_i^t)] \tag{3.18}$$

where:

- ψ_i : incidence angle with respect to the edge;
- $\phi_i^{t/d}$: incidence/diffraction angle with respect to the 0-face of the wedge;
- n_α : wedge inner angle parameter, with the inner angle being given as:

$$\alpha_w = (2 - n_\alpha)\pi \tag{3.19}$$

  where for the typical wedges, one has $\alpha_w = \pi/2$ and $n_\alpha = 3/2$;
- k : propagation constant, i.e. $k = 2\pi/\lambda$;
- L_d : distance parameter, given as:

$$L_d = \frac{r_{ts}r_{sr}\sin^2(\psi_i)}{r_{ts} + r_{sr}} \tag{3.20}$$

  $r_{ts/sr}$ being the distance in between the Tx/Rx antenna and the diffraction point;
- $a_d^{\mp}(\,.\,)$: functions defined as:

$$a_d^{\mp}(x) = 1 + \cos\left[2\pi n_\alpha N_d^{\mp}(x) - x\right] \tag{3.21}$$

  with:

$$N_d^{\mp}(x) = \mathrm{round}\left(\frac{x \mp \pi}{2\pi n_\alpha}\right) \tag{3.22}$$

  where $\mathrm{round}(\,.\,)$ returns the integer closest to the argument;
- $F(\,.\,)$: transition function in the form of a Fresnel integral, given as:

$$F(x) = 2j\sqrt{x}e^{jx}\int_{\sqrt{x}}^{\infty} e^{-jt^2}\,dt \tag{3.23}$$

The geometry associated with the wedge diffraction is shown in Fig. 3.4, where the important parameters in (3.17) and (3.18) are indicated. The conventional incidence plane is dotted in the figure, while the edge-fixed ones are depicted with a grey shade. One should note that the former is defined by antennas positions and the diffraction point, and the latter two by the edge and the Tx and Rx antennas, respectively. The angles in between both edge-fixed planes and the conventional one are equal, being derived in [130, App. III].

Finally, one should note that body-shadowing from the user is not explicitly modelled in this work, but it is assumed to be accounted for by the wearable antenna radiation pattern, obtained with it operating

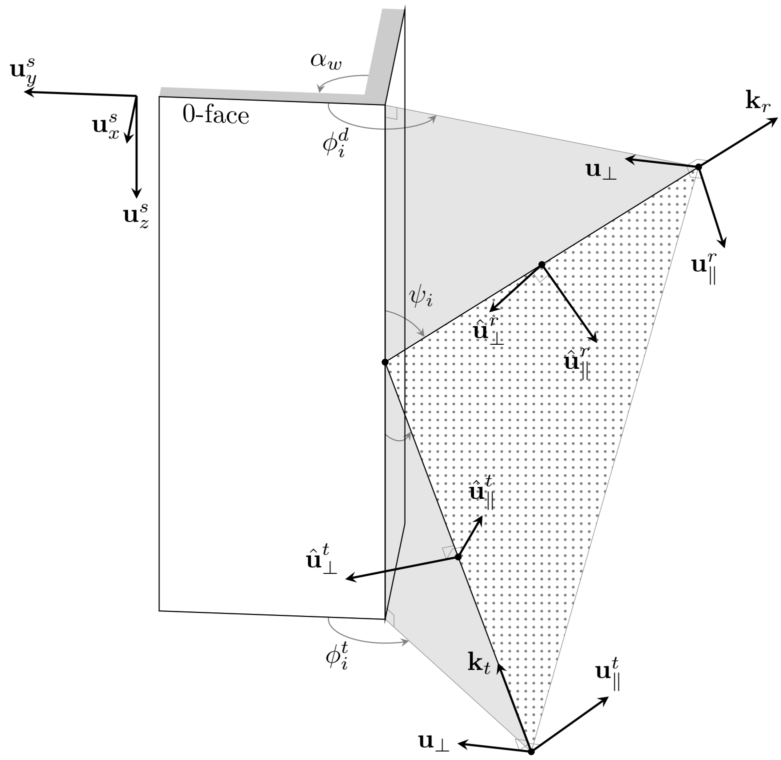

Figure 3.4: Wedge diffraction geometry.

on the body. If a more delicate treatment of the shadowing by the user is required, the UTD for cylinder diffraction [131, 132] can be employed to account for the body-diffracted MPCs that propagate around the body as creeping waves [133, 134]. A similar approach can be adopted for the shadowing from other people obstructing the LoS or MPCs' paths [135]. However, the latter is out of the scope of this work.

3.2.2 Geometry-based derivation

The polarisation matrix elements represent the coupling coefficients in between the θ - and ϕ -polarisations of the Tx and Rx antennas. As demonstrated in what follows, these coupling coefficients depend on the path geometry of an MPC and the involved propagation mechanisms. One should note that the expressions provided herein are general and applicable to any propagation environment geometry.

LoS

Considering the LoS component, for the LoS mismatch angle one has:

$$\cos(\vartheta_{LoS}) = \mathbf{u}_\theta^t \cdot \mathbf{u}_\theta^r \tag{3.24}$$

$$\sin(\vartheta_{LoS}) = \mathbf{u}_\theta^r \cdot \mathbf{u}_\phi^t \tag{3.25}$$

where:

- $\mathbf{u}_{\theta/\phi}^{t/r}$: unit Tx/Rx antenna θ/ϕ -polarisation vector.

The unit polarisation reference vectors for the direct path are obtained as:

$$\mathbf{u}_{\phi}^{t/r} = \frac{\mathbf{k} \times \mathbf{u}_z^{t/r}}{\left\|\mathbf{k} \times \mathbf{u}_z^{t/r}\right\|} \tag{3.26}$$

$$\mathbf{u}_{\theta}^{t/r} = \mathbf{u}_{\phi}^{t/r} \times \mathbf{k} \tag{3.27}$$

with the LoS component DoD/DoA being given as:

$$\mathbf{k} = \frac{\mathbf{r}_r - \mathbf{r}_t}{\|\mathbf{r}_r - \mathbf{r}_t\|} \tag{3.28}$$

where:

- $\mathbf{r}_{t/r}$: Tx/Rx antenna position.

By replacing (3.24) and (3.25) in (3.8), one obtains the polarisation matrix for the LoS component, i.e.

$$\mathbf{H}_{p\,[2\times2]}^{LoS} = \begin{bmatrix} \mathbf{u}_{\theta}^{t} \cdot \mathbf{u}_{\theta}^{r} & \mathbf{u}_{\phi}^{t} \cdot \mathbf{u}_{\theta}^{r} \\ -\mathbf{u}_{\phi}^{t} \cdot \mathbf{u}_{\theta}^{r} & \mathbf{u}_{\theta}^{t} \cdot \mathbf{u}_{\theta}^{r} \end{bmatrix} \tag{3.29}$$

Reflection

The mismatch angles for the first-order reflected MPCs are obtained as (the upper/lower sign corresponds to index t/r):

$$\cos(\vartheta_{t/r}) = \quad \mathbf{u}_{\theta}^{t/r} \cdot \mathbf{u}_{\perp} \tag{3.30}$$

$$\sin(\vartheta_{t/r}) = \pm\mathbf{u}_{\phi}^{t/r} \cdot \mathbf{u}_{\perp} \tag{3.31}$$

where:

- $\mathbf{u}_{\perp}$: unit vector perpendicular to the incidence plane.

The unit polarisation reference vectors are in this case obtained according to:

$$\mathbf{u}_{\phi}^{t/r} = \frac{\mathbf{k}_{t/r} \times \mathbf{u}_z^{t/r}}{\left\|\mathbf{k}_{t/r} \times \mathbf{u}_z^{t/r}\right\|} \tag{3.32}$$

$$\mathbf{u}_{\theta}^{t/r} = \mathbf{u}_{\phi}^{t/r} \times \mathbf{k}_{t/r} \tag{3.33}$$

$$\mathbf{u}_{\perp} = \frac{\mathbf{k}_r \times \mathbf{k}_t}{\|\mathbf{k}_r \times \mathbf{k}_t\|} \tag{3.34}$$

with the DoD/DoA vectors given by (the upper/lower sign corresponds to index t/r):

$$\mathbf{k}_{t/r} = \pm\frac{\mathbf{r}_s - \mathbf{r}_{t/r}}{\left\|\mathbf{r}_s - \mathbf{r}_{t/r}\right\|} \tag{3.35}$$

where:

- $\mathbf{r}_s$: scatterer position, i.e. reflection point.

By replacing (3.32) -(3.34) in (3.10), one obtains the polarisation matrix as:

$$\mathbf{H}_{p\,[2\times2]} = \begin{bmatrix} \mathbf{u}_{\theta}^{r} \cdot \mathbf{u}_{\perp} & -\mathbf{u}_{\phi}^{r} \cdot \mathbf{u}_{\perp} \\ \mathbf{u}_{\phi}^{r} \cdot \mathbf{u}_{\perp} & \mathbf{u}_{\theta}^{r} \cdot \mathbf{u}_{\perp} \end{bmatrix} \begin{bmatrix} R_{\perp} & 0 \\ 0 & R_{\|} \end{bmatrix} \begin{bmatrix} \mathbf{u}_{\theta}^{t} \cdot \mathbf{u}_{\perp} & \mathbf{u}_{\phi}^{t} \cdot \mathbf{u}_{\perp} \\ -\mathbf{u}_{\phi}^{t} \cdot \mathbf{u}_{\perp} & \mathbf{u}_{\theta}^{t} \cdot \mathbf{u}_{\perp} \end{bmatrix} \tag{3.36}$$

The reflection coefficients in (3.36) are obtained according to (3.12) and (3.13), where:

$$\cos(\vartheta_i) = \sqrt{\frac{1}{2}(1 - \mathbf{k}_r \cdot \mathbf{k}_t)} \tag{3.37}$$

$$\sin(\vartheta_i) = \sqrt{\frac{1}{2}(1 + \mathbf{k}_r \cdot \mathbf{k}_t)} \tag{3.38}$$

Diffraction

The mismatch angles for the first-order diffracted MPCs are obtained according to the same expressions as for the reflected ones, with the scatter position in this case being the diffraction point on the edge. For the angle in between the conventional and edge-fixed planes of incidence in (3.16), one has [130, App. III]:[3]

$$\cos(\vartheta_e) = \hat{\mathbf{u}}^t_\perp \cdot \mathbf{u}_\perp \tag{3.39}$$

$$\sin(\vartheta_e) = \hat{\mathbf{u}}^t_\parallel \cdot \mathbf{u}_\perp \tag{3.40}$$

where:

- $\hat{\mathbf{u}}^t_{\perp/\parallel}$: unit vector perpendicular/parallel to the edge-fixed plane of incidence (Fig. 3.4).

With the DoD and DoA given by (3.35) in this case as well, the unit polarisation reference vectors associated with the edge-fixed incidence plane are obtained according to [126, Ch. 6] (the upper/lower sign corresponds to index t/r):

$$\hat{\mathbf{u}}^{t/r}_\perp = \pm\frac{\mathbf{k}_{t/r} \times \mathbf{u}^s_z}{\left\|\mathbf{k}_{t/r} \times \mathbf{u}^s_z\right\|} \tag{3.41}$$

$$\hat{\mathbf{u}}^{t/r}_\parallel = \quad \mathbf{k}_{t/r} \times \hat{\mathbf{u}}^{t/r}_\perp \tag{3.42}$$

where:

- $\mathbf{u}^s_z$: unit z-axis vector of the local coordinate system associated with the wedge, i.e. aligned with the edge (Fig. 3.4).

By replacing (3.39) and (3.40), together with (3.30) and (3.31), one obtains the polarisation matrix as:

$$\mathbf{H}_{p\,[2\times2]} = \begin{bmatrix} \mathbf{u}^r_\theta \cdot \mathbf{u}_\perp & -\mathbf{u}^r_\phi \cdot \mathbf{u}_\perp \\ \mathbf{u}^r_\phi \cdot \mathbf{u}_\perp & \mathbf{u}^r_\theta \cdot \mathbf{u}_\perp \end{bmatrix} \begin{bmatrix} \Gamma_{d11} & \Gamma_{d12} \\ \Gamma_{d21} & \Gamma_{d22} \end{bmatrix} \begin{bmatrix} \mathbf{u}^t_\theta \cdot \mathbf{u}_\perp & \mathbf{u}^t_\phi \cdot \mathbf{u}_\perp \\ -\mathbf{u}^t_\phi \cdot \mathbf{u}_\perp & \mathbf{u}^t_\theta \cdot \mathbf{u}_\perp \end{bmatrix} \tag{3.43}$$

with:

$$\Gamma_{d11} = D^0_r R^0_\perp + D^n_r R^n_\perp - (D^0_i + D^n_i)\left[(\hat{\mathbf{u}}^t_\perp \cdot \mathbf{u}_\perp)^2 - (\hat{\mathbf{u}}^t_\parallel \cdot \mathbf{u}_\perp)^2\right] \tag{3.44}$$

$$\Gamma_{d22} = D^0_r R^0_\parallel + D^n_r R^n_\parallel - (D^0_i + D^n_i)\left[(\hat{\mathbf{u}}^t_\perp \cdot \mathbf{u}_\perp)^2 - (\hat{\mathbf{u}}^t_\parallel \cdot \mathbf{u}_\perp)^2\right] \tag{3.45}$$

$$\Gamma_{d12} = -\Gamma_{d21} = 2\,(\hat{\mathbf{u}}^t_\parallel \cdot \mathbf{u}_\perp)(\hat{\mathbf{u}}^t_\perp \cdot \mathbf{u}_\perp) \tag{3.46}$$

where:

- $R^{0/n}_{\perp/\parallel}$: reflection coefficient for the polarisation perpendicular/parallel to the incidence plane, for reflection on the $0/n$-face of the wedge.

[3] One uses the double angle formulas for sine and cosine to then obtain the elements of the rotation matrix in (3.16).

Considering the remaining parameters required to calculate diffraction coefficients according to (3.17) and (3.18), for the incidence angle with respect to the edge, one has:

$$\sin(\psi_i) = \sqrt{1 - (\mathbf{k}_t \cdot \mathbf{u}_z^s)^2} \tag{3.47}$$

Similarly, the incidence and diffraction angles with respect to the 0-face of the wedge are obtained according to (the upper/lower sign corresponds to index t/d):

$$\phi_i^{t/d} = \arctan\left(\frac{\mp\mathbf{k}_{t/r} \cdot \mathbf{u}_x^s}{\mp\mathbf{k}_{t/r} \cdot \mathbf{u}_y^s}\right) \tag{3.48}$$

where:

- $\mathbf{u}_{x,y}^s$: unit x/y-axis vector of the local coordinate system associated with the wedge (Fig. 3.4).

Finally, the incidence angles for reflections from wedge faces are given by:

$$\cos(\vartheta_i^0) = \max\{-\mathbf{k}_t \cdot \mathbf{u}_x^s, \quad \mathbf{k}_r \cdot \mathbf{u}_x^s\} \tag{3.49}$$

$$\cos(\vartheta_i^n) = \max\{\quad \mathbf{k}_t \cdot \mathbf{u}_y^s, -\mathbf{k}_r \cdot \mathbf{u}_y^s\} \tag{3.50}$$

3.3 Influence of user dynamics

Both displacement and rotation of the antenna affect the channel. The former yields changes in the propagation path geometry, which primarily result in MPCs' phase variation, hence, giving rise to multipath fading. The latter changes the radiation characteristics of the antenna relative to the surroundings, i.e. the spatial characteristics of the radiated field in the Tx mode, or the sensitivity to arriving MPCs in the Rx one. This means that the DoDs/DoAs of the MPCs, as seen by the wearable antenna, are time-variant. These DoDs/DoAs are given by the corresponding azimuth and elevation angles (the upper/lower sign corresponds to index t/r):

$$\phi_{t/r}(t, \hat{\phi}_{t/r}, \hat{\phi}_{t/r}) = \arctan\left(\frac{\pm\mathbf{k}_{t/r}(\hat{\phi}_{t/r}, \hat{\phi}_{t/r}) \cdot \mathbf{u}_y^a(t)}{\pm\mathbf{k}_{t/r}(\hat{\phi}_{t/r}, \hat{\phi}_{t/r}) \cdot \mathbf{u}_x^a(t)}\right) \tag{3.51}$$

$$\psi_{t/r}(t, \hat{\phi}_{t/r}, \hat{\phi}_{t/r}) = \arcsin\left(\pm\mathbf{k}_{t/r}(\hat{\phi}_{t/r}, \hat{\phi}_{t/r}) \cdot \mathbf{u}_z^a(t)\right) \tag{3.52}$$

where:

- $\mathbf{u}_{x/y/z}^a$: unit vector along the $x/y/z$ axis of the antenna coordinate system.

The terms in (3.51) and (3.52) are illustrated in Fig. 3.5, for a rotated patch antenna whose plane lies within the Y-Z plane of the associated local coordinate system, shown as a grey rectangle. One should note that the DoD/DoA vectors in (3.51) and (3.52), $\mathbf{k}_{t/r}$, also change with the antenna displacement. However, these changes are slow over the motion cycle, the antenna rotation having the dominant influence.

A variable DoD/DoA of the MPC yields variations in the associated gain, as one has:

$$G_{t/r}(\phi_{t/r}, \psi_{t/r})_{[\mathrm{dB}]} = 20 \log \left\|\mathbf{g}_{t/r}(\phi_{t/r}, \psi_{t/r})\right\| \tag{3.53}$$

However, user's motion has even a more significant effect on channel characteristics when signal polarisation is considered. In addition to amplitude fluctuations due to variable gain, DoD/DoA variations due

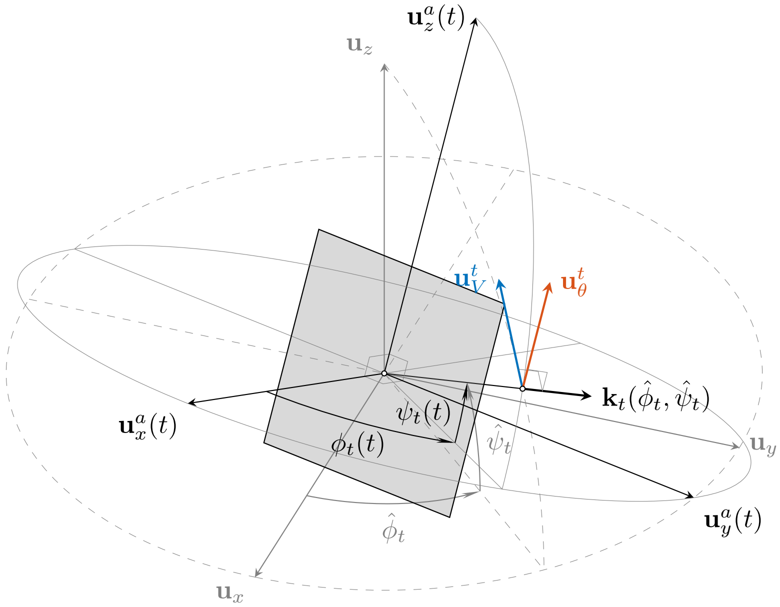

Figure 3.5: AAoD and EAoD in the rotated antenna coordinate system.

to antenna rotation also contribute to the depolarisation effect. The imbalance between gain components results in a rotation of the antenna polarisation relative to the reference, i.e. θ - and ϕ -polarisations. More precisely, considering a linearly polarised antenna, the polarisation angle relative to the θ -polarisation is given as:

$$\vartheta_{pol}^{ta/ra}(\phi_{t/r}, \psi_{t/r}) = \arctan\left(\frac{\left|g_{t/r}^{\phi}(\phi_{t/r}, \psi_{t/r})\right|}{\left|g_{t/r}^{\theta}(\phi_{t/r}, \psi_{t/r})\right|}\right) \tag{3.54}$$

where:

- $g_{t/r}^{\theta/\phi}$: complex Tx/Rx antenna gain in θ/ϕ -polarisation.

This means that the polarisation of a departing MPC on the one hand, and the mismatch in between the polarisations of an arriving MPC and the antenna on the other hand, are changing due to user's motion. This depolarisation mechanism, associated with imperfect polarisation characteristics of practical antennas, affects MPCs as well as the LoS component, thus having an important influence on the average Rx power. This, however, does not apply to antennas with ideal polarisation characteristics, e.g. dipoles, which radiate and receive energy only in the θ-polarisation [55]. This depolarisation mechanism is typically quantified by the antenna XPI, calculated as:

$$X_{pi}^{t/r}(\phi_{t/r}, \psi_{t/r})_{[\mathrm{dB}]} = 20\log\left|\frac{g_{t/r}^{\theta}(\phi_{t/r}, \psi_{t/r})}{g_{t/r}^{\phi}(\phi_{t/r}, \psi_{t/r})}\right| \tag{3.55}$$

The antenna rotation has another, more significant, contribution to the depolarisation effect. The consequent rotation of the antenna polarisation reference vectors, i.e. $\mathbf{u}_\theta^a$ and $\mathbf{u}_\phi^a$, results in a further mismatch between the antenna and the MPC. In the model, this is represented by the LoS mismatch angle in (3.8), and by the Tx and Rx mismatch angles in (3.10).

3.4 Antenna mobility model

This section presents an analytical mobility model for wearable antennas in BANs with dynamic users, developed in order to take the influence of user dynamics into account. The model is simple, yet realistic, with MoCap data being used to calculate its parameters. It is suitable for use with a variety of propagation channel models, including deterministic ray-tracing and stochastic geometry-based ones, but also allows for analytical inference in simplified scenarios.

3.4.1 Position and orientation of the antenna

The uniform motion of a person walking and running is distinctively cyclic, and can be represented as the composition of two components: forward motion at a constant velocity, and a periodic component corresponding to the change in body posture during a motion cycle. Considering the position of an on-body antenna, the former translates into a linear component common to all on-body antennas, describing the position of a reference point associated with the body, while the latter corresponds to the relative motion of the antenna with respect to this reference. Hence, the position of the antenna over time can be represented as:

$$\mathbf{r}_{[\mathrm{m}]}(t) = \mathbf{r}_{0\,[\mathrm{m}]} + v_{u\,[\mathrm{m/s}]}\, t_{[\mathrm{s}]}\, \mathbf{u}_v + \Delta\mathbf{r}_{[\mathrm{m}]}(t) \tag{3.56}$$

where:

- v_u : user's velocity;
- $\mathbf{r}_0$: starting point, i.e.

$$\mathbf{r}_0 = (r_{0,x},\ r_{0,y},\ 0) \tag{3.57}$$

- $\mathbf{u}_v$: unit direction vector, i.e.

$$\mathbf{u}_v = (\cos\phi_u, \sin\phi_u, 0) \tag{3.58}$$

  with ϕ_u being the direction azimuth angle;
- $\Delta\mathbf{r}$: periodic component.

The terms in (3.56) are illustrated in Fig. 3.6. In order to allow for the highest level of flexibility and the most straightforward modification of motion for an arbitrary path, model parameters are calculated for the reference case in which the user starts at the origin and moves in the positive x-axis direction, i.e. $r_{0,x/y} = 0\,\mathrm{m}$ and $\phi_u = 0°$.

Following an approach similar to the one used in computer animation [136], the periodic component is modelled by a Fourier series for each coordinate, i.e. Δr_x, Δr_y, and Δr_z, which can be expressed in a vector form by:

$$\Delta\mathbf{r}(t) = \mathbf{a}_0 + \sum_{n=1}^{N_h} \left[\mathbf{a}_n^c \cos\left(n\frac{2\pi}{T}t\right) + \mathbf{a}_n^s \sin\left(n\frac{2\pi}{T}t\right) \right] \tag{3.59}$$

where:

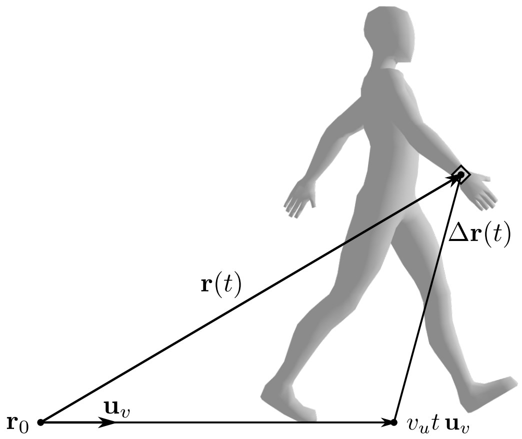

Figure 3.6: Illustration of the model for antenna position.

- N_h : number of harmonics;
- T : motion cycle period;
- $\mathbf{a}_0$: mean values of position coordinates;
- $\mathbf{a}_n^c$: amplitudes of n-th harmonic's cosine component;
- $\mathbf{a}_n^s$: amplitudes of n-th harmonic's sine component.

This approach yields a unified model for all on-body antennas and user motions, where only the values of the parameters change; the period (T) is fixed for a particular user motion, while the amplitude parameters $\mathbf{a}_0$, $\mathbf{a}_n^c$ and $\mathbf{a}_n^s$ vary for antenna's placements and motions. The number of harmonics can be chosen separately for each component, depending on its variability; N_h is chosen according to the most variable component, while the higher harmonics' amplitude parameters are set to zero for the less variable ones. One should note that $\mathbf{a}_0$ obtained for a walking user approximates the antenna position for the static standing posture, hence, it can be used for static off-body channel considerations.

The antenna orientation can be represented as a rotation of the local coordinate system relative to the global one (i.e. $\mathbf{u}_x$, $\mathbf{u}_y$ and $\mathbf{u}_z$), which in turn can be represented by a sequence of Euler rotations [137]. With a chosen axis rotation sequence Z-Y-Z, the antenna orientation is represented by three (proper) Euler angles[4] γ_1, γ_2 and γ_3, corresponding to the successive elementary rotations about the z-, y- and z-axes of the local coordinate system, respectively, as illustrated in Fig. 3.7.

The antenna orientation vectors at the end of the rotation sequence are obtained in the columns/rows of the composite rotation matrix (considering column/row-vector representation) [137], where one has:

$$\begin{aligned}\mathbf{u}_x^a = (\, & \cos\gamma_1\cos\gamma_2\cos\gamma_3 - \sin\gamma_1\sin\gamma_3,\\ & \sin\gamma_1\cos\gamma_2\cos\gamma_3 + \cos\gamma_1\sin\gamma_3,\\ & -\sin\gamma_2\cos\gamma_3) \qquad (3.60)\\ \mathbf{u}_y^a = (\, & -\cos\gamma_1\cos\gamma_2\sin\gamma_3 - \sin\gamma_1\cos\gamma_3,\\ & -\sin\gamma_1\cos\gamma_2\sin\gamma_3 + \cos\gamma_1\cos\gamma_3,\end{aligned}$$

[4]While this notation is chosen for convenience, in computer animation and aerospace engineering Euler angles are typically denoted as α, β, γ or ϕ, θ, ψ, respectively.

$$\sin\gamma_2 \sin\gamma_3) \tag{3.61}$$

$$\mathbf{u}_z^a = (\cos\gamma_1 \sin\gamma_2,\ \sin\gamma_1 \sin\gamma_2,\ \cos\gamma_2) \tag{3.62}$$

With the chosen rotation sequence Z-Y-Z, the first two Euler angles specify the antenna tilt; γ_1 is the azimuth direction in which the antenna is tilted and γ_2 is the tilt angle. The last angle in the sequence, i.e. γ_3, determines the final pointing direction of the antenna.

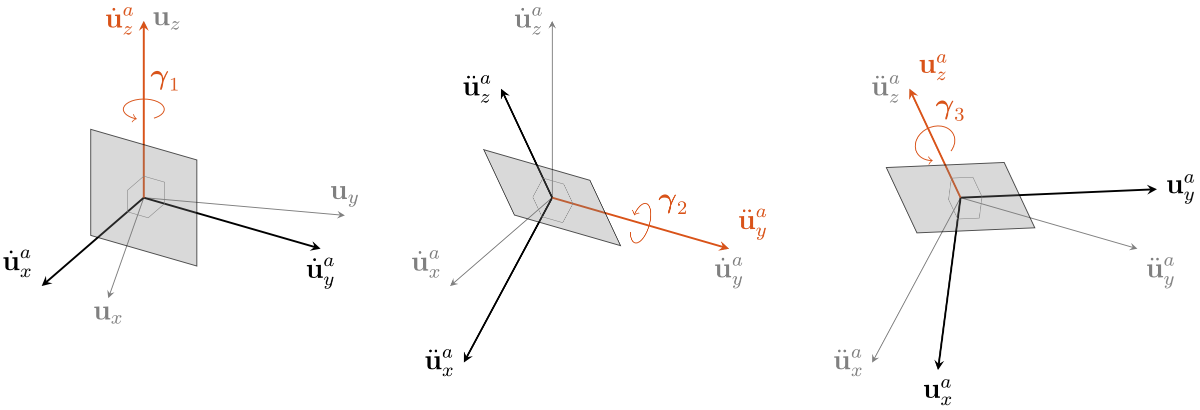

Figure 3.7: Successive Euler rotations, for the axis rotation sequence Z-Y-Z.

For the periodic character of the antenna rotation imposed by motions due to walking or running, Euler angles exhibit periodic variations, hence, they can be modelled via a Fourier series given as:

$$\gamma_i(t) = b_{0,i} + \sum_{n=1}^{N_h} \left[b_{n,i}^c \cos\left(n\frac{2\pi}{T}t\right) + b_{n,i}^s \sin\left(n\frac{2\pi}{T}t\right) \right] \tag{3.63}$$

where:

- $b_{0,i}$: mean value of angle γ_i;
- $b_{n,i}^c$: amplitude of n-th harmonic's cosine component;
- $b_{n,i}^s$: amplitude of n-th harmonic's sine component.

The period of the series for Euler angles (3.63) is the same as that for antenna position (3.59), for each user motion.

3.4.2 Estimation of model parameters

In order to obtain realistic motion, the calculation of the model parameters is based on MoCap data [138]. While these data are provided for the human body, the motion of the attached on-body antennas can be obtained by using the methods from computer animation. To do so, one should consider that MoCap data are provided for a skeleton model that represents the body as a set of bones and connecting joints [137]. The skeleton's motion is provided in terms of the position of an associated reference point and a set of rotations for each joint; the former specifies the global position of the body, and the latter sets the orientations of the associated bones and posture of the body, altogether.

In a way similar to the one used to drive the motion of a character in computer animation, the skeleton with its associated MoCap data can be used to drive the motion of an on-body antenna. This is achieved by associating the antenna with a bone in the skeleton based on the on-body placement, i.e. by defining its position and orientation relative to the bone, and inheriting its motion. Fig. 3.8 shows this association for several on-body antenna placements: front and back sides of the torso (To_F/B), left and right sides of the waist (Wa_L/R), left and right sides of the head (He_L/R), left and right upper arms (AU_L/R), left and right hand wrists (AL_L/R), left and right upper legs (LU_L/R), and left and right lower legs (LL_L/R). These antenna placements are chosen to represent popular BAN applications, such as smart watch, smart glasses, and chest band cardio monitor, among others [1].

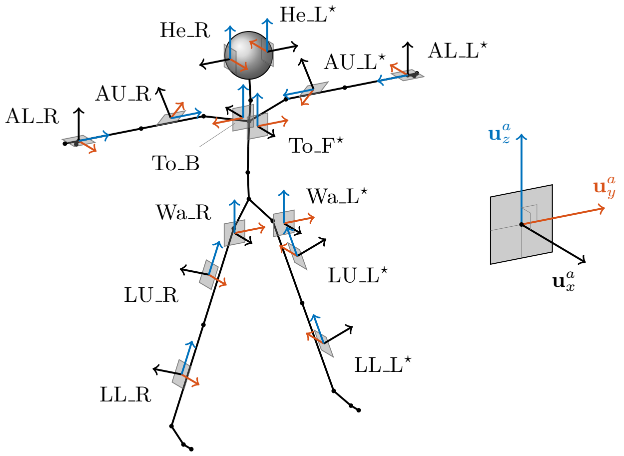

Figure 3.8: Wearable antenna placements and their association with the skeleton model.

With the established antenna-bone association, the antenna motion is obtained by using the MoCap toolbox in MATLAB [139], [140] and the data available in the CMU Graphics Lab Database [138], namely, motions 33 (walking) and 26 (running) for subject 35. A simple linear transformation is applied to the data to obtain the motion with a user moving in the positive x-axis direction, starting at the origin. Then the data corresponding to a single motion cycle period are extracted based on a gait analysis [137]. The parameters of the forward motion component in (3.56) are first calculated by fitting a linear model to the x-axis coordinate of the extracted antenna position, where the obtained slope corresponds to the velocity (v_u). The least squares fit of the series is then performed for the periodic components, where the least number of harmonics is chosen for which the maximum absolute error is below a tolerance threshold, i.e. 5 cm for the position and 10° for the angles. The angle of the relative rotation between the orientations obtained from the proposed model and the MoCap data, i.e. extracted from the axis-angle representation [137], is considered for the latter.

The main goal is to capture the main characteristics of the periodic antenna motion while preserving simplicity. Imposing more stringent constraints on the error tolerance would result in a higher number of harmonics in the Fourier series representation, while just marginally improving the model's accuracy. Since human motion is not perfectly periodic, the periodicity imposed by the Fourier series yields deviations from the MoCap data that are tolerated by the adopted thresholds. If required, these deviations can be simulated by adding additional periodic components to antenna position and orientation, with their period stretching over several (e.g. 2 or 3) motion periods. One could justifiably argue that the antenna position error, in channel modelling applications, has more significance at higher frequencies, e.g millimetre waves. Nonetheless, the above reasoning still applies and one should restrain from over-modelling. Furthermore, one should remember that human motion is not deterministic, thus an effort to improve the model accuracy beyond a certain threshold is not of value for the purpose in mind.

3.4.3 Exploration of symmetries to reduce information

The evident symmetries characterising the human body and its motion allow for a considerable simplification of the model. For the on-body antenna placements shown in Fig. 3.8, it is sufficient to provide the parameters for those marked with a star, while the motion for the remaining ones can be obtained from the symmetry relations, derived in what follows.

With the perfect symmetry of the body and its motion being assumed, one starts by observing that the walking and running motions are characterised by periodic changes in the posture of a person, which yield symmetric movement of the left and right sides of the body, but with an offset of a half the motion period. Hence, exhibited rotations and trajectories traced by two symmetrically placed antennas are images of each other. Considering that the user is aligned with the z-axis and faces the positive x-axis direction, the plane of this symmetry is the X-Z plane.

Since the reflection of a point about the X-Z plane is essentially obtained by changing the sign of the y-coordinate, the positions of the antennas on symmetric placements on the left and right sides of the body are related according to:

$$\Delta r^R_{x/z}(t) = \quad \Delta r^L_{x/z}(t - T/2) \tag{3.64}$$

$$\Delta r^R_{y}(t) = -\Delta r^L_{y}(t - T/2) \tag{3.65}$$

where superscripts L/R indicate the left/right sides of the body.

The orientations of these wearable antennas exhibit states that are also mirrored images of one another, with the matching orientations occurring with half the motion period offset between the two antennas. In order to obtain the symmetry relations for the Euler angles, one should consider the orientation of the antenna over time as a rotation by an angle γ_3, about the axis established by the sequence of the first two elementary rotations (γ_1, γ_2). This axis corresponds to the vector $\mathbf{u}^a_z$ of the antenna's local coordinate system, which is aligned with that of the arm or the leg it is attached to.

For symmetric wearable antenna placements, the corresponding vectors $\mathbf{u}^a_z$ are reflections of one another with respect X-Z plane, and the rotations about these axes are reversed in sense. The latter means that γ_3 is equal in magnitude but reversed in sign for the symmetric placements, while the former and (3.62) yield:

$$\cos\gamma^R_1(t)\sin\gamma^R_2(t) = \quad \cos\gamma^L_1(t - T/2)\sin\gamma^L_2(t - T/2) \tag{3.66}$$

$$\sin\gamma^R_1(t)\sin\gamma^R_2(t) = -\sin\gamma^L_1(t - T/2)\sin\gamma^L_2(t - T/2) \tag{3.67}$$

In turn, the symmetry relations for Euler angles can be written as:

$$\gamma^R_i(t) = (-1)^i\ \gamma^L_i(t - T/2), \quad i = 1, 2, 3 \tag{3.68}$$

These relations do not hold for antennas on the waist and the head. While their positions are related according to (3.64) and (3.65), the Wa_L and Wa_R antennas have the same orientation as they share the common vertical rotation axis (i.e. $\mathbf{u}_z^a$) and face the same side of the body. The He_L and He_R antennas also share the vertical axis, i.e. the one of the head, but face opposite directions. This also means that their orientations are directly related, i.e. without a time offset of $T/2$; thus it comes straightforward that:

$$\gamma_{1/2}^R(t) = \gamma_{1/2}^L(t) \tag{3.69}$$

$$\gamma_3^R(t) = \gamma_3^L(t) + 180^\circ \tag{3.70}$$

By assuming their placement on exactly opposite sides of the head, the distance between the He_L and He_R antennas is equal to the head's diameter, D_H (e.g. 18 cm [113]), but in the direction that varies over a motion cycle, hence:

$$\Delta\mathbf{r}_{[\mathrm{cm}]}^R(t) = \Delta\mathbf{r}_{[\mathrm{cm}]}^L(t) - D_{H\,[\mathrm{cm}]}\ \mathbf{u}_x^{a\,L} \tag{3.71}$$

The case for the To_F and To_B antennas is essentially the same as for the He_L and He_R ones, while the common vertical axis is now the one of the torso. Therefore, (3.69) and (3.70) also hold for the To_F and To_B antennas, where superscripts L/R are replaced by F/B. However, the diameter of the torso, D_T (e.g. 26 cm [113]), should be used in (3.71) instead of the one of the head.

3.4.4 Model parameters

Following the procedure described in Section 3.4.2, the model parameters were calculated from MoCap data for walking and running motions [138] (subject 35, motions 33 and 26, respectively). User's velocity is estimated to be 1.307 m/s and the motion cycle period is 1.142 s for the former, while the respective values are 3.551 m/s and 0.717 s for the latter.

As discussed in Section 3.4.3, the parameters of the Fourier series representation of the periodic components are calculated for the antenna placements indicated by a star in Fig. 3.8. These values are summarised in Table 3.1 for the position coordinates, and in Table 3.2 for the Euler angles representing orientation. For the antenna position (Table 3.1), a single harmonic in the Fourier series is typically sufficient, two being required only for a few components in the case of the walking motion, while two harmonics are also mostly required for the running case. On the other hand, the orientation angles in most cases can be represented by a single harmonic and only a few components require two, for both walking and running.

It is noted that the parameters in Table 3.1 correspond to walking and running motions of a regular person, where variations across different people are expected to be insignificant for channel modelling purposes. Moreover, they correspond to the user moving in the positive x-axis direction of the global coordinate system. The user motion specified by these parameters can be easily modified for arbitrary path and velocity.

For a straight motion path specified by its end points, the direction vector in (3.56) is obtained according to:

$$\mathbf{u}_v = \frac{\mathbf{r}_d - \mathbf{r}_0}{\|\mathbf{r}_d - \mathbf{r}_0\|} \tag{3.72}$$

Table 3.1: Estimated parameters for antenna position (periodic component).

		Walking, $T = 1.142\,\mathrm{s}$					Running, $T = 0.717\,\mathrm{s}$				
Ant.	Comp.	a_0 [cm]	a_1^c [cm]	a_1^s [cm]	a_2^c [cm]	a_2^s [cm]	a_0 [cm]	a_1^c [cm]	a_1^s [cm]	a_2^c [cm]	a_2^s [cm]
To_F	Δr_x	10.1	0.3	0.2	-	-	14.9	0.1	0.4	-	-
	Δr_y	0.1	-0.5	2.4	-	-	-0.6	-2.3	0.3	-	-
	Δr_z	135.5	0.1	-0.1	-	-	134.9	-0.3	-0.9	-3.3	-3.9
He_L	Δr_x	5.0	0.0	-0.8	-	-	7.0	0.8	0.3	-	-
	Δr_y	9.1	-0.3	2.5	-	-	5.9	-0.9	-0.1	-	-
	Δr_z	165.1	-0.2	-0.3	-	-	166.0	-0.3	-1.0	-3.1	-3.6
Wa_L	Δr_x	8.5	0.8	0.7	-1.6	0.7	7	0.7	0.1	0.3	-1.4
	Δr_y	11.9	-2.3	2.3	-	-	12.2	-0.6	-0.8	-	-
	Δr_z	90.9	-1.0	0.3	-	-	90.8	-0.3	-1.6	-2.8	-3.4
AU_L	Δr_x	-0.3	-3.4	-2.7	-	-	0.3	4.1	-5.9	-	-
	Δr_y	22.9	-2.5	1.2	-	-	20.7	0.9	-1.9	-	-
	Δr_z	128.7	-0.5	-0.5	-	-	130.9	0.3	1.4	-3.7	-4.0
AL_L	Δr_x	10.1	-11.3	-8.8	-	-	21.3	2.4	-9.6	1.6	0.9
	Δr_y	27.1	-4.8	1.3	-	-	14.2	-3.7	2.2	-	-
	Δr_z	87.0	-3.1	-2.2	-	-	116.1	-2.9	-11.7	-6.4	-4.1
LU_L	Δr_x	7.9	8.9	1.4	-3.2	-0.9	5.6	-2.1	10.0	1.3	0.2
	Δr_y	13.6	-1.4	1.3	-	-	13.9	1.1	1.0	-	-
	Δr_z	71.1	0.8	-0.2	-	-	71.9	0	0.6	-3.9	-3.2
LL_L	Δr_x	4.2	23.8	8.0	-0.1	-2.5	-4.5	-13.5	23.2	2	-1.3
	Δr_y	10.3	0.0	-0.3	-	-	9.3	3.1	2.8	-	-
	Δr_z	32.2	0.3	-3.9	-1.8	-0.1	39.4	9.9	1.0	-1.3	-1.5

where:

- $\mathbf{r}_d$: destination point.

The azimuth angle of the motion direction is obtained as:

$$\phi_u = \arctan\left(\frac{\mathbf{u}_v \cdot \mathbf{u}_y}{\mathbf{u}_v \cdot \mathbf{u}_x}\right) \tag{3.73}$$

Since the default motion is in the direction of the positive x-axis, an additional rotation about the z-axis for angle ϕ_u has to be applied to the periodic component in (3.56) and orientation vectors (3.60) - (3.62). Considering that Euler rotations are equivalent to the ones about the global (fixed) axis in the reverse order [137, Ch. 2], the latter is equivalent to adding angle ϕ_u to the Euler angle γ_1 (i.e. for all antennas):

$$\hat{\gamma}_1 = \gamma_1 + \phi_u \tag{3.74}$$

where the hat indicates the parameters of the new modified motion, the original values being provided in Table 3.1. In a general case, the direction vector and the corresponding azimuth angle change over time. An arbitrary motion path can be represented by a parametric curve [137, Ch. 3], whose (normalised) first derivative in each point represents the direction vector. If the path curve has a simple analytical expression for the first derivative, the mobility model should remain fairly simple.

Table 3.2: Estimated parameters for antenna orientation (Euler angles, for rotation sequence Z-Y-Z).

		Walking, $T = 1.142\,\mathrm{s}$					Running, $T = 0.717\,\mathrm{s}$				
Ant.	Comp.	b_0 [deg]	b_1^c [deg]	b_1^s [deg]	b_2^c [deg]	b_2^s [deg]	b_0 [deg]	b_1^c [deg]	b_1^s [deg]	b_2^c [deg]	b_2^s [deg]
To_F	γ_1	-23.9	24.1	13.7	-	-	-24.4	-17.5	8.9	-	-
	γ_2	3.9	-	-	-	-	8.8	-	-	-	-
	γ_3	22.8	-19.8	-10.3	-	-	25.6	8.3	-3.7	-	-
He_L	γ_1	-10.0	7.5	5.9	-	-	113.7	-3.2	5.7	-	-
	γ_2	14.8	-	-	-	-	-8.3	-	-	-	-
	γ_3	93.1	-5.2	-3.3	-	-	-32.5	-2.4	-4.1	-	-
Wa_L	γ_1	-24.4	-66.3	23.8	-	-	23.1	0.4	40.4	-	-
	γ_2	-4.9	-	-	-	-	4.7	-	-	-	-
	γ_3	22.8	62.8	-24.9	-	-	-22.8	-5.8	-41.6	-	-
AU_L	γ_1	124.8	45.5	30.1	-	-	-16.6	-16.6	21.6	-	-
	γ_2	-12.6	-	-	-	-	28.1	0.1	18.4	-	-
	γ_3	-16.1	-37.8	-20.6	-	-	110.7	3.7	-11.7	-	-
AL_L	γ_1	24.8	7.8	13.4	-	-	-11.9	-13.5	11.3	-	-
	γ_2	-23.8	12.2	9.0	-	-	-85.6	5.8	29.6	4.5	-0.1
	γ_3	41.8	-2.2	-4.7	-	-	94.9	-3.1	2.2	-	-
LU_L	γ_1	2.0	-5.4	-4.6	-	-	8.4	13.4	-7.2	-	-
	γ_2	-11.7	-22.5	-2.2	5.0	5.1	-11.0	7.1	-29.9	-3.6	-5.5
	γ_3	83.8	2.1	1.6	-	-	84.1	-14.4	9.2	-	-
LL_L	γ_1	3.1	-5.3	4.3	-	-	9.5	-7.7	0.7	-	-
	γ_2	21.2	-19.8	-18.7	-15.0	1.5	46.4	36.7	-8.1	8.6	11.0
	γ_3	82.6	1.4	-7.5	-	-	82.2	9.0	2.7	-	-

Motion velocity can be modified by directly providing a value for the forward motion component in (3.56), and appropriately changing the period of the Fourier series representing the periodic component. For a given velocity ($\hat{v}_u$), the corresponding motion period is obtained according to:

$$\hat{T} = \frac{v_u}{\hat{v}_u}\, T \tag{3.75}$$

where again the hat indicates the parameters of the new modified motion. However, one has to be careful when modifying the velocity, since values far from the ones estimated from the MoCap data may yield unnatural motion. Finally, it should be noticed that the starting posture of the user can be changed as well. This is achieved by setting a common initial phase to all periodic components.

3.5 Scattering cylinder environment

3.5.1 General description

The scattering effects in the propagation environment surrounding the user can be effectively modelled by a simplified geometry. This approach has been taken for a variety of radio channels, being a popular choice for mobile communication [86, 141], and recently adopted for the on-body channel as well [93, 94].

In the latter, scatterers are assumed to be distributed on a circular cylinder, centred around the wearable antenna. The same geometry is adopted herein, but with the scattering cylinder centred around the user, as illustrated in Fig. 3.9. This choice allows for a consistent consideration of wearable antennas on different on-body placements simultaneously.

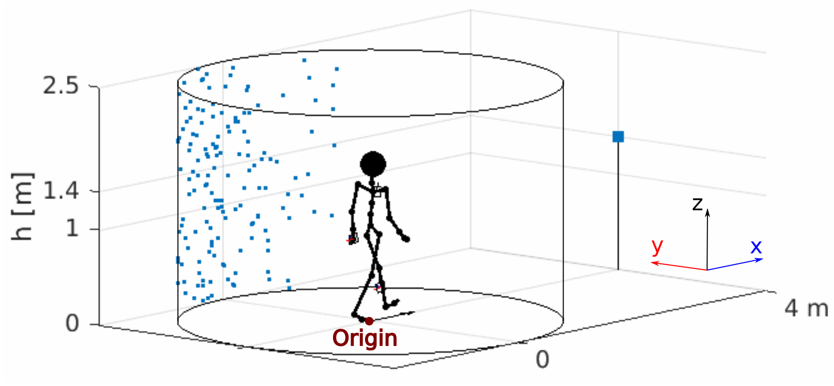

Figure 3.9: Scattering cylinder geometry.

The global coordinate system chosen for reference is such that the user is over the origin, and the off-body antenna is at a specified distance along the x-axis. The user's orientation is specified by the azimuth angle, by default facing in the positive x-axis direction. The scatterers' positions on the cylinder are given in cylindrical coordinates. Therefore, positions of the AP and scatterers are respectively given by:

$$\mathbf{r}_{ap} = (d, 0, h_{ap}) \tag{3.76}$$

$$\mathbf{r}_s^n = (R_s \cos\phi_s^n, R_s \sin\phi_s^n, h_s^n) \tag{3.77}$$

where:

- d : distance between the user and the off-body antenna;
- h_{ap} : off-body antenna height;
- h_s^n : n-th scatterer height;
- ϕ_s^n : n-th scatterer azimuth;
- R_s : scattering cylinder radius.

The scattering cylinder radius can be either a fixed parameter, if one considers a narrowband channel, or a random variable, if different MPCs' delays need to be represented for wideband channel considerations. The wearable antenna's position and orientation is changing over time, according to the presented mobility model (Section 3.4), depending on the on-body antenna placement and the user's motion. By additionally considering the antennas' orientations, the polarisation matrix for the MPC associated with n-th scatterer is obtained according to Section 3.2.2, by replacing the antennas' position vectors according to the assigned Tx and Rx roles.

Finally, with typically clustered distributions of the scatterers being adopted in GBSC models, one might argue that the direct application of the reflection coefficients is not an appropriate approach. If arbitrary distributions of the MPCs' amplitudes are to be used, e.g. as extracted from measurements, the polarisation matrix elements should be additionally normalised by the reflection loss, i.e.

$$R_{loss} = \sqrt{R_{\perp}^2 \cos^2 \vartheta_t + R_{\parallel}^2 \sin^2 \vartheta_t} \tag{3.78}$$

$$= \sqrt{R_{\perp}^2 (\mathbf{u}_{\theta}^{t/r} \cdot \mathbf{u}_{\perp})^2 + R_{\parallel}^2 (\mathbf{u}_{\phi}^{t/r} \cdot \mathbf{u}_{\perp})^2} \tag{3.79}$$

3.5.2 Model simplification

Since the wearable antenna displacement over the motion cycle has a minor effect on the incidence plane inclination and AoDs/AoAs variations it can be neglected, and the channel model can be further simplified by assuming the cylinder is centred around the wearable antenna. One should note that this assumption is valid for off-body channels with a single on-body antenna, while it should be revised in the case that wearable MIMO systems are considered, as the spatial configuration of the antennas is important in the latter case.

Polarisation matrix

The effects of the environment can be separated from those associated with antennas' orientations, thus the wearable antenna rotations with user's motion, if an alternative factorisation of the polarisation matrix is used. By considering the V and H polarisations as a reference, i.e. dependent only on the antennas' positions, the polarisation matrix for the LoS component can be written as:

$$\mathbf{H}_{p\,[2\times 2]}^{LoS} = \mathbf{Q}(\vartheta_{ra})_{[2\times 2]} \mathbf{Q}(\vartheta_{ta})_{[2\times 2]} \tag{3.80}$$

where:

- $\vartheta_{ta/ra}$: angle between the Tx/Rx antenna's θ-polarisation and the V-polarisation reference.

Similarly, for the first-order reflected MPCs one has:

$$\mathbf{H}_{p\,[2\times 2]} = \mathbf{Q}(\vartheta_{ra})_{[2\times 2]} \hat{\mathbf{H}}_{p\,[2\times 2]} \mathbf{Q}(\vartheta_{ta})_{[2\times 2]} \tag{3.81}$$

where:

- $\hat{\mathbf{H}}_p$: polarisation matrix in case the Tx and Rx antennas are vertical;
- $\vartheta_{ts/rs}$: angle between the Tx/Rx antenna's θ-polarisation and the V-polarised reference.

With $\hat{\mathbf{H}}_p$ obtained according to (3.10), i.e. for $\mathbf{u}_z^{t/r} = \mathbf{u}_z$, one additionally has (the upper/lower sign corresponds to index ta/ra):

$$\cos(\vartheta_{ta/ra}) = \frac{\mathbf{u}_V^{t/r} \cdot \mathbf{u}_z^{t/r}}{\sqrt{(\mathbf{u}_V^{t/r} \cdot \mathbf{u}_z^{t/r})^2 + (\mathbf{u}_H^{t/r} \cdot \mathbf{u}_z^{t/r})^2}} \tag{3.82}$$

$$\sin(\vartheta_{ta/ra}) = \pm \frac{\mathbf{u}_H^{t/r} \cdot \mathbf{u}_z^{t/r}}{\sqrt{(\mathbf{u}_V^{t/r} \cdot \mathbf{u}_z^{t/r})^2 + (\mathbf{u}_H^{t/r} \cdot \mathbf{u}_z^{t/r})^2}} \tag{3.83}$$

where:

- $\mathbf{u}_{V/H}^{t/r}$: V/H-polarisation unit vectors at the Tx/Rx antenna, i.e.

$$\mathbf{u}_H^{t/r} = \frac{\mathbf{k}_{t/r} \times \mathbf{u}_z}{\left\|\mathbf{k}_{t/r} \times \mathbf{u}_z\right\|} \tag{3.84}$$

$$\mathbf{u}_V^{t/r} = \frac{\mathbf{u}_H^{t/r} \times \mathbf{k}_{t/r}}{\left\|\mathbf{u}_H^{t/r} \times \mathbf{k}_{t/r}\right\|} \tag{3.85}$$

By expressing the DoD/DoA vectors in terms of the corresponding AoDs/AoAs (with respect to the global coordinate system), and additionally using (3.62), from (3.82) and (3.83) one obtains (the upper/lower sign corresponds to index t/r):

$$\cos(\vartheta_{ta/ra}) = \frac{\cos\gamma_2^{t/r}\cos\hat{\psi}_{t/r} - \sin\gamma_2^{t/r}\sin\hat{\psi}_{t/r}\cos\Delta\hat{\phi}_{t/r}}{\sqrt{(\cos\gamma_2^{t/r}\cos\hat{\psi}_{t/r})^2 + (\sin\gamma_2^{t/r}\sin\hat{\psi}_{t/r}\cos\Delta\hat{\phi}_{t/r})^2}} \tag{3.86}$$

$$\sin(\vartheta_{ta/ra}) = \pm\frac{\sin\gamma_2^{t/r}\sin\Delta\hat{\phi}_{t/r}}{\sqrt{(\cos\gamma_2^{t/r}\cos\hat{\psi}_{t/r})^2 + (\sin\gamma_2^{t/r}\sin\hat{\psi}_{t/r}\cos\Delta\hat{\phi}_{t/r})^2}} \tag{3.87}$$

where:

- $\hat{\phi}_{t/r}$: AAoD/AAoA in the global coordinate system;
- $\hat{\psi}_{t/r}$: EAoD/EAoA in the global coordinate system;
- $\gamma_i^{t/r}$: Euler angles for the Tx/Rx antenna orientation;
- $\Delta\hat{\phi}_{t/r}$: azimuth angle difference:

$$\Delta\hat{\phi}_{t/r} = \hat{\phi}_{t/r} - \gamma_1^{t/r} \tag{3.88}$$

One should note that (3.88) has to take the user's orientation into account for the wearable antenna, for which (3.74) should be used in place of $\gamma_1^{t/r}$.

AoDs and AoAs

In order to take the radiation characteristics of the antennas into account, one considers AoDs/AoAs in the antenna's local coordinate system. With the adopted assumptions and considering the Euler angle representation of antenna orientation in Section 3.4.1, one has:[5]

$$\psi_{t/r} = \arcsin\left(\sin\gamma_2^{t/r}\cos\hat{\psi}_{t/r}\cos\Delta\hat{\phi}_{t/r} + \cos\gamma_2^{t/r}\sin\hat{\psi}_{t/r}\right) \tag{3.89}$$

$$\phi_{t/r} = \arctan\left(\frac{-\sin\gamma_3^{t/r}(\cos\gamma_2^{t/r}\cos\Delta\hat{\phi}_{t/r} - \sin\gamma_2^{t/r}\tan\hat{\psi}_{t/r}) + \cos\gamma_3^{t/r}\sin\Delta\hat{\phi}_{t/r}}{\cos\gamma_3^{t/r}(\cos\gamma_2^{t/r}\cos\Delta\hat{\phi}_{t/r} - \sin\gamma_2^{t/r}\tan\hat{\psi}_{t/r}) + \sin\gamma_3^{t/r}\sin\Delta\hat{\phi}_{t/r}}\right) \tag{3.90}$$

One should note that (3.89) and (3.90), as well as (3.86) and (3.87), hold for all signal components regardless of the involved propagation phenomena, while the AoD/AoA are determined from the corresponding path geometry.

3.5.3 Geometry-based derivation

In order to obtain the polarisation matrices for the LoS component and single-bounce MPCs, one considers the geometry shown in Fig. 3.10. One should note that the wearable antenna is additionally assumed to be the Rx one for convenient presentation, without loss in generality.

[5] By replacing (3.60) - (3.62) in (3.51) and (3.52), and additionally representing the DoD/DoA vectors in terms of the corresponding AAoDs/AAoAs and EAoDs/EAoAs in the global coordinate system.

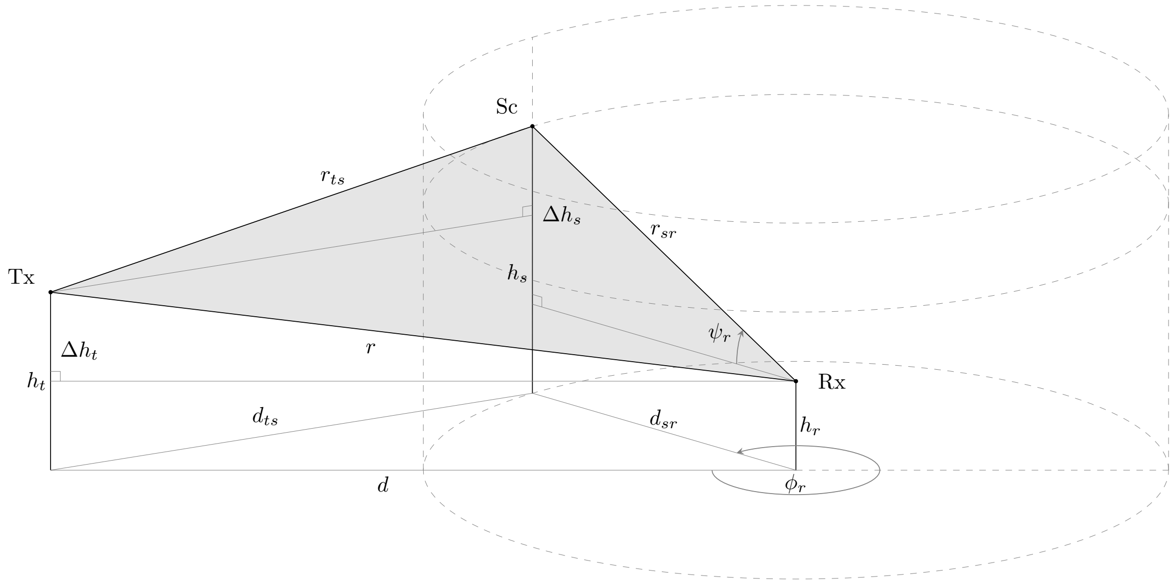

Figure 3.10: Geometry of a scattering cylinder centred around the wearable Rx antenna.

Polarisation matrix

With the adopted Euler angle representation of the antenna orientation, the polarisation matrix for the LoS component is obtained as:[6]

$$\mathbf{H}^{LoS}_{p\,[2\times 2]} = \frac{1}{b_0^t b_0^r} \begin{bmatrix} b_1^t b_1^r - b_2^t b_2^r & b_1^t b_2^r + b_2^t b_1^r \\ -(b_1^t b_2^r + b_2^t b_1^r) & b_1^t b_1^r - b_2^t b_2^r \end{bmatrix} \tag{3.91}$$

with the following notation being used:

$$b_1^{t/r} = \frac{1}{r}\left(d\cos\gamma_2^{t/r} - \Delta h_t \cos\gamma_1^{t/r}\sin\gamma_2^{t/r}\right) \tag{3.92}$$

$$b_2^{t/r} = \sin\gamma_1^{t/r}\sin\gamma_2^{t/r} \tag{3.93}$$

$$b_0^{t/r} = \sqrt{(b_1^{t/r})^2 + (b_2^{t/r})^2} \tag{3.94}$$

where:

- Δh_t : Tx height relative to the Rx, i.e.

$$\Delta h_t = h_t - h_r \tag{3.95}$$

  $h_{t/r}$ being the (absolute) Tx/Rx antenna height;
- d : horizontal Tx - Rx distance;
- r : slant Tx - Rx distance, i.e.

$$r = \sqrt{d^2 + \Delta h_t^2} \tag{3.96}$$

Similarly, for the first-order reflected MPCs one has:

$$\mathbf{H}_{p\,[2\times 2]} = \frac{1}{a_0 b_0^t b_0^r} \begin{bmatrix} b_1^r & b_2^r \\ -b_2^r & b_1^r \end{bmatrix} \begin{bmatrix} R_\perp d^2 r_{ts} r_{sr} - R_\parallel a_1 a_2 & -(R_\perp r_{sr} a_1 + R_\parallel r_{ts} a_2)d \\ (R_\perp r_{ts} a_2 + R_\parallel r_{sr} a_1)d & R_\parallel d^2 r_{ts} r_{sr} - R_\perp a_1 a_2 \end{bmatrix} \begin{bmatrix} b_1^t & b_2^t \\ -b_2^t & b_1^t \end{bmatrix} \tag{3.97}$$

[6] By replacing (3.86) and (3.87) in (3.80), with the global coordinate system AoDs/AoAs obtained from the scenario geometry in Fig. 3.10.

with the following notation being used:

$$a_0 = \frac{d_{ts} d_{sr}}{\sin^2 \hat{\phi}_r} \left[(r \sin \hat{\phi}_r)^2 + \left(\Delta h_t \cos \hat{\phi}_r + \Delta h_s \frac{d}{d_{sr}} \right)^2 \right] \tag{3.98}$$

$$a_1 = \frac{1}{\sin \hat{\phi}_r} \left[\Delta h_t (d_{sr} - d \cos \hat{\phi}_r) + \Delta h_s \left(\frac{d^2}{d_{sr}} - d \cos \hat{\phi}_r \right) \right] \tag{3.99}$$

$$a_2 = \frac{1}{\sin \hat{\phi}_r} \left(\Delta h_t d_{sr} - \Delta h_s d \cos \hat{\phi}_r \right) \tag{3.100}$$

$$b_1^t = \frac{1}{r_{ts}} \left\{ d_{ts}^2 \cos \gamma_2^t - (h_s - h_t) \left[d \cos \gamma_1^t - d_{sr} \cos(\hat{\phi}_r + \gamma_1^t) \right] \sin \gamma_2^t \right\} \tag{3.101}$$

$$b_2^t = \left[d_{sr} \sin(\hat{\phi}_r + \gamma_1^t) - d \sin \gamma_1^t \right] \sin \gamma_2^t \tag{3.102}$$

$$b_1^r = \frac{1}{r_{sr}} \left[d_{sr} \cos \gamma_2^r - \Delta h_s \cos \Delta\hat{\phi}_r \sin \gamma_2^r \right] \tag{3.103}$$

$$b_2^r = \sin \Delta\hat{\phi}_r \sin \gamma_2^r \tag{3.104}$$

where:

- Δh_s : Sc height relative to the Rx, i.e.

$$\Delta h_s = h_s - h_r \tag{3.105}$$

  h_s being the (absolute) Sc height;

- $d_{ts/sr}$: horizontal distance in between Tx/Rx and Sc, i.e.

$$d_{ts} = \sqrt{d^2 + d_{sr}^2 - 2 d d_{sr} \cos \hat{\phi}_r} \tag{3.106}$$

$$d_{sr} = R_s \tag{3.107}$$

- $r_{ts/sr}$: slant distance in between Tx/Rx and Sc, i.e.

$$r_{ts} = \sqrt{d_{ts}^2 + (h_s - h_t)^2} \tag{3.108}$$

$$r_{sr} = \sqrt{d_{sr}^2 + \Delta h_s^2} \tag{3.109}$$

Moreover, (3.94) applies for $b_0^{t/r}$ here as well. If an additional normalisation by the reflection loss is to be performed as discussed in Section 3.5.1, one would in this case have:

$$R_{loss} = \frac{1}{b_0^t} \sqrt{\frac{1}{a_0} \frac{d_{sr}}{d_{ts}} \left[R_\perp^2 (b_1^t d\, r_{ts} + b_2^t a_1)^2 + R_\parallel (b_2^t d\, r_{ts} + b_1^t a_1)^2 \right]} \tag{3.110}$$

One should note that (3.97) generalises the polarised channel models based on GTDe [86, 93, 94], by additionally allowing for arbitrary antennas' orientation. The special case from these models is obtained for vertical antennas, i.e. $\gamma_2^{t/r} = 0$, in which case one has:

$$\mathbf{H}_{p\,[2\times2]} = \hat{\mathbf{H}}_{p\,[2\times2]} = \frac{1}{a_0} \begin{bmatrix} R_\perp d^2 r_{ts} r_{sr} - R_\parallel a_1 a_2 & -(R_\perp r_{sr} a_1 + R_\parallel r_{ts} a_2) d \\ (R_\perp r_{ts} a_2 + R_\parallel r_{sr} a_1) d & R_\parallel d^2 r_{ts} r_{sr} - R_\perp a_1 a_2 \end{bmatrix} \tag{3.111}$$

where the same notation (3.98) - (3.100) is used.

Finally, one additionally considers the small-scale fading effect due to user's movement through the imposed Doppler shift. By considering only the constant velocity of the user's forward motion, the

Doppler shift frequencies in (3.6) and (3.7) are obtained as:

$$f_D^{LoS} = v_u \frac{f_c}{c} \frac{d}{r} \cos \phi_u \tag{3.112}$$

$$f_D^n = v_u \frac{f_c}{c} \frac{d_{sr}}{r_{sr}} \cos(\hat{\phi}_r - \phi_u) \tag{3.113}$$

One should note that the model considerably simplifies by neglecting the periodic antenna velocity component associated with the changes in user's posture. Nonetheless, the choice to consider only the forward motion velocity should have little effect on the channel, especially for wearable antenna placements on the head, torso or waist. Further investigation in this direction is left for future work, where one should investigate whether the increase in model complexity by considering a full velocity vector is justified by a possible improvement in accuracy.

AoDs and AoAs

While (3.89) and (3.90) are given in the general form, with the AoDs/AoAs obtained from the geometry in Fig. 3.10 , for the LoS component one has (the upper/lower sign corresponds to index t/r):

$$\psi_{t/r}^{LoS} = \mp \arcsin \left[\frac{1}{r} (d \cos \gamma_1^{t/r} \sin \gamma_2^{t/r} + \Delta h_t \cos \gamma_2^{t/r}) \right] \tag{3.114}$$

$$\phi_{t/r}^{LoS} = \arctan \left(\frac{\pm c_{t/r} \sin \gamma_3^{t/r} \pm \sin \gamma_1^{t/r} \cos \gamma_3^{t/r}}{\mp c_{t/r} \cos \gamma_3^{t/r} \pm \sin \gamma_1^{t/r} \sin \gamma_3^{t/r}} \right) \tag{3.115}$$

where:

$$c_{t/r} = \cos \gamma_1^{t/r} \cos \gamma_2^{t/r} - \frac{\Delta h_t}{d} \sin \gamma_2^{t/r} \tag{3.116}$$

Similarly, for the MPCs one obtains:

$$\psi_t = \arcsin \frac{1}{d_{ts}} \left\{ \left[d \cos \gamma_1^t - d_{sr} \cos(\hat{\phi}_r + \gamma_1^t) \right] \sin \gamma_2^t + (h_s - h_t) \cos \gamma_2^t \right\} \tag{3.117}$$

$$\psi_r = \arcsin \left\{ \cos \Delta\hat{\phi}_r \sin \gamma_2^r + \frac{\Delta h_s}{d_{sr}} \cos \gamma_2^r \right\} \tag{3.118}$$

$$\phi_{t/r} = \arctan \left(\frac{c_{t/r}^A \cos \gamma_3^{t/r} - c_{t/r}^B \sin \gamma_3^{t/r}}{c_{t/r}^A \sin \gamma_3^{t/r} + c_{t/r}^B \cos \gamma_3^{t/r}} \right) \tag{3.119}$$

where:

$$c_t^A = d_{sr} \sin(\hat{\phi}_r + \gamma_1^t) - d \sin \gamma_1^t \tag{3.120}$$

$$c_t^B = [d \cos \gamma_1^t - d_{sr} \cos(\hat{\phi}_r + \gamma_1^t)] \cos \gamma_2^t - (h_s - h_t) \sin \gamma_2^t \tag{3.121}$$

$$c_r^A = d_{sr} \sin \Delta\hat{\phi}_r \tag{3.122}$$

$$c_r^B = d_{sr} \cos \Delta\hat{\phi}_r \cos \gamma_2^r - \Delta h_s \sin \gamma_2^r \tag{3.123}$$

In conclusion, one should note that the channel model formulation presented in this section is fairly simple and involves straightforward expressions, obtained by adopting a few reasonable assumptions. While being simple, the model still considers the depolarisation effects associated with scattering as well the influence of user dynamics, where the two are separated and represented by individual terms in the polarisation matrix. This simplifies further considerations related to first- and second-orders statistical properties of the channel transmission coefficients between antennas' polarisations, since the multiple integrations involved in the required averaging can be performed sequentially. Most importantly, the simple formulation might lead to close-form expressions for important statistical metrics, such as the autocorrelation function. While pursuing this path is out of the scope of this thesis, it is certainly one of the most important directions to consider in future work. One should also note that the model can be easily adapted for body-to-body channel considerations. In this case, one should consider scattering cylinders at both users' sides, and simply employing the wearable antenna mobility model for both antennas. This is another important direction to be explored in the future.

Chapter 4

Model implementation

This chapter describes the implementation aspects of the off-body channel model developed in Chapter 3. The structure of the simulator is described and the simulation sequence is outlined. The input parameters are listed and the calculation of output metrics is described. The detailed structure of the simulator modules is then provided, followed by the assessment. A strategy is developed for the latter, where each module is assessed separately.

4.1 Simulator structure

Fig. 4.1 outlines the general structure of the simulator based on the developed model, with its general inputs and outputs being indicated. The simulator is organised in the three main modules, each implementing a different aspect of the channel model. These modules and their functionalities within the simulation scope are described in what follows. One should note that the implementation presented here is based on the model for arbitrary geometry developed in Section 3.2.2, where first-order MPCs bouncing from scatterers on the cylinder centred around the user are considered in addition to LoS propagation, as discussed in Section 3.5.

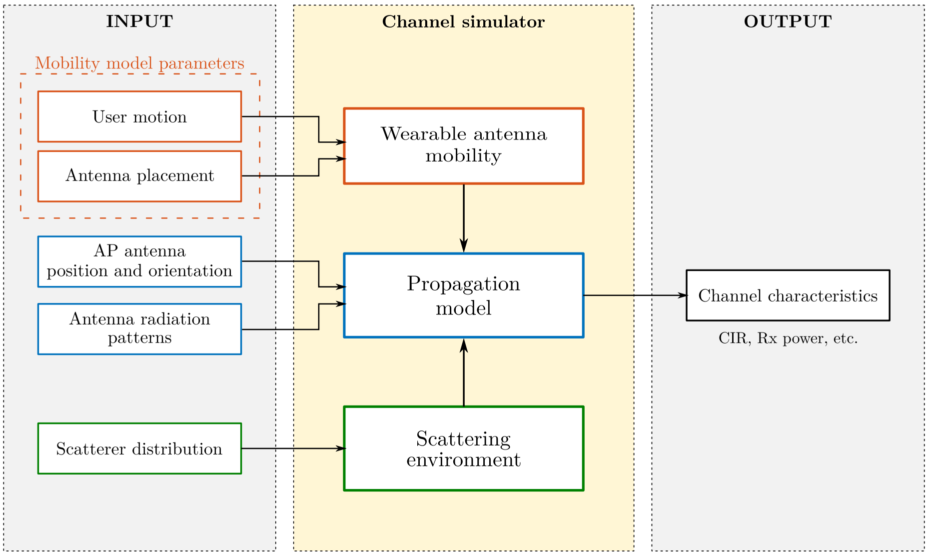

Figure 4.1: Simulator structure.

The propagation model module is the central component of the simulator and it implements the geometry-based off-body channel model, as described in Sections 3.1 and 3.2. This module calculates selected radio channel parameters, e.g. Rx power and CIR, and provides them at the output. Main operations herein are related to the calculation of the polarisation matrix elements based on the scenario's geometry, thus providing the coupling coefficients between the Tx and Rx antennas' polarisation components.

This component is fed by the information from other modules, but also by externally provided input parameters. The former are changing with the simulation time, while the latter are set at the beginning and kept constant during execution. As shown in Fig. 4.1, the external parameters include off-body AP position and orientation, and antenna radiation characteristics specified by gain patterns in θ- and ϕ-polarisations. As discussed in Chapter 3, wearable antennas' gain patterns are assumed to be available for their operation on the body.

The wearable antenna mobility module provides the position and orientation of the on-body antenna at a given time, obtained from the analytical model described in Section 3.4. It requires the specification of the wearable antenna on-body placement and user's motion, provided as an external input. In total, 14 different antenna placements can be specified, with the user walking or running.

The scattering environment module is responsible for providing the spatial configuration of the scatterers considered by the propagation model. In general, this information can be obtained either from an external ray-tracer, with a detailed model of the environment, or specified for a simplified scattering geometry. The simulator was developed for the latter case, where scatterers are assumed to be distributed on a circular cylinder centred around the user (Section 3.5). The main function of this module is to generate the scatterers' positions on the cylinder based on the statistical distributions of the corresponding azimuth angles and heights, specified as an input.

4.2 Simulation procedure

The simulation procedure is outlined by the flow chart shown in Fig. 4.2. One should note that a simulation is performed at sampled time instances, i.e. frames, where an arbitrary sampling resolution can be specified, since the simulator is based on analytical models.

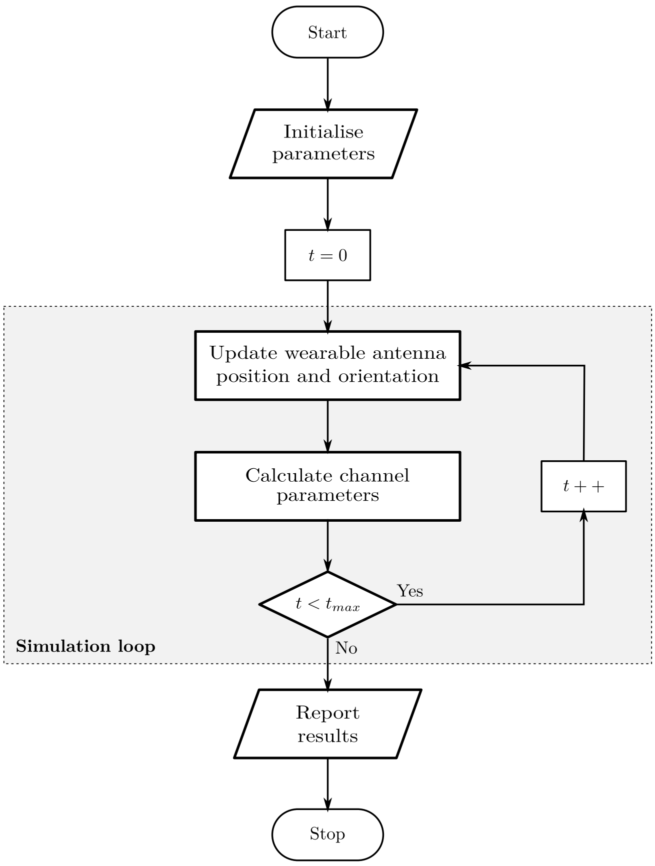

Figure 4.2: Simulation procedure flowchart.

As indicated in the flow chart, when the simulation starts, the first step is the initialisation of parameters according to the input values. In this step, specified radiation patterns are associated with the Tx and Rx antennas, the spatial configuration of the scatterers is established, the off-body AP position and orientation are set, and the wearable antenna mobility model parameters are selected based on motion specification. Following the simulation time initialisation, the simulator enters a loop that iterates through discrete time steps. In each step, the position and orientation of the wearable antenna are updated for the current simulation time according to the mobility model, and the radio channel parameters are calculated. The local simulator time is updated after each iteration and the simulation cycle is repeated.

The loop terminates once the simulation duration time is exceeded, where the ending time mark (t_{max}) is either provided as an input or calculated based on user's velocity and motion path. When the stopping criteria is fulfilled, a report is generated and provided at the output, and the simulation is finally completed.

4.3 Input parameters

As indicated in Fig. 4.1, the simulator takes several inputs that specify the parameters related to all three of its modules. These include te specification of mobility aspect, distribution of scatterers, and additional parameters required by the propagation model. In addition to the operating frequency, the inputs also include user's orientation and distance from the AP, motion type, wearable antenna placement, AP height and orientation, antennas' radiation characteristics, and distribution of the scatterers. These input parameters concern different entities in the simulator, as discussed in what follows.

The wearable antenna mobility is specified by user's motion and on-body placement. While walking and running can be chosen for the former, in total 14 different antenna placements can be specified for the latter, i.e. front and back sides of the torso (To_F/B), left and right sides of the waist (Wa_L/R), left and right sides of the head (He_L/R), left and right upper arms (AU_L/R), left and right hand wrists (AL_L/R), left and right upper legs (LU_L/R), and left and right lower legs (LL_L/R), as shown in Fig. 4.3. These inputs are used for the selection of the corresponding mobility model parameters, including the user's forward velocity, motion cycle period, and parameters of the Fourier series for position and orientation of the antenna, as given in Table 3.1. An additional parameter affecting the wearable antenna motion relative to the AP is user's orientation, which specifies an additional rotation around the user's axis, i.e. global z-axis. This rotation affects DoDs/DoAs of MPCs, and consequently their associated gains and depolarisation due to motion dynamics, as discussed in Section 3.3.

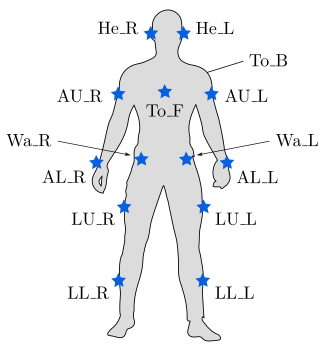

Figure 4.3: Wearable antenna placements supported by the simulator.

The position and orientation of the off-body AP antenna are specified by its distance from the user, height and Euler angles representing its orientation, where the same rotation sequence is adopted as for the wearable antenna, i.e. Z-Y-Z. One should note that these are set at the beginning of a simulation and kept fixed during its execution, as the AP is assumed to be static.

For both wearable and off-body antennas, the simulator requires the specification of their radiation characteristics. These are provided in the form of gain patterns in θ- and ϕ- polarisations, which can be complex to facilitate arbitrary antenna polarisation, i.e. an elliptical one in general. The radiation patterns are assumed to be obtained for the same frequency as the one specified for simulation, but also for antennas' operation on the body, thereby taking the effects of body shadowing and detuning due to body-proximity into account.

Finally, the distribution of scatterers around the user is specified considering the assumed cylinder geometry. Scatterers positions are defined by the radius and cylindrical coordinates, i.e. azimuth angles and heights, specifying their exact location on the cylinder. The radius can be either given as a constant or represented by a random variable, depending if narrow- or wideband channels are considered, respectively. On the other hand, a stochastic approach is taken for the scatterers' azimuth angles and heights, with their statistical distributions provided as an input. For realistic off-body channel simulations, the distributions can be derived from measurements or ray-tracing simulations, in order to match the characteristics of actual propagation environments.

The simulator input parameters are summarised in Table 4.1, where their specification is given as a list of predefined values where applicable, the corresponding symbol being provided otherwise. One should note that the variables associated with wearable and off-body antennas are identified by a or ap in the subscript/superscript, respectively. These should be replaced in the channel model (Chapter 3), according to the associated antenna roles, i.e. Tx or Rx.

Table 4.1: Simulator input parameters.

Parameter	**Specification (possible values)**
Frequency	f_c
User orientation	ϕ_u
User motion	walking, running
Wearable ant. placement	To_F/B, Wa_L/R, He_L/R, AU_L/R, AL_L/R, LU_L/R, LL_L/R
Wearable ant. gain	$g^{\theta}_{wa}(\phi,\psi)$, $g^{\phi}_{wa}(\phi,\psi)$
AP ant. gain	$g^{\theta}_{ap}(\phi,\psi)$, $g^{\phi}_{ap}(\phi,\psi)$
AP distance	d
AP height	h_{ap}
AP orientation	γ_1^{ap}, γ_2^{ap}, γ_3^{ap} (Euler angles)
Sc. cylinder radius	Constant or statistical model for R_s
Sc. heights	Statistical model for h_s
Sc. azimuth distribution	Statistical model for ϕ_s

4.4 Output metrics

In addition to standard outputs, such as Rx power and CIR, a number of different metrics were calculated and reported by the simulator to facilitate the analysis performed in this thesis (Chapter 7). The exact expressions used to calculate these metrics are provided in what follows. One should again note that the simulator works with discrete time, hence, the metrics' values over time are obtained through repeated iterations of the simulation loop, one sample at a time. Their statistics over time are calculated by averaging over sets of samples obtained over the course of a simulation.

The Rx signal power is obtained from the channel transmission coefficient given by (3.2), according to:

$$P_r(t) = \frac{1}{2}\left|h_{ch}(t)\right|^2 P_t \tag{4.1}$$

where:

- P_t : Tx power.

As one of the metrics for quantification of the depolarisation effect, one calculates PLF. It is defined as a squared cosine of the inclination angle between polarisations of the Rx antenna and an arriving signal [55, pp. 69]. With the LoS component being of a particular interest for the analysis, one has:

$$L_{PLF\,[\mathrm{dB}]} = 20\log\left|\cos\left(\vartheta_{pol}^{ra} - \vartheta_{pol}^{ta} + \vartheta_{LoS}\right)\right| \tag{4.2}$$

where ϑ_{LoS} is obtained from (3.24) and (3.25), while ϑ_{pol}^{ta} and ϑ_{pol}^{ra} are given by (3.54).

In order to quantify the signal depolarisation due to wearable antenna rotation, another considered metric is the XPR, defined as the ratio of V- and H-polarisation components' power for a θ-polarised signal at the antenna, where one has:[1]

$$X_{pr}^{t/r}(\hat{\phi}_{t/r}, \hat{\psi}_{t/r})_{[\mathrm{dB}]} = 20\log\left|\frac{\cot\gamma_2\cos\hat{\psi}_{t/r} - \sin\hat{\psi}_{t/r}\cos\Delta\hat{\phi}_{t/r}}{\sin\Delta\hat{\phi}_{t/r}}\right| \tag{4.3}$$

In order to facilitate the analysis of statistics over time, the minimum, maximum, range of variation, mean and standard deviation are calculated according to:[2]

$$\min\{x(t)\}_{[\mathrm{un}]} = \min_{t\in[0,T]} x(t)_{[\mathrm{un}]} \tag{4.4}$$

$$\max\{x(t)\}_{[\mathrm{un}]} = \max_{t\in[0,T]} x(t)_{[\mathrm{un}]} \tag{4.5}$$

$$\Delta\{x(t)\}_{[\mathrm{un}]} = \max\{x(t)\}_{[\mathrm{un}]} - \min\{x(t)\}_{[\mathrm{un}]} \tag{4.6}$$

$$\mu\{x(t)\}_{[\mathrm{un}]} = E_t\{x(t)\}_{[\mathrm{un}]} \tag{4.7}$$

$$\sigma\{x(t)\}_{[\mathrm{un}]} = \sqrt{E_t\left\{\left[x(t)_{[\mathrm{un}]} - \mu_{[\mathrm{un}]}\right]^2\right\}} \tag{4.8}$$

where $E_t(\,.\,)$ denotes averaging operation in time.

[1] This follows from (3.86) and (3.87), by noticing that the considered ratio corresponds to the cotangent of $\theta_{ta/ra}$.

[2] Here, x serves as a dummy variable, i.e. replacing any symbol of the particular metric for which the statistics are calculated. Moreover, [un] in the subscript denotes the unit in which the value is reported.

Similarly, for a comparison of the output Rx power (P_r) from the simulator against a given reference (P_r^{ref}), one calculates the maximum difference, its mean and standard deviation according to:

$$\epsilon_{max}\{P_r(t), P_r^{\text{ref}}(t)\}_{[\text{dB}]} = \max_{t\in[0,T]} \left|P_r(t)_{[\text{dBm}]} - P_r^{\text{ref}}(t)_{[\text{dBm}]}\right| \tag{4.9}$$

$$\epsilon_\mu \left\{P_r(t), P_r^{\text{ref}}(t)\right\}_{[\text{dB}]} = E_t\left\{\left|P_r(t)_{[\text{dBm}]} - P_r^{\text{ref}}(t)_{[\text{dBm}]}\right|\right\} \tag{4.10}$$

$$\epsilon_\sigma\{P_r(t), P_r^{\text{ref}}(t)\}_{[\text{dB}]} = \sqrt{E_t\left\{\left[\left|P_r(t)_{[\text{dBm}]} - P_r^{\text{ref}}(t)_{[\text{dBm}]}\right| - \epsilon_\mu\{P_r(t), P_r^{\text{ref}}(t)\}_{[\text{dB}]}\right]^2\right\}} \tag{4.11}$$

4.5 Simulator development

Following the general overview of the simulator structure and description of the input and output parameters, this section provides a more detailed description of the three main components in Fig. 4.1. A detailed structure is provided for each component, with an outline of its input and output parameters.

One starts with the wearable antenna mobility module, whose structure is shown in Fig. 4.4. Its input parameters include user's motion, antenna placement, and current simulation time. While the former two are provided as inputs to the simulator, the latter is a local parameter driven by the simulation loop (Fig. 4.2). As shown in Fig. 4.4, the external parameters are used in the parameter selection block in order to chose and read the mobility model parameters, i.e. the motion cycle period and amplitudes of the harmonics in Fourier series (Table 3.1). The extracted parameters are then fed to evaluation blocks for periodic antenna displacement and Euler angles for its orientation, where (3.59) and (3.63) are respectively evaluated for the current simulation time. Finally, the antenna orientation vectors are calculated from the obtained Euler angles according to (3.60) - (3.62), and reported at the module's output, together with the antenna position vector.

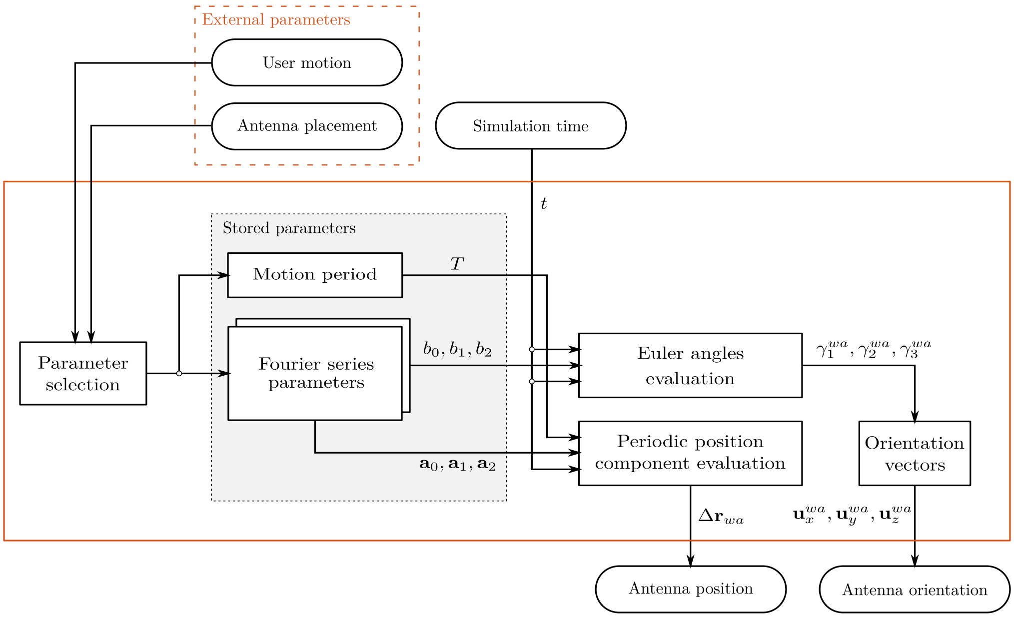

Figure 4.4: Structure of the wearable antenna mobility module.

The structure of the scattering environment block is shown in Fig. 4.5. All inputs to this module are provided from the outside, i.e. specified by the simulator's user. These primarily include statistical models for the positions of scatterers in cylindrical coordinates, i.e. azimuth angles and heights. Based on the provided distributions for the latter, a random number generator is used to obtain azimuth-height pairs for a specified number of scatterers. Together with the cylinder's radius, these pairs define the locations of all scatterers whose position vectors are finally obtained by converting the cylindrical coordinates to the Cartesian ones, i.e. according to (3.77). These are reported at the output, to be considered by the propagation module. Fig. 4.5 shows the case when a narrowband channel is simulated, thus the scattering cylinder is specified as a constant. For wideband channel simulations, on the other hand, this parameter should be also obtained from a random number generator, for each scatterer. Its distribution can be chosen to match channel delay dispersion characteristics estimated from measurements or ray-tracing simulations.

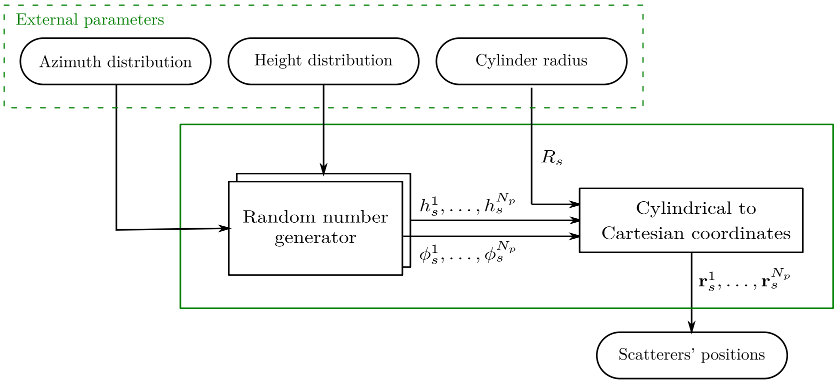

Figure 4.5: Structure of the scattering environment module.

Finally, Fig. 4.6 shows the structure of the simulator's central module, which implements the propagation channel model developed in Sections 3.1 and 3.2. For its operation, this block relies on the mobility module for wearable antenna position and orientation, and the scattering environment one for positions of the scatterers. Together with the off-body antenna's position and orientation provided as an external input, these are used to calculate channel transmission coefficients according to (3.2).

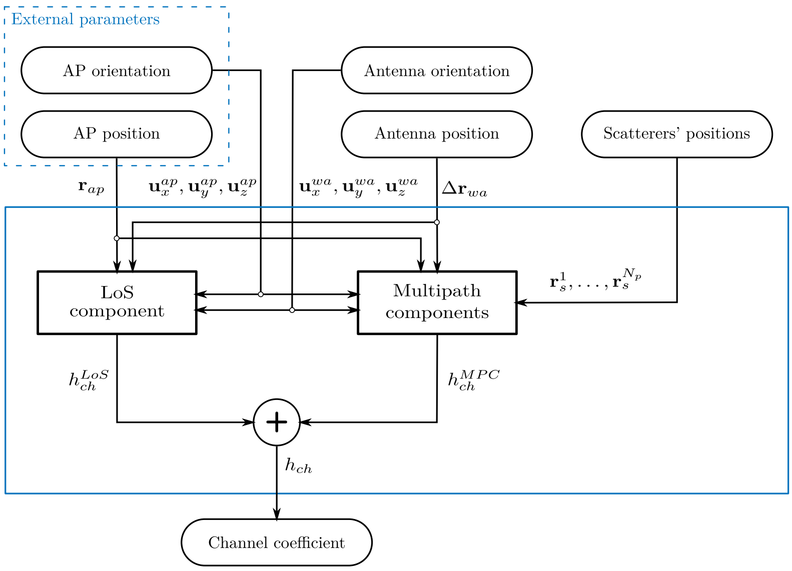

Figure 4.6: Detailed structure of the propagation model module.

The calculation of the contributions from the LoS component and MPCs bouncing from the scattering cylinder is separated in Fig. 4.6, due to principally different forms of the polarisation matrix, as discussed in Section 3.2. One should again note that this structure assumes that the body shadowing effects from the user are embedded in the wearable antennas' radiation patterns used in simulations, thus, there is no need to check if the LoS is obstructed. At the expense of complexity, the simulator could be expanded to consider the shadowing effects more carefully, i.e. take the obstructions of MPCs from arms and legs into account. While being considered for future work, these considerations are out of scope of this thesis.

The structure of the block for calculation of the contribution from scattered MPCs is shown in Fig. 4.7, where the position information is grouped together as well as antenna orientations, in order to avoid cluttered graph. Based on the antenna's orientations and positions of the Tx, Rx and each Sc, this block calculates the baseband channel transmission coefficient considering the MPCs bouncing off the scattering cylinder. The output of this block is essentially the one in (3.2), omitting the LoS component, which is calculated separately. The blocks within the grey frame represent the calculations performed for each MPC, providing the corresponding complex baseband amplitudes associated with each term within the sum in (3.2), whereas the summation block joins the contributions from all paths into a single complex channel coefficient at the output.

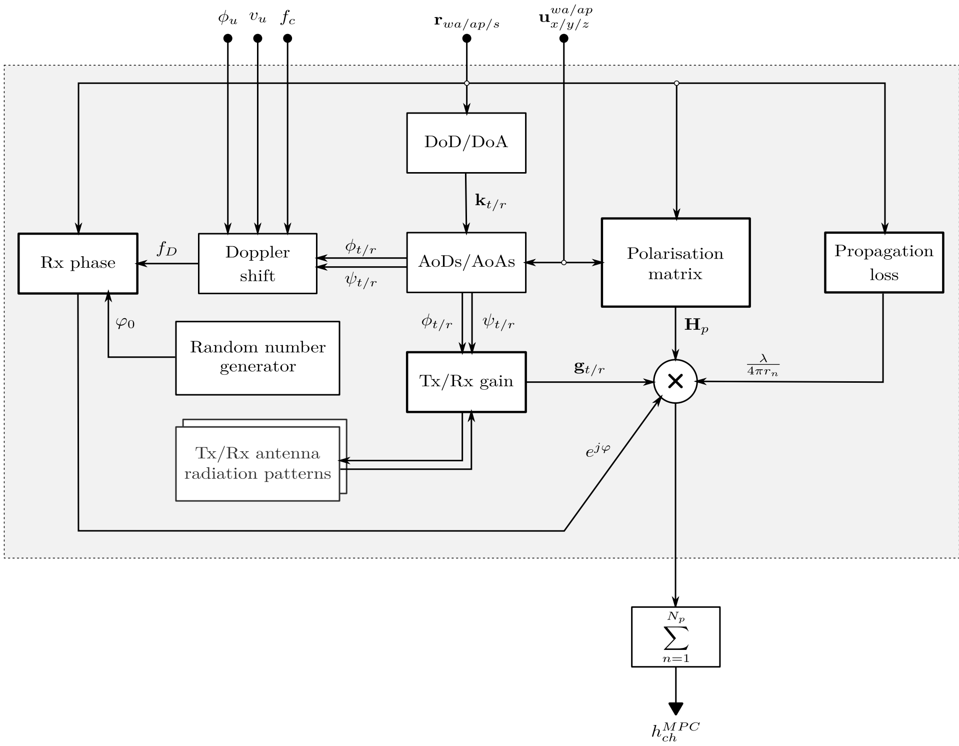

Figure 4.7: Multipath components block structure.

As one observes from Fig. 4.7, the main calculations for individual MPCs include the derivation of the polarisation matrix according to (3.36) and the associated expressions in Section 3.2.2, the calculation of propagation loss and the Rx phase of the MPC, and the extraction of the corresponding Tx and Rx antenna gains from the radiation patterns. These operations are performed in the corresponding blocks, drawn with thicker lines in Fig. 4.7.

In order to extract the antennas gains, the DoD/DoA unit vectors are calculated according to (3.35), which are then used, together with antennas' orientation vectors, to obtain the azimuth and elevation AoDs/AoAs according to (3.4) and (3.5), respectively. The antenna gains for these AoDs/AoAs are finally extracted from the radiation patterns that were previously stored in the local memory, from the simulator input. The propagation loss essentially calculates frequency and distance dependent terms in (3.3), associated with the signal's free-space attenuation. The Rx phase corresponds to the exponential term in (3.2), which is obtained from the Doppler shift frequency and randomly generated initial phase, i.e. uniform in $[0, 2\pi]$. The Doppler shift frequency is calculated considering only the user's forward velocity, while the phase variations due to the antenna displacement relative to the scatterers is taken into account by a phase term dependent on the path length.

One should note that the block for calculation of LoS component in Fig. 4.6 has essentially the same structure as shown in Fig. 4.7, where only the dependence on scatterers' positions is removed and the Rx phase is calculated solely from the direct path length. Therefore, the detailed structure of this block is not shown herein.

4.6 Simulator assessment

This section presents the simulator assessment, considering each module separately. First the implemented mobility model is assessed by analysing the error in antenna position and orientation relative to the skeleton-based model with MoCap data, which is considered as the realistic motion reference. The propagation model is assessed by using the model to replicate scenarios reported in literature, and comparing the obtained results against those reported by the corresponding authors. The assessment of the scattering environment module was not required, as its implementation is based on elementary functions and uses standard random number generators in MATLAB.

4.6.1 Mobility model

In order to analyse the error relative to the realistic motion obtained from the skeleton-based model with MoCap data, two comparative metrics are considered, namely, the maximum distance between antenna positions, $\epsilon_{\Delta\mathbf{r}}$, and the maximum error considering the relative rotation (angle) between orientations obtained from the proposed model and MoCap data, ϵ_{γ}. These metrics, respectively, provide a measure of the error in antenna's position and orientation:

$$\epsilon_{\Delta\mathbf{r}} = \max_{t} \|\Delta\mathbf{r}(t) - \Delta\mathbf{r}_{\mathrm{MC}}(t)\| \tag{4.12}$$

$$\epsilon_{\gamma} = \max_{t} |\Delta\gamma(t)| \tag{4.13}$$

where:

- $\Delta\mathbf{r}_{\mathrm{MC}}$: periodic component of the antenna's position, obtained from MoCap data;
- $\Delta\gamma$: relative rotation angle between orientations given by the model and MoCap data.

The relative rotation angle ($\Delta\gamma$) in (4.13) is obtained from the axis-angle representation of rotation, according to Euler's theorem [137]. The values obtained for the considered antenna placements and user motions are shown in Fig. 4.8. It should be noticed that the index in the acronyms for antenna placements is dropped, as the error applies to the two symmetric antenna placements, i.e. L/R or F/B (Section 3.4.3).

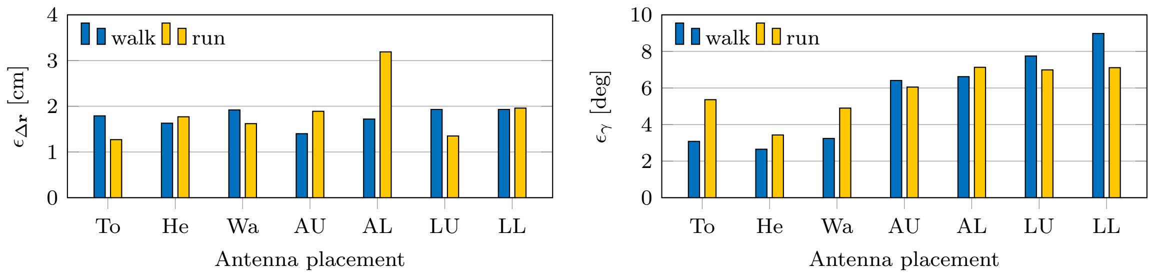

a) Position.

b) Orientation.

Figure 4.8: Antenna mobility model error for position and orientation.

One can observe that the position error is below 2 cm in all cases, except for the wrist antenna (AL) on a running user, for which the maximum distance error is 3.2 cm. Furthermore, the error is similar across antenna placements and motions. Hence, the error is uniform and always within the tolerance, i.e. 5 cm (Section 3.4.2). It should also be noted that the maximum orientation error is found to be 9°, at most, being obtained for the lower leg antenna (LL) on a walking user. In this case, the error is not uniform across different antenna placements; the somewhat higher values are observed for more dynamic on-body antenna placements, i.e. AL, LU and LL. However, it should be pointed out that the higher error maxima for the aforementioned three antenna placements are observed at the end of a motion period. The imperfect periodicity of the human motion yields mismatched on-body antenna orientation at the beginning and the end of a motion period, with this mismatch being more emphasised for the antenna placements on the arms and legs. Therefore, the observed maximum error is actually due to motion cyclification imposed by the mobility model. It is also noteworthy that, if only the inner part of the motion period is considered, the orientation error for these placements is always below 6°, being well within the 10° tolerance (Section 3.4.2). Moreover, the Root Mean Square Error (RMSE) over a motion period is below 5° for all antennas. This error is low in comparison with the typical half-power beam-widths of wearable patch antenna, i.e. grater than 85° [142, 143] and even up to 140° in the measurements presented in this thesis (Section 5.3.2). Therefore, the developed mobility model is perfectly suitable for channel modelling purpose, where this error has a negligible effect.

While the error considered in this section is the one between the model and MoCap data used to calculate its parameters, one could argue that the analysis should be performed for several different subjects and motions. Such a reasoning would then require a comparison for subjects of different gender, age and size, but also variations in the exact antenna placement on the same body part. However, the main goal of this work is to provide a simple parametrised mobility model, which captures the principal characteristics of the human motion. Therefore, the MoCap data used to calculate the parameters were chosen for their high quality, while being representative of an average person.

Following the error analysis, a few notes should be made on the mobility model complexity compared to skeleton-based models with MoCap data. It is easy to notice that the proposed model is superior to the latter in this regard. Considering memory requirements, the skeleton-based models require the storage of MoCap data, which contain a number of channels (components) needed to represent the body's position and posture. These channels contain samples for all body postures over a motion period, where the number of samples depends on the resolution of data, i.e. frame rate. On the other hand, the memory requirements of the proposed model do not depend on the sampling resolution; only the motion period length, average velocity and parameters of the Fourier series (Table 3.1) have to be stored.

The superiority of the proposed model is even more significant when the computational complexity involved in obtaining the antennas' position and orientation at a given time is considered. For skeleton-based models, this requires a chain of recursively applied rotations and offsets through the skeleton hierarchy, in order to obtain the final position and orientation from the relative ones between the parent-child nodes [137]. In a large contrast, the proposed model obtains the antenna orientation by evaluating the Fourier series (3.63) for the corresponding parameters in Table 3.1, whereas the orientation vectors are obtained according to (3.60) - (3.62). Similarly, the position is obtained by first evaluating (3.59) and then (3.56).

For a quantitative reference, the two models can be compared in terms of the number of scalar operations, i.e. multiplication and addition, required to obtain the antenna's position and orientation at a given time. The proposed model requires in total 24 scalar multiplications and 18 additions, as follows from (3.59) and (3.63), with two harmonics being used in the model (Section 3.4.4). On the other hand, the number of operations required for the skeleton-based models depends on the antenna placement (Fig. 3.8). The position and orientation of the associated node in the skeleton structure is obtained through recursive multiplications of 4×4 matrices for each node along the branch [137, Ch. 5]. For the skeleton-based model from [138] (Section 3.4.2), the most demanding case is the wrist antenna (AL_L/R), which requires 8 such multiplications, i.e. 128 scalar multiplications and 96 additions.

Therefore, the proposed model can reduce the number of required multiplications and additions by more than 5 times. One should note that this number does not take the calculations in (3.60) - (3.62) into account[3]. While being performed only once in the proposed model, in the skeleton-based one they are needed to obtain the transformation matrices from Euler angles extracted out of MoCap data for each node, i.e. 8 times for the wrist antenna. Since these involve cumbersome evaluations of trigonometric functions, the achieved reduction in the computation complexity is apparently much greater. However, while the proposed model will certainly reduce the simulation time, its main advantage is a simple mathematical formulation. As such, it should allow for an analytical analysis of some canonical scenarios.

4.6.2 Propagation model

The propagation module assessment was performed by replicating several scenarios chosen from previous studies, selected to test different aspects of the developed channel model. In each case, the

[3] In total 29 sin/cos function evaluations, 16 scalar multiplications and 5 additions.

simulator parameters were set to match the specific description in the corresponding reference, and results are reported in form of figures matching those provided by the authors therein.

Table 4.2 summarises the replicated scenarios, providing a short description, the corresponding reference and indicating the figure with recreated results. Most of them are extracted from mobile communication channel studies, due to a lack of appropriate models for off-body channels, but are general and fit the purpose herein. The considered scenarios and the associated channel model parameters are described in what follows, where the particular aspect of the model being tested is indicated.

One should that the results are not interpreted here, but only the matching between the original and recreated figures is discussed. However, the interested reader should refer to the provided references, where a detailed analysis is typically available.

Table 4.2: List of considered scenarios.

#	Ref.	Fig.	Description
1	[53]	4.9	Two-ray ground-reflection
2	[129]	4.10	Wedge diffraction
3	[86]	4.11	Scattering cylinder reflection depolarisation
4	[85]	4.12	LoS depolarisation due to antenna tilt

Scenario 1 test the implementation of the LoS and reflected MPCs, where the well-known two-ray ground-reflected scenario is recreated. For the assessment purposes, one considers the theoretical two-ray model and the Rx power plots against distance [53]. Fig. 4.9 shows such a graph obtained with the developed model, assuming the following: $f_c = 900\,\text{MHz}$, $h_t = 30\,\text{m}$, $h_r = 2\,\text{m}$ and $P_t = 1\,\text{W}$. The ground is assumed to be perfectly conductive, and ideal H-polarised isotropic antennas are used. The figure also shows the standard log-linear approximation, i.e. with the corresponding path loss exponent of 4, As one observes, the two-ray interference pattern is exactly replicated and the linear approximation shows a perfect match where it applies, i.e. at distances beyond the critical one [53].

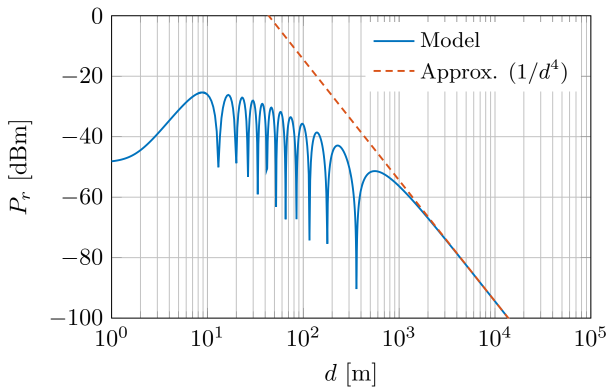

Figure 4.9: Replicated two-ray ground reflected scenario.

Scenario 2 tests the implementation of wedge-diffracted MPCs, by recreating a simple scenario considered by Luebbers [129]. As illustrated in [129, Fig. 2], it involves Tx and Rx placed at the bottom of two opposite sides of a 50 m high hill, i.e. represented by a wedge with an interior angle of 178°. The Tx antenna height is fixed at 10 m, while the Rx one is varied from 2 m to 200 m, i.e. from a deep shadowed region to a high above the hill. The scenario considers LoS propagation, reflection from the side of the hill (face of the wedge) and diffraction over the top, wherever each of these components is present. The total channel transmission coefficient is plotted against the Rx antenna height in [129, Fig. 4] and [129, Fig. 5], respectively, for perfectly conducting wedge with smooth faces and a finite conductivity wedge ($\epsilon_r = 15$, $\sigma = 0.02$ S/m), considering surface roughness given by a terrain height standard deviation of $\sigma_h = 0.5$ m. With the latter being considered herein only for this purpose, the figures are replicated in Figs. 4.10a and 4.10b, respectively. The perfect match between these figures and those in [129] verifies the implementation of all three involved propagation mechanisms. One should note that this scenario is two-dimensional, while the model supports 3D geometry.

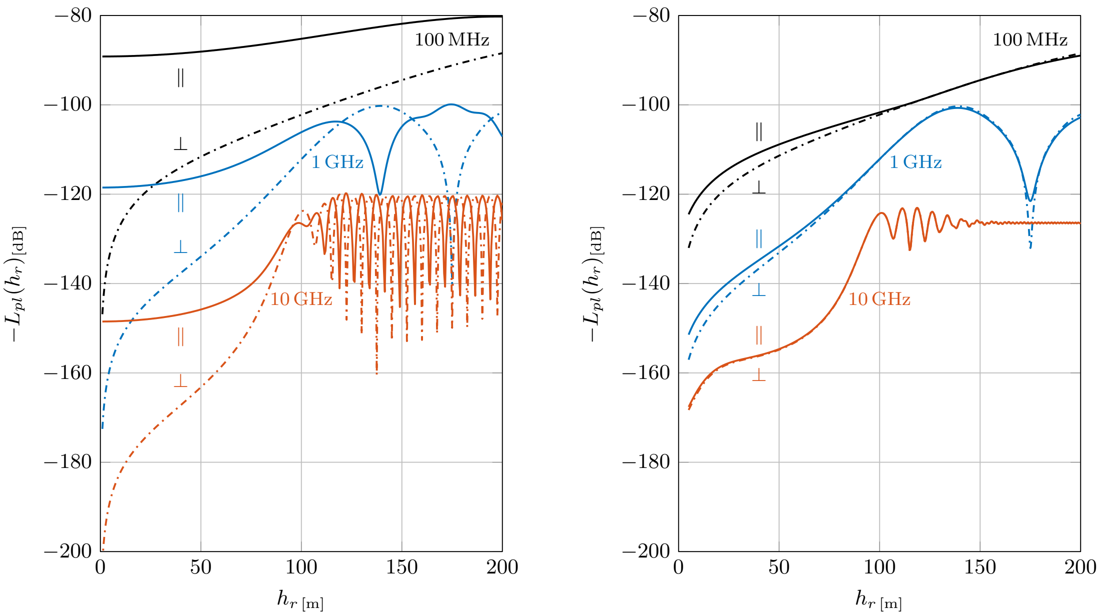

a) Fig. 4 (finite conductivity wedge). b) Fig. 5 (perfectly conducting wedge).

Figure 4.10: Replicated Figs. 4 and 5 from [129].

Scenario 3 tests the polarisation aspect of the model, where a simple mobile communication scenario from [144] was recreated. It considers first-order MPCs reflected from perfectly conducting scatterers, randomly distributed on a circular cylinder centred around the mobile Rx antenna. Their positions are described by AAoAs and EAoAs, where the Von Mises distribution is adopted for the former and cosine for the latter. With the orientation of the street introduced as the parameter affecting the mean AAoA in the Von Mises distribution, the Cross-Polarisation Discrimination (XPD) ($\overline{X}$) is plotted against street orientation angles (ϕ_{st}) in [144, Fig. 3] and [144, Fig. 4] for different numbers of AAoAs (N_{ϕ_r}), EAoAs (N_{ψ_r}) and values of the EAoA distribution parameters, i.e. maximum EAoA (ψ_r^m) and spread parameter (κ). The two figures are replicated in Figs. 4.11a and 4.11b, respectively, where a perfect match is observed. One should note that the authors in [144] consider XPD as the ratio between the coupling coefficients for co- and cross-polarisations of the Tx and Rx antennas, i.e. elements H_{p11} and H_{p22} in the polarisation matrix, where their vertical alignment is assumed.

Scenario 4 tests the implementation aspect concerning LoS signal depolarisation due to antenna

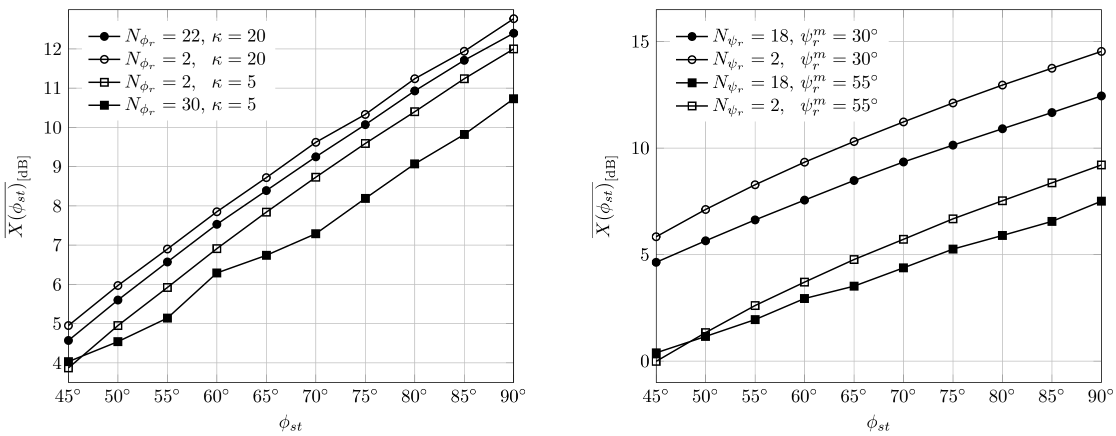

a) Fig. 3 ($N_{\psi_r} = 18$, $N_R = 1$, $\psi_r^m = 30°$).

b) Fig. 4 ($N_{\phi_r} = 22$, $N_R = 1$, $\kappa = 20$).

Figure 4.11: Replicated Figs. 3 and 4 from [144].

tilt, where a mobile communication scenario from [85] was replicated. Its simplified description can be formulated as follows. A mobile Rx antenna is moving over a circular path with the centre in the origin and a 10 m radius; starting at zero azimuth (ϕ_{rx}) and tracing the full circle in the counter-clockwise direction. The base station Tx antenna is on the y-axis, 5 m from the origin, inclined by 45° around the y-axis, while the mobile antenna is inclined by the same angle, but in the direction of its movement in each point on its path. The mobile antenna height was not reported by the authors, so a typical one for hand-held devices was assumed, i.e. 1.5 m. The normalised Rx power plotted against the azimuth angle of the mobile terminal in [85, Fig. 3] is replicated in Fig. 4.12. A comparison between figures shows a match, but with a slight offset in the respective peaks, i.e. as if the mobile antenna in [85] is slightly advancing in azimuth[4]. Since the inspection into the developed model did not reveal any obvious errors, the noticed ambiguities in the scenario description are the likely reason for this slight deviation.

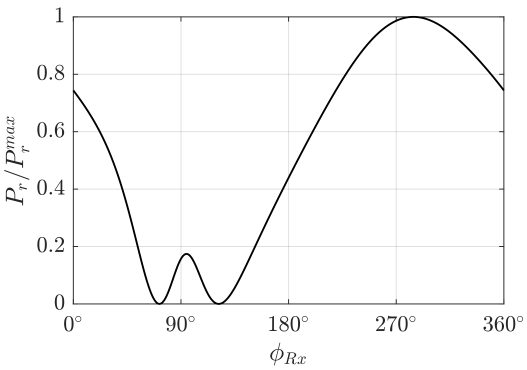

Figure 4.12: Replicated Fig. 3 from [85].

As a final conclusion, the results presented in this section verify the propagation channel development and implementation. The simulator was able to correctly replicate all of the considered scenario, where the perfect match with the results reported in the corresponding references is observed, except

[4]One should also note that the Rx power in [85, Fig. 3] seems not to be normalised to the maximum value, as mentioned in the paper, i.e. curve in the figure peaks at around 0.9.

for the case with ambiguities in the scenario description. Therefore, the simulator is capable of correctly calculating signal components associated with LoS propagation, reflection and diffraction, and properly handle their interaction. It appropriately considers depolarisation of the LoS component and MPCs, considering the influence of antenna orientation and inclination of the incidence plane, but also depolarisation due to interaction with different materials. Together with the realistic simulation of the wearable antenna motion in the mobility model, assessed in the previous section, one finds that the developed simulator captures the characteristics of the off-body channel and allows for its realistic simulation.

Chapter 5

Measurements description

This chapter describes measurements performed as a part of this thesis. These measurements were obtained in two separate campaigns, considering the narrow- and wideband off-body channels at 2.45 GHz, and 5.8 GHz, respectively. Both campaigns were conducted in a common indoor environment, i.e. a meeting room, considering several different wearable antenna placements and user's activities, in order to investigate the associated effects on off-body channel characteristics.

5.1 Measurement campaigns

In order to analyse the off-body channel characteristics based on experimental data, two measurement campaigns were performed in collaboration with colleagues from the Telecommunication Department at Gdansk University of Technology (Gdansk, Poland), who prepared and set up the measurement equipment. The measurements were conducted in an indoor office environment, at the premises of this institution. The focus of both campaigns was on investigating the polarisation characteristics of the channel and the effects associated with user's motion. To facilitate such analysis, the measurements were in both cases performed with two orthogonally polarised off-body antennas, either sequentially or simultaneously, depending on the available equipment. The operating frequencies in both cases are in licence-free ISM frequency bands, considered as the most popular choices for BANs in the past, but also attractive and likely choices for the future ones.

The first campaign aimed to investigate the narrowband off-body channel, considering the influence of body-shadowing, user's posture and dynamics. It involved continuous-wave path loss measurements at 2.45 GHz, for different wearable antenna on-body placements and user's activities, while measurements were repeated for two different persons. Due to limitations of the equipment, measurements in two orthogonal polarisations could be performed only sequentially. While this is a certain drawback, the obtained data still allowed for the analysis of the average polarisation characteristics of the channel. One should note that this campaign was organised and carried out before the work on this thesis started, hence, without participation of the author of this thesis. While the measurements were initially intended to provide data for verification of the simulator developed in [122], the data was found suitable for the analysis in this thesis.

The goal of the second campaign was to complement the narrowband measurements, by considering the wideband off-body channel. It involved CIR measurements at 5.8 GHz with a 500 MHz bandwidth. The measurements were performed in the same room as in the case of the narrowband off-body channel and scenarios similar to the narrowband case were considered. The campaign was organised and carried out within the scope of this thesis, with the author's participation through both planning and execution phases. This allowed for customisation of the measurement scenarios to better fit the purpose of this work. Therefore, more attention was given to the influence of the wearable antenna motion dynamics on the channel. The equipment used in this case allowed simultaneous measurements in the orthogonal polarisations, hence, facilitating the analysis of the instantaneous polarisation characteristics. One should mention that the measurements were performed within the framework of the COST Action CA15104 (IRACON), which also financially supported the campaign through a short-term scientific mission grant assigned to the author.

A detailed description of the measurement campaigns is provided in the rest of this chapter. The measurement environment common to both campaigns is described first, followed by a detailed description of the measurement equipment and scenarios considered for narrow- and wideband channels investigation. The obtained data is analysed in the next chapter, where data processing procedures and considered metrics are also described, followed by the results analysis. Therein, the measurements data were also compared against simulations, in order to validate the off-body channel model proposed in Chapter 3.

5.2 Measurement environment

Both measurement campaigns were performed in a $7 \times 5 \times 3\,\mathrm{m}^3$ meeting room, at GUT. Its floor-plan is shown in Fig. 5.1, while Fig. 5.2 shows images taken from two different corners; Fig. 5.2a shows the image taken from the bottom left corner of the room in Fig. 5.1, while the view in Fig. 5.2b is the one seen from the top right corner.

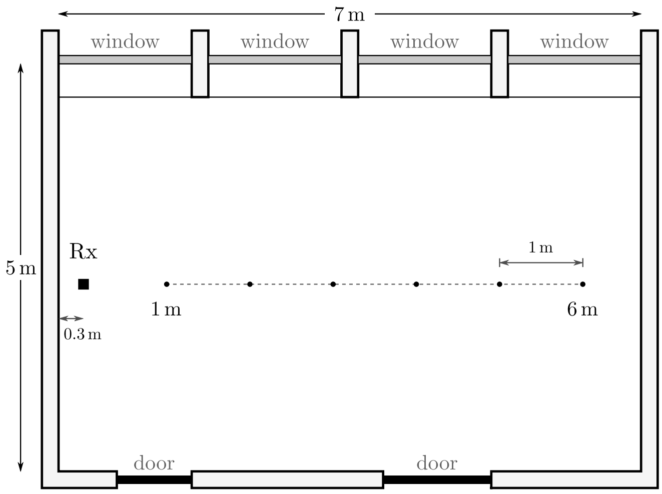

Figure 5.1: Propagation environment floor-plan.

a) View from the bottom left corner in Fig. 5.1.

b) View from the top right corner in Fig. 5.1.

Figure 5.2: Images of the measurement environment, taken during the wideband measurements campaign.

The floor of the room is with PVC coating, while the ceiling is covered with eight regularly distributed light boxes. The top wall in Fig. 5.1 is mostly covered in large windows with PVC frames, a metallic heater being under each of the four windows, at below waist height. While the walls of the room are made of concrete, the right hand side wall in Fig. 5.1 has wooden cupboards covering its whole area.

One should note that the state of the room, considering the objects within, was different at the times the two campaigns were carried out. More precisely, the narrowband measurements were performed with the room being furnished and with the presence of typical objects that give rise to scattering, e.g. tables, chairs, flowers, computers etc, while the room was empty during the wideband measurements. The state of the room in the latter case is shown in Fig. 5.2.

5.3 Narrowband channel measurements

This section describes the narrowband off-body channel measurements at 2.5 GHz, preformed during the first campaign. A description of the scenarios and measurement equipment is provided.

5.3.1 Measurement scenarios

All considered measurement scenarios were with the user and off-body antenna on the line along the room's centre, as illustrated in Fig. 5.1. Moreover, the wearable antenna was connected to the Tx and the off-body one to the Rx, in all considered cases. The latter was placed on a 1.4 m high stand, 30 cm from the wall behind it, as shown Fig. 5.1. Seven different scenarios, illustrated in Figs. 5.3 and 5.4, were considered in total; five involving a static user (S1 - S5), one quasi-dynamic scenario with the user mimicking motion in place (S6), and one true dynamic scenario (S7).

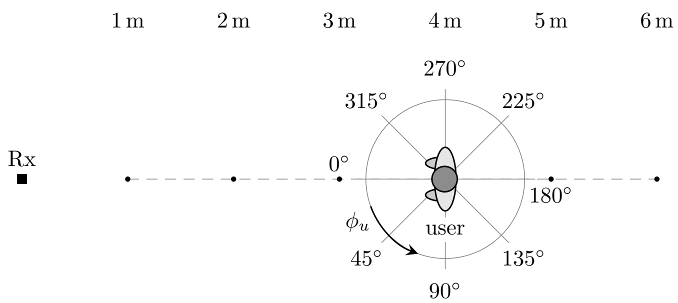

Figure 5.3: Static (S1 - S5) and quasi-dynamic (S6) scenarios.

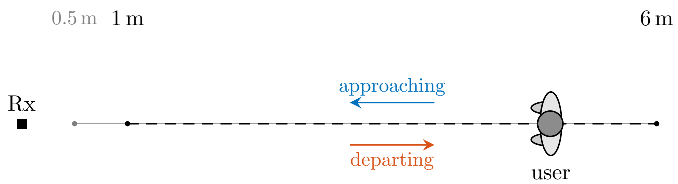

Figure 5.4: Dynamic scenario with the user walking (S7).

The static scenarios differ in considered wearable placements and user postures, i.e. standing (S1 - S3) or sitting (S4 - S5). The difference between the latter two is in the hand placement; the user's arms were on the armrest in S4, whereas in S5 they were in a reading position. The measurements in scenarios S1-S5 were performed with the user standing or sitting at six distances from the off-body antenna; from 1 m to 6 m, with a 1 m step. At each distance, the user performed a full rotation with a 45° step, with 50 samples of the instantaneous path being measured for each orientation (Fig. 5.3).

The quasi-dynamic scenario (S6) is somewhat similar, where instead of being static the user was mimicking a walking motion in place, i.e. as on a treadmill. Moreover, only three user orientations were considered, i.e. 0°, 90°, and 270°, and for each one the instantaneous path loss was measured over a period of 45 s. In the dynamic scenario (S7), the user was walking towards and away from the off-body antenna over the straight path shown in Fig. 5.4, with the closest distance being 1 m and the furthest one 6 m (Fig. 5.4). The measurements were repeated for 12 continuous walks, with the user starting at the further end, approaching the off-body antenna, turning around at 1 m distance and walking back to the starting point.

Three on-body antenna placements were considered as indicated in Fig. 5.5, i.e. front side of the torso (To_F), left side of the head (He_L), and right hand wrist (AL_R). These can be associated with popular BAN applications, namely, chest-mounted fitness band cardio monitor, smart glasses and watches [1]. Measurements were performed with two users, i.e. B1 (male, 1.76 m height, 88 kg weight) and B2 (female, 1.6 m height, 50 kg weight), but also with the antenna on a dielectric cardboard stand, without the presence of the user (NoB). The latter serves as a reference for the analysis of body shadowing effects. All scenarios were performed with B1. B2 was considered in scenarios S1, S4, S6 and S7, and NoB only in S1, S4 and S5.

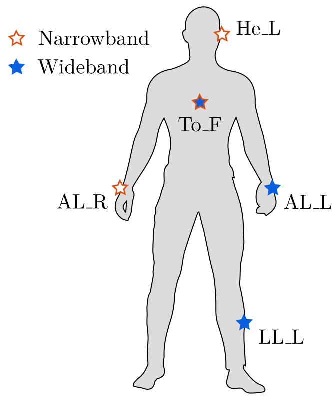

Figure 5.5: Wearable antenna placements considered in narrowband and wideband measurements.

Finally, measurements were sequentially repeated with V- and H-polarised off-body Rx antennas. With a horn antenna being used, this is achieved by simply rotating the antenna on the stand in between the repeated measurements. One should note that, while this approach does not allow for the analysis of channel polarisation characteristics in time, the obtained data can be used to consider these characteristics on average.

Table 5.1 summarises the considered scenarios; the wearable antenna placement, its measured height considering the user standing, considered users and corresponding activities are indicated for each case. One should note that the measured wearable antenna heights closely match those obtained from the mobility model in Chapter 3, considering that the average antenna height for the walking user approximates the standing posture (Table 3.1, parameter a_0 for component Δr_z).

Table 5.1: Summary of narrowband measurement scenarios.

Scenario	S1	S2	S3	S4	S5	S6	S7
AP orientation	V, H						
AP height (h_r)	1.4 m						
Wearable ant. placement	To_F	He_L	AL_R	AL_R	AL_R	AL_R	To_F
Wearable ant. height ($h_{t\,[\mathrm{m}]}$)	1.3	1.65	0.93	0.79	0.85	0.9 - 1	1.3
User/body	B1, B2, NoB	B1	B1	B1, B2, NoB	B1, NoB	B1, B2	B1, B2
User's posture/motion	standing			sitting		walking	

5.3.2 Measurement equipment

The measurements were performed at 2.45 GHz, with the measurement set-up developed at Gdansk University of Technology, shown in Fig. 5.6.

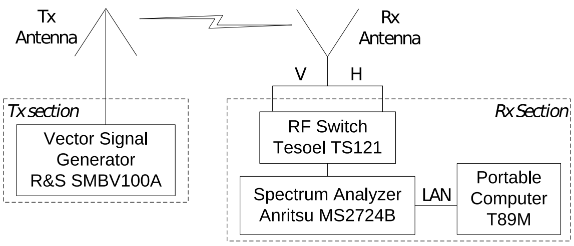

Figure 5.6: Block scheme of the measurement stand.

The Tx section consisted of a vector signal generator R&S SMBV100A [145], a linearly polarised thin micro-strip patch wearable antenna. It has a 3 dBi gain in the maximum radiation direction, and half-power beam-widths of 115° and 140° in the H- and E-planes, respectively. The radiation pattern of this antenna is shown in Fig. 5.7, as measured in an anechoic chamber. One should note that placing the antenna on the body primarily introduces an additional attenuation on the back radiation, without significant change of the front lobe [142]. The connection between signal generator and the antenna was realised using a 7 m long RG174 cable [146]. In order to compensate for cable losses, the Tx section was calibrated so that the Tx power at the antenna terminal was 0 dBm, corresponding to a 3 dBm Equivalent Isotropically Radiated Power (EIRP).

The Rx section consisted of a spectrum analyser Anritsu MS2724B [147], controlled by a computer which also stored the measurement data and performed preliminary calculations. The measurements were performed at a variable sample rate, with the average sampling period of 150 ms and standard deviation of 40 ms. The off-body Rx antenna was a A-info LB-OSJ-0760 [148], a dual-polarised horn antenna designed to operate in the frequency range from 700 MHz to 6 GHz. The antenna was set on a 1.4 m high wooden stand, placed 30 cm from the wall on one side of the room, as shown in Fig. 5.1, its radiation pattern being available in [148]. Switching between V and H polarisations of the antenna was done by using a Tesoel TS121 switch [149]. All connections at the Rx were performed with Huber+Suhner Sucoflex cables [150].

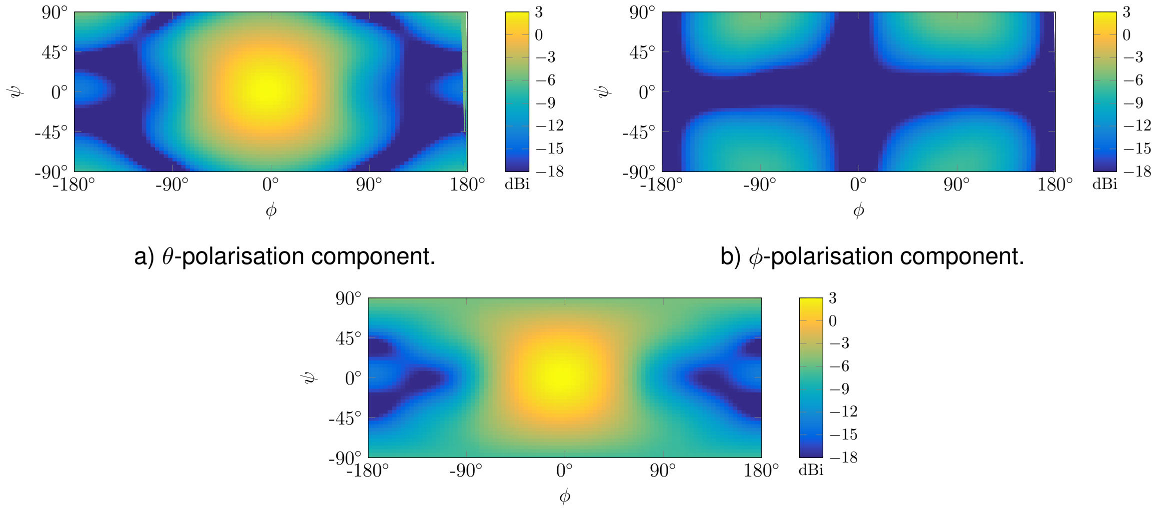

a) θ-polarisation component.

b) ϕ-polarisation component.

c) Total gain.

Figure 5.7: Generalised gain of the on-body patch antenna.

5.4 Wideband channel measurements

This section describes the wideband channel measurements at 5.8 GHz, performed within the second campaign. A description of the scenarios and measurement equipment is provided.

5.4.1 Measurement scenario

The wideband channel measurements were performed for a dynamic scenario, with the user walking towards and away from the off-body antenna, as in the narrowband case scenario (S7) in Section 5.3.1. While the two scenarios are essentially the same, there are slight differences in the set-up, described in what follows.

For the wideband channel measurements the off-body antenna was attached to the wall, 2 m above the floor, acting as a wall-mounted AP. The motion path of the user was slightly longer in this case, with the maximum distance being 6 m and the minimum one 0.5 m. This is illustrated in Fig. 5.4, where the walking path for wideband measurements is represented by a grey solid line, whereas the one for narrowband measurements is depicted by a black dashed line. Instead of a continuous walk towards and then away from the AP, the two walking directions were considered separately in this case, in order to avoid the post-processing required to single out the user approaching and departing cases. This allowed for better synchronisation between different measurements, resulting in a more consistent walking velocity in the repeated measurements. In total, 6 repetitions were considered for each walking direction, with the user velocity being approximately 1.3 m/s.

One should note that the wideband measurements were performed simultaneously with vertical and horizontal dipoles at the off-body side. This circumvents the problems encountered with the narrowband measurements and facilitates the analysis of the instantaneous polarisation characteristics in this case.

For each considered scenario, the measurements were repeated for three wearable antenna placements: on the chest (To_F), left lower arm (AL_L) and left lower leg (LL_L). These are chosen primarily for their different motion dynamics, i.e. To_F being static and the other two dynamic to a different degree. These antenna placements are shown in Fig. 5.5, alongside the those considered in the previous campaign. The common on-body placement for both campaigns is the one on the chest, while the two placements on the wrist are characterised by the same motion dynamics, but with a different perspective of the environment, i.e facing directions.

The scenarios are summarised in Table 5.2, where the measurements were performed for all combinations of the listed parameters. One should note that the measured wearable antenna heights in Table 5.2, as those in Table 5.1, closely match the values obtained from the mobility model (Table 3.1, parameter a_0 for component Δr_z).

Table 5.2: Summary of the measurement scenarios.

AP orientation	V, H
AP height (h_t)	2 m
Wearable ant. placement	To_F, AL_L, LL_L
Wearable ant. heights (h_r)	1.3 m, 0.94 m, 0.32 m
User motion	walking
User direction (ϕ_u)	0° (approaching), 180° (departing)
User distance (d)	$0.5\,\text{m} \leq d \leq 6\,\text{m}$

5.4.2 Measurement equipment

A block diagram of the equipment setup for the wideband channel measurements is shown in Fig. 5.8. The central instrument in this case was a four-port Vector Network Analyser (VNA) Agilent E5071C [151], which supports measurements in the frequency band between 300 kHz and 20 GHz. It was used to record CIR snapshots over time at 5.8 GHz, with a 500 MHz bandwidth.

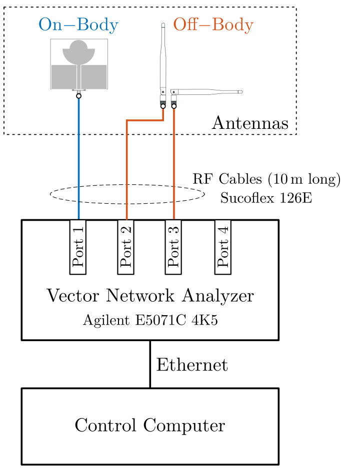

Figure 5.8: Block diagram of the wideband measurement stand.

Prior to measurements, the VNA was calibrated to remove cable delays and attenuation from the s_{21} parameter values, reported at its output. Therefore, the obtained measurement data correspond to the attenuation between the Tx and Rx ports, i.e. system loss [152], with the antenna gain being embedded within. One should also note that the VNA was set to report s_{21} in dB at its output, the phase information being discarded.

A coplanar-fed UWB monopole antenna [153] was connected to the Tx port and used as the wearable one, while two orthogonal dual-band dipoles [154], i.e. vertical and horizontal, were used for simultaneous dual-polarised reception at the off-body side. The connections between the VNA and antennas were realised using 10 m long flexible coaxial cables, Sucoflex 126E [155]. The VNA was controlled via Ethernet connection by a computer, which also stored the data on a local hard drive (Fig. 5.8). A dedicated software was developed by the colleagues from GUT for this purpose, where the National Instruments implementation of the Virtual Instrument Software Architecture (NI-VISA) standard [156] was used.

The VNA measurements are performed in the frequency domain; a frequency-sweeping signal is fed into the Tx port (Port 1), and the response signal from the two Rx ports (Ports 2 and 3) is simultaneously recorded. With a Kaiser-Bessel window ($\beta = 6$) being applied to the obtained Transfer Function, the Inverse Fourier Transform is then performed to obtain the CIR in the delay domain. In total, 401 sample points were obtained for each port, yielding a delay resolution of 0.25 ns over the delay window of 100 ns. The triggering time between successive CIR measurement was variable, being 166.9 ms on average, with a 7.3 ms standard deviation. The Tx power at Port 1 was set to 10 dBm, yielding 4 dBm at the Tx antenna port, as the cable and connectors introduced a 6 dB attenuation (i.e. measured by the manufacturer). The Intermediate Frequency (IF) filter bandwidth was 70 kHz, yielding the noise floor level of -107 dBm The instantaneous noise power was found to be always below the -98 dB mark in the system loss output. The measurement parameters are summarised in Table 5.3.

Table 5.3: Summary of the wideband measurements parameters.

Tx power (port 1)	10 dBm
Center frequency	5.8 GHz
Bandwidth	500 MHz
IF Bandwidth	70 kHz
Tx pulse width	3.9 ns
CIR duration (max. delay)	100 ns
Delay sampling time	0.25 ns
No. of samples per CIR	401
Window function	Kaiser-Bessel ($\beta = 6$)
Triggering time	166.9 ms (avg.), 7.3 ms (std. dev.)

Chapter 6

Measurement-based channel analysis

This chapter presents the analysis of the data obtained from narrow- and wideband off-body channels measurement campaigns, described in the previous chapter. The performed data processing procedures and calculation of considered metrics are described first, followed by a discussion of the obtained results. The channel characteristics are analysed according to the obtained data, where the depolarisation effect and the influence of user's motion receive particular attention.

6.1 Narrowband channel

The analysis of narrowband channel measurements at 2.5 GHz is presented in this section. Data preprocessing is described first, outlining the path loss components extraction procedure, and classification of the measurement samples according to body shadowing from the user and polarisation matching conditions in between the Tx and Rx antennas. The statistical analysis of the path loss components and channel polarisation characteristics is described, followed by results discussion.

6.1.1 Preprocessing and components extraction

In order to facilitate the depolarisation analysis, one has associated the polarisations of the Rx antenna to Co-Polarisation (CP) and Cross-Polarisation (XP) channels for each scenario. Obviously, this association depends on the wearable antenna placement and user posture. On-body placements in static scenarios S1, S2 and S3 imply that the V polarisation of the Rx antenna yields the CP channel, while the H polarisation corresponds to the XP one.

Due to the specific postures, this association is more delicate in S4 and S5. The on-body antenna is basically always horizontal in S4, while the channel polarisation state depends on user's orientation. The antennas' polarisations are matched and the channel is CP for orientation angles (ϕ_u) 0° and 180°, it is XP for this angle being 90° and 270°, while the remaining four orientations (Fig. 5.3) yield polarisations inclined at approximately 45°. The case in scenario S5 is somewhat similar to S4, where the channel varies between matched CP and partially depolarised, with antenna polarisations inclined at $\pm 45°$ at the extreme. In dynamic scenarios S6 and S7, the polarisation matching condition changes due to wearable antenna rotation with the user's movement, while the channel polarisation state for the corresponding static posture is a reasonable reference. Therefore, for S6 and S7 one considers the static posture as in S3 and S1, respectively, where the channel is CP for the vertical off-body antenna.

Prior to the statistical analysis, measurement samples were further classified into three groups according to shadowing by the user, i.e. LoS, NLoS and Quasi-LoS (QLoS), respectively corresponding to the propagation conditions when the direct path is unobstructed, fully and partially obstructed by the user. These groups are intuitively defined with respect to the maximum radiation direction of the wearable antenna (i.e. pointing away from the body), as shown in Fig. 6.1 for the To_F antenna.

The indicated angles correspond to the LoS direction relative to the maximum radiation one (ϕ_{max}). The figure also shows the normalised radiation pattern of the wearable antenna in the azimuth plane, obtained in free space. As one can notice, the gain in QLoS directions is 20 dB lower than the maximum one, which is one of the reasons why this condition is distinguished from the LoS one. The absolute mapping onto user orientation angles is easily obtained as given in Table 6.1, considering that relative DoD angles correspond to the difference $\phi_u - \phi_{max}$. One should note that all samples in scenario S4 are considered QLoS, as the wearable antenna is horizontal in this case.

For each propagation condition, the path loss components were extracted from the instantaneous values, by considering the standard three-component model for the latter, i.e.

$$L_{pl}(d,\phi_u,t)_{[\mathrm{dB}]} = \overline{L_{pl}(d)}_{[\mathrm{dB}]} + \Delta L_{ls}(\phi_u,t)_{[\mathrm{dB}]} + \Delta L_{ss}(\phi_u,t)_{[\mathrm{dB}]} \qquad (6.1)$$

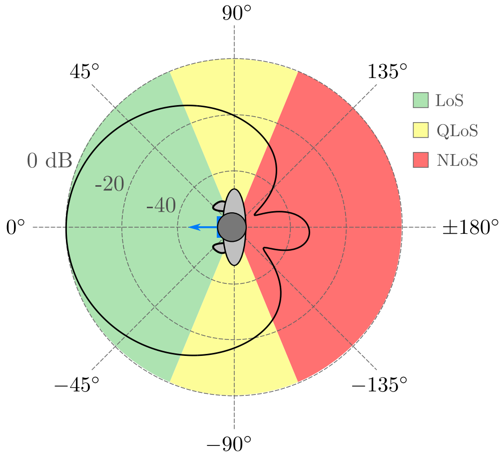

Figure 6.1: Propagation condition classification, shown for the To_F antenna case.

Table 6.1: User orientation angles corresponding to different propagation conditions.

Scenario	S1	S2	S3	S4	S5	S6	S7
ϕ_{max}	0°	270°	90°	-	90°	90°	0°
ϕ_u for LoS [°]	0 45 315	225 270 315	45 90 135	-	45 90 135	90	0
ϕ_u for NLoS [°]	135 180 225	45 90 135	225 270 315	-	225 270 315	270	180
ϕ_u for QLoS [°]	90 270	0 180	0 180	All	0 180	0	-

where:

- $\overline{L_{pl}}$: MPL;
- ΔL_{sh} : large-scale fading;
- ΔL_{mf} : small-scale fading.

The typical log-distance model is adopted for the MPL, i.e.

$$\overline{L_{pl}(d)}_{[\mathrm{dB}]} = \overline{L_{pl}(d_0)}_{[\mathrm{dB}]} + 10\, n_{pl} \log_{10}\left(\frac{d}{d_0}\right) \tag{6.2}$$

where:

- n_{pl} : path loss exponent,
- d_0 : reference distance (i.e. 1 m),
- $\overline{L_{pl}(d_0)}$: value of the MPL at reference distance.

The two fading components are represented by random variables, whose distributions are to be determined from measurement data.

In order to separate the path loss components in (6.1), the small-scale fading was first filtered out. Due to different measurement procedures, the filtering operation depends on the scenario. For the static and quasi-dynamic scenarios (S1-S6), the time average of the instantaneous values was obtained for each distance and user orientation. For the dynamic scenario (S7), a moving average filter with the averaging distance of 10λ was applied, being the standard choice for indoor measurements [157].

In the next step, the MPL model is fitted to the composite path loss obtained after removing the small-scale variations. While the model formulation and procedure of the regression analysis are typical, the approach adopted in this work differs from the common practice. That is, the path loss exponent was constrained to the value obtained for the LoS case in the CP channel (CP-LoS) of a generalised static reference scenario. The latter is obtained by jointly considering all samples classified as CP-LoS in scenarios S1 and S2. With the constrained path loss exponent, only $\overline{L_{pl}(d_0)}$ is estimated from data.

The rationale for this approach follows from the fact that the scatterers in the room remain at similar distances from the user, regardless of the user's distance from the AP, thus the dependence of the MPL on the latter is lost in the NLoS condition. The adopted approach yields a tight MPL model fit when the channel is least affected by propagation phenomena other than the propagation loss, while Goodness of Fit (GoF) practically remains unchanged for the XP channel and other propagation conditions.

Finally, the large-scale fading was obtained by subtracting the MPL values from the composite component (i.e. with small-scale variations filtered out), whereas the small-scale one was obtained by subtracting the composite component from the instantaneous path loss. One should note that only scenarios S6 and S7 are considered for the statistical analysis of fading, since only these involve wearable antenna movement.

6.1.2 Channel analysis description

In order to characterise the channel, several statistical distributions were fitted to extracted fading components, considering the typical choices reported in literature [96]. The considered models are listed below, with the corresponding parameters [54, 158, 159]:

- Rice, with parameters s_{Rice} (non-centrality) and σ_{Rice} (scale);
- Nakagami, with parameters m_{Nak} (shape) and Ω_{Nak} (scale);
- Rayleigh, with a parameter σ_{Ray} (scale);
- Lognormal, with parameters $\mu_{L\,[\mathrm{dB}]}$ (log mean) and $\sigma_{L\,[\mathrm{dB}]}$ (log standard deviation).

The first three are considered for small-scale fading amplitude, while the last one is considered for the large-scale power variation.

Distribution fitting was performed in MATLAB [140], using the built-in function `fitdist` based on maximum-likelihood parameter estimation. The Akaike Information Criterion (AIC) [160], χ^2 and correlation tests [161] were additionally used as GoF metrics. While AIC only establishes a relative ordering among candidates, the χ^2 test gives an absolute measure of how well models fit data. The decision if the test is passed for a given significance is made by comparing the test statistic (χ^2) against the critical value (χ^2_{crit}); the latter depends on the number of distribution parameters and the chosen test significance. Distributions with the χ^2 value lower than the critical one pass the test, and the minimum value corresponds to the best fitting model. For the chosen significance level of 5 %, the critical value is 27.59

for the Rayleigh distribution, and 28.87 for all the others. Finally, the correlation test involved calculation of the correlation coefficient between empirical PDF and the fitted model, where 0.95 was considered as the lowest acceptable value.

Polarisation characteristics of the channel were analysed by considering the XPD [162], calculated as:

$$X_{pd}(d, \phi_u)_{[\mathrm{dB}]} = L_{pl}^{H}(d, \phi_u)_{[\mathrm{dB}]} - L_{pl}^{V}(d, \phi_u)_{[\mathrm{dB}]} \tag{6.3}$$

where:

- $L_{pl}^{V/H}$: path loss for the V-/H-polarised Rx antenna.

It is important to notice that (6.3) considers the average path loss over time, since the measurements with V- and H-polarised Rx antennas were performed sequentially (not simultaneously).

In order to investigate the influence of user orientation on XPD, the values obtained according to (6.3) were further averaged over distances, yielding $\overline{X_{pd}(\phi_u)}$. Similarly, the average XPD for different propagation conditions, i.e. $\overline{X_{pd}^{LoS}}$, $\overline{X_{pd}^{NLoS}}$ and $\overline{X_{pd}^{QLoS}}$, were obtained by averaging over the corresponding user orientation angles (Fig. 6.1). Finally, one should note that the XPD calculated herein was affected by both propagation environment and antenna characteristics.

6.1.3 Path loss and fading statistics

Examples of the instantaneous path loss obtained for the quasi-dynamic (S6) and the dynamic scenario (S7) are shown in Fig. 6.2. The signal shown in Fig. 6.2a is captured for a fixed user's position and orientation, where the observed signal variations originate from the dynamics of the mimicked walk cycle. In addition to the influence of user dynamics, the one of the body characteristics is also apparent. While variation magnitudes are similar for both users, i.e. around 25 dB, the average path loss for the female user (B2) is around 5 dB lower than for the male one (B1), being 46.1 dB for the former and 51.2 dB for the latter. However, one should note that the particular posture of the user could have significantly influenced these results, since the wrist antenna placement is considered in S6.

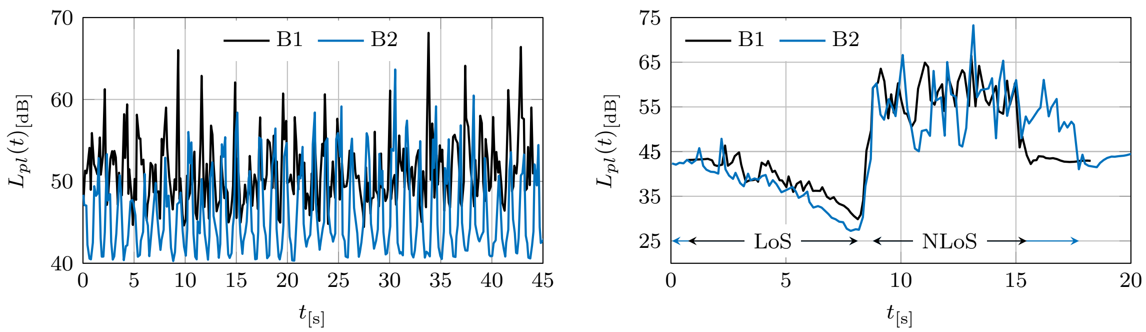

a) Quasi-dynamic scenario (S6). b) Dynamic scenario (S7).

Figure 6.2: Instantaneous path loss obtained for quasi-dynamic and dynamic scenarios.

The path loss in Fig. 6.2b was captured during one of the user's walks in scenario S7; in total 12 being recorded for each Rx polarisation. Path loss values clearly reflect the actions of the user during walk, with a similar behaviour observed for both users. That is, path loss decreases linearly as the user approaches the off-body antenna (LoS), it sharply increases by roughly 33 dB as the user turns around, and then exhibits large variations as the user walks away from the Rx. The dependence on distance in the LoS case is clearly observed, while for the NLoS this trend cannot be distinguished due to the high variability of the Rx coming from the multipath fading. Furthermore, as expected, path loss is much lower in LoS than in NLoS.

The MPL model fitting results are summarised in Table 6.2, showing the estimated values of the MPL model parameter $\overline{L_{pl}(d_0)}$, the corresponding coefficient of determination (R^2) and standard deviation (σ) of the path loss around model prediction. The common path loss exponent is $n_{pl} = 1.71$, being similar to the value in free space. Due to the adopted modelling approach, the tightest fit is expectedly obtained for the CP-LoS case, where the corresponding R^2 is closest to 1 and the standard deviation is the lowest. The QLoS case yields a somewhat looser fit with higher signal deviations, while the loosest fit is obtained for the NLoS case with R^2 being around zero. By considering the $\overline{L_{pl}(d_0)}$ values, one observes that the MPL is, on average, the highest for NLoS case and the lowest for LoS. Therefore, high attenuation and greater Rx signal variations should be expected when the LoS path is obstructed by the user.

Table 6.2: Overview of estimated mean path loss model parameters ($n_{pl} = 1.71$).

		co-polarisation			cross-polarisation		
Scenario	xLoS	$\overline{L_{pl}(d_0)}_{[\mathrm{dB}]}$	R^2	$\sigma_{[\mathrm{dB}]}$	$\overline{L_{pl}(d_0)}_{[\mathrm{dB}]}$	R^2	$\sigma_{[\mathrm{dB}]}$
S1	LoS	31.3	0.75	2.7	47.7	0.72	3.0
	NLoS	48.5	0.12	5.1	55.0	0.04	6.4
	QLoS	42.6	0.02	5.2	47.1	0.39	3.9
S2	LoS	31.7	0.59	3.6	43.4	0.43	4.7
	NLoS	50.8	0.07	6.2	49.6	0.21	4.7
	QLoS	41.7	0.26	4.4	47.7	0.17	5.2
S3	LoS	33.4	0.18	4.7	43.5	0.07	6.0
	NLoS	49.3	0.01	6.8	49.9	0.20	4.4
	QLoS	44.9	0.39	4.8	47.4	0.46	4.7
S6	LoS	32.0	0.54	3.1	39.8	0.80	2.0
	NLoS	49.7	0.00	4.8	51.9	0.77	2.7
	QLoS	41.6	0.69	3.1	48.0	0.94	1.6
S7	LoS	29.8	0.96	0.5	51.0	0.02	3.1
	NLoS	47.7	0.27	2.3	55.2	0.02	2.9

The MPL model fit to measurements is typically much looser in the XP channel, implying a higher degree of randomness in this chase. Higher standard deviations observed for all propagation conditions in this channel, i.e. similar to those in CP-NLoS case, reveal that the magnitude of signal variations are greater as well. Finally, it is evident from $\overline{L_{pl}(d_0)}$ that the overall average path loss is higher. Therefore, a lack of strong signal component in the XP channel is manifested by the lower average Rx power and more severe signal fading than in the CP one.

Since the CP/XP classification is not straightforward for scenarios S4 and S5, the corresponding MPL model fit statistics are provided separately in Table 6.3, distinguishing between channels associated with

V - and H -polarised Rx antennas.

Table 6.3: Overview of estimated mean path loss model parameters for scenarios S4 and S5 ($n_{pl} = 1.71$).

		V-polarised Rx			H-polarised Rx		
Scenario	xLoS	$\overline{L_{pl}(d_0)}_{[\mathrm{dB}]}$	R^2	$\sigma_{[\mathrm{dB}]}$	$\overline{L_{pl}(d_0)}_{[\mathrm{dB}]}$	R^2	$\sigma_{[\mathrm{dB}]}$
S4	QLoS	45.70	0.30	6.7	43.6	0.31	6.4
S5	LoS	33.81	0.40	3.7	36.8	0.44	3.7
	NLoS	51.14	0.00	8.1	50.9	0.23	5.4
	QLoS	43.58	0.20	4.2	45.5	0.47	5.2

As observed from R^2 and σ in scenario S4, the Rx signal is stronger and variations are smaller for the H-polarised Rx antenna. This is explained by the horizontal orientation of the wearable antenna in this case, yielding mismatched and effectively orthogonal polarisations of the antennas. In scenario S5, one observes similar fit statistics for V- and H-polarised Rx antennas in the LoS case. This is due to typical 45° inclination between antennas' polarisations in this scenario, yielding practically equal Rx power in both polarisations. The highest R^2 in this scenario is obtained for the QLoS case, which is not surprising, as the particular antenna placement and user's posture yield matched antennas' polarisations for the corresponding orientations.

In order to observe the effects of polarisation state and propagation conditions on the channel, one considers the estimated MPL model parameter and standard deviation relative to the CP-LoS in each scenario. Fig. 6.3 shows the relative values for $\overline{L_{pl}(d_0)}$ and the standard deviation σ; the former being given as a difference and latter as a ratio. One should note that horizontal lines at 0 dB and 1 in Figs. 6.3a and 6.3b, respectively, correspond to the CP-LoS reference.

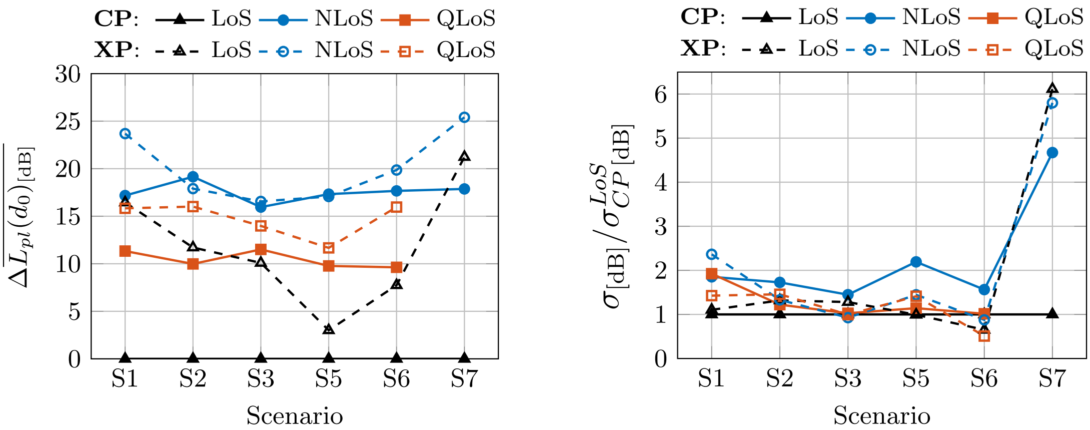

a) MPL at reference distance.

b) Standard deviation.

Figure 6.3: MPL at reference distance and standard deviation of the MPL model fit, relative to the values obtained for CP-LoS.

LoS yields the lowest and NLoS the highest values of $\overline{L_{pl}(d_0)}$, in both polarisations. In the CP channel, $\overline{L_{pl}(d_0)}$ is approximately 10 dB and 17 dB higher for QLoS and NLoS, than for LoS. These differences are not consistent over scenarios for the XP channel, but the relative order is preserved. The values are typically more than 10 dB higher compared to the reference, with only scenario S5 showing a notable deviation; inclined Tx-Rx polarisations due to user's posture in S5 yield lower MPL in this case. The standard deviations for static scenarios in Fig. 6.3b are commonly less than twice the reference value, while a significant deviation is observed for the dynamic scenario S7. This observation fits one's expectation, since the Rx signal is subject to multipath fading due to user's movement in this scenario.

The overall results of Log-normal distribution fitting for the large-scale fading are presented in Table 6.4, showing the estimated parameter values, the number of samples used for the fit (#), the χ^2 test statistic and correlation coefficient, where the latter two serve as GoF metrics. One should recall that the chosen significance level of 5 % yields the critical value of $\chi^2_{crit} = 27.59$, for the Log-normal distribution. While both scenarios S6 and S7 are considered, the results are shown only for S7, the reason being unacceptably bad fit for scenario S6, due to the discrete character of the captured measurements. Namely, the Rx signal was measured at six fixed positions (discrete points), thereby not capturing the transitions between these positions and lacking continuity. The additional reason for the bad fit in this case follows from the periodic effects associated with the wrist antenna, namely, gain variation and depolarisation. The corresponding signal variations do not exhibit a Log-normal distribution, being rather deterministic.

Table 6.4: Overview of Lognormal distribution fitting for large-scale fading ($\chi^2_{crit} = 28.87$).

Channel	User	#	Parameters	χ^2	Corr.
co-polarised	B1	772	$\mu_{L\,[\text{dB}]} = 0$, $\sigma_{L\,[\text{dB}]} = 1.25$	114.84	0.95
	B2	893	$\mu_{L\,[\text{dB}]} = 0$, $\sigma_{L\,[\text{dB}]} = 1.5$	122.22	0.95
cross-polarised	B1	736	$\mu_{L\,[\text{dB}]} = 0$, $\sigma_{L\,[\text{dB}]} = 1.78$	30.52	0.98
	B2	865	$\mu_{L\,[\text{dB}]} = 0$, $\sigma_{L\,[\text{dB}]} = 1.66$	17.84	0.99

The low log standard deviation parameter (σ_L) in all cases, i.e. < 1.8 dB, means that the local average Rx power exhibits small changes in scenario S7. This was expected, considering that the user is walking within a fairly small room in which the propagation characteristics are principally unchanged as the user traverses the considered path, but also the body-shadowing conditions remain constant while the user walks in each direction. Therefore, the path loss variations observed in this scenario are essentially due to multipath effects.

The distribution fitting results for the small-scale fading are summarised in Tables 6.5 and 6.6, where AIC statistic is provided as an additional GoF metric for model ordering. The results in Table 6.5 show that the CP channel in scenario S6 is best described by the Rice distribution, while the Nakagami-m one is the best overall model in scenario S7. However, further inspection of the estimated parameters reveals that the signal variations are generally more severe in S6 than S7. This is implied by the lower values for m_{Nak} and Ω_{Nak} obtained in S6, considering that the former parameter is inversely proportional to fading depth and the latter represents the average fading power [54]. This result can be associated with the wrist antenna displacement rotation due to swinging motion of user's hands during mimicked walk.

One should note that the Rayleigh distribution typically yields the worst fit in both scenarios and for all propagation conditions. Therefore, it is not a suitable model for the considered off-body BAN channel, as expected for a short-distance indoor scenario without physical obstructions of LoS (except by the user's

Table 6.5: Overview of distribution fitting results for small-scale fading in the co-polarised channel.

Scen.	User	xLoS	#	Dist.	Parameters	χ^2	χ^2_{crit}	AIC	Corr.
S6	B1	LoS	1800	Rice	$s_{Rice} = 0.998$, $\sigma_{Rice} = 0.257$	55.59	27.59	150.53	0.98
				Nakagami	$m_{Nak} = 4.28$, $\Omega_{Nak} = 1.129$	47.63	27.59	139.25	0.98
				Rayleigh	$\sigma_{Ray} = 0.751$	1175.28	28.87	1543.48	0.60
		NLoS		Rice	$s_{Rice} = 0.862$, $\sigma_{Rice} = 0.657$	21.84	27.59	2788.19	0.99
				Nakagami	$m_{Nak} = 1.192$, $\Omega_{Nak} = 1.608$	17.56	27.59	2784.28	0.99
				Rayleigh	$\sigma_{Ray} = 0.896$	48.73	28.87	2815.52	0.98
		QLoS		Rice	$s_{Rice} = 0.954$, $\sigma_{Rice} = 0.541$	14.37	27.59	2424.05	0.99
				Nakagami	$m_{Nak} = 1.388$, $\Omega_{Nak} = 1.49$	41.13	27.59	2445.87	0.98
				Rayleigh	$\sigma_{Ray} = 0.864$	130.71	28.87	2552.17	0.93
	B2	LoS		Rice	$s_{Rice} = 0.997$, $\sigma_{Rice} = 0.337$	88.48	27.59	1068.34	0.96
				Nakagami	$m_{Nak} = 2.659$, $\Omega_{Nak} = 1.221$	98.89	27.59	1079.93	0.97
				Rayleigh	$\sigma_{Ray} = 0.781$	667.79	28.87	1825.39	0.73
		NLoS		Rice	$s_{Rice} = 0.971$, $\sigma_{Rice} = 0.489$	22.65	27.59	2164.89	0.99
				Nakagami	$m_{Nak} = 1.568$, $\Omega_{Nak} = 1.421$	41.09	27.59	2180.96	0.99
				Rayleigh	$\sigma_{Ray} = 0.843$	198.21	28.87	2372.47	0.92
		QLoS		Rice	$s_{Rice} = 0.998$, $\sigma_{Rice} = 0.376$	77.50	27.59	1423.18	0.98
				Nakagami	$m_{Nak} = 2.179$, $\Omega_{Nak} = 1.28$	119.02	27.59	1486.82	0.96
				Rayleigh	$\sigma_{Ray} = 0.8$	581.49	28.87	1994.77	0.77
S7	B1	LoS	346	Rice	$s_{Rice} = 0.99$, $\sigma_{Rice} = 0.15$	18.59	27.59	-358.95	0.95
				Nakagami	$m_{Nak} = 11.49$, $\Omega_{Nak} = 1.02$	18.19	27.59	-361.72	0.95
				Rayleigh	$\sigma_{Ray} = 0.72$	669.99	28.87	256.6	0.53
		NLoS	390	Rice	$s_{Rice} = 0.89$, $\sigma_{Rice} = 0.64$	26.44	27.59	605.75	0.93
				Nakagami	$m_{Nak} = 1.27$, $\Omega_{Nak} = 1.6$	25.35	27.59	601.54	0.93
				Rayleigh	$\sigma_{Ray} = 0.89$	39.74	28.87	612.60	0.92
	B2	LoS	423	Rice	$s_{Rice} = 1.0$, $\sigma_{Rice} = 0.14$	25.87	27.59	-487.01	0.97
				Nakagami	$m_{Nak} = 13.03$, $\Omega_{Nak} = 1.04$	29.82	27.59	-466.06	0.96
				Rayleigh	$\sigma_{Ray} = 0.72$	996.64	28.87	301.63	-0.01
		NLoS	442	Rice	$s_{Rice} = 0.06$, $\sigma_{Rice} = 0.94$	11.94	27.59	818.99	0.97
				Nakagami	$m_{Nak} = 0.99$, $\Omega_{Nak} = 1.77$	11.87	27.59	818.97	0.97
				Rayleigh	$\sigma_{Ray} = 0.94$	11.94	28.87	816.97	0.97

body), and with the presence of strong specular reflections.

For the XP channel (Table 6.6), the overall best fitting models in scenarios S6 and S7 are again Rice and Nakagami-m distributions, respectively. However, the GoF metrics are similar for all three considered statistical models. Since the Rayleigh distribution comes as a special case in both other models, this means that the Rx signal exhibits Rayleigh fading in the XP channel. This comes from the fact that the Rx antenna receives most of the energy from depolarised MPCs, arriving after multiple reflections in the environment. That said, due to its generality, the Nakagami-m distribution can be adopted in this channel as well, thus presenting itself as the overall small-scale fading model for the indoor off-body channel.

One should note that the results in scenario S6 show that the considered distributions fit the data very loosely, and the models generally fail the χ^2 test. While this is partially because the user does not really move in this case, the same observations as discussed for the large-scale variations apply

Table 6.6: Overview of distribution fitting results for small-scale in the cross-polarised channel.

Scen.	User	xLoS	#	Dist.	Parameters	χ^2	χ^2_{crit}	AIC	Corr.
S6	B1	LoS	1800	Rice	$s_{Rice} = 0.455$, $\sigma_{Rice} = 0.921$	216.43	27.59	3426.45	0.82
				Nakagami	$m_{Nak} = 0.907$, $\Omega_{Nak} = 1.904$	201.53	27.59	3415.15	0.84
				Rayleigh	$\sigma_{Ray} = 0.976$	216.29	28.87	3424.70	0.82
		NLoS		Rice	$s_{Rice} = 0.049$, $\sigma_{Rice} = 0.971$	85.45	27.59	3399.46	0.99
				Nakagami	$m_{Nak} = 0.917$, $\Omega_{Nak} = 1.889$	75.46	27.59	3390.31	0.99
				Rayleigh	$\sigma_{Ray} = 0.972$	85.50	28.87	3397.45	0.99
		QLoS		Rice	$s_{Rice} = 0.888$, $\sigma_{Rice} = 0.639$	32.19	27.59	2770.95	0.99
				Nakagami	$m_{Nak} = 1.196$, $\Omega_{Nak} = 1.605$	42.77	27.59	2777.23	0.98
				Rayleigh	$\sigma_{Ray} = 0.896$	73.81	28.87	2809.63	0.96
	B2	LoS		Rice	$s_{Rice} = 0.778$, $\sigma_{Rice} = 0.771$	48.44	27.59	3200.79	0.97
				Nakagami	$m_{Nak} = 0.9897$, $\Omega_{Nak} = 1.793$	56.50	27.59	3210.75	0.97
				Rayleigh	$\sigma_{Ray} = 0.947$	56.60	28.87	3208.87	0.97
		NLoS		Rice	$s_{Rice} = 0.103$, $\sigma_{Rice} = 0.940$	57.31	27.59	3181.96	0.98
				Nakagami	$m_{Nak} = 1.002$, $\Omega_{Nak} = 1.779$	57.40	27.59	3181.95	0.98
				Rayleigh	$\sigma_{Ray} = 0.943$	57.32	28.87	3179.95	0.98
		QLoS		Rice	$s_{Rice} = 0.079$, $\sigma_{Rice} = 0.942$	49.95	27.59	3187.35	0.98
				Nakagami	$m_{Nak} = 0.9997$, $\Omega_{Nak} = 1.781$	49.95	27.59	3187.35	0.98
				Rayleigh	$\sigma_{Ray} = 0.944$	49.95	28.87	3185.34	0.98
S7	B1	LoS	346	Rice	$s_{Rice} = 0.85$, $\sigma_{Rice} = 0.67$	10.36	27.59	535.73	0.98
				Nakagami	$m_{Nak} = 1.24$, $\Omega_{Nak} = 1.61$	5.86	27.59	530.62	0.99
				Rayleigh	$\sigma_{Ray} = 0.9$	15.45	28.87	537.85	0.98
		NLoS	390	Rice	$s_{Rice} = 0.05$, $\sigma_{Rice} = 0.95$	9.98	27.59	694.77	0.97
				Nakagami	$m_{Nak} = 1.01$, $\Omega_{Nak} = 1.79$	10.00	27.59	694.76	0.97
				Rayleigh	$\sigma_{Ray} = 0.95$	9.97	28.87	692.75	0.97
	B2	LoS	423	Rice	$s_{Rice} = 0.95$, $\sigma_{Rice} = 0.52$	43.52	27.59	542.20	0.93
				Nakagami	$m_{Nak} = 1.53$, $\Omega_{Nak} = 1.45$	30.09	27.59	530.88	0.95
				Rayleigh	$\sigma_{Ray} = 0.85$	66.58	28.87	570.39	0.88
		NLoS	442	Rice	$s_{Rice} = 0.91$, $\sigma_{Rice} = 0.58$	8.60	27.59	617.48	0.98
				Nakagami	$m_{Nak} = 1.35$, $\Omega_{Nak} = 1.49$	6.96	27.59	611.39	0.98
				Rayleigh	$\sigma_{Ray} = 0.86$	29.42	28.87	632.41	0.95

here as well. Namely, the periodic effects associated with gain variation and depolarisation due to wrist antenna rotation on a waving hand yield variation in the fading parameters, resulting in an essentially non-stationary channel. Scenario S7 is not affected in this way since the antenna is on the chest, hence remaining vertical and fairly static during user's motion.

From the Nakagami-m distribution parameters in Tables 6.5 and 6.6, one finds that the small-scale fading yields greater signal variability and deeper fades in the XP channel. This follows from the lower values for m_{Nak} and higher ones for Ω_{Nak} obtained in this case, considering the previously discussed interpretation of these parameters. This observation is reinforced by the scale parameter values obtained for other distributions, where σ_{Rice} and σ_{Ray} are also always higher in the XP channel.

As examples for visual inspection and to point out the main observations, Fig. 6.4 shows PDF fits for different scenarios and channel polarisation states. Fig. 6.4a shows the Rice PDF fit for the small-scale fading amplitude in the CP channel in scenario S6. The impact of propagation conditions on signal variability is clearly seen from the shape of the fitted PDFs. In the LoS case, the PDF is tall and narrow, thus the Rx signal is concentrated around the mean with typically small variations. On the other hand, the PDF is considerably shorter and wider in the NLoS case, meaning that the Rx signal exhibits considerably larger variations. While the PDF for QLoS is slightly narrower than for NLoS, a similar Rx signal behaviour is expected in both cases.

Fig. 6.4b shows the Nakagami-m and Rayleigh PDF fits for small-scale fading in the NLoS-XP case in scenario S7. The two PDFs completely overlap, thus confirming that the fading is Rayleigh distributed in this case. One should note that this particular case was selected for the best illustration. While the models do not perfectly overlap in other cases, the same tendency is observed.

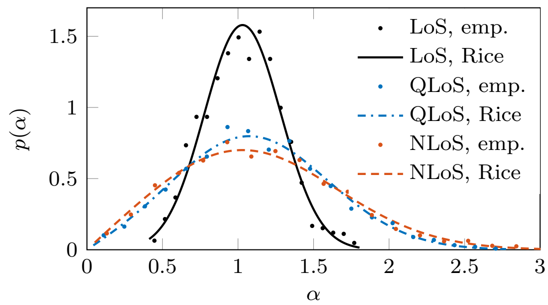

a) Scenario S6, CP channel.

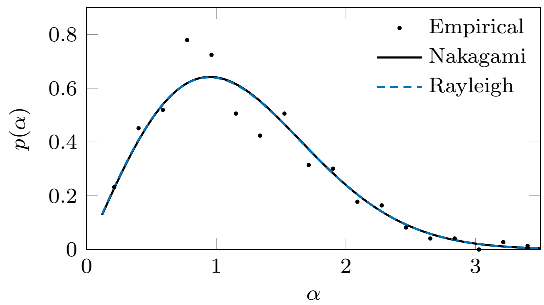

b) Scenario S7, XP channel, NLoS case.

Figure 6.4: Multipath fading PDF fit illustration (male user, B1).

In conclusion, body-shadowing has an important impact on path loss and fading characteristics. LoS obstructions by the user's body are observed to yield up to 33 dB lower average Rx power, and increased signal variation due to multipath effects. The small-scale fading distribution varies from the Rice one, when the antennas' polarisations are matched, to the Rayleigh one in the worst case, when the polarisations are orthogonal. For its flexibility, the Nakagami-m distribution is a suitable statistical model that covers all of these cases and can be used as a simple model for first-hand channel simulation. In this case, the values of m_{Nak} between 1.0 and 13.0 are suitable for the co-polarised channel, and between 0.9 and 1.5 for the cross-polarised one, while the corresponding values of Ω_{Nak} are between 1.0 and 1.8 in both cases. The lower values of m_{Nak} and the higher ones for Ω_{Nak} should be used for NLoS conditions, while the opposite should be adopted for the LoS ones.

The wearable antenna orientation due to user's posture plays an important role on channel characteristics, where the antenna placement on the wrist can result in an orthogonally polarised channel, hence, higher average path loss, as the user sits down with arms on the armrest. Moreover, the antenna rotation during user's motion introduces variation into channel parameters, which cannot be not represented by simple statistical path loss models.

One should note that the model developed in Chapter 3 takes all of these effects into account. However, for the proper consideration of body-shadowing effects, it is of key importance to use polarimetric radiation patterns of wearable antennas obtained for their operation on the body. The principal propagation condition due to body shadowing from the user is specified by choosing the appropriate user' orientation (ϕ_u), depending on the antenna placement, as in Table 6.1.

6.1.4 Polarisation characteristics

The XPD statistics obtained from measurements are summarised in Table 6.7, providing the average XPD for the scenario ($\overline{X_{pd}}$) and for each propagation condition ($\overline{X_{pd}^{LoS}}$, $\overline{X_{pd}^{NLoS}}$ and $\overline{X_{pd}^{QLoS}}$), as well as the corresponding standard deviations (σ_X, σ_X^{LoS}, σ_X^{NLoS} and σ_X^{QLoS}, respectively).

Table 6.7: XPD mean and standard deviation.

		Mean				Standard deviation			
Scenario	User	$\overline{X_{pd}}$ [dB]	$\overline{X_{pd}^{LoS}}$ [dB]	$\overline{X_{pd}^{NLoS}}$ [dB]	$\overline{X_{pd}^{QLoS}}$ [dB]	σ_X [dB]	σ_X^{LoS} [dB]	σ_X^{NLoS} [dB]	σ_X^{QLoS} [dB]
S1	B1	9.7	16.4	6.5	4.5	7.8	2.6	3.9	3.5
	B2	9.5	18.4	5.2	2.5	10.0	3.4	5.0	5.4
	NoB	14.5	20.4	12.0	9.4	8.2	5.8	1.9	5.5
S2	B1	5.4	11.7	-1.3	6.0	7.6	2.4	3.3	3.0
S3	B1	4.6	10.1	0.6	2.5	7.2	1.8	3.7	3.3
S4	B1	-2.1	-	-	-2.1	9.4	-	-	9.4
	B2	-0.8			-0.8	9.6			9.6
	NoB	-0.1			-0.1	11.5			11.5
S5	B1	1.5	3.0	-0.3	1.9	5.9	1.9	5.0	4.1
	NoB	-0.2	-2.2	0.1	2.5	7.4	2.0	4.6	6.5
S6	B1	5.4	7.7	2.2	6.3	3.3	2.6	2.8	2.1
	B2	7.0	6.0	3.4	11.7	4.1	2.3	2.4	2.3

One starts by considering the average scenario XPD, focusing on user B1 first, in order observe the differences between scenarios. XPD varies from -2.1 dB in scenario S4 up to 9.7 dB in S1, while being typically positive and thus indicating that most of the Tx power is preserved within the CP channel. The negative values are obtained in scenario S4, because of mismatched antennas' polarisations due to specific settings, described and discussed previously. Similarly, the 45° inclination in between the antenna polarisations yields XPD around 0 dB in scenario S5.

An interesting observation can be from the results for the average XPD in scenarios S3 and S6, both of which consider the same wearable antenna placement (AL_R), while the user is static in the former and (quasi-)dynamic in the latter. The higher XPD obtained in S6 shows that the channel can actually gain from user dynamics. In this scenario, the wrist antenna was periodically brought in and out of the shadow region during the mimicked walking, whereas it remained shadowed when the user is static in scenario S3. Clearly, this cannot be considered a rule and other cases could yield even opposite results, where the antennas' polarisation characteristics, namely the corresponding XPIs, have an important impact.

The XPD standard deviation in Table 6.7 gives an information about variability of channel polarisation characteristics within each scenario. The highest value for user B1 is obtained in scenario S4, i.e. 9.4 dB, which is due to the specific scenario setting in which the polarisation state of the channel changes from perfectly matched (CP) to orthogonal (XP), as the user completes the full rotation at each distance. A lower but still large XPD variation is observed in scenarios S1 - S3, where the dominant influence is shadowing from the user. Somewhat surprisingly, the XPD variation in the quasi-dynamic scenario S6 is lower than in these static ones; with the standard deviation of only 3.3 dB obtained for user B1. This can be attributed to the “softened” NLoS and QLoS conditions due to wearable antenna movement, hence resulting in a smaller difference in between XPD values in different propagation conditions.

In order to consider the influence of user’s body on the polarisation characteristics, one considers the average XPD available for the male user (B1), the female one (B2) and the absence of user (NoB) in scenario S1. The highest value is obtained for the NoB case, which can be associated with the presence of a polarisation-matched LoS component and first-order specular reflections. Between the two users, slightly higher XPD values are obtained for the male (B1) than for the female (B2). While the size of the body certainly plays a role due to the associated shadowing effects, it is difficult to draw any conclusions with confidence, since the measurements are available only for two persons representing different genders.

A strong dependence of the average XPD on the propagation condition can be observed from Table 6.7. The LoS case expectedly yields the highest XPD, with the maximum of 18.43 dB in scenario S1 (B2). The NLoS and QLoS interchangeably yield the lowest XPD values; NLoS slightly more often. This inconsistency in the order arises due to the strong dependence on the particular multipath configuration in the environment, where a constructive interaction in between specular MPCs can often yield stronger Rx signal in NLoS than in QLoS, although LoS is unobstructed in the later case. The low antenna gain for the QLoS directions in Fig. 6.1 also contributes to such a result. The XPD standard deviations for different propagation conditions in Table 6.7 are considerably lower than the overall values in each scenario (σ_X), thereby revealing that the change in body shadowing conditions is a major source of variation in channel polarisation characteristics within a scenario.

Finally, Fig. 6.5 shows the average XPD as a function of user orientation. The shape of the polygon obtained for each scenario reveals which orientation corresponds to which propagation condition; the polygon is slightly pointed to the LoS direction. Similarly, the area of the polygon somehow reflects the overall isolation between the orthogonal polarisation components.

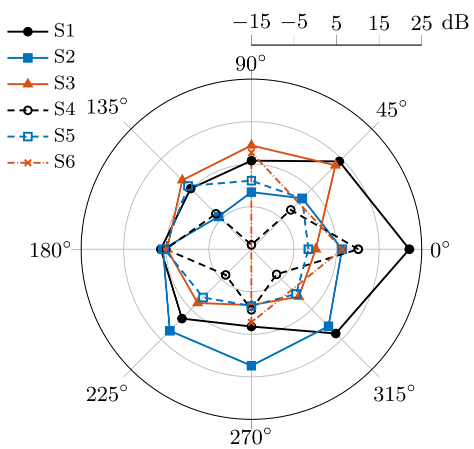

Figure 6.5: XPD as a function of user’s orientation.

While this is misleading for scenario S6, in which measurements were performed only for three orientations of the user, the best isolation between CP and XP channels is seen in scenario S1. The corresponding polygon clearly stands out by its large are, while its shape also indicates that the orientation angles 0° and ±45° correspond to the LoS case. The lowest isolation is obtained for S4 and S6, for which the polygons are the smallest in size. As repeatedly observed from different considered metrics, the energy leakage in between the polarisations in these scenarios is due to physical inclination of the antennas, with the extreme case in scenario S4. One can observe that the polygon has pointed vertices at angles 0° and 180°, for which the Tx and Rx antennas' polarisations align.

In conclusion, body-shadowing has an important effect on off-body channel's polarisation characteristics, where LoS obstructions result in a higher degree of signal depolarisation. Thereby, with the antennas' principal polarisation matched, XPD can vary from 22.1 dB in LoS to 3.2 dB in NLoS, as the user turns around in front of the off-body antenna. The dominant effect on signal depolarisation, however, comes from the wearable antenna orientation due to user's posture. With the on-body placements on wrist, the antennas' principal polarisation can become orthogonal with XPD below -14 dB, as the user sits down with arms on the armrest. As discussed in the previous section, the effects of both body-shadowing and wearable antenna rotation can be replicated by the proposed channel model, where the availability of appropriate wearable antenna radiation patters is important for realistic simulations.

6.2 Wideband channel

This section presents the analysis of data obtained from wideband channel measurements at 5.8 GHz. The data processing procedure is presented first, together with the CIR deconvolution and estimation of CIR parameters. Path loss, polarisation characteristics and the delay dispersion of the channel are analysed.

6.2.1 CIR deconvolution procedure

Due to the finite measurement bandwidth and the windowing operation performed in the VNA, the measured $s_{21}(\tau)$ corresponds to the convolution of the actual CIR and time-domain waveform associated with the window applied in the frequency domain. Thereby, one can write:

$$s_{21}(t,\tau) = \sum_{n=1}^{N_p(t)} A_n(t) e^{-j\varphi_n(t)} w(\tau - \tau_n(t)) \tag{6.4}$$

where:

- w : time-domain waveform corresponding to the frequency-domain windowing function.

One should note that the actual pulse waveform $w(t)$ does not directly correspond to the window function, but is also affected by the antennas' frequency characteristics, which inevitably act as pulse-shaping filters when the channel bandwidth is large. Moreover, (6.4) assumes that all propagation paths have the same effect on the pulse, neglecting path-specific non-linear distortions, due to MPCs' interactions with frequency selective materials.

While the effects associated with propagation through walls can be mostly neglected due to low Tx power, the MPCs interacting with user's body certainly had more effect on the measurement data in the considered setting. However, these effects are ignored and a common pulse waveform is assumed for all paths, considering it is the cumulative result of all frequency selective effects in the system. This is a reasonable assumption, since it is somewhat impossible to de-embed the wearable antennas from the channel, due to random and time-varying effects of the user's body. A Gaussian pulse waveform with the width defined for 25% of the maximum amplitude is adopted herein, i.e.

$$w(t) = e^{-4\ln 4 \frac{t^2}{T_w^2}} \tag{6.5}$$

where:

- T_w : pulse width (i.e. 3.9 ns, Table 5.3).

The CIR deconvolution was performed according to a modification of the procedure described in [163], with the path estimation performed simultaneously in two polarisations to ensure consistency. That is, since the propagation paths depend only on the antennas' positions, the MPCs observed in the orthogonal Rx polarisations should appear at the same delays, however, with different amplitudes, depending on the polarisation upon arrival. Therefore, by considering the delays at which CIRs are sampled as potential arrival times, the MPCs are estimated by solving the following optimisation problem:

$$\begin{aligned}\underset{A_1^{V/H}\dots A_{N_\tau}^{V/H}}{\arg\min} \Bigg\{ & \left(\sum_{n=1}^{N_\tau} A_n^V w(\tau-\tau_n) - \left|s_{21}^V(\tau)\right|\right)^2 \\ & + \left(\sum_{n=1}^{N_\tau} A_n^H w(\tau-\tau_n) - \left|s_{21}^H(\tau)\right|\right)^2 \\ & + \beta_r \sum_{n=1}^{N_\tau} \left|A_n^V + A_n^H\right| \quad \Bigg\}\end{aligned} \tag{6.6}$$

where:

- N_τ : number of considered delays (i.e. 401, Table 5.3);
- τ_n : n-th component's delay, i.e.

$$\tau_n = (n-1)\Delta\tau \tag{6.7}$$

  $\Delta\tau$ being the delay resolution (i.e. 0.25 ns, Table 5.3);
- $A_n^{V/H}$: n-th component's amplitude in the V-/H-polarisations;
- β_r : weight of the regularising term.

The last term in the objective function of (6.6) ensures that the insignificant MPCs' amplitudes are forced to zero in the output. In this way, only a few significant ones likely corresponding to the actual physical paths are preserved in the obtained solution. This regularising term effectively solves the problem of over-fitting, inevitable when the basis set of fitting functions, i.e. number of considered delayed pulses (N_τ), is greater than the number of actual propagation paths (N_p) in CIR. By comparing the solutions for several values as suggested in [163], a suitable value for the associated weight (β_r) is found to be 0.45.

Due to the regularising term, the actual amplitudes of the MPCs obtained from (6.6) have to be re-estimated, which is done by solving a standard Least Squares optimization problem for those paths, separately in two polarisations, i.e.

$$\underset{A_1^{V/H}\dots A_{\hat{N}_\tau}^{V/H}}{\arg\min} \left(\sum_{n=1}^{\hat{N}_\tau} A_n^{V/H} w(\tau - \tau_n) - \left| s_{21}^{V/H}(\tau) \right| \right)^2 \tag{6.8}$$

where:

- $\hat{N}_\tau$: number of significant paths obtained from (6.6).

One should note that both (6.6) and (6.8) were solved by using CVX [164], i.e. a MATLAB toolbox for convex optimisation, developed at Stanford.

Finally, the MPCs whose amplitudes are below the processing threshold are discarded, in order to ensure that the estimated paths are not falsely detected noise artefacts [124]. The adopted threshold of -98 dB is chosen so the instantaneous noise is always below this value in the system loss output. An example of the CIR deconvolution procedure is shown in Fig. 6.6a, while the CIR normalised to unit power is shown in Fig. 6.6b. The introduced error is negligible, where the lines corresponding to the measured (solid) and reconstructed CIRs (dashed) are observed to practically overlap.

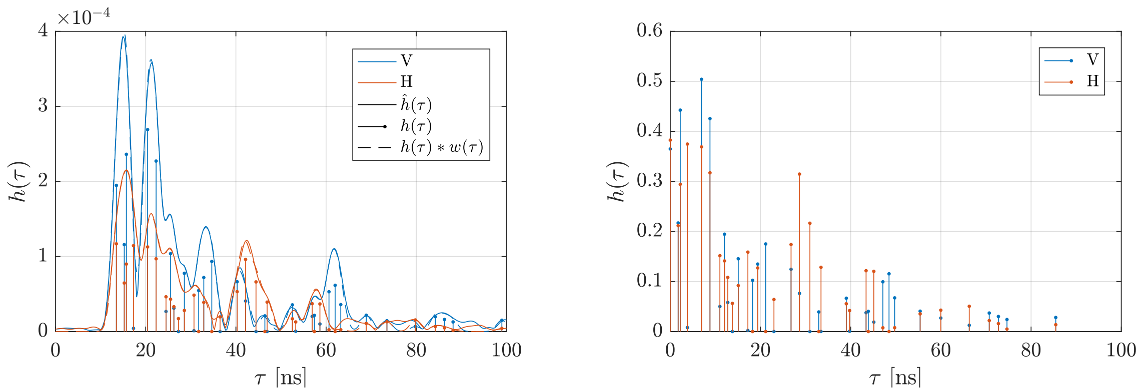

a) Measured, deconvolved and reconstructed CIRs.

b) CIR normalised to unit power.

Figure 6.6: An example of CIR deconvolution and normalisation.

6.2.2 Estimation of CIR parameters

In order to analyse the channel depolarisation and delay spread characteristics, the Rx power, XPD, mean excess delay and standard deviation were calculated based on the estimated MPCs' delays and amplitudes [124, Ch. 4]. These metrics were obtained for each channel snapshot, in both V- and H-polarisations. With five independent measurements being available in each considered case, the average values over the repeated measurement sets were also calculated.

In each polarisation, the Rx power was obtained according to:

$$P_{r\,[\mathrm{dBm}]} = P_{t\,[\mathrm{dBm}]} + 10 \log \left| \sum_{n=1}^{\hat{N}_\tau} A_n^2 \right| \tag{6.9}$$

The instantaneous XPD was then calculated as:

$$\mathrm{X}_{pd\,[\mathrm{dB}]} = P^V_{r\,[\mathrm{dBm}]} - P^H_{r\,[\mathrm{dBm}]} \tag{6.10}$$

The mean excess delay and the standard deviation were obtained as:

$$\overline{\tau} = \frac{\sum_{n=1}^{\hat{N}_\tau} \tau_n A_n^2}{\sum_{n=1}^{\hat{N}_\tau} A_n^2} \tag{6.11}$$

$$\sigma_\tau = \sqrt{\frac{\sum_{n=1}^{\hat{N}_\tau} (\tau_n - \overline{\tau})^2 A_n^2}{\sum_{n=1}^{\hat{N}_\tau} A_n^2}} \tag{6.12}$$

One should note that (6.11) and (6.12) were calculated after the first path delay was subtracted from all components, thus, the dependence on distance was removed. As an example, Fig. 6.7 shows the calculated metrics for the user approaching case, with the antenna on LL_L. Faded lines in the figure correspond to individual measurement repetitions, while the thick ones are obtained as their average.

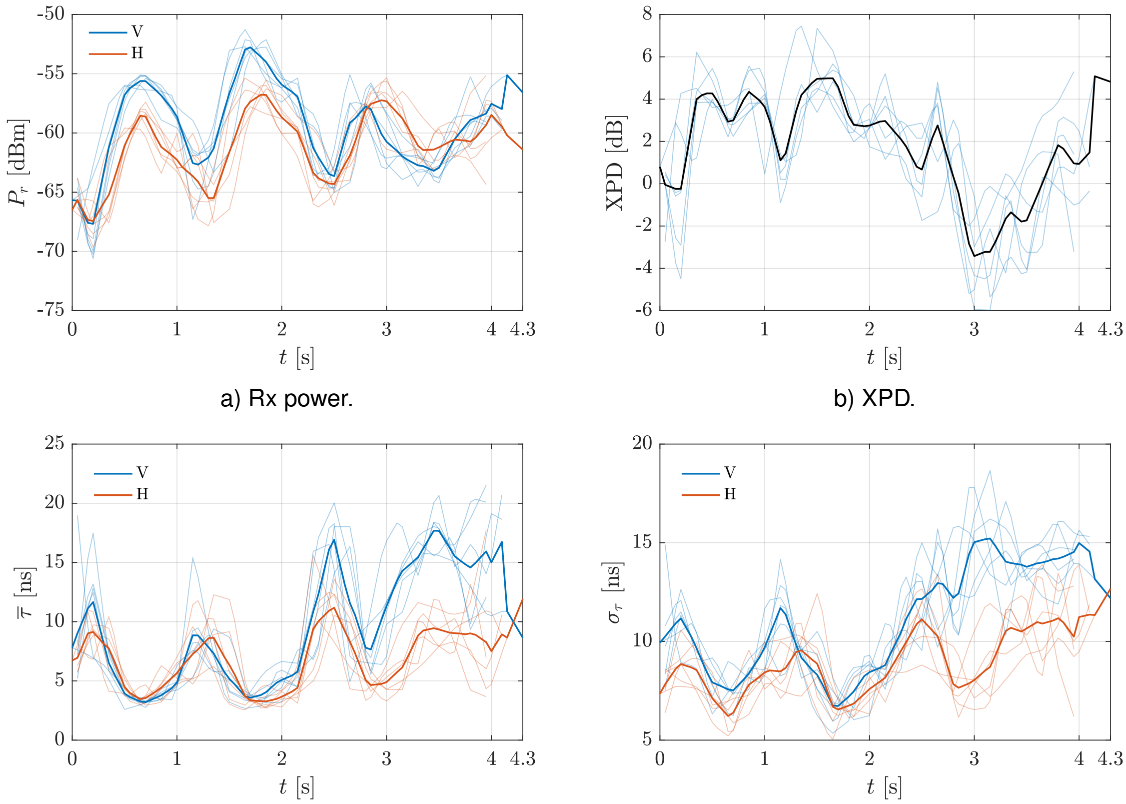

a) Rx power.

b) XPD.

c) Average delay.

d) Delay spread (standard deviation).

Figure 6.7: Instantaneous values of CIR parameters, for the LL_L antenna in the user approaching case.

6.2.3 Path loss and polarisation characteristics

Starting with the path loss and channel polarisation characteristics analysis, Fig. 6.8 shows the Rx power in orthogonal polarisations and the corresponding XPD, obtained for the user approaching and departing cases. The curves in the figure were obtained by averaging over repeated measurements, as previously illustrated in Fig. 6.7, for the LL_L antenna and user approaching. Table 6.8 summarises the global statistics of the Rx power and XPD, obtained by averaging over all channel snapshots captured for a given case, minimum value (min), variation range (Δ), mean (μ) and standard deviation (σ) being calculated according to (4.4) - (4.8), by jointly considering all repeated measurements.

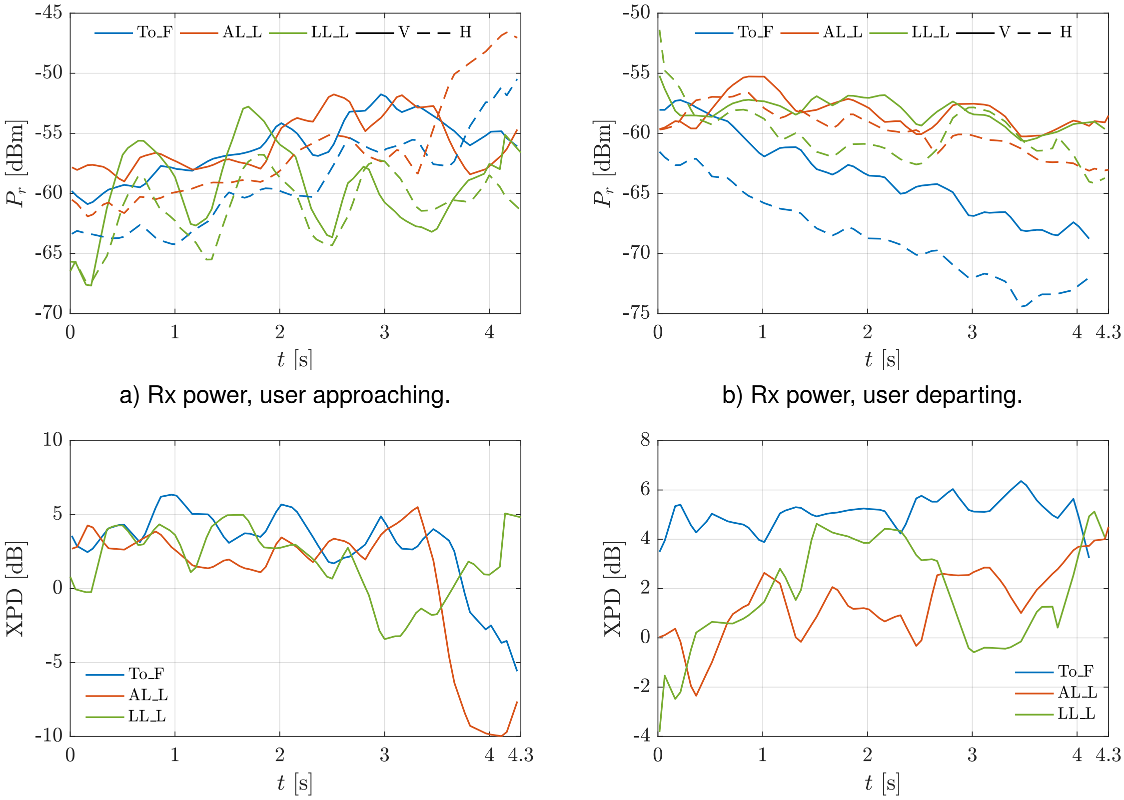

a) Rx power, user approaching.

b) Rx power, user departing.

c) XPD, user approaching.

d) XPD, user departing.

Figure 6.8: Rx power and XPD for user approaching and departing, averaged over repeated measurements.

In the user approaching case, the Rx power varies within a similar range for all three wearable antenna placements, where fairly similar average values are observed in Table 6.8. On the other hand, the dynamics of variations are different, depending on the wearable antenna on-body placement. A steady linear trend with distance is observed for the To_F antenna in Fig. 6.8a, with only small deviations as the user approaches the off-body AP. The other two placements are characterised by dynamic and clearly periodic power variations, which can be associated with changes in user's posture during motion, as they were found to match those in the first path's delay. They are most likely the result of gain variation and depolarisation effects due to wearable antenna rotation during user's motion. The most dynamic case is observed for the LL_L antenna, where the Rx power varies up to 20.1 dB in the V-polarisation.

It is interesting to observe that power variations in the orthogonal polarisations, i.e. V and H, are somewhat synchronised. This translates to considerably slower variations in the corresponding XPD shown in Fig. 6.8c, where one hardly recognises any periodic patterns. As one observes in the figure, the XPD is similar and quite constant at around 2 -3 dB for all three antenna placements, deviating from this value only as the user approaches close to the AP. This XPD value corresponds to the case when the Rx field is inclined at 45° with respect to the V-/H-polarisation, which is likely the case with the LoS component. However, the wearable antenna's polarimetric gain pattern was not available for further inspection at the time of the analysis.

The sudden decrease in the XPD observed when the user gets in the immediate vicinity of the AP is explained by the radiation characteristics of the dipole antennas used at the off-body side. That is,

Table 6.8: CIR parameters global statistics.

		Approaching						Departing					
Ant.		To_F		AL_L		LL_L		To_F		AL_L		LL_L	
AP		V	H	V	H	V	H	V	H	V	H	V	H
P_r [dBm]	min	-66.1	-70.2	-65.0	-68.2	-75.3	-73.9	-74.9	-80.6	-67.3	-69.9	-66.7	-71.1
	Δ	11.6	17.2	10.4	19.9	20.1	14.9	16.3	16.8	11.3	12.7	10.0	15.7
	μ	-60.2	-63.2	-59.8	-60.7	-63.6	-65.2	-67.5	-72.5	-62.4	-63.8	-62.2	-64.0
	σ	2.8	4.2	2.7	4.5	4.1	3.4	3.7	4.0	2.2	2.6	1.7	3.0
XPD [dB]	min	-6.7		-12.8		-6.0		1.1		-4.8		-9.5	
	Δ	15.3		21.3		13.7		7.1		12.0		18.8	
	μ	3.0		0.8		1.6		5.0		1.5		1.8	
	σ	3.2		4.9		3.0		1.7		2.3		2.9	
$\overline{\tau}$ [ns]	min	11.3	1.9	3.0	1.4	2.6	2.5	15.7	14.3	4.0	3.0	3.2	1.9
	Δ	11.9	18.5	16.1	10.8	20.2	15.3	16.4	15.0	20.5	13.1	20.3	13.4
	μ	15.7	13.0	8.8	5.6	9.6	6.8	23.1	21.1	11.8	7.2	8.2	9.0
	σ	2.8	4.1	3.4	2.3	5.7	3.2	3.2	3.0	5.1	2.5	4.0	2.8
σ_τ [ns]	min	6.9	3.8	6.4	2.4	5.3	4.9	8.3	7.3	6.0	5.4	5.7	3.3
	Δ	12.5	9.0	11.2	9.0	13.4	9.4	10.0	8.1	10.9	8.8	10.6	9.2
	μ	11.4	8.3	10.3	7.2	11.0	8.9	12.8	11.0	11.2	8.5	9.5	7.2
	σ	2.7	2.2	2.4	1.8	3.1	2.1	1.7	1.5	2.2	1.7	1.8	2.0

the low wearable antenna elevation relative to the AP (Table 5.2) yields a low corresponding gain of the vertical dipole in the LoS direction at these distances (<1 m), while the maximum gain applies for the horizontal one. This is confirmed by the fading power in the V-polarisation as the user approaches the AP at the end of the path (Fig. 6.8a). This trend is not observed for the LL_L antenna, because the LoS gets partially obstructed by the user in this case.

In the user departing case, one observes a greater difference in the power levels obtained for different wearable antenna placements. As follows from Table 5.2, the To_F antenna receives a considerably lower power compared to the other two antennas in this case, but also compared to the same antenna in the user approaching case. For reference, the Rx power obtained with the To_F antenna is on average 7.3 dB and 9.3 dB lower in the user approaching compared to the departing case, considering the V- and H-polarised off-body antennas, respectively. This is explained by the strong shadowing from the user's torso in this case. On the other hand, the similar average power obtained for the AL_L and LL_L antennas in the departing and approaching cases serve as an evidence of mostly unobstructed LoS.

It is also interesting to observe the consistent linear decrease in Rx power with distance, obtained for the To_F antenna with the user departing. One should note that the instantaneous Rx power variation around this trend in each repeated measurement is within 2 dB. This reveals that the effects of interactions between MPCs are significantly reduced compared to the narrowband channel in Section 6.1, due to the large bandwidth in this case. Similar observation is made for other cases in Fig. 6.8b as well, hence, the periodic effects associated with the wearable antenna rotation during motion have a dominant influence on Rx power variation. These effects are "mid-scale", occurring on the time scale in between the traditionally defined large- and small-scale effects. It is also interesting that the Rx power in

V- and H-polarisations traces almost parallel lines over time for the To_F antenna in the user departing case, which yields an almost constant XPD of 5.0 dB, with only 1.7 dB standard deviation.

In conclusion, the periodic effects associated with changes in the user's posture present themselves as dominant ones, with an important influence of the wearable antenna placement on the dynamics of imposed variations in the communications channel characteristics. The depolarisation effect can vary greatly over the scenario, with XPD varying up to 23.5 dB when the antenna is placed on the wrist. Again, body-shadowing has an important impact on channel characteristics, with the depolarisation effect being more emphasised in LoS conditions. Moreover, the antenna radiation characteristics have an important influence, which is due to the dominant effects coming from the LoS component.

Finally, one should note that the observed periodic effects associated with changes in the user's posture are naturally represented by the wearable antenna mobility model within the channel model developed in Chapter 3. For a realistic replication of the observed Rx signal variations, in addition to the specification of general geometrical relations between the user and the off-body AP, it is important to use the appropriate wearable antenna radiation characteristics.

6.2.4 Delay dispersion characteristics

Fig. 6.9 presents the mean excess delay and standard deviation (delay spread) estimated from CIRs in the two Rx polarisations, where the average over repeated measurements is depicted as in the previous section. The corresponding global statistics are also summarised in Table 6.8. One should note that the mean delay was calculated after subtracting the first path delay from all components in CIR, thereby removing the dependence on distance.

Several important observations can be made from the results, as follows. The mean excess delay is observed to exhibit periodic variations for the AL_L and LL_L antennas, for both user approaching and departing. These variations match those in Rx power (Figs. 6.8a and 6.8b); the maxima in the mean delay occur at minima of the Rx power. In addition, delay spread variations are also found to be periodic and synchronised with those in the mean delay, where both parameters increase and decrease simultaneously. These observations point to the likely cause being the time-variant amplitude of the LoS component, due to polarisation mismatch losses or variable wearable antenna gain in the respective direction.

One should observe that the mean excess delay obtained for the AL_L and LL_L antennas is generally low and with similar average values in the approaching and departing cases, i.e. in between 5.6 ns and 11.8 ns (Table 6.8). This further reinforces the conclusion that LoS is unobstructed for these two antennas in both cases. The mean delay obtained for the To_F antenna is higher, the global average being above 13.0 ns and 21.1 ns in the approaching and departing cases, respectively. While the higher average obtained for the user departing is expected due to strong shadowing by the torso, the one for the user approaching comes as a surprise.

Further inspection of the time evolution of the CIR obtained for this antenna reveals an MPC with delays 15 - 20 ms, which is dominant over the first path/cluster for most of the time. Since this MPC is not observed with the AL_L and LL_L antennas in the approaching case, it likely corresponds to the

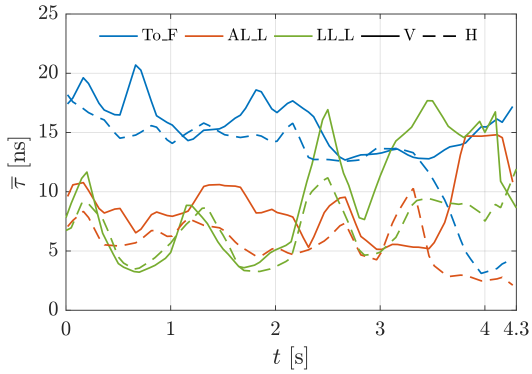

a) Mean delay, user approaching.

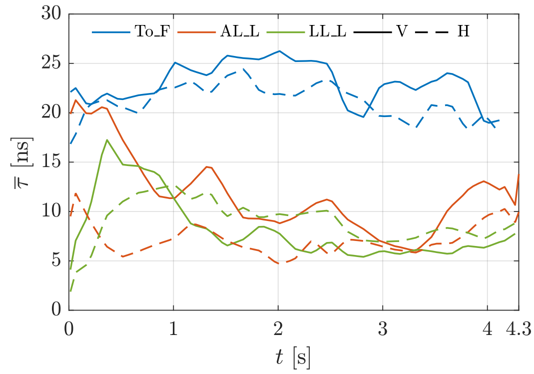

b) Mean delay, user departing.

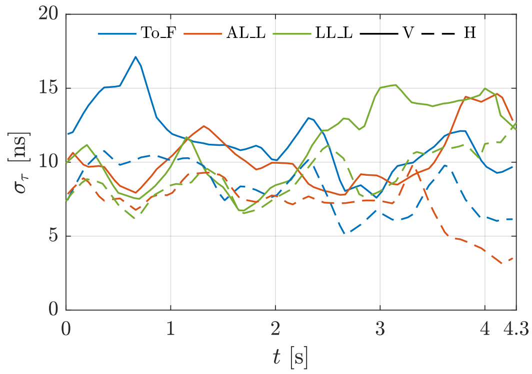

c) Delay spread, user approaching.

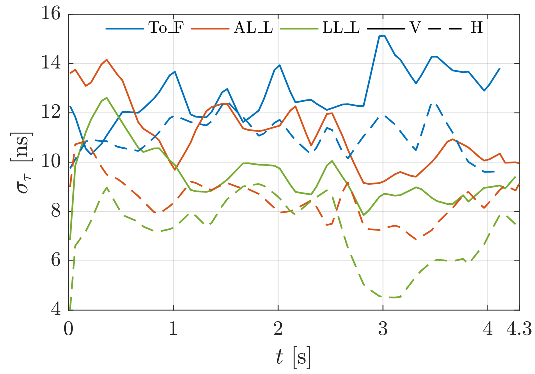

d) Delay spread, user departing.

Figure 6.9: Mean delay and standard deviation for user approaching and departing, averaged over repeated measurements.

specular reflection from the wall on the user's right side, for which the two antennas are shadowed by the user's body. One should note that this side of the room is with windows and metallic heating elements (Fig. 5.2a), which could produce strong MPCs. Moreover, the first path/cluster in the CIR obtained with the To_F antenna is considerably attenuated compared to the other two antennas. This suggests that the LoS direction in the case of the To_F antenna, although unobstructed, falls in an unfavourable radiation direction of the wearable antenna. However, further investigation would require inspection of its radiation pattern.

One should also observe that the general delay spread of the channel is fairly low on average, thus energy is concentrated around the delay of the dominant component. As one reads from Table 6.8, the average delay spread is at most 11.2 ns, i.e. for the To_F antenna and the user approaching. This concentration of energy in the delay-domain further strengthens the impact of signal depolarisation and gain variation associated with the dominant propagation paths.

The most important conclusion following from these results is that all considered CIR parameters vary greatly over time, emphasising the non-stationary character of the off-body channel. The inspection reveals regular periodicity of these variations, which can be associated with the periodic changes of the user's posture during motion and explained by the user-imposed effect (Section 3.3). This underlines the importance of taking the depolarisation effect and the influence of user's motion into account when developing a channel model.

6.3 Model comparison against measurements

Following the measurement-based off-body channel characterisation, the available data are used to validate the channel model developed in Chapter 3. For this purpose, several selected scenarios were replicated using the simulator described in Chapter 4. Thereby, the narrowband measurements scenario S6 and the user approaching case from the wideband measurements on the one hand, and narrowband scenarios S1 and S6 on the other hand, were considered in order to test the model's ability to replicate temporal dynamics and polarisation characteristics of the off-body channel with a dynamic user.

The free space wearable antenna radiation pattern in Fig. 5.7 was used for the simulation of scenarios from narrowband channel measurements, where a shadowing pattern was additionally associated with the antenna to take the body-shadowing from the user into account. This pattern applies an additional loss to MPCs, according to their AAoDs in the local coordinate system, where a simple model similar to the one in [165] is adopted, i.e.

$$L_{sh}(\phi_t)_{[\mathrm{dB}]} = L^{max}_{sh\,[\mathrm{dB}]}\,\frac{1}{2}\left\{1+\cos\left[2(\phi_t-\pi)\right]\right\} \tag{6.13}$$

where:

- L^{max}_{sh} : maximum body-shadowing loss.

The maximum body-shadowing loss of 10 dB is considered for the AL_L and LL_L antennas, while 20 dB is adopted for the To_F one[1]. Moreover, in addition to the LoS component, four scatterers were considered, with the corresponding cylinder radii, azimuth angles and heights being chosen to match the general directions of the specular reflections from the floor, ceiling and side walls.

Fig. 6.10 shows the Rx power obtained from the model (mod.) together with measurements (meas.) in the narrowband scenario S6. It shows a period of 10 s for the case with the user at a distance of 4 m, facing sideways towards the AP, i.e. $\phi_u = 90°$ (Fig. 5.3). The wearable antenna mobility model parameters were modified to match the initial user's posture and motion cycle period, which was found to be 1.1 times longer in the measurement data than the default value in the model, i.e. 1.142 s (Section 3.4.4).

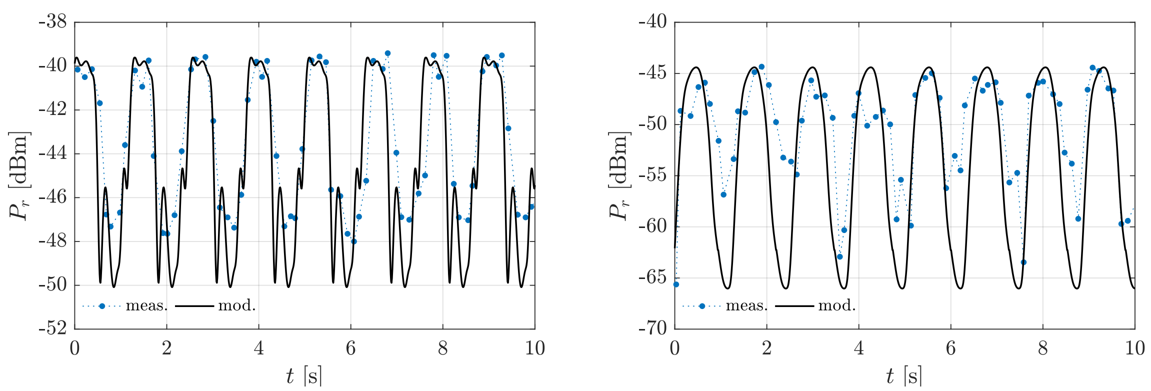

a) V-polarised off-body Rx antenna. b) H-polarised off-body Rx antenna.

Figure 6.10: Replication of the narrowband measurements scenario S6 ($d_u = 4$ m, $\phi_u = 90°$).

[1]This choice was made intuitively, while a detailed investigation would be required for a more justified one.

A very good match between model and measurements is observed in Fig. 6.10, where the periodic Rx power variation is well-represented. This observation is further supported by the calculated RMSE, where 2.2 dB is obtained for the V-polarisation (Fig. 6.10a) and 6.1 dB for the H-polarisation (Fig. 6.10b). One should note that the chosen subset of data is selected for illustration because of its very good alignment, while the error is higher for some of the user's distances and orientations. However, the general trend is matched in all cases.

The observed differences between simulations and measurements follow from several factors. First, the wearable antenna radiation pattern used for simulation was measured in an anechoic chamber, therefore, the effects of body-proximity on its radiation characteristics are not taken into account. Second, due to the intrinsic randomness of human motion, it is practically impossible to perfectly align the simulation results with measurement data. Therefore, a slow variation in the motion cycle period of the user during measurements yields an inevitable error. Finally, the propagation environment is under-represented in the channel model, and the considered MPCs' phases and amplitudes are not exactly matched to reality. However, this is inevitable with any channel model, as simplifications are necessary to make the model useful in practical applications.

Fig. 6.11 shows the results obtained for the wideband measurements scenario with the approaching user (Table 5.2), where the Rx power averaged over repeated measurements is shown for comparison (extracted from Fig. 6.8a). One should note that only the LoS component is considered in this case, as it was observed to dominate the channel. Moreover, the actual radiation pattern of the wearable antenna was not available in this case, whereas the one used for narrowband measurements did not give satisfying results. A patch antenna available from Antenna Toolbox in MATLAB [140] was found to be a better approximation, and was used for simulation in this case[2].

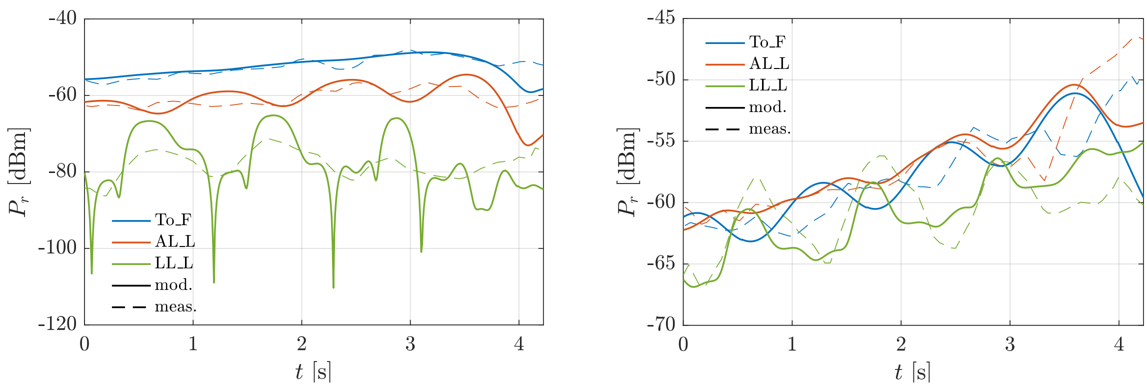

a) V-polarised off-body Rx antenna.

b) H-polarised off-body Rx antenna.

Figure 6.11: Replication of the wideband measurements scenario with the approaching user.

As one observes from Fig. 6.11, the general dynamics of the Rx power variation are well matched by the simulator, where the RMSEs obtained for the To_F, AL_L and LL_L antennas in the V-polarisation are 2.1 dB, 3.4 dB and 6.4 dB, respectively, while being 2.8 dB, 2.4 dB and 2.3 dB in the H-polarisation. However, fixed offsets were introduced beforehand, to match the average Rx power levels[3]. These

[2]This antenna was also used for simulations in Chapter 7, and its radiation pattern is given in Fig. 7.2.

[3]The offsets were actually added to the measured Rx power, as this yields less overlap between curves in the figure. The

differences can be attributed to the inadequate radiation pattern used for simulation, where a misrepresentation of the polarisation characteristics has an important effect. For example, notches observed in the simulated Rx power for the LL_L antenna are associated with polarisation mismatch losses, while they are not present in the measurement data.

For comparison, Fig. 6.12 shows the results obtained with a non-polarised propagation model, as presented in [166]. The RMSEs for the To_F, AL_L and LL_L antennas in this case are 2.0 dB, 1.9 dB and 3.6 dB in the V-polarisation, respectively, while the corresponding values in the H-polarisation are 2.7 dB, 2.9 dB and 2.1 dB. With the lower error being observed, these results imply that the radiation characteristics of the antenna used for measurements are such that the LoS gain in the θ- and ϕ-polarisations varies synchronously, yielding a fairly stable polarisation mismatch during the scenario. This also explains the parallel variation of the Rx power levels in the V- and H-polarisations, previously observed in Fig. 6.8a.

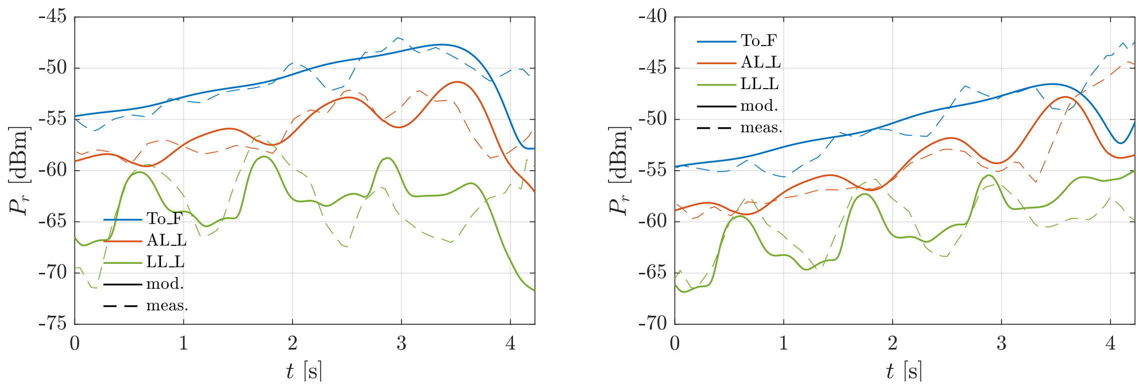

a) V-polarised off-body Rx antenna.

b) H-polarised off-body Rx antenna.

Figure 6.12: Replication of the wideband measurements scenario with the approaching user, using a non-polarised propagation model.

Fig. 6.13 shows the average XPD for different user's orientations in replicated narrowband measurements scenarios S1 and S6. The lines corresponding to the XPD obtained from measurements (dashed) are extracted from Fig. 6.5. As one observes, the simulator recreates general trends of XPD with user's orientation. An RMSE of 8.6 dB is obtained for the static scenario S1, where the difference between model and measurements is the highest for the user facing away from the AP, i.e. $\phi_u = 180°$. If this direction is excluded from calculation, the RMSE is reduced to 7.1 dB.

The observed deviations in this case are somehow expected, because of the change in the antenna's polarisation characteristics when placed on the body, which is not represented in the free space radiation pattern used for simulation. Another important factor, not to be overlooked, is a possible rotation of the wearable antenna during the placement on the body, resulting in a changed ratio of the powers radiated in the V- and H- polarisations.

In the quasi-dynamic scenario S6, RMSE is found to be 7.1 dB, where the largest difference (i.e. 12.3 dB) is observed for the user facing towards the AP, while being below 0.5 dB for other orientations.

offsets introduced for the To_F, AL_L and LL_L antennas in the V-polarisation are 7.7 dB, -0.9 dB and -14.6 dB respectively, while 5.5 dB, 4.1 dB and 4.6 dB were added in the H-polarisation.

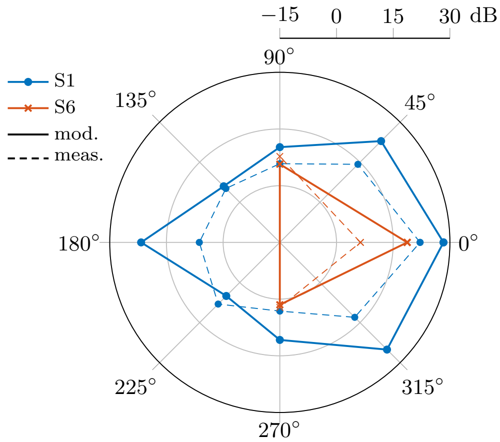

Figure 6.13: Replication of the XPD characteristics in the narrowband scenarios S1 and S6.

Therefore, in this case there is no large deviation of the model from the measurements for the user's orientation associated with the strongest shadowing, i.e. $\phi_u = 270°$. This might be because of the dominant influence of the AL_R antenna rotation during mimicked walk, where XPD is averaged out over time.

Finally, one concludes that the developed model captures the principal characteristics of the off-body channel with dynamic users. If the appropriate input parameters are provided, it can be used to replicate the polarisation characteristics and dynamics signal variations due to user's motion. Further validation of the model should be performed, with the use of adequate antenna radiation characteristics.

Chapter 7

Model-based channel analysis

This chapter presents the simulation-based analysis of the off-body characteristics, considering three scenarios with the dynamic user. The influence of the user dynamics on the channel is investigated considering the wearable antenna placements on the chest, wrist and lower leg, and the user walking and running motion. Following the results discussion, the signal depolarisation mechanisms are identified and analysed in a more detail, considering both those associated with the user's motion as scattering in the environment.

7.1 Scenario description

In order to analyse the depolarisation effect and the influence of user dynamics on the channel, three specific scenarios are simulated, with the illustration given in Fig. 7.1a. Each scenario is repeated for the wearable antenna placements on the chest (To_F), wrist (AL_L) and lower leg (LL_L), as shown in Fig. 7.1b, and for the user walking and running. In addition to the dynamic user case, a static standing user is also considered for reference. In all cases, the off-body Rx antenna is an ideal vertical dipole, placed at a fixed position and a height of 1.4 m. The operating frequency is 2.45 GHz, and the Tx power is 100 mW.

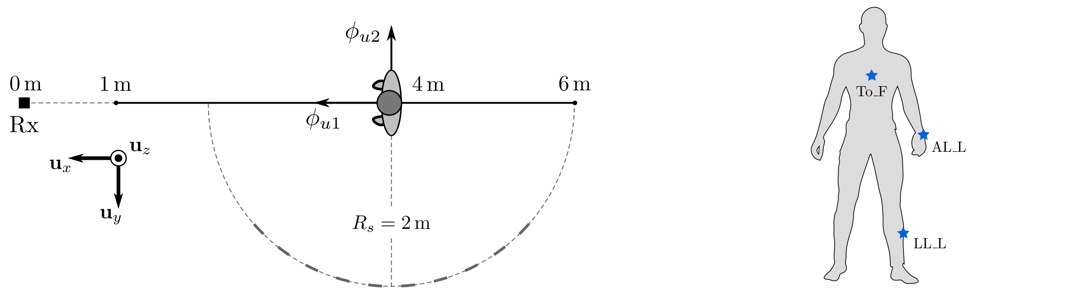

a) Illustration of scenarios. b) Wearable antenna placements.

Figure 7.1: Considered scenarios and wearable antenna placements.

The on-body Tx antenna is a patch, with the maximum total gain of 6.74 dBi and the radiation patterns for θ- and ϕ-polarisations shown in Fig. 7.2; the azimuth and elevation angles in Fig. 7.2 are defined with respect to the local coordinate system of the antenna. Its design is available as one of the examples in the MATLAB Antenna toolbox [140]. The dimensions of the patch and ground plane are 75×37mm^2 and 150×75mm^2, respectively, with the used dielectric substrate parameters $\epsilon_r = 2.7$, $\delta = 0.002$ and $h = 0.8$ mm (thickness). While the antenna was not designed for BAN applications and the gain pattern in Fig. 7.2 is obtained for free-space, it is found suitable for the work presented here.

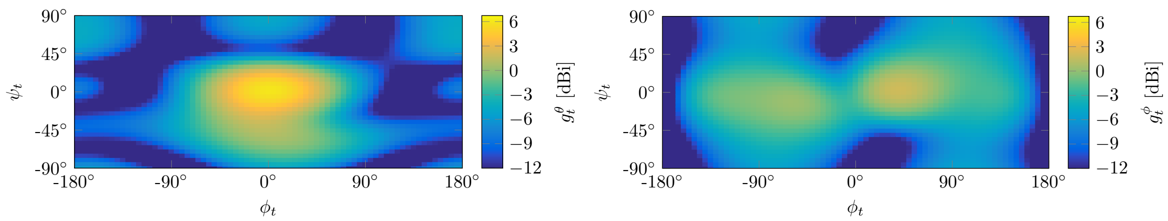

a) θ-polarisation component. b) ϕ-polarisation component.

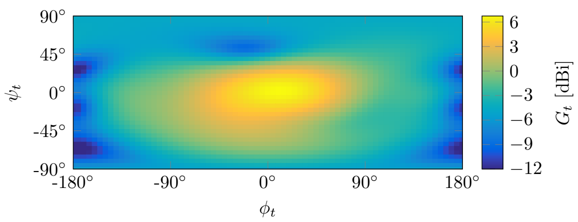

c) Total gain.

Figure 7.2: Generalised gain of the on-body patch antenna.

In Scenario 1, chosen to isolate the influence of user dynamics on the depolarisation effect, the user is at a 4 m distance from the off-body antenna, walking and running in place as on a treadmill. Only the periodic motion component, corresponding to changes in the posture, is considered, the forward motion of the user being taken out. The orientation of the user is chosen depending on the on-body antenna placement, such that the antenna is facing towards the off-body one. That is to say, with respect to Fig. 7.1a, the user is facing in direction ϕ_{u1} for the To_F antenna case, and ϕ_{u2} for the AL_L and LL_L ones. This choice results in the wearable antenna rotation being primarily about the LoS direction in each case, hence, the depolarisation effect is emphasised. Free space propagation is considered in order to isolate the effect of user dynamics, while one should note that all MPCs are affected similarly, regardless of the involved propagation mechanism (see Section 7.3.1).

Following the analysis for the LoS component, Scenario 2 considers the depolarisation of scattered MPCs. The user is at the same distance as in the previous scenario, facing the off-body antenna in all cases (i.e. ϕ_{u1}, Fig. 7.1a). In an approach similar to the one in [141], MPCs are assumed to arrive at the Rx after bouncing from scatterers distributed on a cylinder centred around the user, with a 2 m radius. Scatterers are assumed to be concrete/glass surfaces ($\epsilon_r = 4.11$), several wavelengths in size, oriented so the Snell's law is satisfied [124]. Their positions are specified by randomly generated heights and azimuth angles, the former being uniformly distributed over [0, 2.5] m, and the latter following the Von Mises distribution with the mean (μ_{vm}) of 90° and the spread parameter (κ_{vm}) being 5. These parameters yield scatterers distributed on the user's left, i.e. over the area indicated by the dashed line in Fig. 7.1a. Therefore, the scatterers are in the forward radiation direction of the AL_L and LL_L antennas, the DoDs of the corresponding MPCs being in the same region as that of the LoS component in Scenario 1. One should note that scatterers' positions are generated once and kept fixed during simulation.

Scenario 3 considers the user walking and running towards the off-body antenna over a straight line, starting at 6 m distance and stopping at 1 m. As in Scenario 1, only the LoS component is considered for simplicity, and to keep the focus on the depolarisation effect due to user's motion. The simulation was performed for the polarised channel model and a non-polarised one, in order to evaluate the importance of taking the polarisation aspect of the channel into account. Moreover, the simulation was repeated for the antenna motion obtained from the skeleton-based model with MoCap data (Section 3.4.2), and for the case when only the linear forward motion of the user is considered. In the latter, the periodic component in (3.56) is replaced by a fixed vector of coordinate averages for the walking motion, i.e. the corresponding values of a_0 in Table 3.1. The ideal vertical alignment of the antennas is considered in this case (i.e. $\mathbf{u}_z^a = \mathbf{u}_z$), while the facing direction depends on the antenna placement, taking $\mathbf{u}_x^a = \mathbf{u}_x$ for To_F and $\mathbf{u}_x^a = \mathbf{u}_y$ for AL_L and LL_L antennas (Fig. 7.1a).

7.2 Results analysis

The results obtained in Scenario 1 are given in Figs. 7.3 - 7.6, and Table 7.1. The figures show the Rx power, PLF [55], on-body antenna total gain and XPI during the motion period (T), while the table summarises the corresponding minimum values (min), ranges of variation (Δ), means (μ) and standard deviations (σ), i.e. calculated according to (4.4) - (4.8). The influence of the antenna motion dynamics on the Rx power is apparent from Fig. 7.3. While Rx power remains approximately constant for the To_F antenna, regardless of user's motion, variations up to 37.5 dB are obtained for the AL_L antenna and the user running case. Expectedly, variations are generally more severe for running than walking.

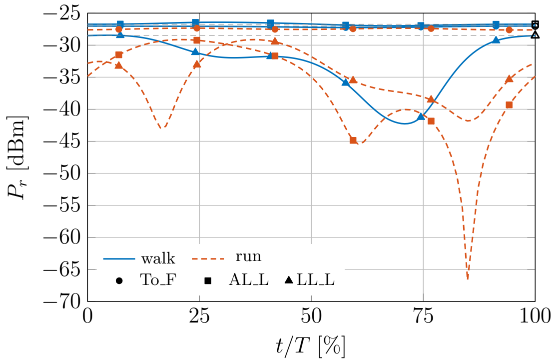

Figure 7.3: LoS component Rx power in Scenario 1.

In order to identify the exact mechanisms responsible for the observed Rx power variations, it is useful to analyse the LoS direction trajectories in the on-body Tx antenna spherical coordinates shown in Fig. 7.4.

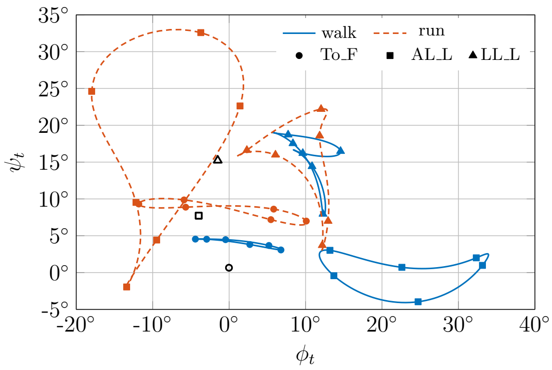

Figure 7.4: LoS direction of departure in Scenario 1.

It is convenient first to consider the static user case, for which DoDs are fixed points, indicated by empty markers in Fig. 7.4. The positions of these points in the figure can be directly explained by the corresponding antenna placements. The azimuth angle indicates the horizontal distance in between the wearable antenna and a plane containing the off-body one and the vertical axis of the user. Thereby, the 0° azimuth obtained for To_F expectedly implies the antenna is on this plane, while the deviations of the angles obtained for AL_L and LL_L reflect the fact that the arms of a standing user are further away from the vertical body axis than the legs are. In a similar way, the elevation angles relate to the antennas' heights. Therefore, the low value (<1°) obtained for the To_F antenna implies its height is similar to that of the off-body antenna, i.e. the difference being approximately 5 cm, while higher values obtained for AL_L and LL_L antennas relate to their lower heights, the difference in this case being 53 cm and 108 cm, respectively. It should be noted that the on-body antenna heights for a static user can be read from Table 3.1, i.e. values of a_0 for Δr_z component.

Table 7.1: Minimum value, the range, mean and standard deviation for Rx power, XPI, Rx polarisation angle and PLF in Scenario 1.

Motion		Walking			Running		
Antenna		To	AL	LL	To	AL	LL
P_r [dBm]	min	-27.2	-27.0	-42.3	-27.6	-66.7	-42.9
	Δ	0.2	0.6	13.8	0.3	37.5	13.8
	μ	-27.1	-26.7	-32.9	-27.5	-37.0	-35.0
	σ	0.1	0.2	4.2	0.1	7.6	3.9
ϕ_t [deg]	min	-4.6	11.8	5.6	-11.8	-18.0	1.0
	Δ	11.6	22.1	8.9	22.0	19.9	12.0
	μ	1.1	23.3	10.6	-0.7	-9.7	9.5
	σ	4.1	7.9	2.5	7.8	6.1	4.1
ψ_t [deg]	min	3.1	-4.1	7.7	6.5	-2.2	3.1
	Δ	1.5	7.1	11.3	3.6	35.2	19.2
	μ	4.0	0.4	15.2	8.5	14.8	14.4
	σ	0.5	2.2	3.4	1.1	12.2	6.1
G_t [dB]	min	6.4	6.0	5.0	5.8	0.1	4.4
	Δ	0.3	0.7	1.6	0.9	6.1	2.3
	μ	6.6	6.4	5.7	6.2	4.3	5.6
	σ	0.1	0.3	0.5	0.3	2.1	0.8
XPI [dB]	min	6.8	2.2	4.9	6.2	5.8	4.6
	Δ	1.8	3.7	1.5	3.1	3.6	3.0
	μ	7.8	3.9	5.7	7.9	8.2	5.9
	σ	0.7	1.3	0.4	1.2	1.1	0.9
θ_r^{pol} [deg]	min	20.1	-0.9	10.9	19.6	-104.0	26.4
	Δ	7.6	21.5	75.8	12.7	64.7	94.4
	μ	23.8	10.6	49.0	25.6	-65.3	75.0
	σ	2.7	7.7	22.7	4.6	23.6	30.2
PLF [dB]	min	-1.1	-0.6	-24.8	-1.5	-42.1	-34.6
	Δ	0.5	0.6	24.6	0.9	39.9	33.6
	μ	-0.8	-0.2	-6.2	-0.9	-9.4	-9.2
	σ	0.2	0.2	6.8	0.3	8.6	7.3

On the other hand, for the dynamic user case, DoDs trace trajectories during a motion cycle. These trajectories reveal the geometric aspect of this effect, regardless of the radiation characteristics of the antenna. The size and shape of the trajectory reflect the principal characteristics and dynamics of the motion for each considered antenna. The wide and short area occupied by the trajectory for the To_F antenna on a walking user implies that the LoS direction varies due to the antenna rotation about the vertical axis of the torso, while there is little effect from the periodic tilt in the posture of a walking user. The trajectory obtained for the AL_L antenna expectedly suggests its more dynamic motion. The 22.1° variation in the azimuth angle (ϕ_t) observed for this antenna in Fig. 7.4 is primarily due to its rotation about the vertical axis of the lower arm, considering the user is turned sideways (left) towards the off-body antenna. The small variation in the elevation (ψ_t) is because of the periodic tilt of the antenna as the hand moves closer and farther from the body during a walking cycle. For the LL_L antenna, one observes larger elevation angles due to the low antenna height. Interestingly, the DoD variation is less severe in this case than for the AL_L antenna, because the lower leg placement dominantly yields rotation of the antenna about the axis normal to its plane. For the setting in Scenario 1, this axis is close to the LoS direction and thereby the rotation has a minor effect on the DoD.

While a similar behaviour across the considered antenna placements is observed for the user running motion, the LoS DoD is generally exhibiting more dynamic variations in this case. Two interesting differences compared to the walking motion can be noticed. First, the DoD trajectory of the To_F antenna is shifted upwards due to notable forward lean in the posture of a running person. Second, the trajectory of the AL_L antenna is in a different region, i.e. rotated and translated, but of somewhat similar shape. This is attributed to the aforementioned horizontal position of the running person's arms. The large elevation angle variation of 35.2° (Table 7.1) can be related to the high antenna gain variation over the motion period.

Fig. 7.5 shows the on-body patch antenna gain value for the LoS direction, as it changes according to the DoD trajectories in Fig. 7.4. While gain variations are relatively small for the specific setting of Scenario 1 (<6.1 dB), namely LoS is always in the forward radiation direction of the on-body antenna, where its gain exhibits the slowest change with DoD, one can expect much greater variations in a general case (see Section 7.3.1).

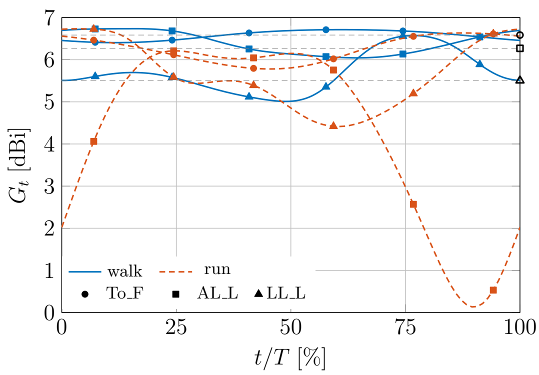

Figure 7.5: On-body antenna gain variation in Scenario 1.

Since Rx power variations in Fig. 7.3 evidently cannot be explained by the variable wearable antenna gain value in direction of the off-body antenna, they can be attributed to the depolarisation effect. For a further analysis, Fig. 7.6 shows the polarisation variation of the impinging field relative to the Rx antenna's co- and cross-polarisation directions (Fig. 7.6a), i.e. $\mathbf{u}^r_{cp}$ and $\mathbf{u}^r_{xp}$, respectively, the corresponding PLF (Fig. 7.6b), and the on-body antenna XPI (Fig. 7.6c). One should note that the reference polarisation directions in Fig. 7.6a account for the antenna XPI. Moreover, only in the angles are important in Fig. 7.6a, while the amplitudes are chosen for convenient visualisation.

The Rx polarisation, and consequently the PLF, are observed to change more significantly for the user running than walking. While the Rx polarisation angle (θ^{pol}_r) variation is negligible for the To_F antenna, it is significant for the AL_L and LL_L ones. For the latter two antennas, the Rx polarisation varies around the cross-polarisation reference (Fig. 7.6a). This results in two PLF minima in Fig. 7.6b, which are matching those observed for the Rx power. These are easily explained by the dynamic

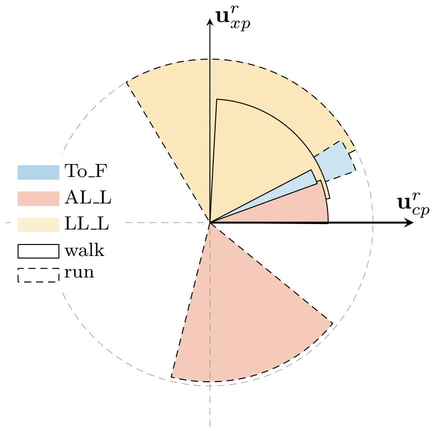

a) Rx polarisation variation (range).

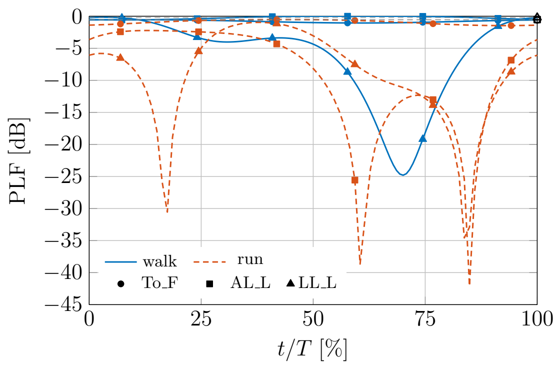

b) PLF as a function of time.

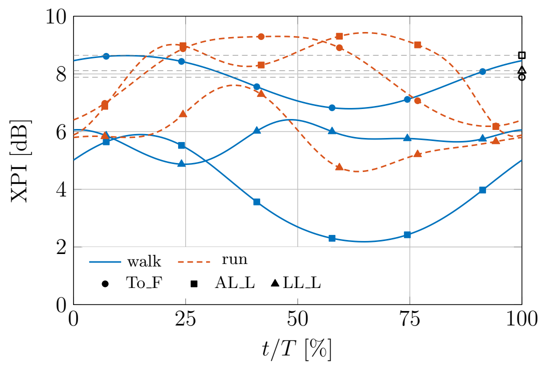

c) On-body antenna XPI as a function of time.

Figure 7.6: Rx signal polarisation variation, PLF and the on-body antenna XPI in Scenario 1.

movement of the legs and the characteristic posture of a running person, with the lower arms being nearly horizontal. The latter effectively results in the AL_L antenna being H-polarised, and the power received by the vertical dipole at the off-body side drops as low as -66.7 dBm (Fig. 7.3). As apparent from Fig. 7.6c, the XPI variation has little impact on the overall depolarisation. Hence, the physical misalignment in between the antennas is the principal cause of the PLF minima observed in Fig. 7.6b. However, as in the case of the antenna gain, XPI variations can have a significant influence in general (see Section 7.3.1).

Following the analysis for the LoS component in Scenario 1, Fig. 7.7 shows the temporal variation of the Rx power for the MPCs reflected on a scattering cylinder in Scenario 2. The corresponding ranges of variation in each considered case are summarised in Table 7.2, being calculated according to (4.6). The obtained results are in line with those for the LoS component; the Rx power exhibits fairly small and slow changes in the case of the To_F antenna, whereas they are large and dynamic for the AL_L and LL_L antennas. In numbers, the Rx power varies as low as 2.5 dB for the To_F antenna and the user walking, while being up to 41.36 dB for the AL_L antenna and the user running. Finally, it should be pointed out that one might argue that direct application of reflection coefficients to MPCs does not give realistic Rx power levels for the scattering cylinder assumption. However, this choice is justified for the purpose herein, i.e. analysis of signal depolarisation in off-body communications with dynamics.

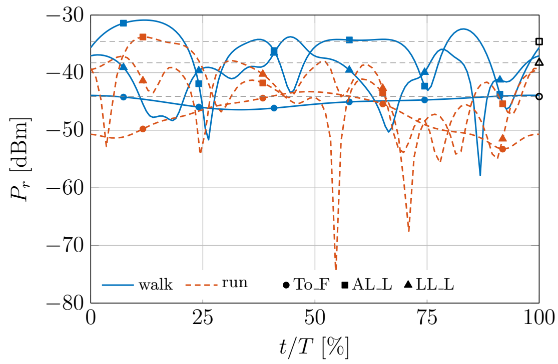

Figure 7.7: Rx power from the MPCs in Scenario 2.

Table 7.2: Range of the Rx power in Scenario 2.

Motion	Walking			Running		
Antenna	To_F	AL_L	LL_L	To_F	AL_L	LL_L
$\Delta P_{r\,[\mathrm{dB}]}$	2.5	20.8	24.1	10.0	41.4	18.5

The results for Scenario 3 are given in Fig. 7.8, which shows the Rx power obtained for the polarised channel model and the non-polarised one. Table 7.3 summarises the statistics of the difference in between the two, with the maximum (ϵ_{max}), mean (ϵ_μ) and standard deviation (ϵ_σ) being calculated according to (4.9) - (4.11). The importance of taking the polarisation aspect of the channel, when dynamic antenna placements are considered, is apparent.

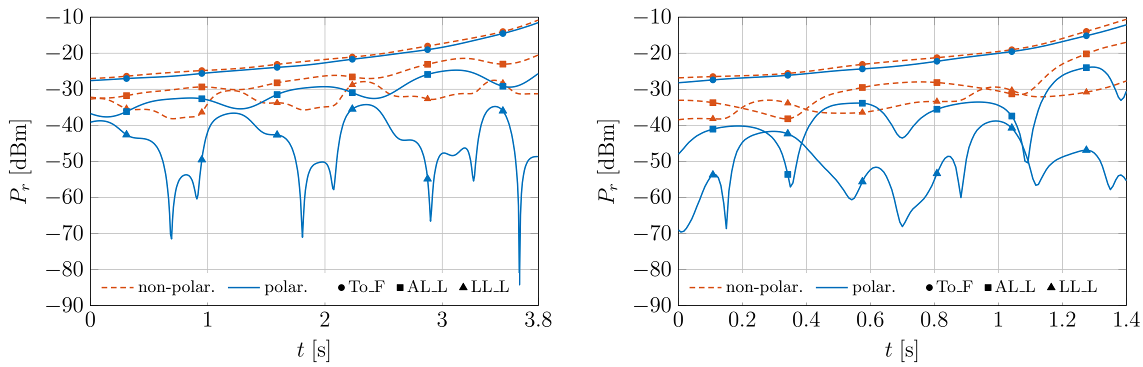

a) User walking.

b) User running.

Figure 7.8: Rx power obtained for the non-polarised and polarised channel models in Scenario 3.

Table 7.3: Statistics of the Rx powers difference for non- and polarised channel models in Scenario 3.

Motion	Walking			Running		
Antenna	To	AL	LL	To	AL	LL
$\epsilon_{max}\{P_r^{\mathrm{non.}}, P_r^{\mathrm{pol.}}\}_{[\mathrm{dB}]}$	1.1	6.5	53.0	1.5	19.5	33.8
$\epsilon_\mu\{P_r^{\mathrm{non.}}, P_r^{\mathrm{pol.}}\}_{[\mathrm{dB}]}$	0.8	4.1	12.2	0.9	7.3	17.8
$\epsilon_\sigma\{P_r^{\mathrm{non.}}, P_r^{\mathrm{pol.}}\}_{[\mathrm{dB}]}$	0.2	1.2	6.3	0.3	4.0	6.8

While the two models give approximately the same Rx power levels in the case of the To_F antenna, large deviations are observed for the AL_L and LL_L ones. The maximum difference for the AL_L antenna is 19.5 dB (running), while the corresponding value for the LL_L antenna is 53 dB (walking), both corresponding to the peak polarisation mismatch losses. The average difference is also high, being up to 7.3 dB and 17.8 dB for the AL_L and LL_L antennas, respectively. The user running case generally yields greater differences in between the models, especially for the AL_L antenna, where the specific posture yields increased depolarisation losses, as discussed previously.

Fig. 7.9 shows the Rx power obtained in Scenario 3, for the three considered mobility models. For its realistic motion, the skeleton-based model with MoCap data can be used as a reference for the evaluation of the two mobility models. Table 7.4 summarises the maximum, mean and standard deviation for the differences between the Rx power obtained from MoCap data (P_r^{MoCap}) and the two considered mobility models ($P_r^{\text{lin./mod.}}$), as calculated according to (4.9) - (4.11).

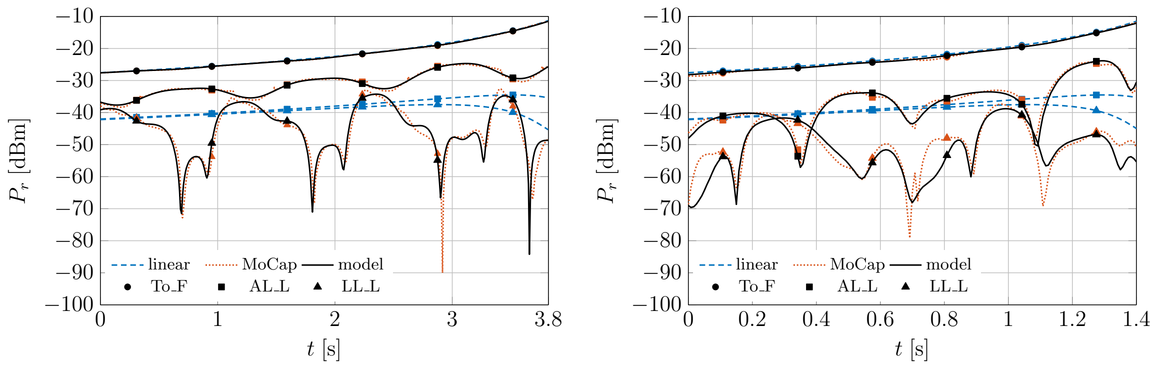

a) User walking.

b) User running.

Figure 7.9: Rx power obtained for the different mobility models in Scenario 3.

Table 7.4: Statistics of the Rx powers difference for MoCap data and mobility models in Scenario 3.

	Motion	Walking			Running		
	Antenna	To_F	AL_L	LL_L	To_F	AL_L	LL_L
lin.	$\epsilon_{max}\{P_r^{\text{lin.}}, P_r^{\text{MoCap}}\}_{[\text{dB}]}$	0.3	10.5	42.3	0.6	16.8	29.3
	$\epsilon_{\mu}\{P_r^{\text{lin.}}, P_r^{\text{MoCap}}\}_{[\text{dB}]}$	0.1	7.1	7.0	0.5	4.2	11.8
	$\epsilon_{\sigma}\{P_r^{\text{lin.}}, P_r^{\text{MoCap}}\}_{[\text{dB}]}$	0.1	1.9	6.3	0.1	3.6	7.6
mod.	$\epsilon_{max}\{P_r^{\text{mod.}}, P_r^{\text{MoCap}}\}_{[\text{dB}]}$	0.2	1.3	30.8	0.7	4.8	14.4
	$\epsilon_{\mu}\{P_r^{\text{mod.}}, P_r^{\text{MoCap}}\}_{[\text{dB}]}$	0.0	0.3	1.8	0.2	0.9	3.0
	$\epsilon_{\sigma}\{P_r^{\text{mod.}}, P_r^{\text{MoCap}}\}_{[\text{dB}]}$	0.0	0.3	2.6	0.2	0.7	3.2

As seen in Fig. 7.9, the linear mobility model fails to capture the characteristic motion pattern observed when the skeleton-based model with MoCap data is used, and yields only a slow change in Rx power due to the decreasing propagation loss as the user approaches the off-body antenna. The difference in both dynamics and range of Rx power variation observed between the two models highlights the importance of using an appropriate mobility model. The availability of such a model is more important as more dynamic the antenna motion is. The maximum observed difference is less than 1 dB for the To_F antenna, while it is greater than 10.5 dB for the AL_L and LL_L ones (Table 7.4); with a maximum of 42.2 dB obtained for the LL_L antenna and user walking motion. This maximum is observed to occur at notch in Rx power, hence being highly sensitive to exact sampling time. However, the average difference between the models is also high for dynamic antenna placements, being up to 11.8 dB for the LL_L antenna and user running. This result is expected, since the torso is fairly static during walking and running motions, while the arms and legs are considerably more dynamic, especially for running.

On the other hand, a very good match is observed between the results obtained for the developed mobility model and the one based on MoCap data. While the maximum difference of 30.8 dB observed for the LL_L antenna and user walking is quite high, this result is a specific one, as it corresponds to a null in the Rx power. The average difference, however, is very low, being below 3 dB for all wearable antenna placements and user's motions.

For comparison, Fig. 7.10 shows the results obtained with a non-polarised propagation model, described in [166]. Table 7.5 summarises the maximum differences between the Rx power obtained from MoCap data and the considered mobility models.

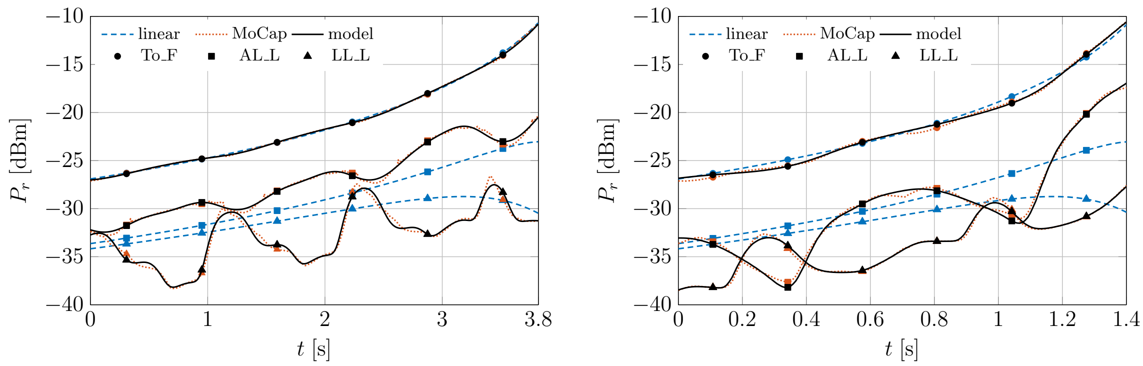

a) User walking.

b) User running.

Figure 7.10: Rx power obtained for the different mobility models in Scenario 3, using a non-polarised propagation model.

Table 7.5: Max. difference between Rx power obtained from MoCap data and the mobility models in Scenario 3.

Motion	Walking			Running		
Antenna	To_F	AL_L	LL_L	To_F	AL_L	LL_L
$\epsilon_{max}\{P_r^{\text{lin.}}, P_r^{\text{MoCap}}\}_{[\text{dB}]}$	0.3	3.7	5.3	0.8	5.9	5.2
$\epsilon_{max}\{P_r^{\text{mod.}}, P_r^{\text{MoCap}}\}_{[\text{dB}]}$	0.2	0.6	1.0	0.5	0.7	0.5

As one observes, with the absence of notches in the Rx power, associated with the polarisation mismatch losses, the differences between the Rx powers are lower. The proposed mobility model shows an excellent match to the one based on MoCap data, where the maximum difference between the corresponding Rx powers is below 1 dB in all cases.

In summary, the results in all scenarios indicate a strong impact of user's motion on the channel, primarily because of the depolarisation effect. While being negligible for wearable antennas on fairly static placements, such as the chest or the head, signal depolarisation can be significant for antennas worn on the arms or the legs. Therefore, this effect should be taken into account by the channel model for off-body communications with dynamic users.

7.3 Depolarisation mechanisms

This section identifies and discusses the signal depolarisation mechanisms, based on the presented channel model. First the effects of user dynamics are considered, followed by a discussion on the depolarisation due to interaction with the environment through scattering mechanisms.

7.3.1 Depolarisation due to antenna dynamics

As discussed in Section 3.3, the wearable antenna motion on a dynamic user has an important and multi-fold influence on the channel. The dominant effect comes from the exhibited antenna rotation, which results in time-varying DoDs/DoAs given by (3.51) and (3.52), in the general form, and by (3.90) and (3.89), as derived for the adopted Euler angles representation of the orientation (Section 3.4.1). These DoDs/DoAs variations further yields time-variant wearable antenna gain in directions of the departing/arriving MPCs.

Fig. 7.11 shows the maximum wearable antenna gain variation over the motion period, for fixed directions in space, given by their azimuth and elevation angles in the global coordinate system (Fig. 7.1a). All figures correspond to the user facing in the direction of the x-axis. The same scale is used in all figures for comparison, while the maximum value in each particular case is indicated in the caption. The

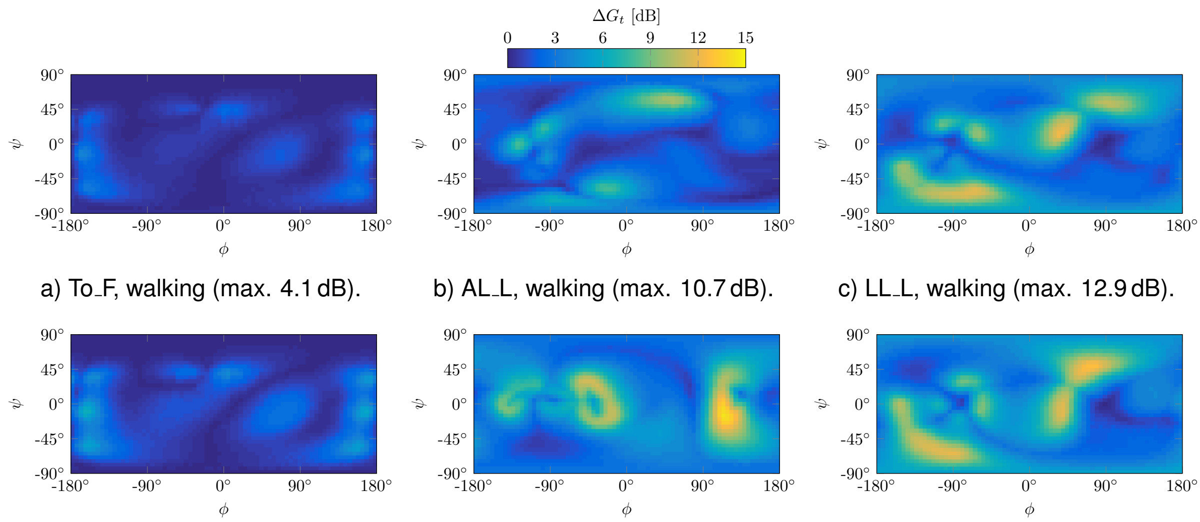

a) To_F, walking (max. 4.1 dB). b) AL_L, walking (max. 10.7 dB). c) LL_L, walking (max. 12.9 dB).

d) To_F, running (max. 6.9 dB). e) AL_L, running (max. 15.0 dB). f) LL_L, running (max. 13.5 dB).

Figure 7.11: Wearable antenna total gain variation due to rotation.

magnitude of gain variations and the number of affected directions are observed to increase with the dynamics of antenna motion. The highest maximum variation is obtained for the wrist antenna and the user running motion (Fig. 7.11e), where a significant area in ϕ-ψ plane exhibits gain variations higher than 10 dB. Therefore, the channel quality can be severely affected should the LoS direction fall in this area.

In addition to amplitude fluctuations due to variable gain, the DoD/DoA variations due to antenna rotation also contribute to the depolarisation effect. The gain imbalance in the two reference polarisations yields time-variant antenna XPI in a given direction, being calculated according to (3.55), where one considers the relation in between the AoDs/AoAs in the local and global coordinate systems, i.e. given by (3.90) and (3.89). This means that the polarisation of a departing MPC on the one hand, and the mismatch in between the polarisations of an arriving MPC and the antenna on the other hand, are changing. This depolarisation mechanism, associated with imperfect polarisation characteristics of practical antennas, affects the MPCs as well as the LoS component, having an important influence on the average Rx power. On the other hand, it does not apply to antennas with ideal polarisation characteristics, e.g. dipoles, which radiate and receive energy only in the θ-polarisation [55].

Fig. 7.12 shows the range of XPI variation across spatial directions, during the motion period, for the considered wearable antenna placements. For the dynamic antenna placements on the AL_L and LL_L, XPI varies more than 30 dB, in a wide range of spatial angles. Since this translates to a rotation of the antenna polarisation in these directions, a high degree of depolarisation can be expected.

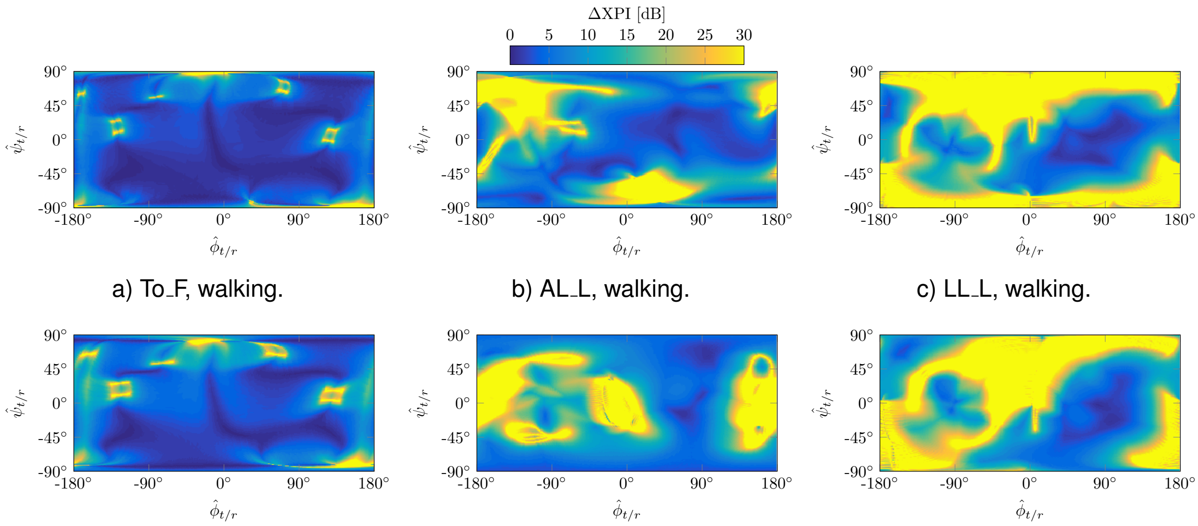

a) To_F, walking.

b) AL_L, walking.

c) LL_L, walking.

d) To_F, running.

e) AL_L, running.

f) LL_L, running.

Figure 7.12: On-body antenna XPI variation over the motion cycle.

In addition to the variable XPI, the antenna rotation has another, more significant, contribution to the depolarisation effect. More precisely, the consequent rotation of the antenna polarisation reference in the direction of a departing or an arriving MPC, i.e. $\mathbf{u}_\theta^a$ and $\mathbf{u}_\phi^a$, results in further mismatch between the antenna and the MPC. In the model, this is represented by the LoS mismatch angle in (3.8), for the LoS component, and the Tx and Rx mismatch angles in (3.10), for scattered MPCs.

The signal depolarisation imposed by this mechanism is merely a result of antenna rotation, and can be analysed independently of the propagation mechanism by choosing a fixed reference. Thereby, considering a V-polarised signal arriving at the antenna, its depolarisation can be quantified by the ratio of the powers received in θ- and ϕ-polarisations. This is equivalent to the ratio of powers radiated in V- and H-polarisations, for a Tx antenna emitting a θ-polarised signal. This XPR is calculated according to (4.3), as discussed in Section 4.4.

Fig. 7.13 shows the minimum XPR across the spatial directions during the motion cycle, considering the antennas on the chest (To_F), left wrist (AL_L) and lower leg (LL_L), with the user walking and running in the x-axis direction. The influence of motion dynamics is apparent. The chest antenna yields the highest minimum XPR (Fig. 7.13a), as it remains fairly vertical and static during the motion cycle.

The values obtained for the wrist and lower leg antennas are considerably lower (Figs. 7.13b and 7.13c). Expectedly, the highest depolarisation is observed for AAoDs/AAoAs around $\pm 90°$, i.e. directions nearly aligned with the axis of antennas' principal rotations. On the other hand, the polarisation remains vertical in the plane perpendicular to this general direction, i.e. the X-Z plane, as indicated by the bright areas at $0°$ and $180°$ in Figs. 7.13b and 7.13c.

The user running case yields more severe depolarisation (Figs. 7.13d - 7.13f), especially for the dynamic antenna placements on the wrist and the lower leg, for which XPR falls below -30 dB for most of the spatial directions. Therefore, high polarisation mismatch losses are anticipated if linearly polarised antennas are employed. One should note that the most severe depolarisation is observed for the wrist antenna (Fig. 7.13e). This is a result of the specific posture of a running person, whose hands are mostly in the horizontal position.

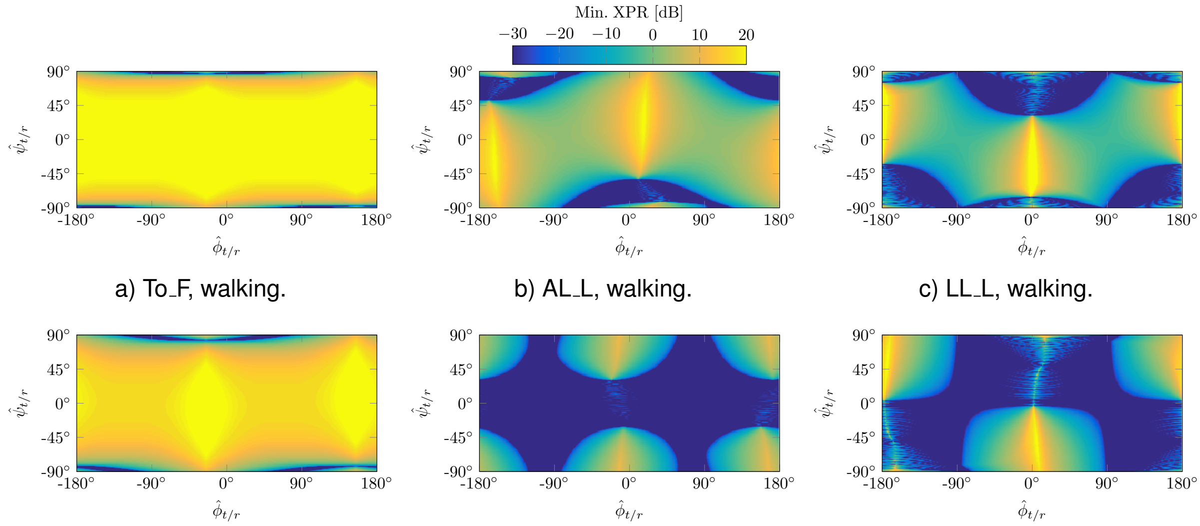

a) To_F, walking. b) AL_L, walking. c) LL_L, walking.

d) To_F, running. e) AL_L, running. f) LL_L, user running.

Figure 7.13: Minimum XPR over the motion cycle.

7.3.2 Depolarisation by scattering

MPCs interacting with objects in the environment are additionally depolarised, two principal factors being responsible: inclination of the incidence plane and polarisation-selective treatment of EM waves by scattering mechanisms. The first one depends only on the propagation path geometry, i.e. relative positions of the Tx, Rx and scatterer. A detailed analysis of this mechanism is available in [93, 86], where a higher relative elevation of a scatterer is observed to result in a more significant depolarisation. This directly implies that 2D propagation models fail to capture this depolarisation mechanism, and 3D models, such as the one presented in this thesis, should be used.

The second aforementioned depolarisation factor is associated with realistic scattering from objects with arbitrary EM properties. For reflected MPCs, depolarisation occurs due to the imbalance in between the reflection coefficients associated with the polarisations perpendicular and parallel to the incidence plane [94]. In order to illustrate signal depolarisation by reflection, Fig. 7.14 shows the incident and reflected E-field vectors in the polarisation plane, for a concrete/glass surface ($\epsilon_r = 4.11$). The vectors are normalised by the amplitude of the incident field, hence, the length of the Rx field vector in the figure corresponds to the incurred loss. This reflection loss and the reflected field polarisation angle are respectively obtained from the reflection coefficients [124], according to (3.14) and (3.15), respectively.

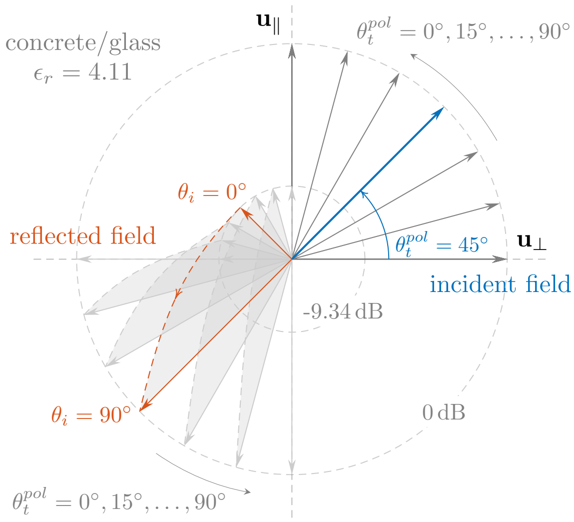

Figure 7.14: Normalised incident and reflected E-field vectors in the polarisation plane, for a concrete/glass surface.

While the reflection loss and signal depolarisation depend on the incident field polarisation, a common pattern can be observed in Fig. 7.14. For the normal incidence, i.e. $\theta_i = 0°$, the perpendicular polarisation component of the field is reversed, and its magnitude is attenuated by 9.34 dB. However, the ratio in between parallel and perpendicular components remains the same, hence, polarisation is preserved. On the other extreme, the grazing incidence, i.e. $\theta_i = 90°$, yields only a phase change by π, while the polarisation and magnitude of the signal are unaffected. For an incident angle in between the two extremes, the reflection loss decreases and polarisation is rotated by an increasing angle as the grazing incidence is approached. Moreover, the polarisation of the reflected field is more sensitive to the incidence angle as more inclined the incident field is towards the plane of incidence. The trajectory of the tip of the reflected field vector in Fig. 7.14 (dashed red line) intersects the horizontal axis for incidence at the Brewster's angle, in which case the reflected field only has the perpendicular component. Polarisation remains unchanged if the incident field is perpendicular or parallel to the incidence plane.

While only linear polarisation of the incident field is considered here, the implications on an arbitrary one are straightforward. The eccentricity of an elliptic polarisation is changed by reflection, due to unequal scaling of the principal axes, whereas a circular polarisation is transformed to an elliptic one, according to the same principle [120]. Moreover, reflections from lossy materials generally result in elliptic polarisation of the reflected field, irrespective of the incident one. For perfectly conducting surfaces the reflected field is unattenuated, its perpendicular component being reversed [124]. Since the reflected field components are equal by the absolute value in this case, the polarisation is preserved. Thereby, the authors of [86, 93] refer to the incidence plane as the Conservation-of-Polarisation plane.

Finally, one should note that the antenna rotation due to user motion also affects the signal depolarisation by reflection and diffraction. Since the antenna's orientation and its XPI determine the incident field polarisation, the extent of depolarisation by reflection will vary in accordance to the antenna rotation. This further emphasises the importance of proper modelling of wearable antenna dynamics.

Chapter 8

Conclusions

This chapter concludes the thesis. A summary of the presented work is given, recalling the main goals and the adopted strategy to meet them. The main results of the work are outlined and the potential directions for the future work are discussed.

8.1 Summary

BANs are foreseen to revolutionise healthcare, to improve logistics support for military teams on the battlefront, and to fundamentally change the human-computer interaction we know today [1], just to name a few applications. Some of the most promising applications exploit the communication between a BAN and the surrounding infrastructure or another nearby BAN, which sparked an interest in off- and body-to-body communications research [57].

Since BANs' performance highly relies on the communication quality, the availability of an appropriate channel model is paramount for optimised system design, which should take the depolarisation effect and the influence of user dynamics into account. In addition to providing a tool for a realistic channel analysis, such a model allows one to investigate the performance of important multi-polarised antenna systems [118], i.e. employed to mitigate fading [80], increase capacity [81], or to facilitate medium sharing among users [123].

A general lack of off-body channel models and failure of the existing ones to appropriately capture the peculiar aspects of BAN channels where the main motivation for the work developed within this thesis. A goal was set to develop an off-body channel model, which appropriately represents the signal depolarisation and the influence of user's motion, primarily the imposed rotation of wearable antennas. Several steps were taken in order to meet this goal. First, a geometry-based polarised channel model was developed by synthesising and generalising the ideas proposed for modelling the LoS component depolarisation due to antenna tilt in [85], and those for signal depolarisation due to reflection in [86, 93, 94].

In order to expand the channel model to take the effects of user's motion into account, an analytical mobility model for wearable antennas on dynamic users was then developed, where various on-body antenna placements are considered, with the user walking or running. The propagation and antenna mobility models together result in a geometry-based channel model for polarised off-body communications with dynamic users. The joint modelling of these two important effects is the main contribution of this work, as such treatment of the off-body channel is not available in literature, to the best of the author's knowledge.

The work in this thesis was developed within the framework of the COST Action CA15104 (IRACON), while its parts were already disseminated in international journals and conferences, and internal reports:

- 3 journal papers were published prior to submission of this thesis, while an additional is currently under review;
- 7 papers were published in conferences;
- 9 technical documents were prepared and presented in IRACON meetings.

The presentation of the work in the thesis is organised in eight chapters. Chapter 1 discusses the motivation and outlines the main goals set for the thesis. The novelty and main contributions of the thesis are pointed out, and a list of published work and internal reports is given. The chapter concludes with a detailed description of the thesis' structure.

Chapter 2 presents a general overview of BAN systems, considering the anticipated applications, associated challenges and requirements, general system architecture and available communication technologies, and finally discussing the specific radio propagation aspects. An overview of the previous work on off-body channel modelling is presented, with a focus on the polarisation aspect of the channel and on the influence of the user's motion on its characteristics. The chapter is concluded with an outline of the main open issues and research gaps, serving as a motivation for the work developed in the following chapters.

Chapter 3 presents a geometry-based polarised off-body channel model considering dynamic users. In the first step, a static channel model is developed from the principles of GO and UTD, taking free space propagation, reflection and diffraction into account. It considers the antennas' radiation characteristics specified by complex antenna gain vectors, i.e. representing gain in two orthogonal polarisations, which thereby facilitate arbitrary antenna polarisation. The signal depolarisation is modelled by matrices associated with each MPC, dependent on the path geometry and the involved propagation mechanism. A general formulation of the model is provided, and the polarisation matrices for LoS component and first-order MPCs are derived for an arbitrary geometry. In the second step, an analytical mobility model for wearable antennas in BANs with dynamic users is developed for a consistent representation of the effects related to user's activity. The model represents motion as a composition of the forward movement at constant velocity and a periodic component associated with variations in the user's posture. The former is represented by a linear function, while the latter is modelled by a Fourier series with two harmonics at most, while model parameters are calculated from MoCap data, thus yielding a simple yet realistic model. Finally, a simplified environment geometry is then discussed for the formulation of a GBSC model, where scattering is assumed to occur in a cylinder centred around the user. With a few additional assumptions, simple expressions for the polarisation matrix are derived, where the depolarisation due to scattering is separated from the user motion effects.

Chapter 4 presents the implementation of the model, outlining its structure and providing a detailed description of its components, as well as a list of input parameters and considered output metrics. The simulator is assessed by considering each of its components individually. The mobility module is validated by comparing the wearable antenna's positions and orientations obtained from the mobility model against those from MoCap data, where a good agreement in between the two is observed. The propagation module is validated by using the developed channel model to replicate a set of scenarios from literature, chosen to asses its different aspects, where an excellent match with results reported in the corresponding references is observed.

Chapter 5 describes two measurement campaigns performed in a meeting room, considering narrow- and wideband off-body channels at 2.45 GHz and 5.8 GHz, respectively. First the common environment in which measurements took place is described, followed by details regarding the considered scenarios and equipment set-up. Both measurements were performed with both V- and H-polarised antennas, either sequentially or simultaneously, in order to investigate the channel's polarisation characteristics. Several different wearable antenna placements and user's activities are considered, in order to investigate the associated effects on the off-body channel characteristics.

Chapter 6 presents the analysis of the measurement data obtained in the two campaigns. Data processing procedures and calculation of the considered metrics are described for both narrow- and wideband measurements. In the former case, these include extraction of path loss components, statistical analysis and model selection for large- and small-scales fading, and analysis of channel's polarisation characteristics. In the latter, one performs CIR deconvolution in order to estimate path delays and amplitudes, which are then used to analyse path loss, depolarisation and delay dispersion characteristics of the channel. The obtained results are discussed, with a great deal of attention given to the depolarisation effect and influence of user dynamics. The measurements data are finally used to validate the developed off-body channel model, where simulation results are compared against measurements for a subset of scenarios.

Chapter 7 presents a simulation-based study of the off-body channel characteristics, using the developed simulator. The chosen scenarios consider different wearable antenna placements with the user walking and running, the goal being to investigate the influence of user dynamics on channel characteristics. A detailed analysis of the depolarisation mechanisms is performed, considering the effects associated with both scattering and user's motion.

Finally, the current chapter concludes the thesis. A summary of the work is presented in the current section, briefly describing the motivation, main goals and contributions of the thesis. Following this outline of the document's structure, the next section points out the main results, and the final one discusses the future work.

8.2 Main results

Motivated by the lack of appropriate off-body BAN channel models that consider the polarisation aspect and take the influence of the user's motion into account, the work within thesis was performed with the goal to develop such a model. The final result of the thesis is a geometry-based polarised BAN channel model for off-body communication with dynamic users, whose development is carried out in two main steps. A polarisation-aware propagation model is developed first, by gathering, modifying and generalising the existing ideas, followed by the development of a mobility model for wearable antennas in BANs with dynamic users.

The proposed analytical antenna mobility model is one of the main contributions of this thesis. It fits the general Reference Point Group Mobility framework, where group mobility associated with the forward motion of the user is represented by a linear model, and Fourier series with at most two harmonics are used to model periodic changes in the individual antenna's position and orientation. It considers users walking and running, with 14 different on-body antenna placements in total, namely, front and back sides of the torso (To_F/B), left and right sides of the waist (Wa_L/R), left and right sides of the head (He_L/R), left and right upper arms (AU_L/R), left and right hand wrists (AL_L/R), left and right upper legs (LU_L/R), and left and right lower legs (LL_L/R). These placements cover the most important BAN applications.

The model provides a realistic antenna motion, as its parameters were calculated from high-resolution MoCap data. With MoCap data serving as reference, the antenna position error is below 2 cm for all on-body placements, except for the wrist one (AL) with the user running, the maximum error being 3.2 cm in this case. Furthermore, the error is similar across antenna placements and motions. The maximum orientation error is found to be at most 9°, for the lower leg antenna (LL) on a walking user. It is noteworthy that the model error is primarily affected by the motion cyclification imposed by the mobility model, with the maxima typically observed at the end of the motion period.

The main advantage of the presented mobility model is its simplicity, making it suitable for employment in BAN channel simulators based on ray-tracing, but also for development of GBSC models, or even for analytical inference in simplified scenarios. It should be pointed out that the model is general and applicable to any communication scenario including wearable antennas. Therefore, it can be used for on-, off- and body-to-body BAN communications. As such, the model is unique and bridges an important gap in the existing literature.

In order to investigate the off-body channel characteristics in a real setting, two measurement campaigns were performed in an indoor office environment at Gdansk University of Technology (Gdansk, Poland). The first campaign considered narrowband and the second one wideband off-body communications, the measurements being performed at 2.45 GHz for the former and at 5.8 GHz the latter, both in licence-free ISM bands. Both measurements were performed with dual-polarised off-body antennas, either sequentially or simultaneously, as the focus was investigation of the depolarisation effect and the influence of user dynamics.

The narrowband measurements were performed for five static scenarios, involving a person standing and sitting, a quasi-dynamic scenario with the user mimicking walking motion in place, and a real dynamic scenario with the user walking towards and away from the off-body antenna. Wearable antenna placements were varied across scenarios, with the ones on the chest, wrist and head being considered. In order to investigate the effects of body-shadowing on the channel, static and quasi-dynamic scenarios measurements were repeated for several user's orientations. Channel characteristics were analysed by decomposing the instantaneous path loss into MPL, represented by a log-distance model, and two random components for the large- and small-scales fading.

A statistical analysis of the path loss components with co- and cross-polarised antennas shows higher attenuation and greater variability of the signal associated with the latter, as indicated by the estimated model parameters. The path loss exponent of 1.79 is estimated when the LoS was clear from body-shadowing, being in agreement with previous measurement-based studies considering indoor environments. Both co- and cross-polarised channels are observed to exhibit lognormal large-scale power variation and Nakagami-m distributed multipath fading. The latter emerged as the best fitting model among other considered distributions, i.e. Rice, Weibull and Rayleigh, where Akaike Information Criterion and χ^2 test were used for ranking and model selection. One should note that the Nakagami-m model parameters for small-scale fading essentially differ in the orthogonal polarisations, where one observes a tendency towards Rice and Rayleigh distributions in co- and cross-polarised channels, respectively.

Body-shadowing is observed to greatly affect path loss and fading characteristics, yielding up to 33 dB additional losses and increased signal variation due to multipath effects when the user obstructs LoS. The polarisation characteristics also depend on body-shadowing conditions, where the highest XPD is observed when LoS is clear from body-shadowing. Considering the antenna on the chest, XPD can vary from 22.1 dB in LoS to 3.2 dB in NLoS, as the user turns around in front of the off-body antenna, even with the antennas' principal polarisation being matched. The wearable antenna placement and body size also show an impact on XPD, higher values being obtained for more corpulent user and antennas on body parts susceptible to stronger shadowing effects, i.e. the chest. These results imply that elevated antenna placements on the head are favourable design choices, where antennas could be integrated in hats, helmets or head-worn devices, such as VR or smart glasses. In the applications involving uniforms, spatial diversity with antennas on the opposite sides of the body should be used to mitigate body-shadowing losses and improve channel quality.

The wearable antenna orientation due to user's posture has a dominant effect on channel characteristics, where the antenna placement on the wrist can result in an orthogonally polarised channel, hence, higher average path loss, as the user sits down with arms on the armrest. This has serious implications on system design choices, where steady body-parts, as the head, chest and upper arm, present themselves as favourable choices for antenna placement from this aspect. With the uncertainties related to random human motion, the employment of polarisation diversity with dual-polarised wearable antennas would significantly improve channel quality. This design choice would help to overcome polarisation mismatch losses due to uncontrolled antenna placement in widespread BAN employments, where wearable devices are likely to be handled by non-professionals.

The wideband channel measurements were performed considering a dynamic user scenario with the user approaching to and departing from the off-body antenna, as in the narrowband campaign. The measurements were performed simultaneously with V- and H-polarised off-body antennas, while being repeated for a wearable one on the chest, wrist and lower leg. Results show a significant influence of user dynamics on CIR parameters. The Rx power obtained for the wrist and lower leg antennas is observed to exhibit periodic variations, associated with changes in user's posture during motion. The mean delay and standard deviation vary synchronously, with their local maxima matching the minima in the corresponding Rx power. These variations can be related to time-variant antenna gain and polarisation mismatch losses due to wearable antenna rotation on a dynamic user.

In a similar way as in the narrowband channel case, body shadowing is observed to yield lower Rx power and increased channel delay dispersion. In addition to LoS obstructions, those associated with specular reflection paths can also have a significant effect on CIR, i.e. on the total Rx power and delay characteristics. With the user and AP in the same room, the off-body channel is observed for have a low delay spread, where most of the energy is transferred by one or two dominant MPCs. As a reference, the average delay spread is found to be at most 11.2 ns, i.e. for the To_F antenna and the user approaching.

Following channel characterisation, measurement data were used for model validation. A few scenarios were selected to test the models ability to replicate temporal dynamics and polarisation characteristics of the channel with static and dynamic users. Results show a good match between simulations and measurements, where the main signal trends are appropriately reproduced by the simulator. Considering the Rx power over time, RMSE is found to be typically below 3 dB in the considered scenarios, where mismatch in the mean power levels is not considered. Similarly, the simulator was able to reproduce the general XPD behaviour with user's orientation relative to the AP, with RMSE being 7.1 dB in the two considered scenarios. However, one should note that the observed errors are in great part due to inappropriate wearable antenna radiation patterns used for simulation, and the inability to perfectly align the data for comparison, due to the random nature of human motion.

With the developed channel model showing a good match with measurements, it was used to investigate off-body channel characteristics with a dynamic user, walking or running, considering antenna placements on the chest, wrist and lower leg. Simple simulation scenarios were chosen with the goal to analyse Rx power variations due to user's activity, primarily due to signal depolarisation. Therefore, the focus is on the LoS component, for which this effect is most obvious.

Results show that the periodic wearable antenna rotation on the user yields high polarisation mismatch losses and a consequent significant variation in Rx power during a motion cycle. These effects are highly dependent on the antenna placement and the type of user's motion. The Rx power is observed to vary as much as 37.5 dB in a free space propagation scenario, i.e. for the antenna on the wrist and the user running. A similar behaviour is observed for an NLoS scenario, where a maximum variation of 41.4 dB is obtained for the same case. On the other hand, for the user walking with antenna on the chest, these variations are as low 0.2 dB and 2.5 dB in the two propagation scenarios, respectively.

Further investigation shows that wearable antenna dynamics result in large AoA/AoD variations of MPCs arriving to or departing from the on-body antenna. For the LoS component, these are up to 22.1° in azimuth and 35.2° in elevation, when the user is running and the antenna is on the wrist, while the time-variant AoA/AoD can generally yield a large gain variation, only up to 6.1 dB being observed in the considered scenario. Analysis of the PLF showed that the polarisation mismatch losses due to wearable antenna rotation are the major cause of Rx power variation.

A comparison between the Rx power levels obtained with polarised and non-polarised channel models was also performed, considering a free space scenario. The observed difference is very high for antennas on the wrist and the lower leg, i.e. up to 53 dB for the latter one. The average difference is also high, being 7.3 dB and 17.8 dB for the two antennas, respectively. On the other hand, the difference is negligible for the antenna on the chest, i.e. at most 1.5 dB in the worst case. These results underline the importance of considering the depolarisation effect and the influence of user dynamics in BAN channel models with dynamic wearable antenna placements.

The most important conclusion following from this work is that the channel modelling approach for BAN communications has to be changed. While the standard statistical model with three-component path loss is widely adopted by researchers, its suitability for BANs is arguable. Communication channels in these networks are characterised by dynamic changes in the principal parameters due to signal depolarisation, where user's motion plays an important role. These effects easily break the stationary channel assumptions for which the standard statistical models were developed. Therefore, an alternative approach is required to take the inevitable non-stationary effects into account. Moreover, the basic statistical models seem even less appropriate if mmWave communications are considered, where the channel dynamics are more important than the average statistics, which are considered as standard metrics for channels below 6 GHz.

By introducing the user dynamics' effects in a polarisation-aware geometry-based channel model, this thesis shifts from the standard off-body channel modelling perspective. The depolarisation effect and the influence of user dynamics are considered jointly, like in no other BAN channel model proposed previously. It allows one to consider arbitrary antennas' radiation characteristics, including gain and polarisations, arbitrary orientation of the off-body antenna and considers dynamic motion of the wearable one, according to the respective on-body placement and user's motion. The model can be used for realistic simulation of dynamic off-body channel for improved system performance evaluation, in order to make a step towards more energy-efficient BAN design.

8.3 Future work

By jointly modelling the depolarisation effect and the influence of the user dynamics, the channel model developed within this thesis bridges an important gap in the existing literature. However, several improvements can be made to the developed simulator, in pursue for even more realistic BAN channel model or its simplification. Moreover, the model can be modified and extended for simulation of other communication scenarios, not only the off-body one. These possible improvements and modifications, but also other open issues remaining to be addressed in the future work are discussed in what follows.

As an important step in the future work, one should further validate different properties of the model based on measurements. This requires a dedicated measurement campaign tailored for testing different aspects of the channel model, including first- and second-order statistics. This campaign should circumvent some of the shortcomings associated with the measurement set-up that was available for the measurements presented in this thesis.

As an important direction to pursue in the future, one considers the further model development for scattering cylinder geometry, where the simple polarisation matrix expressions derived at the end of Chapter 3 could lead to close-form expressions for the first- and second-order statistics of the Rx signal variation. In addition to the facilitation of the analysis of channel characteristics, these would in turn lead to a simplified statistical model for channel fading. Such a model would take the effects of signal depolarisation and user dynamics into account more appropriately than the existing ones. It would further simplify channel simulation in network- and system-level simulators, for performance evaluation purposes. As the following step, one should investigate if a direct link between the parameters of the geometry-based channel model and statistical fading models could be derived, considering the standard Rice and Nakagami-m distributions but also less widely known ones as $\kappa/\eta - \mu$.

Additional geometries should be considered for the scattering environment, where an elliptical cylinder with the Tx and Rx antennas in its foci should be one of the candidates for indoor channels. The best geometry should be chosen based on measurements performed in different environments. One should note that only simple modifications of the model are required in this case, since the expressions derived in Chapter 3 can be easily adapted to facilitate different specification of the scatterers' positions.

With the recent popularity of mmWave communications, the interest in mmWave BANs is also on the rise. With the depolarisation effect being recognised as one of the key challenges at these frequencies, i.e. due to scarce multipath conditions and high reliance on LoS and specular reflections, the model developed in this thesis could be adapted for mmWave off-body channel considerations. With appropriate models for scatterer dynamics, the model can be employed for a spatially consistent simulation of mmWave channels. One should note that none of the available mmWave channel models consider the influence of user dynamics, to the best of the author's knowledge. Therefore, such a model would provide a valuable contribution to channel model development for the fifth generation of mobile networks.

Another valuable direction to explore is the employment of the developed channel model for the performance analysis of wearable MIMO systems, i.e. the actual physical implementation or the virtual perspective of it. While the general geometry formulation can be be readily applied, minor modifications of the simplified model in Section 3.5.3 are required to allow for such analysis. That is, relative positions between antennas should be considered in order to appropriately represent spatial cross-correlation between different on-body antennas.

The channel model presented in this thesis can be also expanded to facilitate body-to-body communication. While the proposed wearable antenna mobility model can be already used at both communication ends, hence taking both user's dynamics into account, the scattering geometry should be reconsidered for the GBSC model. In this case, two cylinders centred around each user present themselves as a more appropriate model for the scattering environment. With this geometry being adopted, in addition to single-bounce MPCs associated with each cylinder, those interacting with scatterers on both cylinders should be also considered, in a similar way as previously proposed for vehicular mobile-to-mobile channels [86].

Finally, one should note the channel model developed in this thesis is not limited only to BANs. The influence of the antennas' orientations on the channel are generally neglected in the literature on mobile communications, whereas the methodology developed in this thesis could be used to take these effects into account. Therefore, the channel model presented in Chapter 3 can be expanded to consider mobile communications as well. It could be used to develop a polarised MIMO channel model for multi-polarised multi-antenna systems in future mobile communication networks.

References

[1] P. S. Hall and Y. Hao, *Antennas and Propagation for Body-Centric Wireless Communications*, 2nd ed. Norwood, MA, USA: Artech House, 2012.

[2] H. J. Wilson. (2013) Wearables in the Workplace. Harvard Business Review. [Online]. Available: https://hbr.org/2013/09/wearables-in-the-workplace

[3] E. Waltz. (2016, Apr.) Rocky Start for Wearables in Professional Sports Games. IEEE Spectrum: Technology, Engineering, and Science News. [Online]. Available: http://spectrum.ieee.org/the-human-os/biomedical/devices/rocky-start-to-wearables-in-professional-sports?utm_source=feedburner&utm_medium=feed&utm_campaign=Feed%3A+IeeeSpectrum+%28IEEE+Spectrum%29

[4] Lily, Camera Drone. https://www.lily.camera. [Accessed: Nov. 2018].

[5] COST Action CA15104, IRACON. http://www.iracon.org/. [Accessed: Nov. 2018].

[6] T. G. Zimmerman, "Personal Area Networks: Near-field intrabody communication," *IBM Systems Journal*, vol. 35, no. 3.4, pp. 609–617, 1996. [Online]. Available: https://doi.org/10.1147/sj.353.0609

[7] S. Ullah, H. Higgins, B. Braem, B. Latre, C. Blondia, I. Moerman, S. Saleem, Z. Rahman, and K. S. Kwak, "A Comprehensive Survey of Wireless Body Area Networks: On PHY, MAC, and Network Layers Solutions," *Journal of Medical Systems*, vol. 36, no. 3, pp. 1065–1094, June 2012. [Online]. Available: http://dx.doi.org/10.1007/s10916-010-9571-3

[8] E. Jovanov, A. Milenkovic, C. Otto, and P. C. de Groen, "A wireless body area network of intelligent motion sensors for computer assisted physical rehabilitation." *Journal of NeuroEngineering and Rehabilitation*, vol. 2, no. 1, pp. 1–10, Mar. 2005. [Online]. Available: http://dx.doi.org/10.1186/1743-0003-2-6

[9] H. Y. Chan and J. Yuan, "Current-Mode Temporal Difference CMOS Imager for Capsule Endoscopy," in *Proc. BIOCAS'07 - IEEE Biomedical Circuits and Systems Conference*, Montreal, Canada, Nov. 2007. [Online]. Available: http://dx.doi.org/10.1109/BIOCAS.2007.4463348

[10] World Health Statistics 2016. http://www.who.int/en/news-room/fact-sheets/detail/the-top-10-causes-of-death. [Accessed: Nov. 2018].

[11] Collection of Free Vector Art. http://www.vecteezy.com. [Accessed: Nov. 2018].

[12] A. Pantelopoulos and N. Bourbakis, “A Survey on Wearable Sensor-Based Systems for Health Monitoring and Prognosis,” *IEEE Transactions on Systems, Man, and Cybernetics—Part C: Applications and Reviews*, vol. 40, no. 1, pp. 1–12, Jan. 2010. [Online]. Available: http://dx.doi.org/10.1109/TSMCC.2009.2032660

[13] M. Chen, S. Gonzalez, A. Vasilakos, H. Cao, and V. C. Leung, “Body Area Networks: A Survey,” *Mobile Networks and Applications*, vol. 16, no. 2, pp. 171–193, Apr. 2010. [Online]. Available: http://dx.doi.org/10.1007/s11036-010-0260-8

[14] V. Shnayder, B.-R. Chen, K. Lorincz, T. R. Jones, and M. Welsh, “Sensor Networks for Medical Care,” Division of Engineering and Applied Sciences, Harvard University, Cambridge, MA, USA, Technical Report TR-08-05, Aug. 2005. [Online]. Available: http://www.eecs.harvard.edu/~shnayder/papers/codeblue-techrept05.pdf

[15] T. Gao, T. Massey, L. Selavo, D. Crawford, B. R. Chen, K. Lorincz, V. Shnayder, L. Hauenstein, F. Dabiri, J. Jeng, A. Chanmugam, D. White, M. Sarrafzadeh, and M. Welsh, “The Advanced Health and Disaster Aid Network: A Light-Weight Wireless Medical System for Triage,” *IEEE Transactions on Biomedical Circuits and Systems*, vol. 1, no. 3, pp. 203–216, 2007. [Online]. Available: http://www.eecs.harvard.edu/~shnayder/papers/ieee07-triage.pdf

[16] D. Curtis, E. Shih, J. Waterman, J. Guttag, J. Bailey, T. Stair, R. Greenes, and L. Ohno-Machado, “Physiological Signal Monitoring in the Waiting Areas of an Emergency Room,” in *Proc. BodyNets’08 - 3rd ICST International Conference on Body Area Networks*, Tempe, AZ, USA, Mar. 2008. [Online]. Available: http://dx.doi.org/10.4108/ICST.BODYNETS2008.2968

[17] M. Sung, C. Marci, and A. Pentland, “Wearable feedback systems for rehabilitation,” *Journal of Neuroengineering and Rehabilitation*, vol. 2, no. 17, pp. 1–12, June 2005. [Online]. Available: http://dx.doi.org/10.1186/1743-0003-2-17

[18] M. Di Rienzo, F. Rizzo, G. Parati, G. Brambilla, M. Ferratini, and P. Castiglioni, “MagIC System: a New Textile-Based Wearable Device for Biological Signal Monitoring. Applicability in Daily Life and Clinical Setting.” in *Proc. IEEE-EMBS’05 - 27th Annual International Conference of the Engineering in Medicine and Biology Society*, Shanghai, China, Jan. 2005. [Online]. Available: http://dx.doi.org/10.1109/IEMBS.2005.1616161

[19] R. Paradiso, G. Loriga, and N. Taccini, “A Wearable Health Care System Based on Knitted Integrated Sensors,” *IEEE Transactions on Information Technology in Biomedicine*, vol. 9, no. 3, pp. 337–344, 2005. [Online]. Available: http://dx.doi.org/10.1109/TITB.2005.854512

[20] P. Pandian, K. Mohanavelu, K. Safeer, T. Kotresh, D. Shakunthala, P. Gopal, and V. Padaki, “Smart Vest: Wearable multi-parameter remote physiological monitoring system,” *Medical Engineering & Physics*, vol. 30, no. 4, pp. 466–477, May 2008. [Online]. Available: http://dx.doi.org/10.1016/j.medengphy.2007.05.014

[21] N. Oliver and F. Flores-Mangas, “HealthGear: A real-time wearable system for monitoring and analyzing physiological signals,” in *Proc. BSN’06 - International Workshop on Wearable and Implantable Body Sensor Networks*, Cambridge, MA, USA, Apr. 2006. [Online]. Available: http://dx.doi.org/10.1109/BSN.2006.27

[22] C. D. Katsis, G. Ganiatsas, and D. I. Fotiadis, “An integrated telemedicine platform for the assessment of affective physiological states.” *Diagnostic pathology*, vol. 1, no. 1, pp. 1–16, Aug. 2006. [Online]. Available: http://dx.doi.org/10.1186/1746-1596-1-16

[23] K. Lorincz, B.-r. Chen, G. W. Challen, A. R. Chowdhury, S. Patel, P. Bonato, and M. Welsh, “Mercury: A Wearable Sensor Network Platform for High-fidelity Motion Analysis,” in *Proc. SenSys’09 - 7th ACM Conference on Embedded Networked Sensor Systems*, Berkeley, CA, USA, Nov. 2009. [Online]. Available: https://doi.org/10.1145/1644038.1644057

[24] E. Farella, A. Pieracci, L. Benini, L. Rocchi, and A. Acquaviva, “Interfacing human and computer with wireless body area sensor networks: the WiMoCA solution,” *Multimedia Tools and Applications*, vol. 38, no. 3, pp. 337–363, July 2008. [Online]. Available: http://dx.doi.org/10.1007/s11042-007-0189-5

[25] C. Mundt, K. Montgomery, U. Udoh, V. Barker, G. Thonier, A. Tellier, R. Ricks, R. Darling, Y. Cagle, N. Cabrol, S. Ruoss, J. Swain, J. Hines, and G. Kovacs, “A Multiparameter Wearable Physiologic Monitoring System for Space and Terrestrial Applications,” *IEEE Transactions on Information Technology in Biomedicine*, vol. 9, no. 3, pp. 382–391, 2005. [Online]. Available: http://dx.doi.org/10.1109/TITB.2005.854509

[26] C. Gopalsamy, S. Park, R. Rajamanickam, and S. Jayaraman, “The Wearable Motherboard™: The first generation of adaptive and responsive textile structures (ARTS) for medical applications,” *Virtual Reality*, vol. 4, no. 3, pp. 152–168, 1999. [Online]. Available: http://dx.doi.org/10.1007/BF01418152

[27] R. W. Hoyt, J. Reifman, T. S. Coster, and M. J. Buller, “Combat medical informatics: present and future,” in *Proc. AMIA Symposium*, San Antonio, TX, USA, Nov. 2002. [Online]. Available: http://www.ncbi.nlm.nih.gov/pmc/articles/PMC2244161/

[28] T. G. Zimmerman, “Personal Area Networks (PAN): Near-Field Intra-Body Communication,” Master’s thesis, Massachusetts Institute of Technology (MIT), Cambridge, MA, USA, 1995. [Online]. Available: http://cba.mit.edu/docs/theses/95.09.zimmerman.pdf

[29] B. Zhen, M. Patel, S. Lee, E. Won, and A. Astrin, “TG6 Technical Requirements Document (TRD),” *IEEE P802.15-08-0644-09-0006*, pp. 1–15, 2008. [Online]. Available: https://mentor.ieee.org/802.15/dcn/08/15-08-0644-09-0006-tg6-technical-requirements-document.doc

[30] *ICNIRP Guidelines for limiting exposure to time-varying electric, magnetic, and electromagnetic fields (up to 300 GHz)*, ICNIRP Guideline, Apr. 1998. [Online]. Available: http://www.icnirp.org/cms/upload/publications/ICNIRPemfgdl.pdf

[31] *IEEE Standard for Safety Levels With Respect to Human Exposure to Radio Frequency Electromagnetic Fields, 3 kHz to 300 GHz*, IEEE Standard C95.1-2005, Apr. 2006. [Online]. Available: http://dx.doi.org/10.1109/IEEESTD.2006.99501

[32] S. K. S. Gupta, T. Mukherjee, and K. K. Venkatasubramanian, *Body Area Networks: Safety, Security, and Sustainability*. Cambridge, UK: Cambridge University Press, 2013.

[33] A. Kurs, A. Karalis, R. Moffatt, J. Joannopoulos, P. Fisher, and M. Soljacic, “Wireless Power Transfer via Strongly Coupled Magnetic Resonances,” *Science*, vol. 317, no. 5834, pp. 83–6, July 2007. [Online]. Available: http://dx.doi.org/10.1126/science.1143254

[34] T. Torfs, V. Leonov, C. Van Hoof, and B. Gyselinckx, “Body-Heat Powered Autonomous Pulse Oximeter,” in *Proc. Sensors’06 - 5th IEEE Conference on Sensors*, Daegu, South Korea, Oct. 2006. [Online]. Available: http://dx.doi.org/10.1109/ICSENS.2007.355497

[35] E. Romero, R. Warrington, and M. Neuman, “Energy Scavenging Sources for Biomedical Sensors,” *Physiological Measurement*, vol. 30, no. 9, pp. 35–62, Aug. 2009. [Online]. Available: http://dx.doi.org/10.1088/0967-3334/30/9/R01

[36] E. Post and M. Orth, “Smart Fabric, or ’Wearable Clothing’,” in *Proc. ISWC’97 - 1st International Symposium on Wearable Computers*, Cambridge, MA, USA, Oct. 1997. [Online]. Available: http://dx.doi.org/10.1109/ISWC.1997.629937

[37] J. Walk, J. Weber, C. Soell, R. Weigel, G. Fischer, and T. Ussmueller, “Remote Powered Medical Implants for Telemonitoring,” *Proceedings of the IEEE*, vol. 102, no. 11, pp. 1811–1832, Nov. 2014. [Online]. Available: http://dx.doi.org/10.1109/JPROC.2014.2359517

[38] M. Ghovanloo and S. Atluri, “A Wide-Band Power-Efficient Inductive Wireless Link for Implantable Microelectronic Devices Using Multiple Carriers,” *IEEE Transactions on Circuits and Systems—Part I: Regular Papers*, vol. 54, no. 10, pp. 2211–2221, Oct. 2007. [Online]. Available: http://dx.doi.org/10.1109/TCSI.2007.905187

[39] M. Seyedi, B. Kibret, D. T. Lai, and M. Faulkner, “A Survey on Intrabody Communications for Body Area Network Applications,” *IEEE Transactions on Biomedical Engineering*, vol. 60, no. 8, pp. 2067–2079, Aug. 2013. [Online]. Available: http://dx.doi.org/10.1109/TBME.2013.2254714

[40] K. Hachisuka, T. Takeda, Y. Terauchi, K. Sasaki, H. Hosaka, and K. Itao, “Intra-Body Data Transmission for the Personal Area Network,” *Microsystem Technologies*, vol. 11, no. 8, pp. 1020–1027, July 2005. [Online]. Available: http://dx.doi.org/10.1007/s00542-005-0500-1

[41] N. Cho, J. Yoo, S.-j. Song, J. Lee, S. Jeon, and H.-J. Yoo, “The Human Body Characteristics as a Signal Transmission Medium for Intrabody Communication,” *IEEE Transactions on Microwave Theory and Techniques*, vol. 55, no. 5, pp. 1080–1086, May 2007. [Online]. Available: http://dx.doi.org/10.1109/TMTT.2007.895640

[42] D. Lindsey, E. McKee, M. Hull, and S. Howell, “A New Technique for Transmission of Signals from Implantable Transducers,” *IEEE Transactions on Biomedical Engineering*, vol. 45, no. 5, pp. 614–9, May 1998. [Online]. Available: http://dx.doi.org/10.1109/10.668752

[43] M. S. Wegmueller, M. Oberle, N. Felber, N. Kuster, and W. Fichtner, “Signal Transmission by Galvanic Coupling Through the Human Body,” *IEEE Transactions on Instrumentation and Measurement*, vol. 59, no. 4, pp. 963–969, Apr. 2010. [Online]. Available: http://dx.doi.org/10.1109/TIM.2009.2031449

[44] J. Bae, H. Cho, K. Song, H. Lee, and H.-J. Yoo, “The Signal Transmission Mechanism on the Surface of Human Body for Body Channel Communication,” *IEEE Transactions on Microwave Theory and Techniques*, vol. 60, no. 3, pp. 582–593, Mar. 2012. [Online]. Available: http://dx.doi.org/10.1109/TMTT.2011.2178857

[45] N. Haga, K. Saito, M. Takahashi, and K. Ito, “Equivalent Circuit of Intrabody Communication Channels Inducing Conduction Currents Inside the Human Body,” *IEEE Transactions on Antennas and Propagation*, vol. 61, no. 5, pp. 2807–2816, May 2013. [Online]. Available: http://dx.doi.org/10.1109/TAP.2013.2246534

[46] Bluetooth Special Interest Group. https://www.bluetooth.com. [Accessed: Nov. 2018].

[47] *IEEE Standard for Information Technology – Telecommunications and Information Exchange Between Systems – Local and Metropolitan Area Networks – Specific Requirements. - Part 15.1: Wireless Medium Access Control (MAC) and Physical Layer (PHY) Specifications for Wireless Personal Area Networks (WPANs)*, IEEE Standard 802.15.1-2005, June 2005. [Online]. Available: http://dx.doi.org/10.1109/IEEESTD.2005.96290

[48] M. Honkanen, A. Lappetelainen, and K. Kivekas, “Low End Extension for Bluetooth,” in *Proc. RAWCON’04 - IEEE Radio and Wireless Conference*, Atlanta, GA, USA, 2004. [Online]. Available: http://dx.doi.org/10.1109/RAWCON.2004.1389107

[49] ZigBee Alliance. http://zigbee.org. [Accessed: Nov. 2018].

[50] *IEEE Standard for Local and Metropolitan Area Networks - Part 15.4: Low-Rate Wireless Personal Area Networks (LR-WPANs)*, IEEE Standard 802.15.4-2011, 2011. [Online]. Available: http://dx.doi.org/10.1109/IEEESTD.2011.6012487

[51] *IEEE Standard for Information Technology – Telecommunications and Information Exchange Between Systems – Local and Metropolitan Area Networks – Specific Requirement Part 15.4: Wireless Medium Access Control (MAC) and Physical Layer (PHY) Specifications for Low-Rate Wireless Personal Area Networks (WPANs)*, IEEE Standard 802.15.4a-2007, 2007. [Online]. Available: http://dx.doi.org/10.1109/IEEESTD.2007.4299496

[52] *IEEE Standard for Local and Metropolitan Area Networks – Part 15.6: Wireless Body Area Networks*, IEEE Standard 802.15.6-2012, Feb. 2012. [Online]. Available: http://dx.doi.org/10.1109/IEEESTD.2012.6161600

[53] J. D. Parsons, *The Mobile Radio Propagation Channel*, 2nd ed. London, UK: John Wiley & Sons, 2000.

[54] M. K. Simon and M.-S. Alouini, *Digital Communication over Fading Channels*, 2nd ed. Hoboken, NJ, USA: John Wiley & Sons, 2005. [Online]. Available: http://dx.doi.org/10.1002/0471715220

[55] C. A. Balanis, *Antenna Theory: Analysis and Design*, 2nd ed. New York, NY, USA: John Wiley & Sons, 1997.

[56] M. Mackowiak and L. M. Correia, "A Statistical Model for the Influence of Body Dynamics on the Gain Pattern of Wearable Antennas in Off-Body Radio Channels," *Wireless Personal Communications*, vol. 73, no. 3, pp. 381–399, May 2013. [Online]. Available: http://dx.doi.org/10.1007/s11277-013-1193-x

[57] S. L. Cotton, R. D'Errico, and C. Oestges, "A Review of Radio Channel Models for Body Centric Communications," *Radio Science*, vol. 49, no. 6, pp. 371–388, June 2014. [Online]. Available: https://dx.doi.org/10.1002%2F2013RS005319

[58] M. Mackowiak and L. M. Correia, "Statistical Path Loss Model for Dynamic Off-Body Channels," in *Proc. PIMRC'14 - 25th Annual International Symposium on Personal, Indoor, and Mobile Radio Communication*, Washington, DC, USA, 2014. [Online]. Available: https://doi.org/10.1109/PIMRC.2014.7136131

[59] K. K. Cwalina, S. J. Ambroziak, and P. Rajchowski, "An Off-Body Narrowband and Ultra-Wide Band Channel Model for Body Area Networks in a Ferryboat Environment," *Applied Sciences*, vol. 8, no. 6, June 2018. [Online]. Available: https://doi.org/10.3390/app8060988

[60] S. L. Cotton, "A Statistical Model for Shadowed Body-Centric Communications Channels: Theory and Validation," *IEEE Transactions on Antennas and Propagation*, vol. 62, no. 3, pp. 1416–1424, Mar. 2014. [Online]. Available: http://dx.doi.org/10.1109/TAP.2013.2295211

[61] S. K. Yoo, S. L. Cotton, P. C. Sofotasios, and S. Freear, "Shadowed Fading in Indoor Off-Body Communication Channels: A Statistical Characterization Using the κ-μ/Gamma Composite Fading Model," *IEEE Transactions on Wireless Communications*, vol. 15, no. 8, pp. 5231–5244, Aug. 2016. [Online]. Available: https://doi.org/10.1109/TWC.2016.2555795

[62] S. K. Yoo and S. L. Cotton, "Composite Fading in Non-Line-of-Sight Off-Body Communications Channels," in *Proc. EuCAP'17 - 11th European Conference on Antennas and Propagation*, Paris, France, Mar. 2017. [Online]. Available: https://doi.org/10.23919/EuCAP.2017.7928458

[63] S. K. Yoo, P. C. Sofotasios, S. L. Cotton, M. Matthaiou, M. Valkama, and G. K. Karagiannidis, "The η-μ/Inverse Gamma Composite Fading Model," in *Proc. PIMRC'15 - 26th Annual International Symposium on Personal, Indoor, and Mobile Radio Communications*, Hong Kong, China, Aug. 2015. [Online]. Available: https://doi.org/10.1109/PIMRC.2015.7343288

[64] S. L. Cotton, W. G. Scanlon, and J. Guy, “The κ-μ Distribution Applied to the Analysis of Fading in Body to Body Communication Channels for Fire and Rescue Personnel,” *IEEE Antennas and Wireless Propagation Letters*, vol. 7, pp. 66–69, 2008. [Online]. Available: http://dx.doi.org/10.1109/LAWP.2008.915807

[65] S. L. Cotton and W. G. Scanlon, “Channel Characterization for Single- and Multiple-Antenna Wearable Systems Used for Indoor Body-to-Body Communications,” *IEEE Transactions on Antennas and Propagation*, vol. 57, no. 4, pp. 980–990, Apr. 2009. [Online]. Available: https://doi.org/10.1109/TAP.2009.2014576

[66] S. L. Cotton, A. McKernan, and W. G. Scanlon, “Received Signal Characteristics of Outdoor Body-to-Body Communications Channels at 2.45 GHz,” in *Proc. LAPC’11 - Loughborough Antennas Propagation Conference*, Loughborough, UK, Nov. 2011. [Online]. Available: https://doi.org/10.1109/LAPC.2011.6114147

[67] S. L. Cotton, W. G. Scanlon, and A. McKernan, “Improving Signal Reliability in Outdoor Body-to-Body Communications Using Front and Back Positioned Antenna Diversity,” in *Proc. EuCAP’12 - 6th European Conference on Antennas and Propagation*, Prague, Czech Republic, Mar. 2012. [Online]. Available: https://doi.org/10.1109/EuCAP.2012.6206649

[68] S. L. Cotton, “Shadowed Fading in Body-to-Body Communications Channels in an Outdoor Environment at 2.45 GHz,” in *Proc. IEEE-APS APWC’14 - Topical Conference on Antennas and Propagation in Wireless Communications*, Palm Beach, Netherlands Antilles, Aug. 2014. [Online]. Available: https://doi.org/10.1109/APWC.2014.6905548

[69] ——, “Human Body Shadowing in Cellular Device-to-Device Communications: Channel Modeling Using the Shadowed κ-μ Fading Model,” *IEEE Journal on Selected Areas in Communications*, vol. 33, no. 1, pp. 111–119, Jan. 2015. [Online]. Available: https://doi.org/10.1109/JSAC.2014.2369613

[70] R. Rosini, R. Verdone, and R. D’Errico, “Body-to-Body Indoor Channel Modeling at 2.45 GHz,” *IEEE Transactions on Antennas and Propagation*, vol. 62, no. 11, pp. 5807–5819, Nov. 2014. [Online]. Available: https://doi.org/10.1109/TAP.2014.2352631

[71] F. Mani and R. D’Errico, “A Spatially Aware Channel Model for Body-to-Body Communications,” *IEEE Transactions on Antennas and Propagation*, vol. 64, no. 8, pp. 3611–3618, May 2016. [Online]. Available: https://doi.org/10.1109/TAP.2016.2570260

[72] S. L. Cotton, Y. J. Chun, W. G. Scanlon, and G. A. Conway, “Path Loss Models for Indoor Off-body Communications at 60 GHz,” in *Proc. APSURSI’16 - IEEE Antennas and Propagation Society International Symposium*, Fajardo, Puerto Rico, July 2016. [Online]. Available: https://doi.org/10.1109/APS.2016.7696427

[73] S. K. Yoo, S. L. Cotton, Y. J. Chun, W. G. Scanlon, and G. A. Conway, “Channel Characteristics of Dynamic Off-Body Communications at 60 GHz Under Line-of-Sight (LOS) and Non-LOS

Conditions," *IEEE Antennas and Wireless Propagation Letters*, vol. 16, pp. 1553–1556, Feb. 2017. [Online]. Available: https://doi.org/10.1109/LAWP.2017.2650863

[74] S. K. Yoo, S. L. Cotton, R. W. Heath, and Y. J. Chun, "Measurements of the 60 GHz UE to eNB Channel for Small Cell Deployments," *IEEE Wireless Communications Letters*, vol. 6, no. 2, pp. 178–181, Apr. 2017. [Online]. Available: https://doi.org/10.1109/LWC.2017.2650225

[75] S. K. Yoo, S. L. Cotton, Y. J. Chun, and W. G. Scanlon, "Fading Characterization of UE to Ceiling-Mounted Access Point Communications at 60 GHz," in *Proc. EuCAP'18 - 12th European Conference on Antennas and Propagation*, London, UK, Apr. 2018.

[76] X. Zhao, Q. Wang, S. Li, S. Geng, M. Wang, S. Sun, and Z. Wen, "Attenuation by Human Bodies at 26 and 39.5 GHz Millimeter Wavebands," *IEEE Antennas and Wireless Propagation Letters*, vol. 16, pp. 1229–1232, Nov. 2017. [Online]. Available: https://doi.org/10.1109/LAWP.2016.2629023

[77] A. Maltsev, I. Bolotin, A. Lomayev, A. Pudeyev, and M. Danchenko, "User Mobility Impact on Millimeter-Wave System Performance," in *Proc. EuCAP'16 - 10th European Conference on Antennas and Propagation*, Davos, Switzerland, Apr. 2016. [Online]. Available: https://doi.org/10.1109/EuCAP.2016.7481505

[78] S. Jaeckel, L. Raschkowski, S. Wu, L. Thiele, and W. Keusgen, "An Explicit Ground Reflection Model for mm-Wave Channels," in *Wkshps of WCNCW'17 - IEEE Wireless Communications and Networking Conference Workshops*, San Francisco, CA, USA, Mar. 2017. [Online]. Available: https://doi.org/10.1109/WCNCW.2017.7919093

[79] E. Zöchmann, K. Guan, and M. Rupp, "Two-Ray Models in mmWave Communications," in *Proc. SPAWC'17 - 18th International Workshop on Signal Processing Advances in Wireless Communications*, Sapporo, Japan, July 2017. [Online]. Available: https://doi.org/10.1109/SPAWC.2017.8227681

[80] R. Vaughan, "Polarization Diversity in Mobile Communications," *IEEE Transactions on Vehicular Technology*, vol. 39, no. 3, pp. 177–186, Aug. 1990. [Online]. Available: http://dx.doi.org/10.1109/25.130998

[81] M. R. Andrews, P. P. Mitra, and R. deCarvalho, "Tripling the Capacity of Wireless Communications Using Electromagnetic Polarization," *Nature*, vol. 409, no. 6818, pp. 316–318, Jan. 2001. [Online]. Available: http://dx.doi.org/10.1038/35053015

[82] T. S. Rappaport, S. Sun, R. Mayzus, H. Zhao, Y. Azar, K. Wang, G. N. Wong, J. K. Schulz, M. Samimi, and F. Gutierrez, "Millimeter Wave Mobile Communications for 5G Cellular: It Will Work!" *IEEE Access*, vol. 1, pp. 335–349, May 2013. [Online]. Available: https://doi.org/10.1109/ACCESS.2013.2260813

[83] A. Maltsev, E. Perahia, R. Maslennikov, A. Sevastyanov, A. Lomayev, and A. Khoryaev, "Impact of Polarization Characteristics on 60-GHz Indoor Radio Communication Systems," *IEEE Antennas and Wireless Propagation Letters*, vol. 9, pp. 413–416, Apr. 2010. [Online]. Available: https://doi.org/10.1109/LAWP.2010.2048410

[84] W. Roh, J. Y. Seol, J. Park, B. Lee, J. Lee, Y. Kim, J. Cho, K. Cheun, and F. Aryanfar, "Millimeter-Wave Beamforming as an Enabling Technology for 5G Cellular Communications: Theoretical Feasibility and Prototype Results," *IEEE Communications Magazine*, vol. 52, no. 2, pp. 106–113, Feb. 2014. [Online]. Available: https://doi.org/10.1109/MCOM.2014.6736750

[85] S. Jaeckel, K. Borner, L. Thiele, and V. Jungnickel, "A Geometric Polarization Rotation Model for the 3-D Spatial Channel Model," *IEEE Transactions on Antennas and Propagation*, vol. 60, no. 12, pp. 5966–5977, Dec. 2012. [Online]. Available: http://dx.doi.org/10.1109/TAP.2012.2214017

[86] S.-C. Kwon and G. Stüber, "Geometrical Theory of Channel Depolarization," *IEEE Transactions on Vehicular Technology*, vol. 60, no. 8, pp. 3542–3556, Oct. 2011. [Online]. Available: http://dx.doi.org/10.1109/TVT.2011.2163094

[87] T. Svantesson, "A Physical MIMO Radio Channel Model for Multi-Element Multi-Polarized Antenna Systems," in *Proc. VTC'01-Fall - 54th IEEE Vehicular Technology Conference*, Atlantic City, NJ, USA, Oct. 2001. [Online]. Available: http://dx.doi.org/10.1109/VTC.2001.956941

[88] ——, "Antennas and Propagation from a Signal Processing Perspective," Ph.D. dissertation, Chalmers University of Technology, Göteborg, Sweden, May 2001. [Online]. Available: http://www.pcc.lth.se/publications/papers/2001/Theses/tomaso.pdf

[89] K. Yazdandoost and R. Miura, "Antenna polarization mismatch in BAN communications," in *Proc. IMWS-BIO'13 - IEEE MTT-S International Microwave Workshop Series on RF and Wireless Technologies for Biomedical and Healthcare Applications*, Singapore, Dec. 2013. [Online]. Available: http://dx.doi.org/10.1109/IMWS-BIO.2013.6756209

[90] L. Vallozzi, P. Van Torre, C. Hertleer, H. Rogier, M. Moeneclaey, and J. Verhaevert, "Wireless Communication for Firefighters Using Dual-Polarized Textile Antennas Integrated in Their Garment," *IEEE Transactions on Antennas and Propagation*, vol. 58, no. 4, pp. 1357–1368, Apr. 2010. [Online]. Available: http://dx.doi.org/10.1109/TAP.2010.2041168

[91] P. V. Torre, L. Vallozzi, C. Hertleer, H. Rogier, M. Moeneclaey, and J. Verhaevert, "Indoor Off-Body Wireless MIMO Communication With Dual Polarized Textile Antennas," *IEEE Transactions on Antennas and Propagation*, vol. 59, no. 2, pp. 631–642, Feb. 2011. [Online]. Available: http://dx.doi.org/10.1109/TAP.2010.2096389

[92] P. F. Cui, W. J. Lu, Y. Yu, B. Xue, and H. B. Zhu, "Off-Body Spatial Diversity Reception Using Circular and Linear Polarization: Measurement and Modeling," *IEEE Communications Letters*, vol. 22, no. 1, pp. 209–212, Jan. 2018. [Online]. Available: https://doi.org/10.1109/LCOMM.2017.2762324

[93] S.-C. Kwon, G. Stüber, A. Lopez, and J. Papapolymerou, “Geometrically Based Statistical Model for Polarized Body-Area-Network Channels,” *IEEE Transactions on Vehicular Technology*, vol. 62, no. 8, pp. 3518–3530, Oct. 2013. [Online]. Available: http://dx.doi.org/10.1109/TVT.2013.2262691

[94] ——, “Polarized Channel Model for Body Area Networks Using Reflection Coefficients,” *IEEE Transactions on Vehicular Technology*, vol. 64, no. 8, pp. 3822–3828, Aug. 2015. [Online]. Available: http://dx.doi.org/10.1109/TVT.2014.2358576

[95] T. Uusitupa and T. Aoyagi, “Analysis of Dynamic On-Body Communication Channels for Various Movements and Polarization Schemes at 2.45 GHz,” *IEEE Transactions on Antennas and Propagation*, vol. 61, no. 12, pp. 6168–6179, Dec. 2013. [Online]. Available: https://doi.org/10.1109/TAP.2013.2281369

[96] D. B. Smith, D. Miniutti, T. A. Lamahewa, and L. W. Hanlen, “Propagation Models for Body-Area Networks: A Survey and New Outlook,” *IEEE Antennas and Propagation Magazine*, vol. 55, no. 5, pp. 97–117, Oct. 2013. [Online]. Available: http://dx.doi.org/10.1109/MAP.2013.6735479

[97] R. Bhagavatula, C. Oestges, and R. W. Heath, “A New Double-Directional Channel Model Including Antenna Patterns, Array Orientation, and Depolarization,” *IEEE Transactions on Vehicular Technology*, vol. 59, no. 5, pp. 2219–2231, June 2010. [Online]. Available: https://doi.org/10.1109/TVT.2010.2045775

[98] R. Fu, Y. Ye, and K. Pahlavan, “Characteristic and Modeling of Human Body Motions for Body Area Network Applications,” *International Journal of Wireless Information Networks*, vol. 19, no. 3, pp. 219–228, July 2012.

[99] R. D’Errico and L. Ouvry, “Delay Dispersion of the On-Body Dynamic Channel,” in *Proc. EuCAP’10 - 4th European Conference on Antennas and Propagation*, Barcelona, Spain, Apr. 2010. [Online]. Available: https://ieeexplore.ieee.org/document/5505301?arnumber=5505301

[100] G. Makhoul, F. Mani, R. D’Errico, and O. Oestges, “Time Correlation Properties of Dynamic Mobile to Mobile Channels in Indoor Environments,” in *Proc. EuCAP’16 - 10th European Conference on Antennas and Propagation*, Davos, Switzerland, Apr. 2016. [Online]. Available: https://doi.org/10.1109/EuCAP.2016.7481961

[101] A. F. Molisch, *Wireless Communications*, 2nd ed. Chichester, UK: John Wiley & Sons, 2011.

[102] T. Camp, J. Boleng, and V. Davies, “A Survey of Mobility Models for Ad Hoc Network Research,” *Wireless Communications and Mobile Computing*, vol. 2, no. 5, pp. 483–502, Aug. 2002. [Online]. Available: http://dx.doi.org/10.1002/wcm.72

[103] H. Ren and M. Q.-H. Meng, “Understanding the Mobility Model of Wireless Body Sensor Networks,” in *Proc. ICIA’06 - International Conference on Information Acquisition*, Weihai, China, Aug. 2006. [Online]. Available: https://doi.org/10.1109/ICIA.2006.306015

[104] M. Nabi, M. Geilen, and T. Basten, “MoBAN: A Configurable Mobility Model for Wireless Body Area Networks,” in *Proc. SIMUTools’11 - 4th International ICST Conference on Simulation Tools and Techniques*, Barcelona, Spain, Mar. 2011. [Online]. Available: http://dl.acm.org/citation.cfm?id=2151054.2151088

[105] M. Gallo, P. S. Hall, and M. Bozzetti, “Use of Animation Software in the Simulation of On-Body Communication Channels,” in *Proc. LAPC’07 - Loughborough Antennas Propagation Conference*, Loughborough, UK, Apr. 2007. [Online]. Available: https://doi.org/10.1109/LAPC.2007.367437

[106] M. Gallo, P. S. Hall, Y. I. Nechayev, and M. Bozzetti, “Use of Animation Software in Simulation of On-Body Communications Channels at 2.45 GHz,” *IEEE Antennas and Wireless Propagation Letters*, vol. 7, pp. 321–324, July 2008. [Online]. Available: https://doi.org/10.1109/LAPC.2007.367437

[107] M. Gallo, P. S. Hall, Q. Bai, Y. I. Nechayev, C. C. Constantinou, and M. Bozzetti, “Simulation and Measurement of Dynamic On-Body Communication Channels,” *IEEE Transactions on Antennas and Propagation*, vol. 59, no. 2, pp. 623–630, Feb. 2011. [Online]. Available: https://doi.org/10.1109/TAP.2010.2093498

[108] T. Aoyagi, I. Iswandi, M. Kim, J.-I. Takada, K. Hamaguchi, and R. Kohno, “Body Motion and Channel Response of Dynamic Body Area Channel,” in *Proc. EuCAP’11 - 5th European Conference on Antennas and Propagation*, Rome, Italy, Apr. 2011.

[109] C. Oliveira and L. M. Correia, “Perspectives for the use of MIMO in Dynamic Body Area Networks,” in *Proc. EuCAP’13 - 7th European Conference on Antennas and Propagation*, Gothenburg, Sweden, Apr. 2013. [Online]. Available: https://ieeexplore.ieee.org/document/6546312/

[110] S. L. Cotton, W. G. Scanlon, and B. K. Madahar, “Millimeter-Wave Soldier-to-Soldier Communications for Covert Battlefield Operations,” *IEEE Communications Magazine*, vol. 47, no. 10, pp. 72–81, Oct. 2009. [Online]. Available: https://doi.org/10.1109/MCOM.2009.5273811

[111] S. L. Cotton, W. G. Scanlon, and P. S. Hall, “A Simulated Study of Co-channel Inter-BAN Interference at 2.45 GHz and 60 GHz,” in *Proc. EuWIT’10 - 3rd European Wireless Technology Conference*, Paris, France, 2010. [Online]. Available: http://ieeexplore.ieee.org/abstract/document/5615120/

[112] M. Mackowiak and L. M. Correia, “Modelling Dynamic Body-to-Body Channels in Outdoor Environments,” in *Proc. URSI-GASS’14 - XXXI URSI General Assembly and Scientific Symposium*, Beijing, China, Aug. 2014. [Online]. Available: https://doi.org/10.1109/URSIGASS.2014.6929652

[113] Iswandi, A. Aoyagi, M. Kim, and J.-I. Takada, “The Utilization of Body Skeleton Model for Modeling the Dynamic BAN Channels,” in *Proc. EuCAP’12 - 6th European Conference on Antennas and Propagation*, Prague, Czech Republic, Mar. 2012. [Online]. Available: https://doi.org/10.1109/EuCAP.2012.6206616

[114] M. M. Alam and E. B. Hamida, “Towards Accurate Mobility and Radio Link Modeling for IEEE 802.15.6 Wearable Body Sensor Networks,” in *Proc. WiMob’14 - 10th International Conference on Wireless and Mobile Computing, Networking and Communications*, Larnaca, Cyprus, Oct. 2014. [Online]. Available: https://doi.org/10.1109/WiMOB.2014.6962186

[115] M. M. Alam, E. B. Hamida, D. B. Arbia, M. Maman, F. Mani, B. Denis, and R. D’Errico, “Realistic Simulation for Body Area and Body-To-Body Networks,” *Sensors*, vol. 16, no. 4, Apr. 2016. [Online]. Available: http://dx.doi.org/10.3390/s16040561

[116] K. Y. Yazdandoost and K. Sayrafian-Pour, “Channel Model for Body Area Network (BAN),” *IEEE P802.15-08-0780-09-0006*, 2009. [Online]. Available: https://mentor.ieee.org/802.15/dcn/08/15-08-0780-09-0006-tg6-channel-model.pdf

[117] B. Denis, O. P. Pasquero, R. D’Errico, N. Amiot, B. Uguen, E. Plouhinec, S. Avrillon, M. Mhedhbi, J. G. A. Mauricio, C. Goursaud, J.-M. Gorce, and J. Hamie, “CORMORAN - Final Simulattion Tool,” National Agency for Research, Paris, France, Technical Report D2.6, 2015. [Online]. Available: http://pylayers.github.io/pylayers/deliverables/CORMORAN_D2.6_Final_V1.1.pdf

[118] Y. He, X. Cheng, and G. L. Stüber, “On Polarization Channel Modeling,” *IEEE Wireless Communications*, vol. 23, no. 1, pp. 80–86, Feb. 2016. [Online]. Available: https://doi.org/10.1109/MWC.2016.7422409

[119] L. Akhoondzadeh-Asl, P. S. Hall, Y. Nechayev, and I. Khan, “Depolarization in On-Body Communication Channels at 2.45 GHz,” *IEEE Transactions on Antennas and Propagation*, vol. 61, no. 2, pp. 882–889, Feb. 2013. [Online]. Available: http://dx.doi.org/10.1109/TAP.2012.2224833

[120] C. A. Balanis, *Advanced Engineering Electromagnetics*, 2nd ed. New York, NY, USA: John Wiley & Sons, 2012.

[121] C. Oliveira, M. Mackowiak, and L. M. Correia, “Modelling On- and Off-Body Channels in Body Area Networks,” in *Proc. IMOC’13 - SBMO/IEEE MTT-S International Microwave Optoelectronics Conference*, Rio de Janeiro, Brazil, Aug. 2013. [Online]. Available: https://doi.org/10.1109/IMOC.2013.6646610

[122] M. Mackowiak and L. M. Correia, “MIMO Capacity Analysis of Off-Body Radio Channels in a Street Environment,” in *Proc. VTC’13-Spring - 77th IEEE Vehicular Technology Conference*, Dresden, Germany, June 2013. [Online]. Available: https://doi.org/10.1109/VTCSpring.2013.6692632

[123] S. C. Kwon and G. L. Stüber, “Polarization Division Multiple Access on NLoS Wide-Band Wireless Fading Channels,” *IEEE Transactions on Wireless Communications*, vol. 13, no. 7, pp. 3726–3737, July 2014. [Online]. Available: https://doi.org/10.1109/TWC.2014.2314118

[124] T. S. Rappaport, *Wireless Communications: Principles and Practice*. Upper Saddle River, NJ, USA: Prentice Hall PTR, 2002.

[125] R. Kouyoumjian and P. Pathak, "A Unifm Geometrical Theory of Diffraction for an Edge in a Perfectly Conducting Surface," *Proceedings of the IEEE*, vol. 62, no. 11, pp. 1448–1461, Nov. 1974. [Online]. Available: http://dx.doi.org/10.1109/PROC.1974.9651

[126] D. A. McNamara, C. W. Pistorius, and J. Malherbe, *Introduction to the Uniform Geometrical Theory of Diffraction*. Norwood, MA, USA: Artech House, 1990.

[127] M. Shafi, M. Zhang, A. L. Moustakas, P. J. Smith, A. F. Molisch, F. Tufvesson, and S. H. Simon, "Polarized MIMO Channels in 3D: Models, Measurements and Mutual Information," *IEEE Journal on Selected Areas in Communications*, vol. 24, no. 3, pp. 514–527, Mar. 2006. [Online]. Available: https://doi.org/10.1109/JSAC.2005.862398

[128] A. Maltsev, R. Maslennikov, A. Lomayev, A. Sevastyanov, and A. Khoryaev, "Statistical Channel Model for 60 GHz WLAN Systems in Conference Room Environment," *Radioengineering*, vol. 20, no. 2, pp. 409–422, June 2011. [Online]. Available: https://www.radioeng.cz/fulltexts/2011/11_02_409_422.pdf

[129] R. Luebbers, "Finite Conductivity Uniform GTD Versus Knife Edge Diffraction in Prediction of Propagation Path Loss," *IEEE Transactions on Antennas and Propagation*, vol. 32, no. 1, pp. 70–76, Jan. 1984. [Online]. Available: http://dx.doi.org/10.1109/TAP.1984.1143189

[130] R. Kouyoumjian and P. Pathak, "The Dyadic Diffraction Coefficient for a Curved Edge," Ohio State University, ElectroScience Laboratory, Columbus, OH, USA, Technical Report 3001-3, Aug. 1973, prepared under Grant NGR 36-008-144 for NASA, Langley Research Center. [Online]. Available: https://ntrs.nasa.gov/archive/nasa/casi.ntrs.nasa.gov/19740020597.pdf

[131] B. R. Levy and J. B. Keller, "Diffraction by a Smooth Object," *Communications on Pure and Applied Mathematics*, vol. 12, no. 1, pp. 159–209, Feb. 1959. [Online]. Available: https://doi.org/10.1002/cpa.3160120108

[132] P. Pathak, W. Burnside, and R. Marhefka, "A Uniform GTD Analysis of the Diffraction of Electromagnetic Waves by a Smooth Convex Surface," *IEEE Transactions on Antennas and Propagation*, vol. 28, no. 5, pp. 631–642, 1980. [Online]. Available: https://doi.org/10.1109/TAP.1980.1142396

[133] E. Plouhinec, B. Uguen, M. Mhedhbi, and S. Avrillon, "3D UTD Modeling of a Measured Antenna Disturbed by a Dielectric Circular Cylinder in WBAN Context," in *Proc. VTC'14-Spring - 79th IEEE Vehicular Technology Conference*, Seoul, South Korea, May 2014.

[134] T. Mavridis, L. Petrillo, J. Sarrazin, D. Lautru, A. Benlarbi-Delai, and P. De Doncker, "Near-Body Shadowing Analysis at 60 GHz," *IEEE Transactions on Antennas and Propagation*, vol. 63, no. 10, pp. 4505–4511, Oct. 2015. [Online]. Available: https://doi.org/10.1109/TAP.2015.2456984

[135] M. Ghaddar, L. Talbi, T. A. Denidni, and A. Sebak, "A Conducting Cylinder for Modeling Human Body Presence in Indoor Propagation Channel," *IEEE Transactions on*

Antennas and Propagation, vol. 55, no. 11, pp. 3099–3103, Nov. 2007. [Online]. Available: https://doi.org/10.1109/TAP.2007.908563

[136] M. Unuma, K. Anjyo, and R. Takeuchi, "Fourier Principles for Emotion-based Human Figure Animation," in *Proc. SIGGRAPH'95 - 22nd Annual Conference on Computer Graphics and Interactive Techniques*, Los Angeles, CA, USA, Aug. 1995. [Online]. Available: https://doi.org/10.1145/218380.218419

[137] R. Parent, *Computer Animation: Algorithms and Techniques*, 3rd ed. Waltham, MA, USA: Elsevier, 2012.

[138] Carnegie Mellon University, Graphics Lab – Motion Capture Database. http://mocap.cs.cmu.edu/. [Accessed: Apr. 2019].

[139] MATLAB Motion Capture Toolbox. http://inverseprobability.com/mocap. [Accessed: Apr. 2019].

[140] MathWorks, MATLAB. http://www.mathworks.com. [Accessed: Apr. 2019].

[141] J. D. Parsons and A. Turkmani, "Characterisation of Mobile Radio Signals: Model Description," *IEE Proceedings I (Communications, Speech and Vision)*, vol. 138, no. 6, pp. 549–556, Dec. 1991. [Online]. Available: http://dx.doi.org/10.1049/ip-i-2.1991.0072

[142] M. Mackowiak, C. Oliveira, and L. M. Correia, "Radiation Pattern of Wearable Antennas: A Statistical Analysis of the Influence of the Human Body," *International Journal of Wireless Information Networks*, vol. 19, no. 3, pp. 209–218, July 2012. [Online]. Available: http://dx.doi.org/10.1007/s10776-012-0188-y

[143] C. Medeiros, A. Castela, J. Costa, and C. Fernandes, "Evaluation of Modelling Accuracy of Reconfigurable Patch Antennas," in *Proc. of ConfTele'07 - Conference on Telecommunications*, Peniche, Portugal, May 2007. [Online]. Available: https://www.it.pt/Publications/PaperConference/4395

[144] S.-C. Kwon and G. Stüber, "Wireless Polarized-Channel Simulator," in *Proc. VTC'14-Fall - 80th IEEE Vehicular Technology Conference*, Vancouver, BC, Canada, 2014. [Online]. Available: http://dx.doi.org/10.1109/VTCFall.2014.6966234

[145] *Vector Signal Generator SMBV100A, Operating Manual*, Rohde & Schwarz, Feb. 2015. [Online]. Available: https://www.rohde-schwarz.com/pt/manual/r-s-smbv100a-vector-signal-generator-operating-manual-manuals-gb1_78701-37699.html

[146] *Flexible Coax Cable Single Shielded with Black PVC Jacket RG174, Technical Data Sheet*, Pasternack, Jul. 2015. [Online]. Available: https://www.pasternack.com/images/ProductPDF/RG174A-U.pdf

[147] *Spectrum Master, High Performance Handheld Spectrum Analyzer MS2724B, Technical Data Sheet*, Anritsu, Nov. 2017. [Online]. Available: http://www.technicaldiagnostic.com/Equipment/SpecSheets/Anritsu%20MS2724B.pdf

[148] *0.7-6.0 GHz Open Boundary Quad-Ridged Horn LB-OSJ-0760, Technical Specification*, A-Info, Feb. 2015. [Online]. Available: http://www.ainfoinc.com/en/pro_pdf/new_products/antenna/Dual%20Polarization%20Horn%20Antenna/tr_LB-OSJ-0760.pdf

[149] *Electromechanical Coaxial Switch TS121*, Tesoel, Feb. 2015. [Online]. Available: http://www.tesoel.se/ts-100.html

[150] *Coax Cable Sucoflex 104*, Helmut Singer Elektronik, Jul. 2015. [Online]. Available: http://www.helmut-singer.de/pdf/sucoflex104pb.pdf

[151] *Vector Network Analyzer E5071C ENA, Data Sheet*, Keysight Technologies, May 2018. [Online]. Available: https://literature.cdn.keysight.com/litweb/pdf/5989-5479EN.pdf?id=862560

[152] *The Concept of Transmission Loss for Radio Links*, ITU-R Recommendation P.341-6, 2016. [Online]. Available: https://www.itu.int/rec/R-REC-P.341-6-201609-I/en

[153] M. Koohestani, N. Pires, A. K. Skrivervik, and A. A. Moreira, "Influence of the Human Body on a New Coplanar-fed Ultra-Wideband Antenna," in *Proc. of EuCAP'12 - 6th European Conference on Antennas and Propagation*, Prague, Czech Republic, Mar. 2012. [Online]. Available: https://doi.org/10.1109/EuCAP.2012.6205976

[154] *Dual-Dand Dipole Antenna VERT 2450, Data Sheet*, Ettus Research LLC, May 2018. [Online]. Available: https://kb.ettus.com/images/9/9e/ettus_research_vert2450_datasheet.pdf

[155] *Coax Cable Sucoflex 126*, Huber+Suhner, May 2018. [Online]. Available: https://docs-emea.rs-online.com/webdocs/1558/0900766b81558961.pdf

[156] *VISA, Universal I/O Interface Software*, National Instruments, May 2018. [Online]. Available: http://sine.ni.com/nips/cds/view/p/lang/en/nid/12145

[157] R. A. Valenzuela, O. Landron, and D. L. Jacobs, "Estimating Local Mean Signal Strength of Indoor Multipath Propagation," *IEEE Transactions on Vehicular Technology*, vol. 46, no. 1, pp. 203–212, Feb. 1997. [Online]. Available: http://dx.doi.org/10.1109/25.554753

[158] C. Walck, *Hand-book on Statistical Distributions for Experimentalists*, University of Stockholm, Stockholm, Sweden, 2007. [Online]. Available: http://www.stat.rice.edu/~dobelman/textfiles/DistributionsHandbook.pdf

[159] *Probability Distributions Relevant to Radiowave Propagation Modelling*, ITU-R Recommendation P.1057-4, July 2015. [Online]. Available: https://www.itu.int/rec/R-REC-P.1057-4-201507-I/en

[160] K. P. Burnham and D. R. Anderson, *Model Selection and Multimodel Inference*, 2nd ed. New York, NY, USA: Springer, 2002. [Online]. Available: http://dx.doi.org/10.1007/b97636

[161] A. M. Mathai and P. Rathie, *Probability and Statistics*. London, UK: Macmillan Press, 1977.

[162] *Definitions of Terms Relating to Propagation in Non-Ionized Media*, ITU-R Recommendation P.310-9, Aug. 1994. [Online]. Available: https://www.itu.int/rec/R-REC-P.310-9-199408-I/en

[163] J.-J. Fuchs, “Multipath Time-Delay Detection and Estimation,” *IEEE Transactions on Signal Processing*, vol. 47, no. 1, pp. 237–243, Jan. 1999. [Online]. Available: https://doi.org/10.1109/78.738263

[164] CVX: Matlab Software for Disciplined Convex Programming. http://cvxr.com/cvx/. [Accessed: Apr. 2019].

[165] K. Turbic, S. J. Ambroziak, and L. M. Correia, “A Body-Shadowing Model for Off-Body and Body-to-Body Communications,” in *Proc. URSI’18 - Baltic URSI Symposium*, Poznan, Poland, May 2018. [Online]. Available: https://doi.org/10.23919/URSI.2018.8406703

[166] K. Turbic, L. M. Correia, and M. Beko, “A Mobility Model for Wearable Antennas on Dynamic Users,” *IEEE Access*, vol. 6, no. 1, pp. 63 635–63 648, Dec. 2018. [Online]. Available: https://doi.org/10.1109/ACCESS.2018.2877500